Radboud Repository

Radboud University Nijmegen

PDF hosted at the Radboud Repository of the Radboud University Nijmegen

The following full text is a publisher's version.

For additional information about this publication click this link.
http://hdl.handle.net/2066/45154

Please be advised that this information was generated on 2017-12-06 and may be subject to change.

Complex Hydrides

A collection of Density Functional studies

M. J. van Setten

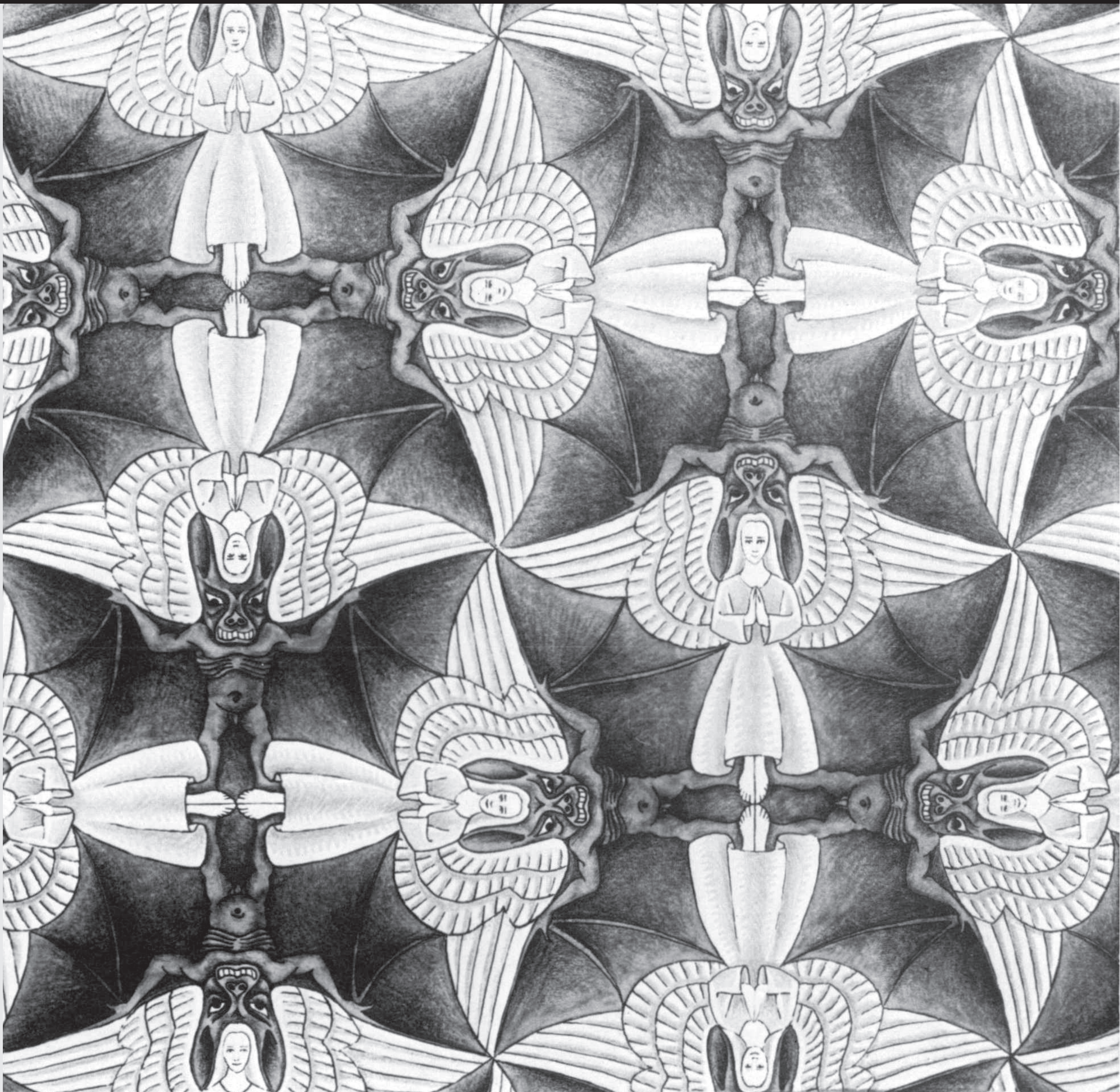

Complex Hydrides

A collection of Density Functional studies

Een wetenschappelijke proeve op het gebied van de Natuurwetenschappen,
Wiskunde en Informatica.

Proefschrift

ter verkrijging van de graad van doctor
aan de Radboud Universiteit Nijmegen
op gezag van de rector magnificus prof. mr. S.C.J.J. Kortmann,
volgens besluit van het College van Decanen
in het openbaar te verdedigen op donderdag 28 augustus 2008
om 15.30 uur precies.

door

Michiel Jan van Setten
geboren op 14 april 1978
te Vlissingen.

Promotor	Prof. dr. R. A. de Groot
Copromotores	Dr. ir. G. A. de Wijs
	Dr. G. Brocks (Universiteit Twente)
Manuscriptcommissie	Prof. dr. A. P. M. Kentgens (Chairman)
	Prof. dr. R. Griessen (Vrije Universiteit Amsterdam)
	Prof. dr. E. J. Baerends (Vrije Universiteit Amsterdam)

The work presented in this thesis is part of the Sustainable Hydrogen programme of the "Advanced Catalytic Technologies for Sustainability (ACTS)" and the "Stichting voor Fundamenteel Onderzoek der Materie (FOM)", both financially supported by the "Nederlandse Organisatie voor Wetenschappelijk Onderzoek (NWO)".

Kaft:
Studie van regelmatige vlakvulling met engelen en duivels
M.C. Escher 1941

ISBN/EAN 978-90-6464-254-8

for Vera, Raphael and Gabrielle

Angels and Demons

The drawing "angels and demons" by M.C. Escher on the cover of this thesis nicely captures the essence of solid state hydrogen storage. One can imagine that angels put together closely in a confined space will live in peace whereas demons will most probably start a fight and destroy the confinement. However, when angels are placed in between, the demons can't see each other and hence can be brought more closely together than without the angels present.

Hydrogen molecules have a similar relationship with each other as the demons and with most metals as the demons with the angels. Pure metals form strongly bound and closely packed structures. Hydrogen on the other hand is a rather voluminous gas under ambient conditions. The hydrogen molecules dislike each other so much that how ever hard you push them together they will never form a liquid at temperatures above 32 K. However, when hydrogen, in the atomic form, enters a metal the hydrogen atoms become "shielded" by the metal atoms and can come far closer together than without the metal atoms present. A density about three times larger and liquid hydrogen can be achieved in this way.

In life we also need the angels to bear the ever present demons - sometimes we even need the demons on their own right to bear the angels. In the last years many angels have stood my me to bear the larger and smaller demons. Especially I would like to thank a few of them.

Gilles de Wijs, my daily supervisor, taught me about everting I know about DFT calculations, I had no experience in that field to begin with. Together we started to explore the world of hydrogen storage materials. Gilles, thanks for all the endless discussions and friendly advice. My promotor Rob de Groot has been of much help in offering other views on problem that were not yet considered, thanks for that. The other members of the electronic structure of materials group Jisk, Matthé, Luviu, Changming, Remco and Karol I thank for the nice environment and all the more and less scientific discussions.

A special word of thanks goes to my second copromotor Geert Brocks form Twente who has been a critical reader and corrector of almost al the work presented in this thesis. Victor and Suleyman, also from Twente, thanks for the joined publications.

A lot of the work in this thesis was aided or initiated by the many discussions and collaborations with the Condensed Matter Physics group at the Vrije Universteit have contributed to the research in this thesis. I which to thank Ronald Griessen and Bernard Dam and the PhD. students and post-docs, Robin, Dana, Andrea and Marta, of their group for this.

At the final part of my PhD. research I spent about half a year at the hydrogen storage group of Maximilian Fichtner at the Forschungszentrum Karlsruhe. I which to thank him

and Wiebke and Nobuko for the wonderful possibility to work inside an experimental group.

During my PhD. research within the ACTS Sustainable hydrogen program I have enjoyed many formal and informal discussion, lectures and workshops organized within this program. I which to thank the members of the programm committee for all these. This entire project would, in fact, not have been possible without the financial support from the ACTS Sustainable hydrogen program and FOM.

Finally I want to thank all my friends and family for their support, especially my parents, for making all of this possible in the first place, my brother, and my parents in law for the endless hours of baby sitting. And then there is my little 'arch' angel Raphael who almost seems quantum mechanical in nature in his ability to be in a super position of angel and demon - just blink your eyes and he may have flipped to the other state - but who has always been a help, in both of his appearances. The most important angel, however, came just when I was to lose the other most important one and has become a stronger angel ever since. Vera, "tot de lucht".

Michiel van Setten
Heidelberg, April 2008

Contents

Chapter 1

Hydrogen as a fuel

Since the beginning of the industrial revolution mankind has engaged itself in an ever increasing struggle for cheaper and more efficient energy sources and carriers. Starting from coal, with the discovery of the steam engine in 1792, the market converged to lighter and easier to handle oil around 1900. Subsequently, around 1950, a (partial) conversion to natural gas began. This gradual conversion towards lighter materials meant a conversion towards materials containing less carbon and more hydrogen, which increases the energy density. The final step in this conversion is that towards the use of pure hydrogen as an energy carrier. This final step is fundamentally different from the previous. Where coal, oil and natural gas can be mined hydrogen needs to be produced using a primary energy source. Hydrogen, therefore, is only an energy carrier rather than an energy source.

There are many reasons for this last transition and to leave the fossil fuels. One of the most important is that burning fossil fuels produces the greenhouse gas CO_2. At present the CO_2 concentration in the atmosphere is much higher than it has been in the past 400.000 years. CO_2, and other greenhouse gasses, reflect infra-red radiation. Increased concentrations of greenhouse gasses in the atmosphere disturb the subtle equilibrium between incident heat from the sun and heat radiated from the Earth's surface. In principle fossil fuels could be used without releasing CO_2 into the atmosphere. This can be achieved by separating the CO_2 from the other exhaust gasses and subsequently storing it. Especially separating the CO_2 is expensive and significantly lowers the overall efficiency of the energy production. However, even when all CO_2 would be segregated the usage of fossil fuels poses a large problem.

Oil, coal and also nuclear energy are reaching a global peak in production where on the other hand the demand for energy is increasing. In the case of oil and natural gas all large fields have already passed their peak production and it is not to be expected that new large fields will be discovered. The production of oil has already peaked in 2006 and will start to decline at a rate of several percent per year.[1] In the case of coal the two largest producers, the USA and China, have already passed the peak in the production of high quality coal. In the period of 1987 to 2005 the total global coal reserves have been downgraded by 15% and the total global resources by 50%. The overall global production is expected to peak around 2025 at a production of at best 30% above current production.[2] At current demand the proven reserves and stocks of uranium will be exhausted in thirty years and neither breeding nor thorium reactors will play a significant roll in this timescale due to their long lead times in development and market penetration.[3] Additionally, the number of scheduled new reactors does not come close to replacing, let alone increasing, the current installed nuclear capacity.

To cover the energy demand, renewable energy sources will be needed. The two most promising, wind power and solar power, however produce electricity or heat and cannot be turned on when and where energy is needed. The usage of these therefore implies the need for an efficient energy storage and transport system.

Since hydrogen can be produced from water, either thermally of via electrolysis, it can be produced whenever a source of energy is available. Other energy carriers always need additional materials. Batteries need metals and have a relatively low gravimetric energy density. Another option, synthetic carbon based fuels, need a supply of carbon. This carbon can in the long run only come from returning the CO_2 that is produced in burning the synthetic fuel. Segregating the CO_2 and returning it to a regeneration plant seriously decreases the efficiency of using a carbon based synthetic fuel as energy carrier.

An advantage of hydrogen over the previous energy carriers is that it can, rather efficiently, be converted into electricity by using a fuel cell. The most likely candidate of for this mobile application is the proton exchange membrane (PEM) fuel cell. The combination of a fuel cell and electric engine is far more efficient than an internal combustion engine (ICE) running on hydrogen. Additionally, using a fuel cell only produces water vapor as exhaust whereas an ICE on hydrogen (and air) also produces NO_x. Another advantage of this approach is that an electric engine produces far less noise than an ICE and shows less wear due to the smaller amount of moving parts. The disadvantage of the fuel cell is that they are still expensive and require precious metals.

The transition towards hydrogen as a carrier is different from the steps to oil and natural gas in yet an other important way. Oil is far more convenient to handle than coal and natural gas has good transport properties. Hydrogen, on the other hand is worse in almost every aspect. The problems with hydrogen start with its low density. At atmospheric pressure one kilogram of hydrogen takes a volume of 11 m^3. Hydrogen gas can be compressed but the decrease in volume is by far not as large as for natural gas. One of the main bottlenecks in the transition towards an economy based on hydrogen as a fuel is hence the storage of hydrogen.

Especially for mobile application the challenge of storing hydrogen is a hard one. Many factors need to be considered when searching for an applicable storage system. The US department of energy (DOE) together with the US car industry have formulated demands for a storage system for mobile application. A summary of these demands is given in Figure 1.1. From these targets originates the, often cited, 6 to 10 wt.% of hydrogen in a storage system. It must be noted, however, that European and Japanese car industries are already willing to accept a 5 wt.% hydrogen storage system.

Handling hydrogen safely asks for new rules and regulations. Hydrogen has rather different physical properties than the currently used fuels, see Table 1.1. The main reason for caution when using hydrogen is the large heat of combustion and the broad range of fractions in air that lead to a combustible mixture. Depending on the constitution,

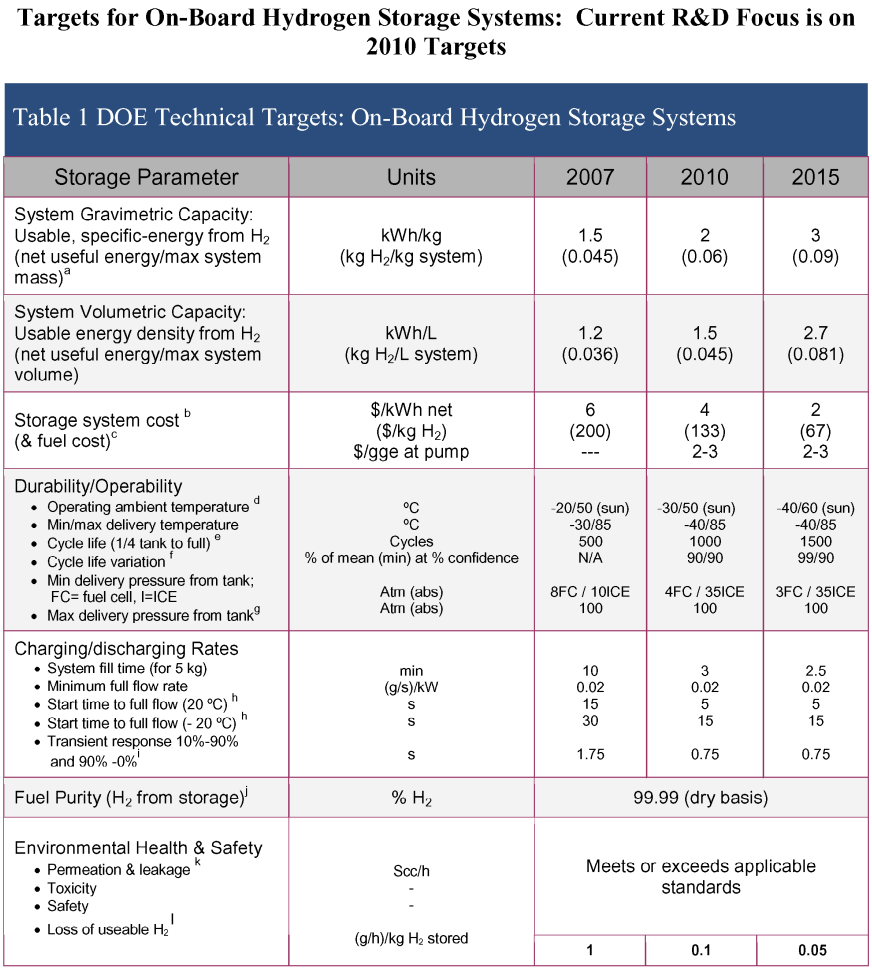

Targets for On-Board Hydrogen Storage Systems: Current R&D Focus is on 2010 Targets

Table 1 DOE Technical Targets: On-Board Hydrogen Storage Systems

Storage Parameter	Units	2007	2010	2015
System Gravimetric Capacity: Usable, specific-energy from H_2 (net useful energy/max system mass)[a]	kWh/kg (kg H_2/kg system)	1.5 (0.045)	2 (0.06)	3 (0.09)
System Volumetric Capacity: Usable energy density from H_2 (net useful energy/max system volume)	kWh/L (kg H_2/L system)	1.2 (0.036)	1.5 (0.045)	2.7 (0.081)
Storage system cost [b] (& fuel cost)[c]	$/kWh net ($/kg H_2) $/gge at pump	6 (200) ---	4 (133) 2-3	2 (67) 2-3
Durability/Operability				
• Operating ambient temperature [d]	°C	-20/50 (sun)	-30/50 (sun)	-40/60 (sun)
• Min/max delivery temperature	°C	-30/85	-40/85	-40/85
• Cycle life (1/4 tank to full) [e]	Cycles	500	1000	1500
• Cycle life variation [f]	% of mean (min) at % confidence	N/A	90/90	99/90
• Min delivery pressure from tank; FC= fuel cell, I=ICE	Atm (abs)	8FC / 10ICE	4FC / 35ICE	3FC / 35ICE
• Max delivery pressure from tank[g]	Atm (abs)	100	100	100
Charging/discharging Rates				
• System fill time (for 5 kg)	min	10	3	2.5
• Minimum full flow rate	(g/s)/kW	0.02	0.02	0.02
• Start time to full flow (20 °C) [h]	s	15	5	5
• Start time to full flow (- 20 °C) [h]	s	30	15	15
• Transient response 10%-90% and 90% -0%[i]	s	1.75	0.75	0.75
Fuel Purity (H_2 from storage)[j]	% H_2	99.99 (dry basis)		
Environmental Health & Safety				
• Permeation & leakage [k]	Scc/h	Meets or exceeds applicable standards		
• Toxicity	-			
• Safety	-			
• Loss of useable H_2 [l]	(g/h)/kg H_2 stored	**1**	**0.1**	**0.05**

Figure 1.1: *DOE targets for hydrogen storage for mobile applications.*

temperature and pressure of the mixture of hydrogen and air, combustion can involve laminar and flagrant flame propagation and detonation. The high diffusion coefficient and auto ignition temperature on the other hand provide handles for reducing risks.

A final issue with hydrogen is that when in contact with metals, hydrogen has the tendency to dissociate and penetrate the metal, which causes embrittlement. This final problem, as we will see, may hold the key to solving the storage problem.

In the following sections the options for hydrogen storage are briefly discussed. More

Table 1.1: *Selected physical properties of hydrogen compared to petrol vapor and propane.*

	Petrol vapor	Propane	Hydrogen
Combustible fraction in air (%)	1.03 - 6.0	1.7 - 10.9	4 - 75
Laminar flame velocity (m/s)	0.4	0.4	2.7
Diffusion coefficient (cm^2/s)	0.05	0.12	0.61
Heat of combustion (MJ/kg)	40	50	140
Auto ignition temperature (°C)	215	450	585

detailed discussions on the aspects of the various options for hydrogen storage can be found in some selected extensive review papers on hydrogen storage in general,[4–7] in metal hydrides,[8] in complex hydrides,[9] in metal organic frameworks,[10] and on combined reactions.[11] In the October 2007 thematic issue on hydrogen of Chemical Reviews (volume 107, issue 10) many additional reviews on these topics can be found.

Pressurized gas

The most obvious and most often used way to store hydrogen is as a pressurized gas. Depending on the type of container the maximal pressure ranges from 200 bar, in steel containers, to 800 bar, in composite containers. However, where liquid petrol gas stays liquid at moderately elevated pressures, about 25 bar depending on temperature and composition, hydrogen does not. The volume reduction that is gained by pressurizing the gas is therefore limited. In fact, even at 800 bar, the volumetric density of 36 kg/m^3 is small for automotive applications. Besides this obvious disadvantage such high pressures bring other problems. Bringing the gas to these tremendous pressures costs a lot of energy. Producing a pressure of 800 bar at room temperature consumes about 2.21 kwh/kg, about 14% of the lower heating value of hydrogen combustion. Furthermore the handling and generation of these kind of pressures is technologically far from trivial.

Cryogenic liquid

The volume of the stored hydrogen can also be reduced by liquefying it. Hydrogen can be made liquid by cooling it below 21.2 K at 1 bar. Storing it in this way meets the volumetric demand; the volumetric density of liquid hydrogen is 70.8 kg/m^3. The problems and disadvantages of liquid storage, however, are even larger than those of pressurized gas storage. Cooling hydrogen to the temperature where it becomes liquid takes at least 15.2 kwh/kg, almost half of the lower heating value of hydrogen combustion. The second main problem is boil-off. Because there is no existing liquid phase above the critical temperature of hydrogen (33 K) liquid hydrogen has to be stored in an open system in order to avoid an pressure buildup. Depending on the size, shape, and thermal isolation the boil-off loss typically ranges from 0.06% per day for 50.000 m^3 tanks to 0.4% for 50 m^3 tanks.

Oxidation of metals

In an indirect way hydrogen can be stored in reactive metals such as lithium, sodium, aluminum or zink. These metals can be easily reacted with water forming the corresponding hydroxides and hydrogen. To close the cycle the hydroxides can be thermally reduced in a solar furnace. This way of producing hydrogen is in fact one of the oldest known. For instance the hydrogen used in the first zeppelins was produced in this way. The main advantage of this method is that a reasonably high gravimetric hydrogen content can be reached, 6.3 wt.%, and that the desorption reaction is fast and requires no heating like with use of hydrides. The main disadvantage of this method is that the regeneration of the oxides usually requires high temperatures and large amounts of energy (the maximum energy conversion efficiency is 29%). This means that the regenerations needs to be done in large centralized plants and hence requires additional transport.

Physisorbed

Physisorption of gas molecules on a surface is the result of Van der Waals interactions between the two. The binding energy is usually of the order of 0.01–0.1 eV. Due to this weak interaction a significant physisorption only occurs below room temperature.

Various high surface area materials have been investigated for the use of hydrogen storage by means of physisorption. Carbon nanotubes have been shown to take up to 1 wt.% of hydrogen. The maximal absorption theoretical capacity is 2 wt.%. Metal organic frameworks (MOF) have a capacity up to 4.5 wt.% at 78 K and 1 wt.% at room temperature and 20 bar. Improvements are not expected to increase these numbers needed to reach the gravimetric storage targets and hence physisorption is not likely to be a useful option for hydrogen storage.

Metal hydrides

Many metals, alloys and intermetallic compounds can react with hydrogen to form metal-hydrides. The bonding in the metal hydrides ranges from ionic to metallic to covalent and there is no always a clear distinguishing between these kinds of bonding. This section discusses hydrogen storage in ionic and metallic hydrides.

Storing hydrogen in metal hydrides can be rather efficient if the metal to hydride transition has the right thermodynamics. When the hydride formation enthalpy is about 40 kJ/mol H_2 the system will have an equilibrium pressure of 1 bar at room temperature. Increasing the temperature hence produces an overpressure of hydrogen. When such a storage system is used in combination with a PEM fuel cell, which operates at about 90°C, the rest heat of the fuel cell can be used to drive the hydrogen desorption reaction.

Alkali and alkaline earth metals all form ionic hydrides. They have a fixed stoichiometry, one hydrogen atom per alkali atom and two per alkaline earth atom. These ionic hydrides are all far too stable to be used for hydrogen storage. MgH_2, being the least stable still has a hydride formation enthalpy of -0.78 eV/H_2.

The majority of the transition metals and lanthanides form metallic hydrides. Metallic hydrides usually occur in various stoichiometries and are stable in a range around the stoichiometric composition. The main problem with these hydrides is that the hydrogen content is too low (< 4 wt.%). On the other hand, due to the almost endless possibility to produce alloys, hydrides with almost perfect thermodynamics and kinetics can be produced, like $LaNiH_5$ and FeTiH.

Complex hydrides

Under complex hydrides are usually understood those hydrides that contain complex anions in which the hydrogen atoms are bound more or less covalently to a central atom. Two classes of these, the alanates and boranates, are discussed in first part of this thesis. They consist of $(AlH_4)^-$ or $(BH_4)^-$ anions and have been shown to exist with almost all alkali and alkali earth elements. The boranates have also been found to form with several transition metals. The large amount of possible combinations in this class of hydrides makes it possible to engineer their properties. An other class of complex hydrides is formed by combinations of magnesium and late transition metals. The most famous one is Mg_2NiH_4. Two magnesium atoms donate their two electrons to a NiH_4 cluster which then has eighteen electrons to form a closed shell configuration. Also the combinations of magnesium with iron and cobalt are known to form similar hydrides. Although the kinetics of the desorption reactions of these hydrides are better then that of MgH_2 the thermodynamics are far from favorable. Furthermore, the weight percentage of hydrogen in these hydrides is rather low. In this class also some possibility of optimization exists by using different combinations of transition metals. This class of materials is discussed in more detail in the second part of this thesis.

Composite reactions

One of the most recent developments in solid state hydrogen storage is the combination of a complex hydride and a simple (binary) hydride.

One example is a combination of an amide, containing NH_2 units, and a simple hydride forming an imide, containing NH units, and hydrogen. The prototype reaction is that of lithium amide with lithium hydride:

$$LiNH_2 + LiH \leftrightarrow Li_2NH + H_2 \tag{1.1}$$

An other type of composite reactions combines boranates with simple hydrides. An example of this is the combination of lithium boranate with magnesium hydride:

$$LiBH_4 + MgH_2 \leftrightarrow LiH + MgB_2 + 4H_2 \tag{1.2}$$

In this reaction 11.5 wt.% of hydrogen is released and the thermodynamics are close to ideal. The kinetics, however still need improvements.

This method of combined reactions is promising because many reversible reactions have been found. In both types of composite reactions there are two, possible different, metals involved. This gives ample possibility to engineer the reaction enthalpy. A general problem with these composite reactions is that they all involve mass transport since it are solid state reactions. The kinetics of the reactions is hence a problem. An additional problem with the amide-imide systems is that the hydrogen storage capacity is not very high, maximally 6.5 wt.% when both the amide and the hydride contains lithium.

Chapter 2

Methodology

This thesis describes research on two classes of possible hydrogen storage materials, alanates and boranates and magnesium based complex hydrides. The materials in question are studied by calculating their properties. The work presented here deals with so-called first principles calculations. This means that we work with the real systems and use quantum mechanics. This field is known as computational solid state physics.

The field of computational solid state physics, or in a broader sense, computational materials science can be seen as a third leg of solid state physics next to experimental and theoretical solid state physics. It is comparable to what in chemistry is known as quantum chemistry with the difference that in chemistry the emphasis more is on molecules in contrast to solids. Computational solid state physics is different from theoretical solid state physics in the sense that in the first approximations are made to calculate, from first principles, the properties of real materials whereas in the second model systems are studied exactly.

The properties of a material are determined by its chemical composition and (crystal) structure. These two, and all its physical and chemical properties, are linked by the electronic structure, the energy levels and dispersion of these levels of the electrons in the material. Hence, studying the properties of a material automatically means studying its electronic structure. Choosing the method for performing electronic structure calculations is a matter of finding a balance between the accuracy of the method and the size of the systems that it can be used for. Given a certain amount of computing capacity, the more accurate the method the smaller the systems that can be treated. The method used here is density functional theory (DFT). Using state of the art DFT methods it is possible to calculate properties of solids with up to several hundreds of atom in the unit cell.

In the following sections the methods and theory that have been used are discussed in more detail. The first section contains a brief description of the basics of density functional theory. In the subsequent sections the actual implementation of DFT for solids and the theory used in combination with DFT is discussed.

Density functional theory

Density functional theory provides a formalism for calculating the electronic structure of materials from first principles. Via the electronic structure it gives excess to many physical and chemical properties. The basic concept of DFT is that the electron density is treated as the variational quantity. This means that the total energy of the system is written as a functional $E[n(\mathbf{r})]$ of the electron density $n(\mathbf{r})$. The ground state energy E_0 is than the minimum of this functional by varying over all densities yielding the same total number of particles. There are, however, many ways to construct such a functional.

Currently the best results for the total energy are obtained by separating the energy functional $E[n(\mathbf{r})]$ according to Kohn and Sham:[12]

$$E[n(\mathbf{r})] = T_0[n(\mathbf{r})] + \int d\mathbf{r}\; n(\mathbf{r}) \left\{ V_{ext}(\mathbf{r}) + \frac{1}{2} V_c(\mathbf{r}) \right\} + E_{xc}[n(\mathbf{r})] \tag{2.1}$$

where $T_0[n(\mathbf{r})]$ is the kinetic energy that a system with density $n(\mathbf{r})$ would have would there be no electron-electron interaction, $V_{ext}(\mathbf{r})$ an external potential and $V_c(\mathbf{r})$ the classical Coulomb potential for electrons. The final term $E_{xc}[n(\mathbf{r})]$ is called the exchange correlation functional and contains, by definition, all contributions not contained in the previous. Kohn and Sham proved that such an exchange correlation functional exists, which provides the correct energy of a system with density $n(\mathbf{r})$ in an external potential $V_{ext}(\mathbf{r})$. The prove however does not include what the exchange correlation functional looks like. In the so-called local density approximation (LDA) it is locally approximated by that of a homogenous electron gas. More elaborate, and more accurate, approximations also contain gradients of electron densities. Currently most used are the so-called generalized gradient approximations (GGA).

In Kohn-Sham theory the electron density is parameterized in terms of non-interacting one electron orbitals; $n(\mathbf{r}) = \sum_{n=1}^{N} |\phi_n(\mathbf{r})|^2$. The kinetic energy in Equation 2.1 can than be written as

$$T_0[n(\mathbf{r})] = \sum_{n=1}^{N} \int d\mathbf{r}\; \phi_n^*(\mathbf{r}) \left(-\frac{\hbar^2}{2m} \nabla^2 \right) \phi_n(\mathbf{r}) \tag{2.2}$$

Applying the variational principle, $\delta E[n(\mathbf{r})]/\delta n(\mathbf{r}) = 0$, to Equation 2.1, can now be written as a variation to the ϕ_n^* under the normality constraint $< \phi_n|\phi_n >= 1$

$$\delta \left\{ E[n(\mathbf{r})] - \sum_n \epsilon_n (< \phi_n|\phi_n > -1) \right\} = 0 \tag{2.3}$$

This finally leads, after diagonalizing $\epsilon_{m,n}$, to a Schrödinger-like Equation for noninteracting particles in an effective local potential $V(\mathbf{r}) = V_{ext}(\mathbf{r}) + V_c(\mathbf{r}) + \delta E_{xc}[n(\mathbf{r})]/\delta n(\mathbf{r})$:

$$\left(-\frac{\hbar^2}{2m} \nabla^2 + V(\mathbf{r}) \right) \phi_n(\mathbf{r}) = \epsilon_n \phi_n(\mathbf{r}) \tag{2.4}$$

These equations are known as the Kohn-Sham equations and need to be solved self-consistently. The total energy is obtained by summing over ϵ_n, correcting for double counting, and adding the electrostatic energy of the nuclei.

In the Born-Oppenheimer approximation the movements of the nuclei and the electrons are decoupled. This makes it possible to treat the nuclei classically, which is a reasonable approximation in most cases. The external potential in the Kohn-Sham equations than becomes a function of the positions of the atoms. In this way we can calculate the total energy of a system as a function of the atomic positions. A general review on DFT can be found in Ref. 13.

Actual implementation of DFT for solids

In a crystalline solid we are dealing with a system with translational invariance; the material can be viewed as consisting of periodically repeated unit cells. This gives rise to a periodic potential for the electrons. According to Bloch's theorem this implies that the wavefunction can be written as a cell-periodic part times a phase factor with a well defined quantum number $\mathbf{k}$:

$$\Psi_{n\mathbf{k}}(\mathbf{r}) = u_{n\mathbf{k}}(\mathbf{r})e^{i\mathbf{k}\cdot\mathbf{r}} \tag{2.5}$$

The periodic part can be written as a sum of plane waves.

$$u_{n\mathbf{k}}(\mathbf{r}) = \sum_{\mathbf{G}} c_{n\mathbf{k}\mathbf{G}} e^{i\mathbf{G}\cdot\mathbf{r}} \tag{2.6}$$

Where the $\mathbf{G}$'s are the reciprocal lattice vectors. A complete basis set would consist of infinitely many plane waves. In practice the basis set needs to be truncated at a certain kinetic energy, i.e., only plane waves are used up to a certain energy cutoff, $\frac{\hbar^2}{2m}|\mathbf{G}+\mathbf{k}|^2 < E_{cut}$.

Since the system has translational invariance in real space it also has translational invariance in reciprocal space, $\mathbf{k}$-space. Therefore only $\mathbf{k}$-vectors in the primitive cell in reciprocal space, the first Brillouin zone, need to be considered. By using the expansion in plane waves the transformation of wavefunctions represented in real space to wavefunctions represented in reciprocal space can be performed using fast fourier transforms (FFT). This gives a computational advantage since multiplications in one are simply additions in the other, and convolutions in one are multiplications in the other.

In the region around the nuclei expansion in plane waves is too expensive due to rapid oscillations of the wave function. The strategy to solve this problem is to divide the wavefunction into two parts, a part living in spheres around the atoms and a part outside the spheres. This can be done effectively by using an expansion in spherical Bessel functions in the core region in combination with a plane wave expansion outside. The parts inside and outside are then matched with value and derivative at the sphere boundary.

The so-called all-electron (AE) Kohn-Sham wavefunctions are now parameterized in a combination of two basis sets. However, these AE wavefunctions are still computationally cumbersome. It is useful to map the AE wavefunctions Ψ_n into fictitious so-called pseudo (PS) wavefunctions $\tilde{\Psi}_n$. Outside the core region the two wavefunctions are identical but inside the core region the PS wavefunction is simpler, having less oscillations. Blöchl has shown that this mapping can be performed linearly by using partial waves and projector functions, the method is hence called the projector augmented wave (PAW) method.[14] In the PAW method the physical relevant AE wavefunction can be recovered from the PS wavefunction by the linear transformation:

$$\Psi_n = \tilde{\Psi}_n - \sum c_{lmI}\tilde{\phi}_{lmI} + \sum c_{lmI}\phi_{lmI} \tag{2.7}$$

with $c_{lmI} =< \tilde{p}_{lmI}|\tilde{\Psi} >$. The lm label the angular momentum quantum numbers and I the atomic site. The $\tilde{p}_{lmI}$ are the fixed projector functions and the ϕ_{lmI} and $\tilde{\phi}_{lmI}$ the so-called AE and PS partial waves respectively. The PS wavefunctions $\tilde{\Psi}_n$ are described in a plane wave expansion in all space. This linear transformation is a big advantage as compared to earlier pseudo potential methods like the norm conserving (NC-PP) and ultra soft (US-PP) pseudo potential methods, as we now have attained an effective all-electron method that allows to keep the full nodal structure of the (valence) wave functions. Additionally an approximation is usually made in which the core electrons are kept fixed at their atomic orbitals. This is reasonable since these do not play a significant role in chemical binding.

The above is incorporated in the Vienna *Ab initio* Simulation Package (VASP)[15–19] that was used to perform most of the calculations discussed in this thesis. A complete, and well tested, database of PAW potentials, including multiple options for the number of treated valence electrons, in both GGA and LDA, is available. In VASP various routines to perform Brillouin zone integrations, like different smearing methods and tetrahedron methods,[20] are available. In combination with different ways of generating smart meshes, gamma centered and Monkhorst-Pack,[21] to perform the Brillouin zone integrations this leads to an effective and tunable treatment of these integrations. Many numerical methods, varying from fast but less stable to slow but vary stable, are implemented to obtain a self consistent solution to the Kohn-Sham equations.

Forces on atoms

The forces on atoms are usually defined as the total derivative of the energy with respect to the atomic positions,

$$\mathbf{F} = -\frac{dE}{d\mathbf{R}} \tag{2.8}$$

In a plane wave basis set wavefunctions are independent of the atomic positions. All derivatives of the wavefunctions with respect to atomic coordinates therefor disappear, simplifying the final expression considerably. In the PAW method, as well as in some pseudo potential methods, complications arise because the augmentation spheres are dependent on the positions of the atoms. However, defining the overlap operator S by $\left\langle \widetilde{\Psi}_n \middle| S \middle| \widetilde{\Psi}_m \right\rangle = \delta_{nm}$ the total derivative of the energy can be written by

$$\frac{dE}{d\mathbf{R}} = \sum_n f_n \left\langle \widetilde{\Psi}_n \middle| \frac{\partial(H - \epsilon_n S)}{\partial\mathbf{R}} \middle| \widetilde{\Psi}_m \right\rangle + \frac{\partial U_{nuclei}}{\partial\mathbf{R}} \tag{2.9}$$

with f_n the orbital occupation numbers and U_{nuclei} the electrostatic interaction energy of the nuclei.[22] In this way all dependence on the atomic positions is included in the Hamilton and overlap operators H and S respectively. This expression is in fact equivalent to the Helmmann-Feynman force theorem because the pseudo wavefunctions are not explicitly depending on the atomic positions. A full derivation of the forces in the PAW method is given by Kresse and Joubert.[19]

The forces calculated in this way can be used to minimize the ground state total energy with respect to the positions of the ions. In this way the crystal structure of a material can be optimized.

Equation of state

Optimizing the cell volume by using DFT can be a tricky business. The plane wave basis sets are usually generated once for the entire calculation. When during calculation the cell volume changes this can result in total energies that are not comparable and hence lead to a wrong cell volume.

An accurate way to circumvent this problem is by keeping the cell volume fixed in each run. By calculating the optimal geometries for a set of volumes, using the same kinetic energy cutoff in each calculation, one can obtain the total energy as a function of volume with the same accuracy for all volumes. The volume with minimal total energy can be obtained by fitting an equation of state to this data.

An additional advantage of this method is that it is the first step in calculating the volume expansion as a function of temperature in the quasi-harmonic approximation. To this end the phonon density of states, see the next section, needs to be calculated at each volume. At each temperature one can than obtain the free energy as a function of volume and fit an equation of state to this data. The following shows the derivation of the Murnaghan equation of state.[23]

For a solid we can define the bulk modulus as

$$B = -V \left(\frac{\partial P}{\partial V} \right)_T . \tag{2.10}$$

In first order in pressure the bulk modulus can be expressed as:

$$B = B_0 + B_0' P. \tag{2.11}$$

Inserting this expansion into Equation 2.10 we find the two following equivalent relations:

$$V(P) = V_0 \left(1 + B_0' \frac{P}{B_0} \right)^{-\frac{1}{B_0'}} \tag{2.12}$$

$$P(V) = \frac{B_0}{B_0'} \left(\left(\frac{V_0}{V} \right)^{B_0'} - 1 \right) . \tag{2.13}$$

Because the total energy converges faster with respect to the basis set than the pressure it is more accurate to fit the expression for the energy as a function of the volume:

$$E(V) = E_0 + \frac{B_0 V}{B_0'} \left(\frac{(V_0/V)^{B_0'}}{B_0' - 1} + 1 \right) - \frac{B_0 V_0}{B_0' - 1} \tag{2.14}$$

Phonons and thermodynamics

Since DFT provides us with the total energy as a function of the atomic positions it can be used to calculate the vibrational spectra of a solid. By occupying the obtained spectrum according to Bose-Einstein statistics one can additionally obtain information on the thermodynamical properties of a material.

In the direct method the vibrational spectra are calculated by displacing the ions finite distances from their equilibrium positions. In principle each atom has to be displaced in three linearly independent directions. Using the symmetry of the crystal the number of displacements can usually be decreased significantly. The calculated forces caused by these displacements are used to construct the force constant matrix. In the harmonic approximation the force constant matrix is given by:

$$\Psi_{\alpha\beta}\begin{pmatrix} lm \\ \kappa\mu \end{pmatrix} \approxeq -\frac{\mathbf{F}_{\beta}\binom{lm}{\kappa\mu}}{\mathbf{u}_{\alpha}\binom{l}{\kappa}} \tag{2.15}$$

with $\mathbf{F}$ the force induced by the displacement $\mathbf{u}$, l, m label the cells, κ, μ the atoms, and α, β the cartesian directions. To calculate the forces accurately one usually needs to perform the calculations in a super-cell. Using a super-cell is needed to minimize the effect the, simultaneous, displacement of the periodic images of the displaced atom.

From the forces constant matrix the dynamical matrix is constructed according to:

$$D_{\alpha\beta}\begin{pmatrix} \mathbf{k} \\ \mu\kappa \end{pmatrix} = \frac{1}{\sqrt{M_{\mu} M_{\kappa}}} \sum_{l} \Psi_{\alpha\beta}\begin{pmatrix} lm \\ \kappa\mu \end{pmatrix} \exp\left[i\mathbf{k} \cdot \left(\mathbf{R}\begin{pmatrix} m \\ \mu \end{pmatrix} - \mathbf{R}\begin{pmatrix} l \\ \kappa \end{pmatrix} \right) \right] \tag{2.16}$$

with M_{μ}, κ the masses and $\mathbf{R}$ the equilibrium positions. The squares of the phonon eigenfrequencies are then given as the eigenvalues $\omega^2(\mathbf{k})$ of the dynamical matrix $D_{\alpha\beta}\binom{\mathbf{k}}{\mu\kappa}$. A more extended description of this method and the application to diamond and graphite can be found in Kresse *et al.*, Ref. 24.

When we neglect the PV term (i.e. the distinction between energy and enthalpy), which is a good approximation for solids, Gibbs free energy $G(T)$ is calculated as

$$G(T) = E^{\text{tot}} + H^{\text{vib}}(T) - TS^{\text{vib}}(T) \tag{2.17}$$

with

$$H^{\text{vib}}(T) = \int d\omega \; g(\omega) \left\{ \frac{1}{2}\hbar\omega + \hbar\omega n(\omega) \right\} \tag{2.18}$$

and

$$S^{\text{vib}}(T) = k_B \int d\omega\, g(\omega) \left\{ \beta\hbar\omega n(\omega) - \ln\left[1 - e^{-\beta\hbar\omega}\right] \right\} \tag{2.19}$$

where $g(\omega)$ is the phonon density of states, $n(\omega) = [\exp(\beta\hbar\omega) - 1]^{-1}$ is the Bose-Einstein occupation number and $\beta = 1/k_B T$. The first term in the integral of Equation 2.18 gives the Zero Point Energy and the second term gives the finite temperature contribution.

Using these expressions the changes in entropy, enthalpy and Gibbs free energy for a reaction can be calculated. When molecular hydrogen is involved in a reaction we need to treat H_2 at the same level of theory.

The treatment of H_2

DFT calculations for solids are most effectively performed using a plane wave basis set with periodic boundary conditions. To calculate a molecule using the same implementation of DFT the molecule has to be placed in a large box. Since the box is repeated periodically it needs to be large enough that the periodic images do not interact. For H_2 a cubic box with sides of about 20 Å is sufficient.

The equilibrium distance calculated with DFT in the PW91 GGA approximation[25] is 0.7486 Å, the vibrational frequency is 4350 cm^{-1} and a dissociation energy 4.57 eV, which compare reasonably well with the experimental values of 0.7461 Å, 4401 cm^{-1} and 4.48 eV, respectively.[26,27]

The vibrational ZPE for the hydrogen molecule can be calculated from the energy levels of a Morse potential,

$$E(n) = \hbar\omega\left(n + \frac{1}{2}\right) - \frac{1}{4D_e}\left[\hbar\omega\left(n + \frac{1}{2}\right)\right]^2, \tag{2.20}$$

where ω is the vibration frequency and D_e is the dissociation energy.

We can also consider the zero point rotational energy (ZPRE) of the hydrogen molecules. Assuming that ortho- and para-hydrogen are produced in a proportion of three to one, the average ZPRE of a hydrogen molecule is 0.011 eV, using the energy levels given from "Molecular Spectra and Molecular Structure".[27]

The temperature dependent enthalpy and entropy of H_2 for various pressures can be obtained from literature.[28] By shifting these data to be zero at 0K and adding the electronic total and zero point energy calculated using DFT, we obtain numbers that can be used in combination with the temperature dependent entropy and enthalpy for solids from the previous section.

Optical properties

The optical properties of solids can be described by the complex dielectric function $\varepsilon(\omega) = \epsilon_1(\omega) + i\epsilon_2(\omega)$, with ω the frequency of the electromagnetic waves. Connected to the dielectric function is the complex optical conductivity $\sigma(\omega) = \sigma_1(\omega) - i\sigma_2(\omega)$. The relation between $\sigma(\omega)$ and $\epsilon(\omega)$ is given by:

$$\sigma(\omega) = \frac{\omega}{4\pi}\epsilon_2(\omega) - i\frac{\omega}{4\pi}\left(\epsilon_1\left(\omega\right) - 1\right) \tag{2.21}$$

The plane wave solution of the wave equation in a crystalline medium gives

$$c^2(\mathbf{k}.\mathbf{k}) = \omega^2\epsilon \tag{2.22}$$

with c the speed of light in vacuum and $\mathbf{k} = \mathbf{k}_1 + i\mathbf{k}_2$ the complex wave vector. When a plane wave is incident normally on the flat surface of an absorbing medium, $\mathbf{k}_1$ and $\mathbf{k}_2$ are parallel. In this case we find

$$\omega^2\epsilon = c^2(k_1^2 - k_2^2 + 2ik_1k_2) \tag{2.23}$$

The optical constants, the refractive index n and the extinction coefficient κ, are defined by

$$n = \frac{c}{\omega}k_1 \tag{2.24}$$

$$\kappa = \frac{c}{\omega}k_2 \tag{2.25}$$

Gathering the above we find the following relations between the real and imaginary parts of ε and the optical constants

$$\varepsilon_1 = n^2 - \kappa^2 \tag{2.26}$$

$$\varepsilon_2 = 2n\kappa \tag{2.27}$$

$$n = \frac{1}{\sqrt{2}}\sqrt{\epsilon_1 + \sqrt{(\epsilon_1)^2 + (\epsilon_2)^2}} \tag{2.28}$$

$$\kappa = \frac{1}{\sqrt{2}}\sqrt{-\epsilon_1 + \sqrt{(\epsilon_1)^2 + (\epsilon_2)^2}} \tag{2.29}$$

The field amplitudes in the wave are damped according to the factor

$$e^{(-k_2z)} = e^{(-\kappa\omega z/c)} \tag{2.30}$$

where the z-axis is normal to the surface. We define the reflectance as the fraction of the incident energy which is reflected. At normal incidence we have the following expression for the reflectance:

$$R = \frac{(n-1)^2 + \kappa^2}{(n+1)^2 + \kappa^2} \tag{2.31}$$

A convenient relation between the real and imaginary part of the dielectric function is given by the Kramers-Kronig relations:

$$\begin{aligned} \varepsilon_1(\omega) - 1 &= \frac{2}{\pi} \mathrm{P} \int_0^\infty d\omega' \, \varepsilon_2(\omega') \frac{\omega'}{\omega'^2 - \omega^2} && (2.32) \\ \varepsilon_2(\omega) &= \frac{2}{\pi} \mathrm{P} \int_0^\infty d\omega' \, \left(\varepsilon_1(\omega') - 1\right) \frac{\omega}{\omega^2 - \omega'^2} && (2.33) \end{aligned}$$

Where P denotes the principal value of the integral.

Interband transitions

The optical absorption is determined by the quantum mechanical transition rate for exiting an electron in an initial quantum state i to a final quantum state j. This transition rate, $W_{i \to j}$, is given by Fermi's golden rule

$$W_{i \to j} = \frac{2\pi}{\hbar} |M_{ij}|^2 g(\hbar\omega), \tag{2.34}$$

where the M_{ij} are the optical transition matrix elements and $g(\hbar\omega)$ is the joint density of states.

In the DFT framework described here, the matrix elements can be calculated in the random phase independent particle approximation, i.e. considering only direct transitions from occupied to unoccupied Kohn-Sham orbitals. When local field effects are neglected, the imaginary part of the macroscopic dielectric function, $\varepsilon^{(2)}_{\text{inter}}(\omega)$, has the form:

$$\begin{aligned} \varepsilon^{(2)}_{\text{inter}}(\hat{\mathbf{q}}, \omega) &= \frac{8\pi^2 e^2}{V} \lim_{|\mathbf{q}| \to 0} \frac{1}{|\mathbf{q}|^2} \times && (2.35) \\ & \sum_{\mathbf{k},v,c} |\langle u_{c,\mathbf{k}+\mathbf{q}} | u_{v,\mathbf{k}} \rangle|^2 \, \delta(\epsilon_{c,\mathbf{k}+\mathbf{q}} - \epsilon_{v,\mathbf{k}} - \hbar\omega) \end{aligned}$$

where $\hat{\mathbf{q}}$ denotes the direction of $\mathbf{q}$ and $v, \mathbf{k} + \mathbf{q}$ and $c, \mathbf{k}$ label single particle states that are occupied and unoccupied in the ground state, respectively. ϵ, u are the single particle energies and the translationally invariant parts of the wave functions. V is the volume of the unit cell. A derivation of this expression and discussion on its implementation can be found in Gajdoš *et al.*, Ref. 29.

Intraband transitions

When the material in question is a metal we cannot suffice by only looking at direct interband transitions. The electrons at the Fermi level will also be able to undergo transitions within a single energy band, so-called intraband transitions. This can be approximated by adding a Drude contribution of free electrons with the correct density and effective mass. This density and effective mass give rise to a free electron gas plasma frequency, which determines the intraband contribution to the dielectric function. The plasma frequency ω_p can be calculated as an integral over the Fermi surface according to:

$$\omega^2_{\mathrm{p}(\alpha\beta)} = \frac{4\pi e^2}{V\hbar^2}\sum_{n,\mathbf{k}} 2g_\mathbf{k}\frac{\partial f(\epsilon_{n\mathbf{k}})}{\partial\epsilon}\left(\mathbf{e}_\alpha\frac{\partial\varepsilon_{n\mathbf{k}}}{\partial\mathbf{k}}\right)\left(\mathbf{e}_\beta\frac{\partial\varepsilon_{n\mathbf{k}}}{\partial\mathbf{k}}\right) \tag{2.36}$$

with $g_\mathbf{k}$ the weight factors, and $f(\epsilon_{n\mathbf{k}})$ the occupation function. Further details on the calculation of the plasma frequency can be found in Harl *et al.*, Ref.[30]

The intraband dielectric function, $\varepsilon_\mathrm{intra}(\omega) = \varepsilon^{(1)}_\mathrm{intra}(\omega) + i\varepsilon^{(2)}_\mathrm{intra}(\omega)$, is calculated from the free electron plasma frequency ω_p:

$$\varepsilon^{(1)}_\mathrm{intra}(\omega) = 1 - \frac{\omega^2_\mathrm{p}}{\omega^2+\gamma^2} \tag{2.37}$$

$$\varepsilon^{(2)}_\mathrm{intra}(\omega) = \frac{\gamma\omega^2_\mathrm{p}}{\omega^3+\omega\gamma^2} \tag{2.38}$$

Alanates and Boranates

Chapter 3

Introduction

Reproduced, in part, with permission from:
Electronic structure & formations energy of hydroaluminates & hydroborates
MS 2192 Encyclopedia of Materials: Science and Technology-Updates
M.J. van Setten

Copyright 2007 by Elsevier Limited

Most of the tetrahydroaluminates and tetrahydroborates have been known to exist for a few decades. The tetrahydroaluminates are also frequently referred to in literature as the alanates and the tetrahydroborates as borohydrides or boranates. The nomenclature adopted here follows the recommendations of the IUPAC.

Currently both the tetrahydroaluminates and the tetrahydroborates are under interest due to their possible use as hydrogen storage materials. Most contain more hydrogen per cubic meter than even liquid hydrogen. Moreover, when they consist of light elements they can also have a very high gravimetric hydrogen density, e.g., $LiBH_4$ has a gravimetric density of 18 wt.%. The renewed interest started with the discovery by Bogdanovíc[31] that the hydrogen desorption reaction of sodium tetrahydroaluminate, $NaAlH_4$, could be made reversible by titanium chloride doping. Two extensive and comprehensive reviews on hydrogen storage in general and on solid state hydrogen storage are published by Züttel[5] and Bogdanovíc.[6]

Hydrogen storage in these hydrides is based on the following thermodynamics. At room temperature and under atmospheric pressure they are thermodynamically stable. By increasing the temperature the dehydrogenated phase gains more in free energy than the hydrogenated phase because of the dominance of the entropy of the hydrogen gas. This causes the hydrogen to be released at a specific temperature, depending on the stability of the hydride. Since energy production from hydrogen is most effective using a fuel cell, the energetics of the storage method would be optimal if the rest heat of the fuel cell can be used to drive the desorption reaction. For the optimal application in combination with a proton exchange membrane (PEM) fuel cell, which operates at about 90°C, the hydrogen storage material should have an equilibrium pressure of 1 bar at room temperature. To accomplish this, the hydrogen desorption enthalpy should be about 39.2 kJ/mol H_2.

The alkali tetrahydroaluminates and tetrahydroborates show the following desorption reactions:

$$\mathrm{AAlH_4} \rightarrow \frac{1}{3}\mathrm{A_3AlH_6} + \frac{2}{3}\mathrm{Al} + \mathrm{H_2} \rightarrow \mathrm{AH} + \mathrm{Al} + \frac{3}{2}\mathrm{H_2} \tag{3.1}$$

and

$$\mathrm{ABH_4} \rightarrow \mathrm{ABH_2} + \mathrm{H_2}\ ? \rightarrow \mathrm{AH} + \mathrm{B} + \frac{3}{2}\mathrm{H_2} \;\text{ or }\; \mathrm{ABH_4} \rightarrow \mathrm{AB} + 2\mathrm{H_2} \tag{3.2}$$

with A an alkali element. The alkaline earth hydroaluminates and tetrahydroborates according to:

$$\mathrm{E(AlH_4)_2} \rightarrow\ ?\ \rightarrow \mathrm{EH_2} + 2\mathrm{Al} + 3\mathrm{H_2} \tag{3.3}$$

and

$$\mathrm{E(BH_4)_2} \rightarrow \mathrm{EH_2} + 2\mathrm{B} + 3\mathrm{H_2} \;\text{ or }\; \mathrm{E(BH_4)_2} \rightarrow \mathrm{EB_2} + 4\mathrm{H_2} \tag{3.4}$$

with E an alkaline earth element. As indicated by the question marks, some of the intermediate reaction steps are still under discussion.[9] The alkali metals have been shown to form stable hexahydroaluminates, which introduces an intermediate step in the hydrogen desorption reaction. The tetrahydroborates in principle decompose in a one step reaction no mater which cation is involved. Depending on desorption temperature the formation of diborane, B_2H_6, or metal-boron species, e.g. MgB_2, is also possible. The mechanisms of the tetrahydroborate desorption reactions however are not fully known. Since the simple hydrides, like sodium hydride, are rather stable a final dehydrogenation step, removing the hydrogen from the simple hydrides, takes to much energy to be technologically of interest.

For the materials to be technologically interesting the above reactions should also be reversible. By applying a hydrogen pressure on the dehydrogenated phase the hydrides should be formed again. Whereas thermodynamic conditions are in principle favorable, as similar conditions apply to the dehydrogenation, kinetic barriers are generally found to severely hamper the re-hydrogenation reaction. Up until now only for sodium tetrahydroaluminate this reversibility has been demonstrated to occur at favorable thermodynamic conditions by using a catalyst by Bogdanovíc.[31] The mechanism of the catalyzed reaction however is still a topic of active research.

A final major technical issue is related to the thermal conductivity of materials involved in the hydrogen de/absorption reactions. During loading with hydrogen, even with the optimal thermodynamics, a substantial amount of heat, about 0.50 MW, will be generated. Because the hydrides in general have a rather low thermal conductivity - $NaAlH_4$ has a thermal conductivity of 0.55 W/mK - dissipating this heat is a problem, especially when the loading, or refueling, is to be performed in a reasonable time span.

As mentioned, the primary requirements for a hydride to be a useful hydrogen storage material is that the hydrogen desorption enthalpy is about 39.2 kJ/mol H_2 and that it has a high gravimetric hydrogen density, at least 6 wt.% (DOE targets are 6 wt.% (2010) and 9 wt.% (2015) for the entire storage system). Of all the pure hydroaluminates or tetrahydroborates only $Mg(BH_4)_2$ is the only candidate which may have the right properties for hydrogen storage. The search for the optimal material is therefore extending towards mixtures, see e.g., Tang *et al.*Ref. 32, However, to obtain a good intuition and toolkit to investigate these, a thorough knowledge of the pure hydroaluminates and tetrahydroborates is essential. In the following we present the current state of knowledge concerning electronic structure and formation enthalpy of the hydroaluminates and tetrahydroborates from a theoretical point of view. We start with a discussion on the tetrahydroaluminates and tetrahydroborates and come back to the hexahydroaluminates.

Electronic structure and density functional calculations

Both the tetrahydroaluminates and the tetrahydroborates have been studied extensively by means of electronic structure calculations. Density functional theory (DFT) calculations in the generalized gradient approximation (GGA) have been shown to give good results for the crystal structures. In fact, in a number of cases the ground state crystal structure has been predicted by DFT calculations before exact experimental determinations were made. This is partly caused by experimental complications in these materials. Due to their relatively low stability it is hard to grow single crystals for X-ray measurements. Moreover, it is problematic to accurately determine the hydrogen positions with X-rays. The high neutron scattering cross-section of hydrogen, 82.03 barn, limits the applicability of neutron diffraction. In the case of the tetrahydroborates the high neutron absorption cross-section of boron atoms, 767.8 barn, complicates matters even further.

A rather successful method in predicting crystal structures by means of DFT calculations has been the application of trial structures. In this method the crystal structures of a large number of known compounds with the same stochiometry and comparable ionic radii are used as starting input. The atoms of the known compounds are replaced by the corresponding atoms of the unknown hydride and the atomic positions and lattice parameter of the crystal structure are relaxed. The predicted structure is the one with the lowest calculated free energy.

A second important contribution of DFT studies lies in the understanding of the crystal bonding in the materials. By studying charge distributions, energy level splittings, electron localization functions and crystal orbital overlap population a good understanding of the nature of the involved chemical bonding can be obtained.

The electronic structure of the tetrahydrides

The tetrahydroaluminates and tetrahydroborates are composed of an ionic lattice of metal cations, e.g., Na^+ or Mg^{2+}, and $(AlH_4)^-$ or $(BH_4)^-$ complex anions respectively. Except for beryllium, which is only known to form a tetrahydroborate, all alkali and alkaline earth metals can form tetrahydroaluminates and tetrahydroborates. Furthermore scandium, hafnium and zirconium have been shown to form tetrahydroborates.

The hydrogen atoms are bound covalently to the Al/B atoms with a bond length of about 1.62/1.20 Å. The bonding has a highly ionic character in the case of aluminum due to the rather large difference in electron-negativity between hydrogen and aluminum. For boron this difference is much smaller and the bonding is more covalent in nature. Because both aluminum and boron have only three valence electrons they need an extra electron to be able to form four bonds with hydrogen atoms and thus obtain an octet closed shell configuration. Because of the tetrahedral geometry the valence band splits into two regions. The lowest, containing two electrons per Al/BH_4 unit, has a mixture of aluminum/boron *s* and hydrogen *s*-character and the upper one, containing the remaining six electrons, is a mixture of aluminum/boron *p* and hydrogen *s*-character. In a single separated cluster the splitting in the valence region is a complete splitting in distinct energy levels. In the crystal the splitting becomes broadened by band dispersion but in almost all cases the splitting in distinct peaks remains intact. The electronic densities of state of the tetrahydroaluminates are shown in Figure 3.1 and those of the tetrahydroborates in Figure 3.2.

All tetrahydroaluminates and tetrahydroborates have been found to be large band gap insulators. A striking particularity is that the band gaps in the DFT calculations are in all cases around 5 eV for the tetrahydroaluminates, $MAlH_4$ type, and around 6 eV for the alkali and alkaline earth tetrahydroborates.[1] Tetrahydroborates with cations from the third column and higher of the periodic table show d-states in the band gaps, located on the metal atoms. When, for sake of the argument, we ignore these, the band gaps are roughly the same as well. In first order the size of these band gaps can be explained by the electrostatic terms in the energies of the valence and conduction bands. Not only the valence band but also the conduction band is strongly dominated by the complex anions. The difference, however, is that where the valence wave functions are rather localized, the conduction band wave functions are rather delocalized. The valence wave functions are therefore, in first order, insensitive to the ion-ion separation and the energy of the conduction wave functions is proportional to be inverse of the ion-ion separation. Since in all tetrahydroaluminates and tetrahydroborates this separation is rather similar the band gap between the valence and conduction band is as well. In the tetrahydroborates we even see a negative correlation between the inverse of the cation radius and the band gap. A more detailed discussion on this effect is given in Chapter 5 in the specific case of the tetrahydroaluminates.

The electronic structure of the hexahydroaluminates

The hexahydroaluminates, i.e. M_3AlH_6 M = Li, Na, K etc., differ in a number of ways from the tetrahydrides. First of all they only form with aluminum and alkali cations. The aluminum atoms are octahedrally coordinated with an Al–H bond length of around 1.74 Å. The densities of states of these materials show a three fold splitting in the valence region.

---

[1] DFT calculations generally have the tendency to underestimate the band gap. To correct for this a far more elaborate GW calculation can be performed which takes into account quasi particle corrections. For the tetrahydroaluminates this has been shown to increase the band gap by about 2 eV. A more extensive discussion is given in Chapter 5

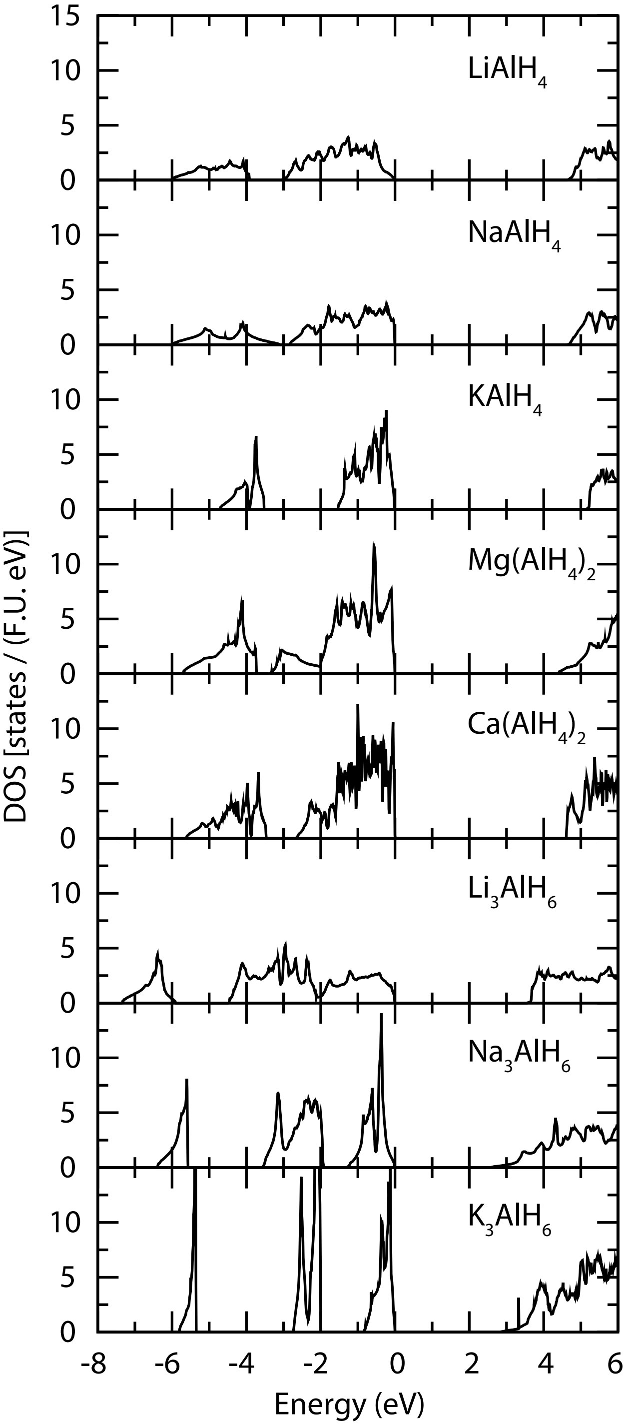

Figure 3.1: *Electronic densities of state of the hydroaluminates (states per formula unit per eV). The Fermi level is placed at the top of the valence band.*

The lowest peak has mainly a mixed hydrogen s and aluminum p character, the middle peak hydrogen s and aluminum p and the peak just below the Fermi level has hydrogen s and aluminum $d(e_g)$ character. The band gaps of these materials vary more those of the

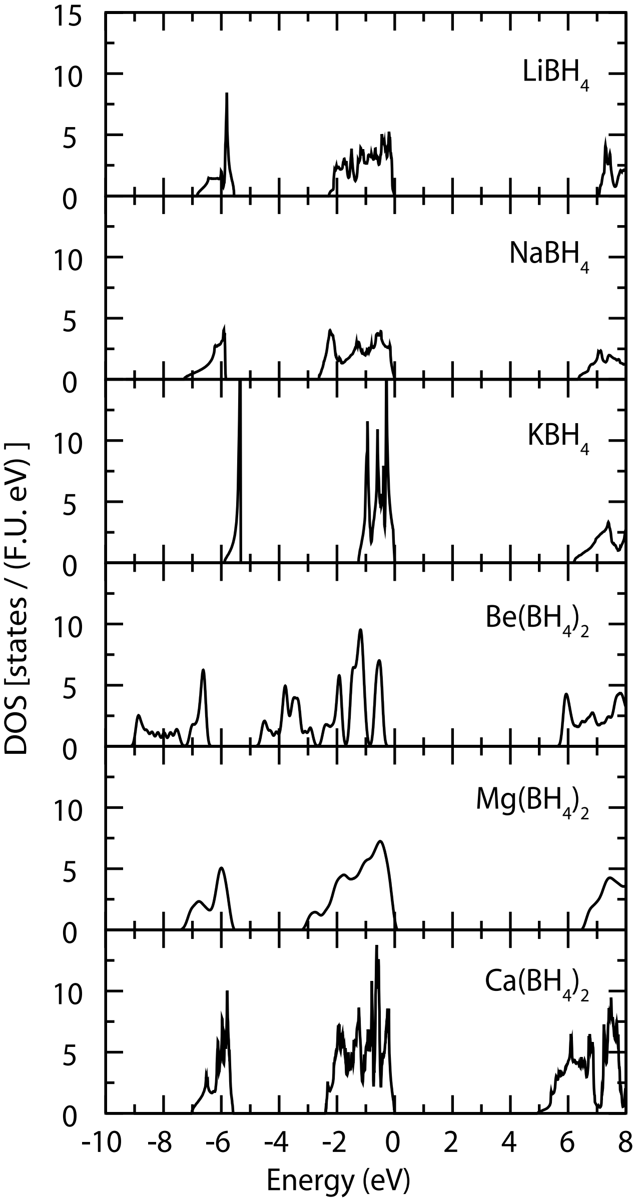

Figure 3.2: *Electronic densities of state of the hydroborates (states per formula unit per eV). The Fermi level is placed at the top of the valence band.*

tetra hydroaluminates. This can also be understood from the electrostatic point of view. Since the alkali ions are three times more abundant in the hexahydroaluminates than in the tetrahydroaluminates they have a larger effect on the packing. The size difference of the cations now causes the packing of the complex anions to substantially differ for the various cations. The electrostatic contributions to the energies of the wave functions therefore also differ significantly.

Table 3.1: *Formation enthalpies (kJ/mol A/BlH$_4$), at 0K, of the hydroaluminates and tetrahydroborates calculated using DFT-GGA. The values given do not contain ZPE corrections.*

	Li	Na	K	Be	Mg	Ca
ΔE aluminates	-102.69	-98.52	-131.88		-30.89	-103.56
ΔE borates	-208.00	-201.84	-240.78	-75.24	-129.34	-202.50

Formation enthalpy

Density functional calculations

State-of-the-art to calculate formation enthalpies is by means of density functional calculations (DFT). The formation enthalpy is calculated by subtracting the total energies of the reactants, E_R, from the total energy of the product, E_P:

$$\Delta E = \Sigma E_P - \Sigma E_R \tag{3.5}$$

For solids the total energies are usually calculated using a code based on periodic boundary conditions. In this way calculations can be performed for materials with up to several hundreds of atoms in the unit cell, using a plane wave basis set. Molecules can also be described, provided they are decoupled form their periodic images by using a large unit cell.

When DFT calculations are used to compare total energies of various crystal structures for one material the energy differences can be calculated with an accuracy of about 0.1 kJ/mol. When materials of different compositions are involved this accuracy can in general not be reached. This is especially the case for hydrogen desorption reactions, where typically metals, insulators and molecules are involved. For the tetrahydroaluminates a root mean square deviation of about 5 kJ/mol AH$_4$, A = Al or B, between DFT and experimental is observed. Values, calculated using the VASP code,[15–18] for the formation enthalpies from the elements are given in table (fe).

It has been shown by various calculations that the vibrational zero point energy (ZPE) forms a significant contribution to the formation enthalpies of hydroaluminates and tetrahydroborates. The ZPE of a solid can be calculated from the phonon frequencies. In a solid with n atoms in the unit cell we have 3n degrees of freedom and hence, counting the degeneracies, as many phonon branches. In the harmonic approximation the ZPE of each mode becomes $\frac{1}{2}\hbar\omega$ with ω the phonon frequency. By summing over all frequencies we obtain the total ZPE per unit cell.

In general the ZPE of the bulk metals is rather small. The main difference between the hydrogenated and dehydrogenated phase comes from the difference between the ZPE of hydrogen molecules and that of de hydride. In the hydride the main contribution comes from the Al–H or B–H stretch modes. These stretch modes are weaker than the H-H mode in the molecule but there are twice as many. The result is that the ZPE in the hydrogenated phase is higher than in the dehydrogenated phase, causing a destabilization of the hydride. The effect is usually of the order of 20 kJ/mol AlH_4 and 30 kJ/mol BH_4.

Models

Two semi-empirical models have been proposed to describe and explain the formation enthalpies of the tetrahydroaluminates and tetrahydroborates. One is based on the electron negativity of the metal cation and the other on a modified Born-Haber cycle.

Nakamori et al have shown that the stabilities of the tetrahydroborates have a strong correlation with the Pauling electronegativity χ_P of the metal cation.[33] When a linear relation is assumed the absolute mean error is only 10.4 kJ/mol BH_4. The ZPE contribution is here estimated from calculations of a single $(BH_4)^-$ anion and a H_2 molecule to be 33 kJ/mol BH_4. The correlation is show in Figure 3.3 and given by the relation (in kJ/mol BH_4):

$$\Delta H = 248.7\chi_P - 390.8 \tag{3.6}$$

The correlation is explained by assuming that the charge transfer from the cations to the $(BH_4)^-$ is the key factor in the stability of the tetrahydroborates. The Pauling electronegativity is based on the difference of binding energies between elements and hence is a suitable measure.

The second model for the formation enthalpies, discussed in detail in Chapter 10, is based on a modified Born-Haber cycle. The formation enthalpy is calculated by adding the energies to dissociate the elemental solids and hydrogen molecules, to form the ions and to form the ionic crystal. The formation of the complex anions is calculated by adding the energy gained by adding one electron to the aluminum/boron atom and four times the covalent hydrogen-aluminum/boron bond strength. An accurate value for the crystal energy can be obtained from a simple Born model for the potential between the cations and anions. It takes into account an electrostatic attractive potential between point charges at the centers of the ions and a repulsive short-range potential $r^{-\bar{n}}$, where $\bar{n}$ is the average Born exponent:

$$E_{\text{crys}} = \frac{M_c Z_A Z_C e^2}{4\pi\varepsilon_0 r_0}\left(1 - \frac{1}{\bar{n}}\right) \tag{3.7}$$

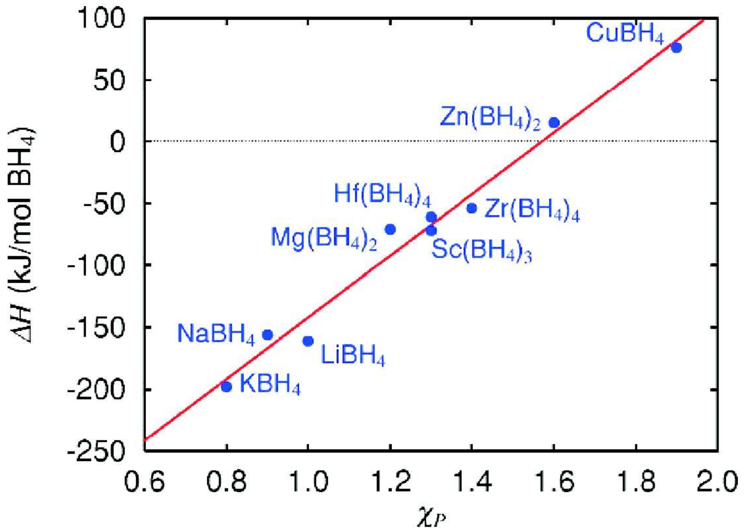

Figure 3.3: *Correlation between the Pauling electronegativity of the cation and formation enthalpy of the tetrahydroborates. Reprinted figure with permission from: Yuko Nakamori, Kazutoshi Miwa, Akihito Ninomiya, Haiwen Li, Nobuko Ohba, Shin-ichi Towata, Andreas Züttel, and Shin-ichi Orimo; Phys. Rev. B, 74, 045126 (2006); Copyright (2006) by the American Physical Society*

where M_c is the Madelung constant, Z_A and Z_C the number charges on the anion and cation respectively and r_0 the shortest anion-cation distance. For r_0 the sum of ionic radii is used, with the Al–H and B–H distance as complex anion radius. The use of the Al–H and B–H distance as anion radius in fact underestimates the inter atomic distances in the crystals by about 20%. Using this effective radius compensates for other contributions to the binding such as multipole terms and polarization effects, which are not in the model. It was shown that one can even take an average value for the Madelung constant, averaging over materials with the same ionic stochiometry, and eventually obtain root-mean-square deviations from experimental and DFT values of 26.1 and 31.9 kJ/mol AH_4 respectively. Comparison of the model with experimental and DFT values is shown in Figure 3.4.

A tetrahydroborate is in general more stable then the tetrahydroaluminate with the same cation. Studying the various contributions in this model to the formation enthalpy learns that the main cause for this is the difference in crystal energy. The BH_4 clusters are considerably smaller than the AlH4 clusters, giving rise to a stronger ionic binding. The difference, however, between the compounds with different cations is small. The decrease of dissociation energy and ionization potential with increasing atomic number (that increases the stability) is almost compensated by the decrease in crystal energy caused by the increasing ionic radius (that decreases the stability).

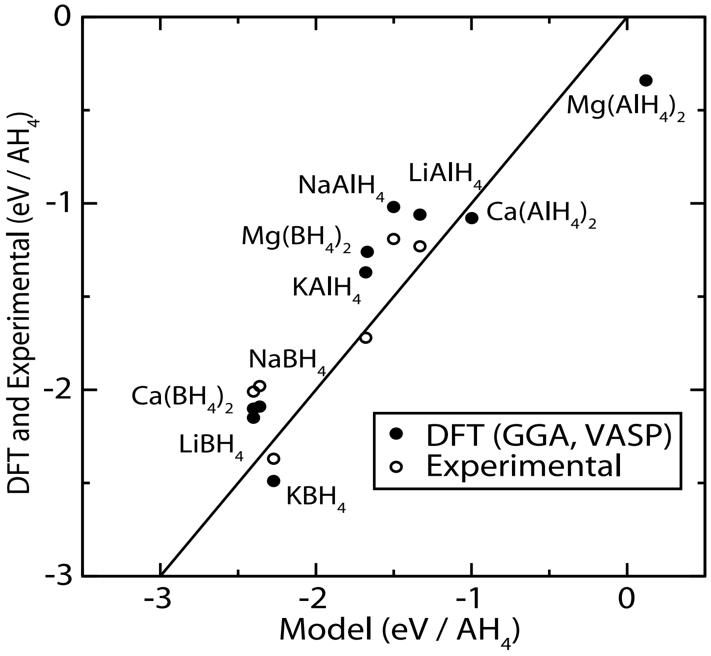

Figure 3.4: *Comparison of the formation enthalpies predicted by the Born-Haber model with DFT and experimental values. Reprinted with permission from: M.J. van Setten, G.A. de Wijs and G. Brocks; J. Phys. Chem. C 111, 9592-9594; Copyright (2007) American Chemical Society.*

Chapter 4

Magnesium alanate, $Mg(AlH_4)_2$

Reproduced with permission from:
Ab initio study of $Mg(AlH_4)_2$
M. J. van Setten, V. A. Popa, G. A. de Wijs, and G. Brocks
Phys. Rev. B **72**, 073107 (2005)
Copyright 2005 by the American Physical Society

Abstract

Magnesium alanate $Mg(AlH_4)_2$ has recently raised interest as a potential material for hydrogen storage. We apply *ab initio* calculations to characterize structural, electronic and energetic properties of $Mg(AlH_4)_2$. Density functional theory calculations within the generalized gradient approximation (GGA) are used to optimize the geometry and obtain the electronic structure. The latter is also studied by quasi-particle calculations at the GW level. $Mg(AlH_4)_2$ is a large band gap insulator with a fundamental band gap of 6.5 eV. The hydrogen atoms are bonded in AlH_4 complexes, whose states dominate both the valence and the conduction bands. On the basis of total energies, the reaction enthalpy for decomposing $Mg(AlH_4)_2$ into bulk magnesium, bulk aluminum and hydrogen gas is 0.17 eV/H_2 (at $T = 0$). Including corrections due to the zero point vibrations of the hydrogen atoms this number decreases to 0.10 eV/H_2. The enthalpy of the dehydrogenation reaction $Mg(AlH_4)_2 \rightarrow MgH_2 + 2Al + 3H_2(g)$ is close to zero, which impairs the potential usefulness of magnesium alanate as a hydrogen storage material.

Introduction

The interest in alanate compounds as hydrogen storage materials was recently rekindled as the kinetics of hydrogen adsorption/desorption improved dramatically by the addition of transition metal catalysts.[6,31] Alanates $MAlH_4$, with M a lightweight alkaline metal, have a high gravimetric hydrogen density, which is essential for their application as storage materials. Most attention up to now has gone to sodium alanate, $NaAlH_4$, which has a hydrogen capacity of 7.5 wt. %.[6,34,35] It releases hydrogen in a two stage process. The two stages involve reaction enthalpies that are sufficiently small to be of interest, namely 0.38 and 0.34 eV per H_2 molecule respectively. However, only three out of four hydrogen atoms are released in this process, which lowers the effective hydrogen storage capacity. This has stimulated the search for other suitable alanates.

Alanates $M(AlH_4)_2$, with M a lightweight alkaline earth metal, have an even higher gravimetric hydrogen density. Recent interest turned to magnesium alanate, $Mg(AlH_4)_2$, which has a hydrogen capacity of 9.3 wt. %.[36–39] Upon heating $Mg(AlH_4)_2$ releases hydrogen according to the reaction

$$Mg(AlH_4)_2 \rightarrow MgH_2 + 2Al + 3H_2(g). \tag{4.1}$$

Since decomposition of MgH_2 takes place at too high a temperature to be of practical use,[6,40] it is the amount of hydrogen released in Reaction 4.1 that determines the actual storage capacity of $Mg(AlH_4)_2$. Still, this relatively large amount of 7.0 wt. % makes magnesium alanate a good candidate for hydrogen storage. Only little is known about the thermodynamics of this material, however.[41] Since up to now its synthesis has proceeded via an indirect route, the first question is whether $Mg(AlH_4)_2$ is thermodynamically stable with respect to decomposition into its elements. The answer to this question is relevant in the search for a more direct synthesis route.

A second question concerns the reaction enthalpy of Reaction 4.1. The ideal hydrogen storage material should produce a hydrogen pressure of 0.1 MPa at room temperature. The entropy contribution of hydrogen gas at this temperature favors the right-hand side of Reaction 4.1. At $T = 0$ the hydrogen desorption reaction should therefore have an enthalpy of ~ 0.4 eV per desorbed H_2 molecule.[6] Furthermore, the kinetics of hydrogen adsorption/desorption should be sufficiently fast. Finding ways of improving the kinetics can start from understanding the bonding in $Mg(AlH_4)_2$, which is determined by the electronic structure of the material.

In this paper we report the results of an *ab initio* study on the properties of magnesium alanate. The structure is optimized and the electronic structure is calculated. We characterize the bonding in $Mg(AlH_4)_2$ and calculate the enthalpy of decomposition into its elements, as well as the enthalpy of the dehydrogenation reaction, Reaction 4.1.

Computational methods

Total energies are calculated within density functional theory (DFT), using the PW91 generalized gradient approximation (GGA) functional.[25] We use the projector augmented wave (PAW) method[14, 19] and a plane wave basis set, as implemented in the Vienna *Ab initio* Simulation Package (VASP).[15–17] The atomic positions and the cell parameters, including the cell volume, are optimized by minimizing the forces and stresses. A $7 \times 7 \times 7$ Monkhorst-Pack **k**-point mesh is used for sampling the Brillouin zone.[21] A kinetic energy cutoff of 312 eV is used for the plane wave basis set. The reaction enthalpies are calculated using a higher kinetic energy cutoff of 700 eV to ensure convergence.

If we calculate reaction enthalpies from total energy differences only, we neglect the contributions from atomic vibrations. Such contributions are negligible for heavy elements, whereas they may be significant for hydrogen. For each compound involved in the reaction we calculate its zero point vibrational energy (ZPVE), $\frac{1}{2}\hbar \sum_j \omega_j$, resulting from the vibrational modes j in the optimized structure. Vibrational frequencies ω_j are generated from a dynamical matrix, whose matrix elements (i.e., the force constants) are calculated using a finite difference method.[24] For the hydrogen molecules we calculate a ZPVE of 0.29 eV, in good agreement with the value of 0.27 eV obtained from the experimental frequency.[27] We also consider the zero point rotational energy (ZPRE) of the hydrogen molecules. Assuming that ortho- and para-hydrogen are produced in a proportion of three to one, the average ZPRE of a hydrogen molecule is 0.011 eV, using the energy levels given in Ref. 27. In summary, the reaction enthalpies ΔH are calculated from

$$\Delta H = \sum_f \left(E_f^{\mathrm{tot}} + E_f^{\mathrm{ZPVE}}\right) + E_{H_2}^{\mathrm{ZPRE}} - \sum_i \left(E_i^{\mathrm{tot}} + E_i^{\mathrm{ZPVE}}\right) \tag{4.2}$$

where $E_{f/i}^{\mathrm{tot}}$ denotes the total electronic energy of the reaction products f or reactants i, $E_{f/i}^{\mathrm{ZPVE}}$ are the corresponding ZPVEs, and $E_{H_2}^{ZPRE}$ is the ZPRE of all hydrogen molecules involved in the reaction. By varying the computational parameters, in particular the PAW potentials, we estimate that reaction enthalpies are converged on a scale of 0.05 eV.

DFT calculations using the common density functionals give adequate values for ground state properties such as total energies and vibrational frequencies. Excited state properties are not given accurately, e.g., the electronic band gap is typically underestimated by $\sim 50\%$. This in fact stems from an unjustified interpretation of the Kohn-Sham eigenvalues of DFT as excitation energies. To calculate single-particle excitation energies, one should solve a quasi-particle equation using the non-local, energy dependent self-energy. The *GW* technique approximates the self-energy by a dynamically screened exchange interaction. Constructing this interaction from the orbitals and eigenvalues obtained in a DFT calculation with the local density approximation (LDA) is called the

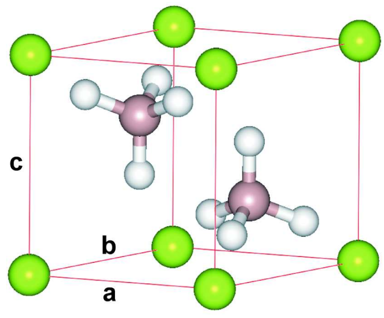

Figure 4.1: *Crystal structure of* $Mg(AlH_4)_2$*; space group* $P\bar{3}m1$

G_0W_0 approximation. It leads to accurate band structures and band gaps for a wide range of semiconductors and insulators.[42] GW calculations have also been successfully applied to metal hydrides.[43,44]

We start from an LDA calculation using norm conserving pseudo potentials and a plane wave kinetic energy cutoff of 748 eV.[45] The screened interaction G_0W_0 is then calculated using the real space, imaginary time formalism.[44,46] For these calculations we use 350 LDA states, a $13 \times 13 \times 19$ real space grid sampling of the unit cell, and an interaction cell consisting of $5 \times 5 \times 4$ unit cells. The quasi-particle equation is solved while neglecting the off-diagonal elements of the self-energy between the LDA states. We estimate that the quasi-particle band gap of $Mg(AlH_4)_2$ is numerically converged to within ±0.02 eV.

Crystal structure

Magnesium alanate has a CdI_2 structure with the Mg atoms on the Cd positions and AlH_4 tetrahedra on the I positions; the space group is $P\bar{3}m1$ (164).[38] The structure basically consists of AlH_4 tetrahedra which form close packed double layers perpendicular to the c-axis, alternated with a layer of Mg atoms, as shown in Figure 4.1.

Starting from the experimental structure proposed in Ref. 38, we optimize the atomic positions and cell parameters. As it turns out, for unit cell volumes in the range 125-150 $Å^3$ the total energy only weakly depends upon the volume. We map out the total energy as a function of the cell volume. At each volume we optimize the atomic positions and the cell shape, and allow for breaking the symmetry. Interpolating this energy versus volume curve gives a minimum energy at a cell volume of 143.26 $Å^3$. Optimizing the structure at this volume gives the final results shown in Table 4.1. The calculated structure has $P\bar{3}m1$ symmetry and is in good agreement with the recently obtained experimental structure extracted from X-ray and neutron powder diffraction data.[39]

The Al-Al nearest neighbor distance within a double layer is 3.91 Å, whereas the

Table 4.1: *Optimized crystal structure of $Mg(AlH_4)_2$, compared to the experimental structure at 8 K from Ref. 39.*

Cell parameters		a	b	c
	calc.	5.23	5.23	6.04
	exp.	5.21	5.21	5.84
Wyckoff positions		x	y	z
Mg (1a)	calc.	0	0	0
	exp.	0	0	0
Al (2d)	calc.	1/3	2/3	0.706
	exp.	1/3	2/3	0.699
H1 (2d)	calc.	1/3	2/3	0.442
	exp.	1/3	2/3	0.424
H2 (6i)	calc.	0.168	−0.168	0.812
	exp.	0.167	−0.167	0.811

shortest Al-Al distance between two double layers is 4.66 Å. Mg atoms occupy octahedral interstitial sites between two double layers with Mg-Al distances of 3.50 Å. The AlH_4 tetrahedra are slightly distorted, but they retain a threefold rotation axis parallel to the **c**-axis. The Al-H1 and Al-H2 bond lengths are 1.60 and 1.62 Å and the H1-Al-H2 and H2-Al-H2 bond angles are 113.0° and 105.8°. The geometry of the AlH_4 tetrahedra is similar to that found in isolated $(AlH_4)^-$ ions, where the Al and H atoms are covalently bonded.[147] This geometry is quite different from those found in neutral AlH_x clusters.[48] The minimum Al-H and H-H distances between atoms of different AlH_4 tetrahedra is 3.14 Å and 2.63 Å respectively, indicating that the AlH_4 tetrahedra are clearly separated. The Mg atoms are octahedrally coordinated by H2 atoms with a Mg-H distance of 1.89 Å and H-Mg-H angles of 86.9° and 93.1°. This coordination is not unlike that found in MgH_2.

---

[1] For comparison, the ionic radii of Al^{3+}, Mg^2+ and H^- are 0.51, 0.65 and 2.08 Å , and the covalent radii of Al, Mg and H are 1.26, 1.30 and 0.31 Å . L. Pauling, *The nature of chemical bonds*, (Cornell University Press, 1973).

Electronic structure

Figure 4.2(a) shows the electronic density of states (DOS) of magnesium alanate obtained from the DFT/GGA calculation. It can be compared to the calculated DOS of the lattice of $(AlH_4)^-$ tetrahedra, shown in Figure 4.2(b). Here the Mg ions have been removed and replaced by a homogeneous positive background charge. The similarities between Figures 4.2(a) and (b) demonstrate that the $(AlH_4)^-$ ions strongly contribute to both the valence and the conduction bands of $Mg(AlH_4)_2$. Such a dominance of the anion is also observed in the simple ionic compound NaCl.[49, 50]

Projecting the valence states on atomic orbitals shows that Al and H contribute a comparable amount, which is a strong indication for covalent bonding within the $(AlH_4)^-$ tetrahedra. The splitting into two valence bands, as is most clearly visible in Figure 4.2(b), is a remnant of the splitting between states of s-like (A_1) and p-like (T_2) symmetry in a single tetrahedron. In an isolated $(AlH_4)^-$ ion, the sp-gap is $\sim$ 4 eV. This gap is closed to a certain extent by the interaction between the $(AlH_4)^-$ ions, which results in a band dispersion of 2-3 eV. It shows that, although the interaction between the $(AlH_4)^-$ tetrahedra is not negligible, it is weaker than the interaction within a single tetrahedron.

If we compare the valence bands of Figures 4.2(a) and (b) in more detail, we observe a small peak in the DOS of $Mg(AlH_4)_2$, which occurs within the sp-gap mentioned above. This peak results from the hybridization between H and Mg s states. Hybridization with Mg p and d states also gives less clearly visible contributions at higher energy. In any case, the H-Mg hybridization is much weaker than the H-Al hybridization.

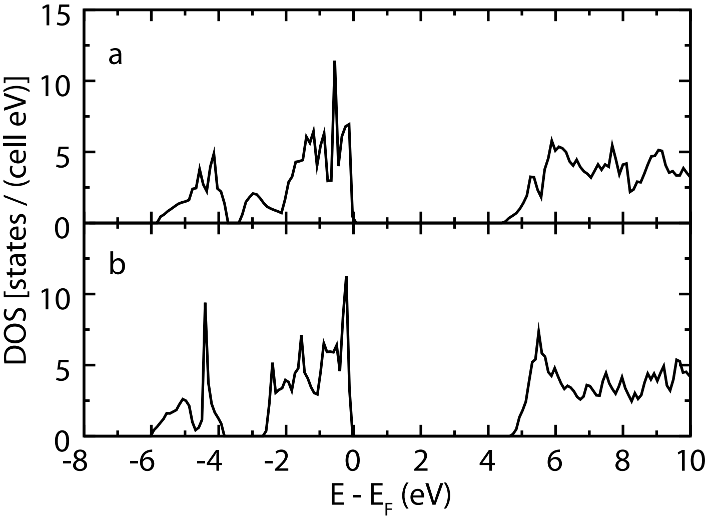

Figure 4.2: *(a) The DFT/GGA electronic density of states (DOS) of* $Mg(AlH_4)_2$. *The zero of energy is at the top of the valence band. (b) DOS of* $(AlH_4^-)_2$ *with a positive homogenous background charge.*

The GW band structure of $Mg(AlH_4)_2$ is shown in Figure 4.3. It has an indirect band gap, where the bottom of the conduction band is located at A and the top of the valence band at 0.7AH, $\left[\mathrm{A} = \left(0, 0, \frac{1}{2}\right), \ \mathrm{H} = \left(\frac{1}{3}, \frac{1}{3}, \frac{1}{2}\right)\right]$. The band gap as obtained from the G_0W_0 calculation is 6.47 eV. This classifies $Mg(AlH_4)_2$ as a large band gap insulator, which is typical for ionic compounds. The dispersions of the highest valence and the lowest conduction bands in a direction along the **c**-axis are rather small. The direct band gap at A is 6.88 eV; the direct band gap at Γ is 6.85 eV. The total valence band width is 5.99 eV. The valence bands are split into two sets, the lower and upper set having a width of 2.05 eV and 3.57 eV, respectively. The two sets are separated by a small gap of 0.36 eV.

The layered structure of $Mg(AlH_4)_2$ does not imply that the interactions in the compound are strongly anisotropic. The dispersions of the bands in various directions are similar, compare e.g. the ΓA and the ΓM directions $\left[\mathrm{M} = \left(\frac{1}{2}, 0, 0\right)\right]$. This indicates that the interactions between the ions within a layer (the **ab**-plane) are comparable to those perpendicular to the layers.

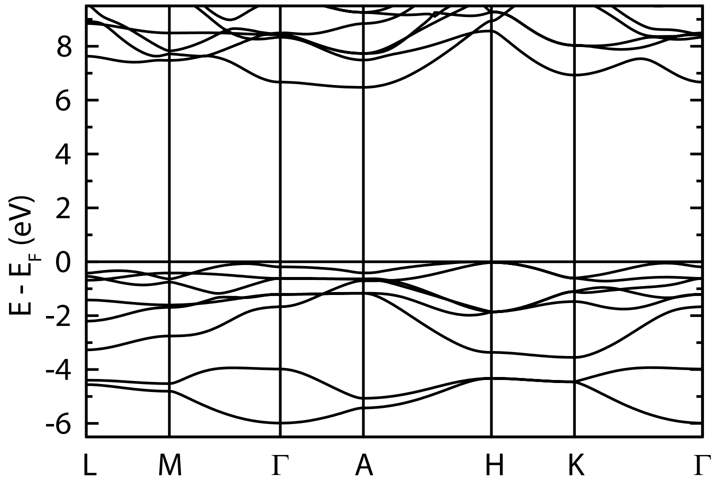

Figure 4.3: *GW band structure of* $Mg(AlH_4)_2$*. The zero of energy is at the top of the valence band.*

Reaction enthalpies

Decomposing $Mg(AlH_4)_2$ into its elements corresponds to the reaction

$$Mg(AlH_4)_2 \rightarrow Mg + 2Al + 4H_2(g). \tag{4.3}$$

Here Mg and Al are in the crystalline phase, whereas H_2 is in the gaseous phase. For aluminum we use the fcc structure with a lattice parameter of 4.05 Å and for magnesium we used the hcp structure with lattice parameters a = 3.21 Å, c = 5.21 Å. The total

Table 4.2: *Total energies (with respect to non spin polarized model atoms), zero point vibrational energies (ZPVE) and zero point rotational energy (ZPRE) in eV/formula unit.*

	E^{TOT}	E^{ZPVE}	E^{ZPRE}
Mg	−1.524	0.026	
Al	−3.698	0.037	
H_2	−6.803	0.266	0.011
MgH_2	−8.983	0.402	
$Mg(AlH_4)_2$	−36.764	1.520	

energies and ZPE corrections are given in Table 4.2. From these numbers, the reaction enthalpies are then calculated using Equation 4.2.

The reaction enthalpy of Reaction 4.3 is 0.16 eV per H_2 molecule on the basis of total energies. If we include the ZPE, the reaction enthalpy decreases to 0.08 eV/H_2. Since the reaction enthalpy of Reaction 4.3 is positive, it should, in principle, be possible to synthesize $Mg(AlH_4)_2$ from the elements. Note that at this energy scale, the contributions due to the zero point motions of the hydrogen atoms are not negligible. In general, they tend to make a negative contribution to the reaction enthalpy for decomposing the metal hydride, since the motion of a hydrogen atom in the crystal is more confined than in the gas phase.

To calculate the reaction enthalpy of Reaction 4.1 one also needs the optimized structure and ZPVE of MgH_2. MgH_2 has space group $P4_2/mnm$ (136) and its calculated lattice parameters are $a = 4.51$ Å and $c = 3.01$ Å. The magnesium and hydrogen atoms are at the $2a$ and $4f$ ($x = 0.304$) Wyckoff positions, respectively. As a check on the accuracy of these calculations we can also extract the reaction enthalpy of decomposing MgH_2 into its elements

$$MgH_2 \rightarrow Mg + H_2(g). \tag{4.4}$$

The reaction enthalpy of Reaction 4.4 is 0.66 eV/H_2 without ZPE corrections and 0.56 eV/H_2 with ZPE corrections. This is in reasonable agreement with the value of 0.76 eV/H_2, which is extracted by extrapolating the experimental results to zero temperature.[40,51]

For other metal hydrides our calculations also underestimate the decomposition enthalpy, although usually by a smaller amount. This would indicate a systematic error of up to 0.2 eV on the calculated enthalpies, which is larger than the spread of 0.05 eV caused by using different PAW potentials.[52] However, this does not alter our conclusions.

The calculated reaction enthalpy of Reaction 4.1 is -0.008 eV per H_2 molecule in the gas phase, without ZPE correction. This is negligibly small, but consistent with earlier experimental data.[41] Moreover, including the ZPE correction makes the reaction enthalpy slightly more negative, i.e. -0.08 eV/H_2. In any case this number is significantly less than the ~ 0.4 eV/H_2, which, based on thermodynamics, is required to make $Mg(AlH_4)_2$ a good material for hydrogen storage. Further investigations are needed to see whether e.g. alloying would increase the stability of magnesium alanate.

Acknowledgements

We thank Prof. Dr. R. A. de Groot, Prof. Dr. P. J. Kelly, and Dr. B. Dam for helpful discussions. This work is part of the research programs of ‘Advanced Chemical Technologies for Sustainability (ACTS)’ and ‘Stichting voor Fundamenteel Onderzoek der Materie (FOM)’, financially supported by ‘Nederlandse Organisatie voor Wetenschappelijk Onderzoek (NWO)’.

Chapter 5

Optical properties of alanates

Reproduced with permission from:
Electronic structure and optical properties of lightweight metal hydrides
M. J. van Setten, V. A. Popa, G. A. de Wijs, and G. Brocks
Phys. Rev. B **75**, 035204 (2007)
Copyright 2007 by the American Physical Society

Abstract

We study the dielectric functions of the series of simple hydrides LiH, NaH, MgH_2 and AlH_3, and of the complex hydrides Li_3AlH_6, Na_3AlH_6, $LiAlH_4$, $NaAlH_4$ and $Mg(AlH_4)_2$, using first principles density functional theory and *GW* calculations. All compounds are large gap insulators with *GW* single particle band gaps varying from 3.5 eV in AlH_3 to 6.6 eV in $LiAlH_4$. Despite considerable differences between the band structures and the band gaps of the various compounds, their optical responses are qualitatively similar. In most of the spectra the optical absorption rises sharply above 6 eV and has a strong peak around 8 eV. The quantitative differences in the optical spectra are interpreted in terms of the structure and the electronic structure of the compounds. In the simple hydrides the valence bands are dominated by the hydrogen atoms, whereas the conduction bands have mixed contributions from the hydrogens and the metal cations. The electronic structure of the aluminium compounds is determined mainly by aluminium hydride complexes and their mutual interactions.

Introduction

The large scale utilization of hydrogen as a fuel crucially depends on the development of compact hydrogen storage materials with a high mass content of hydrogen.[6] Hydrides of group I-III metals in the upper rows of the periodic table could meet this requirement. These metals are sufficiently light for their hydrides to have a large gravimetric hydrogen density; for instance, MgH_2 contains 7.7 wt.% hydrogen. One must be able to extract hydrogen at a moderate temperature, however, and therefore the metal hydride should be neither too stable nor too unstable. Simple metal hydrides do not satisfy this demand. For example, the binding energy of MgH_2 is too large,[40, 51] whereas the binding energy of AlH_3 is close to zero.[53]

This has stimulated research into binary intermetallic hydrides such as the alanates $MAlH_4$, $M(AlH_4)_2$, with M and M′ a light alkali and alkaline earth metal, respectively. Some of the properties of these compounds have indeed improved as compared to the simple hydrides, but the compound that meets both the stability and the storage capacity demands has not been found yet. Whereas sodium alanate, $NaAlH_4$, releases hydrogen in two reaction stages with enthalpies close to the ideal value, its active gravimetric hydrogen density is only 5.5 wt.%.[6, 31, 34] Magnesium alanate, $Mg(AlH_4)_2$, and lithium alanate, $LiAlH_4$, have a higher active gravimetric hydrogen density of 7.0 and 8.0 wt.%, respectively. However, they are not sufficiently stable with respect to decomposition into simpler hydrides.[52, 54–58]

A suitable ternary intermetallic hydride might satisfy all requirements. The number of possible ternary compounds is very large, however, and searching for the optimal composition becomes very tedious, unless one uses a combinatorial approach. Such techniques have been proposed recently, in which thin films are grown with tunable composition gradients.[59–61] The composition is then a function of the position on the film. This avoids having to synthesize all compositions individually, but one still needs to be able to identify the most promising ones. It is proposed that identification can be based upon the optical properties of suitable metal hydrides being very different from those of their host metals.[60] This has first been demonstrated conclusively for YH_3,[62] and since then for a number of other so-called “switchable mirror" rare earth and transition metal compounds.[63–69] The compounds that absorb the maximum amount of hydrogen, become semiconductors or insulators.

If one applies this technique to group I-III metal hydrides, it is relevant to know how the optical properties of these compounds depend on their composition and structure. In this paper we report a systematic first principles study of the band gaps, the electronic structure and the optical properties of group I-III metal hydrides. Band gaps and single particle excitations are calculated within the *GW* quasi-particle approach; optical excitations are obtained using the random phase approximation (RPA). We focus upon a number of elements that are of interest for lightweight metal hydrides, i.e., Li, Na, Mg and Al. In particular, we consider the series of simple metal hydrides LiH, NaH, MgH_2, AlH_3 and the binary metal hydrides Li_3AlH_6, Na_3AlH_6, $LiAlH_4$, $NaAlH_4$ and $Mg(AlH_4)_2$.[34,35,38,55,70–74] The trends in the optical spectra and electronic structure are discussed and interpreted in terms of the structure and bonding of the materials.

This paper is organized as follows. In Sec. II we outline the computational methods used in our study. The results are presented in Sec. III, first for the simple hydrides, then for the binary M_3AlH_6 hydrides and finally for the $MAlH_4$ alanates. Secs. IV and V contain the discussion and a summary.

Computational methods

The results discussed in this paper are obtained using a combination of density functional theory (DFT) and *GW* calculations. DFT is used at generalized gradient approximation (GGA) level to optimize the ground state structure and obtain single particle wave functions to be used in the calculation of the optical response. *GW* is used to generate single particle excitation energies within the quasi-particle (QP) approximation, starting from DFT in the local density approximation (LDA) wavefunctions and eigenvalues. The optical response is given by the frequency dependent dielectric function, which is calculated within the random phase approximation (RPA). In the latter we use single particle wave functions and excitation energies and neglect exciton and local field effects. The main difference between the DFT and the QP excitation spectra is the size of the fundamental band gap between occupied and unoccupied states, whereas the dispersion of the bands is quite similar. We use a scissors operator to the DFT eigenvalues to approximate QP excitation energies on a dense grid in the Brillouin zone, which is required to calculate the dielectric function.

DFT ground state calculations

DFT total energies are calculated with the PW91 GGA functional[25] and the projector augmented wave (PAW) method,[14,19] as implemented in the Vienna *Ab initio* Simulation Package (VASP).[15–17] We use standard frozen core PAW potentials and a plane wave basis set with a kinetic energy cutoff of 312 eV. The tetrahedron scheme is applied for the Brillouin zone integration using **k**-point meshes with a spacing between 0.01 and 0.03 Å^{-1}. The cell parameters and the atomic positions within a unit cell are optimized by minimizing the total energy, except for the alkali alanates, where only the atomic positions are optimized and the cell parameters are taken from literature. For the alkali alanates various extensive studies have been reported on the crystal structure, both experimental and theoretical. For these materials the DFT/GGA crystal structure results agree well with experimental values, see, e.g., Refs.[75] and.[76] Furthermore calculations using slightly different lattice parameters, agree well on the electronic structure of the materials. These optimized structures are used as input for the *GW* calculations.

GW calculations

DFT calculations generally give good results for ground state properties, but not for excited states. The electronic band gap, for instance, can be underestimated by $\sim 50\%$, and even more than that for small band gap materials. This stems from an unjustified interpretation of the DFT (Kohn-Sham) eigenvalues as single particle excitation energies. The latter can be obtained from the quasi-particle (QP) equation, which involves the non-local, energy dependent self-energy Σ,

$$\begin{aligned}\left[-\frac{1}{2}\nabla^2 + v_{\text{ext}}(\mathbf{r}) + V_H(\mathbf{r})\right]\psi_{n\mathbf{k}}(\mathbf{r}) &\quad + \\ + \int d\mathbf{r}'\ \Sigma(\mathbf{r},\mathbf{r}';\epsilon_{n\mathbf{k}})\psi_{n\mathbf{k}}(\mathbf{r}') &= \epsilon_{n\mathbf{k}}\psi_{n\mathbf{k}}(\mathbf{r}),\end{aligned} \tag{5.1}$$

where v_{ext} stands for the sum of all nuclear or ionic potentials, V_H is the electrostatic or Hartree potential resulting from the electrons, $\psi_{n\mathbf{k}}(\mathbf{r})$ is the QP wave function, and $\epsilon_{n\mathbf{k}}$ is the QP energy, i.e., the single particle excitation energy. In practice Equation 5.1 is solved using a number of approximations. The *GW* technique approximates the self-energy Σ by a dynamically screened exchange potential. A large variety of *GW* implementations exist, in which quite different levels of approximation are used. Reviews of the *GW* method can be found in Refs.[42,77,78] We will explain our procedure in this section and benchmark it on simple hydrides in the next section.

The G_0W_0 approximation is commonly defined by constructing the self-energy Σ from the orbitals and eigenvalues obtained in a DFT/LDA..[42,77–79] If the QP and DFT/LDA wave functions do not differ significantly, i.e., $\psi_{n\mathbf{k}}(\mathbf{r}) \approxeq \psi^{\text{LDA}}_{n\mathbf{k}}(\mathbf{r})$, then Equation 5.1 is approximated by[80,81]

$$h_{n\mathbf{k}} + \Sigma_{n\mathbf{k}}(\epsilon_{n\mathbf{k}}) = \epsilon_{n\mathbf{k}}, \tag{5.2}$$

where $h_{n\mathbf{k}} = \langle\psi^{\text{LDA}}_{n\mathbf{k}}| -\frac{1}{2}\nabla^2 + v_{\text{ext}} + V_H|\psi^{\text{LDA}}_{n\mathbf{k}}\rangle$ and $\Sigma_{n\mathbf{k}} = \langle\psi^{\text{LDA}}_{n\mathbf{k}}|\Sigma|\psi^{\text{LDA}}_{n\mathbf{k}}\rangle$. Equation 5.2 is non-linear in $\epsilon_{n\mathbf{k}}$ and it is solved by a root-searching technique.[1] In principle it is possible to base a G_0W_0 calculation upon orbitals and eigenvalues of any independent particle

---

[1] The QP energies $\epsilon_{n\mathbf{k}}$ are complex. The real parts comprise the band structure and are used as single particle excitation energies. The imaginary parts give the inverse QP lifetimes.

Hamiltonian, derived, e.g., from Hartree-Fock or DFT/GGA. However, the most widely tested G_0W_0 approach uses DFT/LDA orbitals and eigenvalues as starting point, which is the approach we use here. Calculations within this scheme have been applied to a wide range of semiconductors and insulators. They lead to band gaps that are usually within 10% of the experimental values, although occasionally somewhat larger deviations are found.[42, 77, 78]

Since GW calculations are computationally demanding, all electron calculations are generally possible only for relatively small unit cells.[82] In order to decrease the computational demands pseudopotentials are used to represent the ion cores and only the valence electrons are treated explicitly. The effects of this approximation are discussed in the literature.[42, 77, 82] In principle, an overlap between core and valence charge densities contributes to the screening, and thus to the self-energy. This contribution is neglected in a pseudopotential approach, but a simple estimate of its effect is made by adding

$$(V_{xc}[\rho_v + \rho_c] - V_{xc}[\rho_v])_{n\mathbf{k}}, \tag{5.3}$$

to the QP energies, where V_{xc} is the LDA exchange-correlation potential, $\rho_{c,v}$ are the core and valence charge densities, and $n\mathbf{k}$ indicates the expectation value with respect to an LDA wave function as in Equation 5.2.[43, 44] We will benchmark the effects of the pseudopotential approximation on the quasi-particle gaps of hydrides in the next section.

The QP equation, Equation 5.1, is not related to DFT, but the scheme outlined above depends on LDA eigenvalues and wave functions through the G_0W_0 approximation for the self-energy and through the approximation represented by Equation 5.2. The dependence on LDA eigenvalues can be avoided by constructing the self-energy (GW) from QP energies and solve the QP equation self-consistently. We have previously observed that self-consistency on the eigenvalues is in fact vital to obtain good results for small band gap semiconductors that are incorrectly described by LDA as being metallic.[43, 44] For large band gap materials, however, this self-consistency does not improve upon the G_0W_0 results.[83] The dependence on LDA wave functions can be relaxed by solving Equation 5.1 instead of Equation 5.2. However, for large band gap materials this changes the results only marginally.[83] The dependence of the self-energy on the LDA wave functions is not that easily avoided. Self-consistency applied to QP wave functions worsens the results as compared to the G_0W_0 approximation.[83]

Since all hydrides considered in this paper turn out to be large band gap insulators, we use the G_0W_0 approximation to calculate the QP spectrum. Starting from the optimized structures we generate wave functions and eigenvalues from an LDA calculation with norm-conserving pseudopotentials and a plane wave kinetic energy cutoff of 748 eV.[45] The self-energy G_0W_0 is calculated using the real space, imaginary time formalism.[44, 46, 84, 85]

We include 350 LDA states, use a real space grid mesh with a typical spacing of 0.3-0.4 Å and an interaction cell parameter of $\sim$ 25 Å . The QP equation is solved in the approximation represented by Equation 5.2. We estimate that with these parameters QP band gaps are converged numerically to within ±0.02 eV.

Macroscopic dielectric function

Optical excitations are two-particle excitations, but neglecting excitonic effects they can be approximated by transitions between single particle states. Experimentally, the binding energy of the lowest lying exciton in LiH is less than 0.05 eV.[86,87] In this paper we assume that excitonic effects can be neglected. In addition we neglect local field effects.

If we consider quasi-particles as independent particles, then the imaginary part of the macroscopic dielectric function obtains the simple form[88–90]

$$\begin{aligned}\varepsilon^{(2)}(\hat{\mathbf{q}},\omega) &= \frac{8\pi^2 e^2}{V} \lim|\mathbf{q}\rightarrow 0|\frac{1}{|\mathbf{q}|^2}\sum_{\mathbf{k}vc} \\ &\quad \times| < u_{c\mathbf{k}+\mathbf{q}}|u_{v\mathbf{k}} > |^2\,\delta(\epsilon_{c\mathbf{k}+\mathbf{q}}-\epsilon_{v\mathbf{k}}-\hbar\omega), \qquad (5.4)\end{aligned}$$

where $\hat{\mathbf{q}}$ gives a direction, $v\mathbf{k}$ ($c\mathbf{k}$) label single particle states that are occupied (unoccupied) in the ground state, and ϵ, u are the single particle energies and the translationally invariant parts of the wave functions; V is the volume of the unit cell. We have assumed spin degeneracy.

Almost all optical data on hydrides are obtained on micro- or nano-crystalline samples whose crystallites have a significant spread in orientation. The most relevant quantity then is the directionally averaged dielectric function, i.e., $\varepsilon^{(2)}(\omega)$ averaged over $\hat{\mathbf{q}}$. Equation 5.4 involves calculating $u_{c\mathbf{k}+\mathbf{q}}$ for small $\mathbf{q}$ and each $\mathbf{k}$ and extrapolating to $\mathbf{q}=0$. Details on the implementation can be found in Refs.[29,91]

The summation over the Brillouin zone in Equation 5.4 is performed using a weighted tetrahedron scheme.[92] We found that this scheme allows for a faster convergence with respect to the number of $\mathbf{k}$-points than various smearing methods. To calculate the dielectric tensor, we use the same plane wave kinetic energy cutoff and $\mathbf{k}$-point mesh as for the DFT/GGA calculations. The number of empty bands included is sufficiently large as to describe all transitions up to at least 16 eV.

If the imaginary part of the dielectric function, $\varepsilon^{(2)}(\omega)$, is calculated for all frequencies ω, then the real part, $\varepsilon^{(1)}(\omega)$, can be obtained by a Kramers-Kronig transform. The static component $\varepsilon^{(1)}(0)=\varepsilon^{\infty}$ can also be calculated using density functional perturbation theory. Since the latter calculation includes local field effects, comparing ε^{∞} obtained with the two techniques is one indication for the importance of these effects.[29]

In order to produce the right band gap one should use the *GW* QP energies in Equation 5.4. The $\mathbf{k}$-point mesh used in an ordinary *GW* calculation is not sufficiently dense to obtain an accurate dielectric function, however, and it is computationally very expensive to increase the density of this mesh. As we will show below, the main difference between the *GW* and the GGA energies for the systems studied, is the size of the band gap between the occupied and the unoccupied states. The differences between the dispersions of the *GW* and GGA bands are relatively small. Therefore we adopt a simple "scissors" operator approximation for the energy differences in Equation 5.4,[90]

$$\epsilon_{c\mathbf{k}+\mathbf{q}} - \epsilon_{v\mathbf{k}} = \epsilon^{GGA}_{c\mathbf{k}+\mathbf{q}} - \epsilon^{GGA}_{v\mathbf{k}} + E^{GW}_{gap} - E^{GGA}_{gap}. \tag{5.5}$$

Results

Simple hydrides

Test calculations Calculations on LiH and NaH are relatively straightforward because these compounds have a simple rocksalt structure. They can be used to benchmark the calculations. The calculated single particle band gaps of LiH and NaH are listed in Table 5.1. As is usual, DFT severely underestimates the gap, with LDA giving smaller values than GGA. Our calculated *GW* gaps for LiH and NaH are close to those obtained in recent PAW all-electron G_0W_0 calculations (based upon LDA orbitals and eigenvalues).[93, 94] As stated in the previous section, our calculations use pseudopotentials and take into account explicitly the valence electrons only. The *GW* band gaps as calculated from the QP energies obtained by solving Equation 5.2, are indicated by E_g^{GW} in Table 5.1. They are somewhat larger than the PAW values. If one applies the core correction of Equation 5.3, our *GW* band gaps become somewhat smaller than the PAW values, as shown by the column marked $E_g^{GW,\mathrm{core}}$ in Table 5.1. The differences between the pseudopotential and the PAW *GW* gaps are small, however, i.e. of the order of 2-4% and the PAW values are in between the $E_g^{GW,\mathrm{core}}$ and E_g^{GW} values.

The band gap of LiH given in Ref. 87 has been calculated using the rather crude COSHEX approximation, which is known to lead to a much higher gap.[93] The value given in Ref. 95 is much higher than that obtained in other *GW* calculations, including ours, for which we have no explanation. The experimental band gap of LiH is higher than the calculated *GW* values,[86] but the difference is within the usual 5-10%.[42, 77, 78] To our knowledge no experimental data are available for NaH.

The band gap of MgH_2 is calculated for the optimized rutile or α-structure,[54] which is the most stable structure at room temperature and ambient pressure.[98] The $E_g^{GW,\mathrm{core}}$ value we obtain is very close to that cited in Ref. 96. A recently obtained PAW value for

Table 5.1: *Single particle band gaps E_g (eV) of simple hydrides from DFT (GGA and LDA) and GW calculations. $E_g^{GW,\mathrm{core}}$ refers to applying the correction of Equation 5.3.*

	E_g^{GGA}	E_g^{LDA}	E_g^{GW}	$E_g^{GW,\mathrm{core}}$	*GW* lit.
LiH	3.00	2.61	4.75	4.54	4.64^1, 5.24^2, 5.37^3 $4.99^{\mathrm{exp},4}$
NaH	3.79	3.42	5.87	5.50	5.68^5
MgH_2	3.79	3.36	5.64	5.32	5.25^6, 5.58^7
AlH_3	2.18	1.79	4.31	3.54	

the band gap of MgH_2 is again in between our $E_g^{GW,\mathrm{core}}$ and E_g^{GW} values.[97] For AlH_3 no other data are available to our knowledge. One can observe that core effects are relatively large in this compound.

In the following we will use the $E_g^{GW,\mathrm{core}}$ values. The validity of using the scissors operator approximation for calculating the optical response, see Equation 5.5, is illustrated by comparing band widths calculated with DFT and *GW*. The valence band widths are given in Table 5.2. The difference between the *GW* and the LDA values is within 3% and the difference between the *GW* and the GGA values is within 10%. Note that the latter is on the same scale as the difference between the LDA and the GGA values. This accuracy is acceptable for our purposes. We have also checked in more detail that the dispersions of the individual bands in the DFT and *GW* band structures are very similar.

Table 5.2: *Valence band widths (eV) from DFT (GGA and LDA) and GW calculations. The directionally averaged real part of the static dielectric constant, calculated with (LFE) and without local field effects.*

	GGA	LDA	*GW*	$\varepsilon^{\infty}_{LFE}$	ε^{∞}
LiH	5.41	5.62	5.81	4.28	4.34
NaH	3.58	4.00	3.99	3.03	3.06
MgH_2	6.34	6.62	6.66	3.90	3.98
AlH_3	8.60	8.82	8.92	4.43	4.55

Table 5.2 also lists the static dielectric constant calculated with and without local field effects. The small differences between these numbers give no indication for large

local field effects.

LiH and NaH The calculated optimized lattice parameters of LiH and NaH in the rock salt structure are 4.02 and 4.83 Å, respectively. These values are somewhat smaller than the experimental lattice parameters of 4.09 and 4.91 Å due to neglecting the zero point motions of the hydrogen atoms, as discussed in Ref. 99.

The band structures and the directionally averaged $\varepsilon^{(2)}(\omega)$ of LiH and NaH are shown in Figure 5.1. The valence bands in both LiH and NaH are strongly dominated by hydrogen, which reflects the ionic character of the bonding.[87,93–95] The conduction bands have a mixed hydrogen and cation character. The lattice parameter of LiH is significantly smaller than that of NaH. Because of the smaller distance between the hydrogen atoms the band widths in LiH are generally larger than in NaH. This is most easily observed in the valence band, whose dispersion is quite similar in LiH and NaH, but the (GW) valence band width in LiH is 5.81 eV, whereas in NaH it is 3.99 eV.

The conduction bands of the two compounds are qualitatively different. In LiH the conduction band minimum is at X, whereas in NaH it is at L, which causes the gap in LiH to be direct, whereas in NaH it is indirect. In NaH there is little participation of cation states in the lower lying conduction bands. A calculation on an fcc lattice of H^- ions with the NaH lattice parameter and a homogeneous background charge instead of the Na^+ cations, gives essentially the same band structure. In LiH the participation of the Li cations to the conduction band is larger. The conduction band minimum at X is lowered in energy because here the Li-2p state participates in a bonding combination with hydrogen states. Similarly, the conduction band minimum at L is raised in energy because the Li-2s state contributes to an anti-bonding combination with hydrogen states.

The differences between the band structures of LiH and NaH lead to markedly different dielectric functions, as is shown in the lower panel of Figure 5.1. The calculated direct optical gap in LiH is 4.54 eV, whereas in NaH it is a much larger 6.37 eV. The main peak in the NaH spectrum originates from transitions at L and X, whose onset is at comparable photon energies. Both valence and conduction bands of NaH have hydrogen character and the oscillator strength of these transitions is rather large. The result is a sharp and dominant peak just above the onset of the optically allowed transitions.

The optical spectrum of LiH has more structure. The onset at 4.54 eV is due to transitions at X, and at a somewhat higher energy transitions near K and W contribute. At energies $\sim$ 9 eV transitions at L become allowed, which results in a peak in the dielectric function at that energy. Since the bands of LiH have a larger dispersion than those of NaH, the optical response of LiH is spread out over a larger energy range.

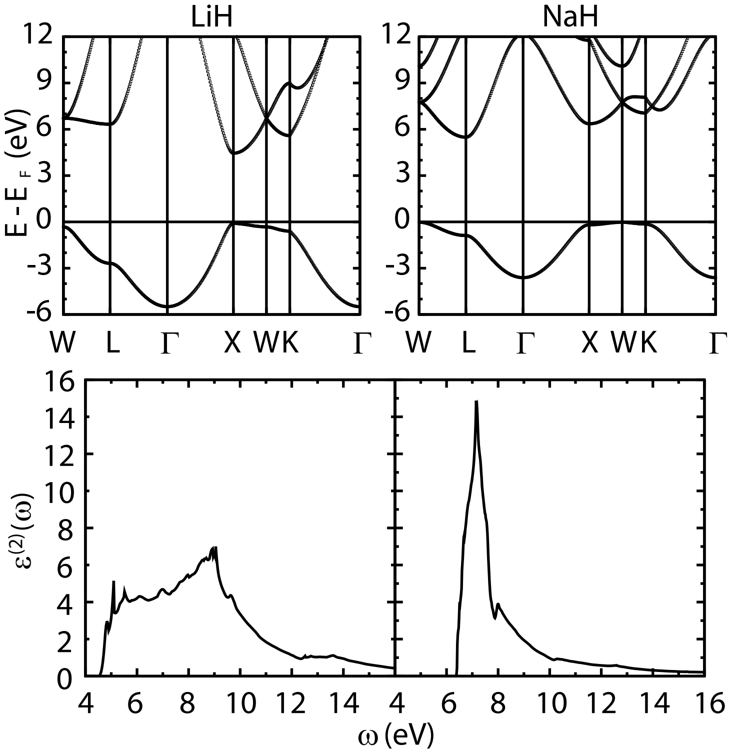

Figure 5.1: *Upper panels: electronic band structures of LiH and NaH. The zero of the energy scale is at the top of the valence band. Lower panels: imaginary parts of the directionally averaged macroscopic dielectric functions of LiH and NaH. The calculated optical gaps of LiH and NaH are 4.54 and 6.37 eV, respectively. Unless explicitly stated otherwise, the results presented in the figures are based upon GGA calculations modified by a scissors operator extracted from the GW results.*

MgH_2 α-MgH_2 has the rutile structure, i.e. space group $P4_2/mnm$ with Mg, H atoms in $2a$, $4f$ Wyckoff positions, respectively, and two formula units per unit cell. The optimized calculated lattice parameters are $a = 4.52$ Å and $c = 3.01$ Å, with the H atoms at $x = 0.304$. This is in good agreement with the experimental values $a = 4.50$ Å, $c = 3.01$ Å and $x = 0.304$.[100] The magnesium atoms are sixfold octahedrally coordinated by the hydrogen atoms at distances between 1.94 and 1.96 Å. Each MgH_6 octahedron shares the hydrogen atoms at its corners with neighboring octahedra. Each hydrogen atom is shared by three octahedra and is therefore coordinated by three magnesium atoms.

The band structure of MgH_2 is shown in Figure 5.2, and agrees with the results in Refs.[97,101] There is a small hybridization between the H and the Mg states in the valence bands, with the lowest two valence bands having some Mg s and the highest two having some Mg p character, respectively. As in the case of LiH and NaH, the valence bands have a dominant hydrogen character, however. The conduction bands have a mixed magnesium hydrogen character and the bottom of the conduction band has a considerable Mg $3s$

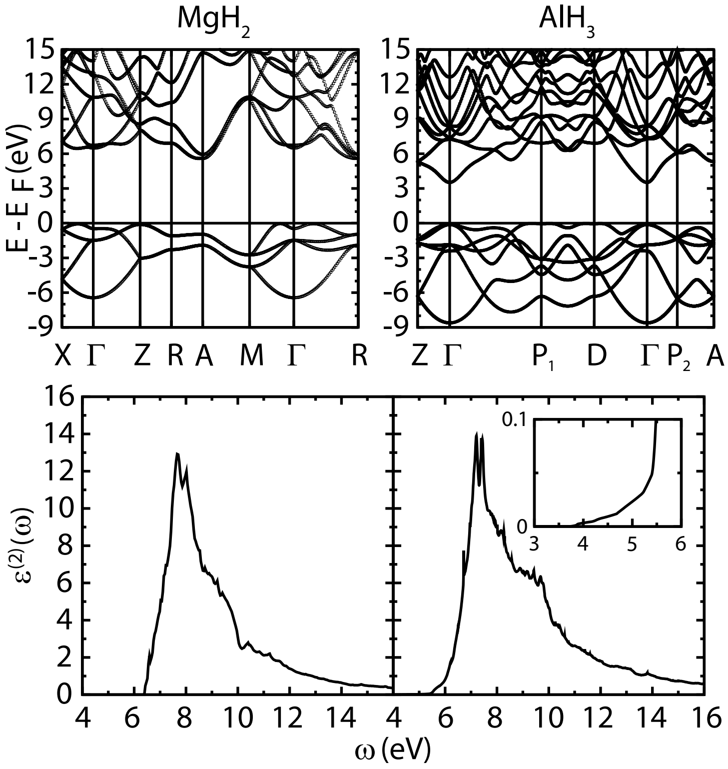

Figure 5.2: *Upper panels: electronic band structures of MgH_2 and AlH_3. The zero of the energy scale is at the top of the valence band. P_1 and P_2 correspond to the points (0.5,-1,0.5) and (0.5,0.5,0.5). Lower panels: imaginary parts of the directionally averaged macroscopic dielectric functions of MgH_2 and AlH_3. The calculated optical gaps of MgH_2 and AlH_3 are 6.19 and 3.54 eV, respectively.*

contribution. MgH_2 has a calculated indirect gap of 5.32 eV, see Table 5.1, whereas the direct optical gap is 6.19 eV. The experimental optical gap obtained in Ref. 96 is 5.6 ± 0.1 eV, which would indicate that our *GW* result overestimates the gap by 10%.

The lower panel of Figure 5.2 shows the dielectric function of MgH_2. It is in general agreement with that obtained in a recent GW/PAW calculation.[97] The onset of optical transitions occurs almost at the same energy at various regions throughout the Brillouin zone, which results in a steep rise of the dielectric function and a peak close to 8 eV. At energies above 9 eV transitions from the lower valence bands start to play a role, see for instance the interval Z-M in the upper panel of Figure 5.2. This results in a shoulder in the dielectric function at $\sim$ 9 eV. Finally, the shoulder at $\sim$ 11 eV in the spectrum involves transitions to higher lying conduction bands, associated with rather delocalized states having considerable Mg character.

AlH_3 AlH_3 has a rhombohedral structure with space group $R\overline{3}c$ and the Al, H atoms in the $6b$, $18e$ Wyckoff positions, respectively. The unit cell contains two formula units. The optimized lattice parameters are $a = 4.49$ Å and $c = 11.82$ Å, with the H atoms at $x = 0.623$. These values are in good agreement with the experimental values $a = 4.45$ Å, $c = 11.80$ Å and $x = 0.628$.[102] The interatomic Al-Al distances in the ab plane and along the c axis are 4.45 Å and 3.24 Å, respectively. The aluminium atoms form a distorted face centered structure, where each Al atom is octahedrally coordinated by H atoms with an Al-H distance of 1.75 Å. Each AlH_6 octahedron shares its corners with neighboring octahedra and each H atom at a corner forms a bridge between two Al atoms. Since these bridges are not linear, i.e. the Al-H-Al bond angle is 141°, the octahedra are tilted with respect to one another.

The band structure of AlH_3 is shown in Figure 5.2. There is hybridization between H and Al states, but the six valence bands are dominated by hydrogen, as are the valence bands of the other hydrides. In contrast to MgH_2, AlH_3 has a direct band gap, which is located at Γ. The band gap is 3.54 eV, which is notably smaller than the gap in the other hydrides discussed above. This is caused by a single conduction band that disperses to ~ 2 eV below the other conduction bands. This band has a large Al $3s$ contribution.

The dielectric function of AlH_3 is shown in the lower panel of Figure 5.2. Although the optical response starts at the direct gap of 3.54 eV, see the inset in Figure 5.2, it reaches significant values only above 6 eV. The weak response between 3.54 and 6 eV is caused by the fact that only a single conduction band contributes with a low density of states. Moreover, since that band has Al $3s$ character, whereas the valence bands have dominant H character, the oscillator strength of these transitions is small. The dielectric function rises sharply above 6 eV and peaks above 7 eV. The spectrum has a distinct broad shoulder between 9 and 10 eV and also some weaker shoulders at higher energies.

In order to interpret the dielectric function it is instructive to analyze the total density of states (DOS) and the local density of states (LDOS) of AlH_3. These are shown in Figure 5.3. The valence DOS has a sharp peak just below the Fermi level and two broad peaks at ~ -2.5 eV and ~ -6 eV below the Fermi level. These three peaks originate from respectively $3s$, $3p$ and $3d$ aluminium states hybridizing with the $1s$ hydrogen states, as can be observed in the upper two panels of Figure 5.3. In the solid the states are broadened into strongly overlapping bands. In the dielectric function transitions from the highest two of these valence peaks gives rise to the structure between 6 and 10 eV in Figure 5.2. The energy associated with transitions from the lowest valence peak is too high to give any significant contribution to the dielectric function.

Qualitatively the optical spectra of AlH_3 and MgH_2 show some similarity, despite the difference in structure between these materials. In both cases the dielectric function

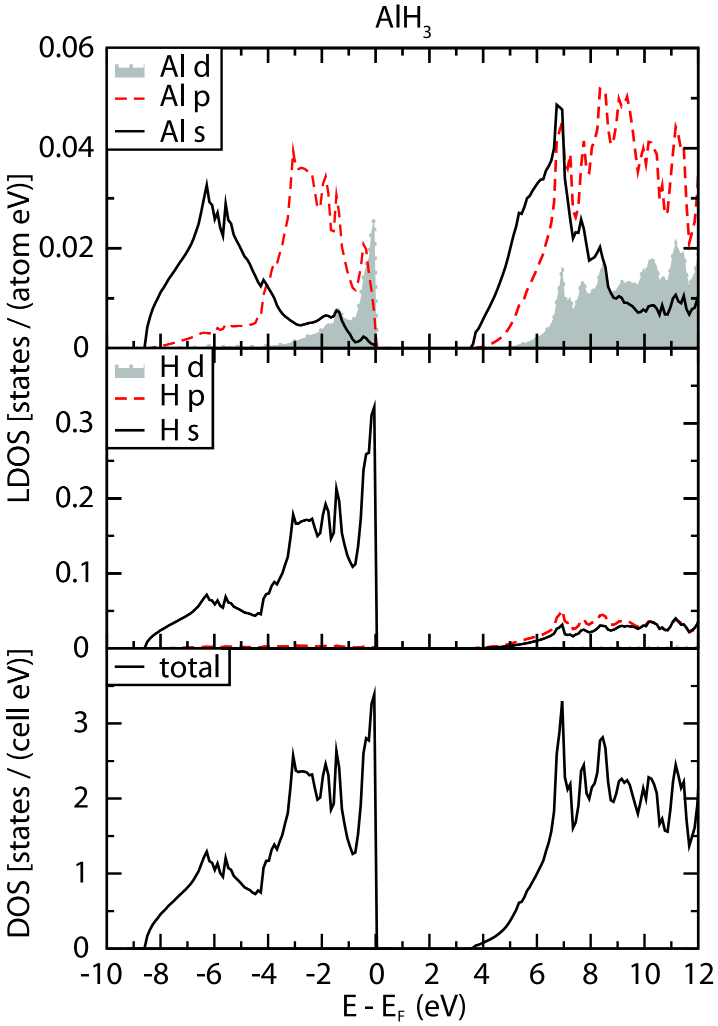

Figure 5.3: *Local densities of states (LDOS) in atomic angular momentum projection; bottom panel: total density of states. The Fermi energy is at the top of the valence band.*

sharply rises above 6 eV and peaks between 7 and 8 eV. The spectrum of AlH_3 is broader due to a larger dispersion of the bands, reflecting the somewhat denser packing of the hydrogen atoms in this compound. From Figure 5.1 one observes that the dielectric function of NaH also rises steeply above 6 eV and peaks just above 7 eV. The spectrum of NaH is narrower than that of MgH_2 and AlH_3, reflecting the less dense packing of hydrogen atoms in this compound, which results in a smaller band dispersion. Only the spectrum of LiH is qualitatively different as it rises below 5 eV in a broad shoulder. As discussed in Section 5, there is a significant contribution from the Li states in this case.

The binary hydrides Li_3AlH_6 and Na_3AlH_6

The optimized atomic positions of Li_3AlH_6 and Na_3AlH_6 are given in Table 5.3. Both Li_3AlH_6 and Na_3AlH_6 consist of a stacking of AlH_6 octahedra and alkali cations. The octahedra are slightly distorted with Al-H distances of 1.75 Å in Li_3AlH_6 and 1.78 to 1.80 Å in Na_3AlH_6. These compounds contain a relatively large fraction of alkali cations. Since sodium atoms are larger than lithium atoms, the distance between the AlH_6 octahedra in Na_3AlH_6 is considerably larger. The Al-Al distance in Na_3AlH_6 is 5.59 Å, whereas in Li_3AlH_6 it is 4.88 Å. As for the simple hydrides discussed in Section 5, this size effect leads to noticeable differences in the electronic structure and the optical properties of Li_3AlH_6 and Na_3AlH_6.

The local electronic densities of states (LDOS) of both compounds is given in Figure 5.4. As in AlH_3 the valence bands have dominant hydrogen character, although there is Al character mixed in. The splitting into three peaks with approximate relative intensity 1:3:2 can be interpreted in terms of an octahedral ligand field splitting.[35, 110] The peaks correspond respectively to the $3s$, $3p$ and $3d(e_g)$ aluminum states hybridizing with the $1s$ hydrogen levels in the AlH_6 octahedra. As can be observed in Figure 5.4 the *spd* splitting in Li_3AlH_6 and Na_3AlH_6 is comparable, which reflects the similarity of the AlH_6 octahedral structure in both compounds. Comparing to Figure 5.3 one observes that the splitting is also comparable to that in AlH_3, again suggesting the similarity in the octahedral structure.

The interaction between the octahedra in the solid results in a broadening of the three peaks. Unlike in AlH_3 the AlH_6 octahedra in Li_3AlH_6 and Na_3AlH_6 are not directly connected, which limits the interaction and the broadening. Therefore, the three peaks remain non-overlapping. One expects their widths to increase as the distance between the octahedra decreases and indeed the valence peaks in the DOS of Li_3AlH_6 are wider than in Na_3AlH_6. The conduction band of both compounds is rather featureless up to at least 22 eV. There is somewhat more cation s character at the bottom of the conduction band in Na_3AlH_6, whereas the bonding in Li_3AlH_6 probably has a somewhat more covalent character, as in the simple hydrides.

The calculated band gaps are given in Table 5.4. As discussed in Section 5, DFT calculations severely underestimate the gap, with LDA giving a ~ 0.5 eV smaller value than GGA. The most important results are in the last two columns of Table 5.4, which give the GW single particle gap and the direct optical gap. The single particle gap is indirect in Li_3AlH_6 and direct in Na_3AlH_6. Previous GW calculations on Na_3AlH_6, by Peles *et al.*Ref. 35, agree well with our value.[2] The fairly large difference between the

---

[2] In Ref. 35 a value of 4.6 eV is given for the single particle gap of Na_3AlH_6. This value is obtained by applying a G_0W_0 shift to the GGA band gap, whereas we apply the shift to the LDA gap. The

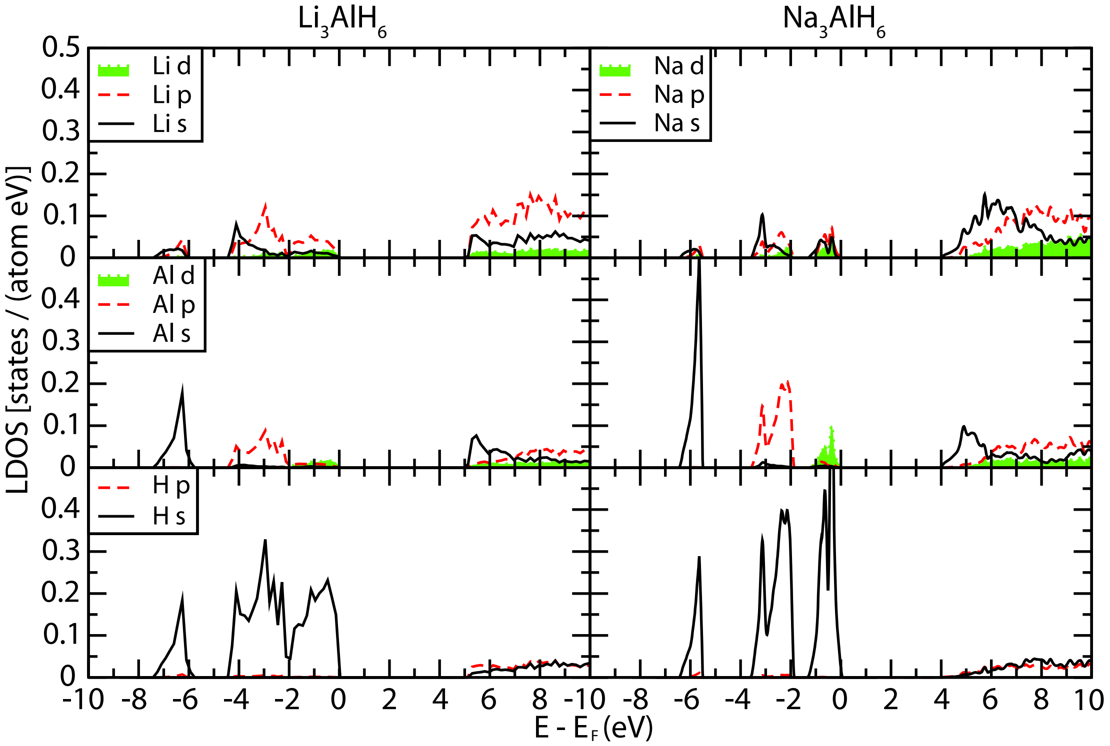

Figure 5.4: *Local densities of states (LDOS) of Li_3AlH_6 and Na_3AlH_6. For clarity the area under the d-line is shaded. The Fermi energies are at the top of the valence band. The conduction band DOS is almost constant up to at least 22 eV. We use atomic radii* 0.79, 1.23, 1.59, 1.36 *and* 0.81 *Å for H, Li, Na, Mg and Al, respectively.*

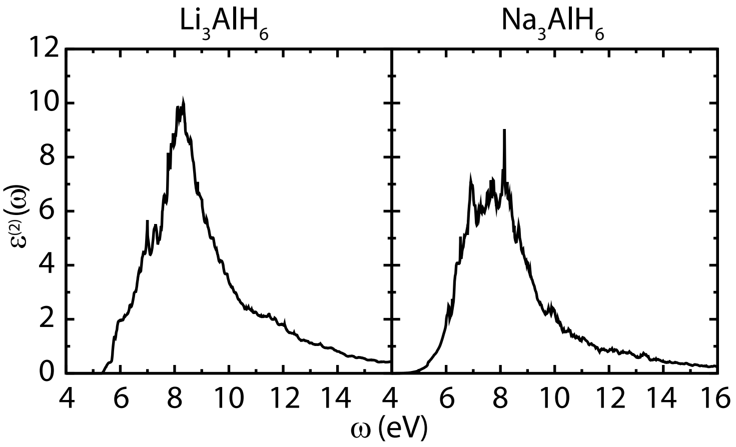

Figure 5.5: *Imaginary parts of the directionally averaged macroscopic dielectric functions of Li_3AlH_6 and Na_3AlH_6.*

gaps of Li_3AlH_6 and Na_3AlH_6 is striking. Moreover, the fact that the gap of Li_3AlH_6 is larger is somewhat counterintuitive. Naively one would expect that the larger broadening of the AlH_6 octahedron levels discussed above would narrow the gap, since it leads to a larger valence band width. The origin of the band gap difference between Li_3AlH_6 and Na_3AlH_6 is discussed in Section 5.

The directionally averaged dielectric functions of Li_3AlH_6 and Na_3AlH_6 are shown in Figure 5.5. The dielectric function of Li_3AlH_6 has a shoulder starting above 6 eV, a peak just above 8 eV and a shoulder below 12 eV. Since the conduction band DOS is rather uniform and featureless up to at least 22 eV, these features in the dielectric function can be directly linked to transitions from the three octahedron valence peaks.

Despite the much smaller band gap of Na_3AlH_6 the dielectric function starts to increase appreciably only at an energy between 5 and 6 eV, which is not that much lower than in Li_3AlH_6. Transitions from the top two valence peaks give rise to the complicated pattern between 6 and 9 eV; transitions from the third valence peak gives the above 10 eV. Qualitatively these spectra have a resemblance to that of AlH_3, see Figure 5.2, reflecting the dominant role played by the AlH_6 octahedra.

The binary hydrides $LiAlH_4$, $NaAlH_4$ and $Mg(AlH_4)_2$

The optimized structures of $LiAlH_4$, $NaAlH_4$ and $Mg(AlH_4)_2$ are given in Table 5.3. For $LiAlH_4$ and $NaAlH_4$ we have used the experimental unit cells and optimized the atomic positions only; for $Mg(AlH_4)_2$ we have also optimized the size and shape of the unit cell.[54] All three materials consist of a packing of AlH_4 tetrahedra and alkali or alkaline earth cations. The tetrahedra are slightly distorted and the Al-H distances vary from 1.62 to 1.65 Å in $LiAlH_4$, 1.64 Å in $NaAlH_4$ and from 1.60 to 1.62 Å in $Mg(AlH_4)_2$. Unlike the two compounds discussed in the previous section, the volume fraction taken up by the cations is relatively small and the distance between the AlH_4 tetrahedra is hardly influenced by the size of the cations. The Al-Al distance is 3.75 Å in $LiAlH_4$, 3.78 Å in $NaAlH_4$ and 3.86 Å in $Mg(AlH_4)_2$.

The LDOS of $LiAlH_4$, $NaAlH_4$ and $Mg(AlH_4)_2$ is shown in Figure 5.6. As for the compounds discussed before, the valence bands have dominant hydrogen character with some Al character mixed in. The splitting into two peaks with approximate relative intensity 1:3 is due to a tetrahedral ligand field splitting of the Al $3p$ and $3s$ levels hybridized with H $1s$ levels in AlH_4.[35,109] The splitting is comparable in all three compounds, which reflects the similarity of the structure and bonding of the AlH_4 tetrahedra in these compounds.

---

difference with our value of 3.94 eV then mainly reflects the difference between the LDA and GGA gaps, see Table 5.4. Experience indicates that applying a G_0W_0 shift to the LDA gap generally results in a value that is within 10% of the experimental single particle gap, see Refs.[42,78]

The interaction between the tetrahedra causes a broadening of these levels in the solid. Figure 5.6 shows that also the resulting band widths of these valence states is comparable in all three compounds. Apparently the widths are not extremely sensitive to the details of the structure, which are quite different for $LiAlH_4$, $NaAlH_4$ and $Mg(AlH_4)_2$. They are sensitive to the distance between the tetrahedra, but this is comparable for the three compounds.

Compared to the valence bands, the features in the conduction bands are less distinct. Both in $NaAlH_4$ and in $Mg(AlH_4)_2$ the bottom of the conduction band has considerable s character derived from the empty $3s$ state of the cation. The conduction band in $LiAlH_4$ is featureless. The LDOS on the Al atoms is very similar in $NaAlH_4$ and in $Mg(AlH_4)_2$, but there are small differences with $LiAlH_4$. There is significant Al d character in the valence band in the latter compound, and almost none in the other two compounds. In the conduction band of $LiAlH_4$ there is a considerable Al s contribution, and much less in the other compounds.

In order to evaluate these differences we have also calculated the LDOS for the $LiAlH_4$ structure with the Li^+ ions replaced by a uniform positive background. The LDOS on the Al atoms then becomes very similar to that in the $NaAlH_4$ and $Mg(AlH_4)_2$ compounds. All these features indicate that $NaAlH_4$ and $Mg(AlH_4)_2$ can be considered as ionic compounds, i.e., as a packing of AlH_4^- anions and Na^+ or Mg^{2+} cations, whereas in $LiAlH_4$ there may be a stronger covalent contribution.

The calculated band gaps are given in Table 5.4. The GW single particle band gaps of the three compounds are almost the same and also in the optical gaps there is very little difference. Previous GW calculations on $NaAlH_4$, by Peles *et al.*Ref. 35, agree well with our value.[3] This similarity indicates that the electronic structure around the band gap is foremost determined by the $(AlH_4)^-$ tetrahedra. The distances between these tetrahedra are similar in these three compounds and apparently the detailed differences in their packing are relatively unimportant.

This conclusion is strengthened by the dielectric function, which is shown in Figure 5.7. The maximal dielectric response of $Mg(AlH_4)_2$ is somewhat smaller than that of $LiAlH_4$ and $NaAlH_4$, but the shape of the three curves is remarkably similar. The double peak structure of the valence band of the LDOS, which appears in all three compounds in Figure 5.6, is almost washed out in the dielectric response. Transitions from the lowest valence band can be recognized only as a faint shoulder near 10 eV. It is then not surprising

---

[3] In Ref. 35 a value of 4.6 eV is given for the single particle gap of Na_3AlH_6. This value is obtained by applying a G_0W_0 shift to the GGA band gap, whereas we apply the shift to the LDA gap. The difference with our value of 3.94 eV then mainly reflects the difference between the LDA and GGA gaps, see Table 5.4. Experience indicates that applying a G_0W_0 shift to the LDA gap generally results in a value that is within 10% of the experimental single particle gap, see Refs.[42, 78]

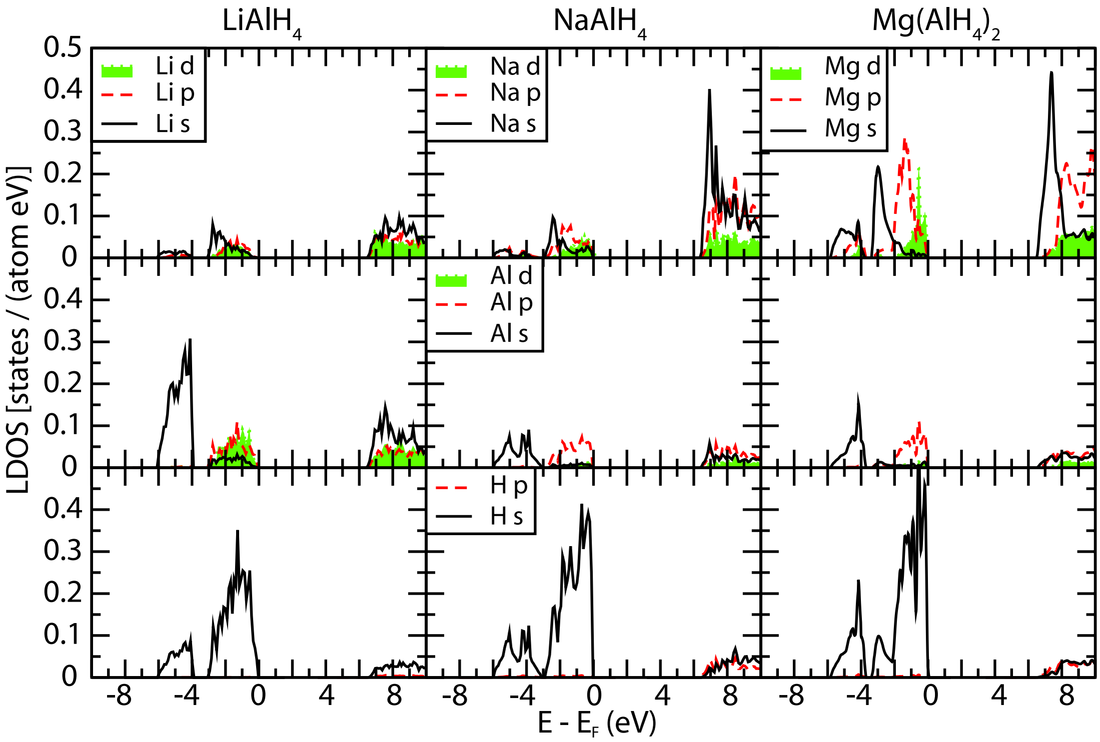

Figure 5.6: *Local densities of states (LDOS) of LiAlH$_4$, NaAlH$_4$ and Mg(AlH$_4$)$_2$.For clarity the area under the d-line is shaded. The Fermi energies are at the top op of the valence band. The conduction band DOS is almost constant up to at least 22 eV. We use atomic radii* 0.79, 1.23, 1.59, 1.36 *and* 0.81 *Å for H, Li, Na, Mg and Al, respectively.*

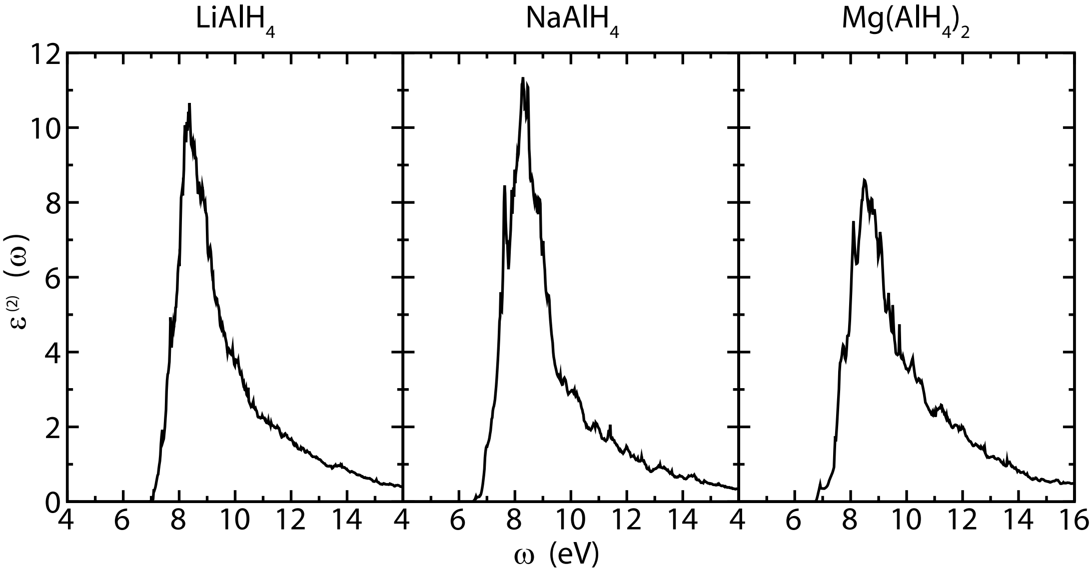

Figure 5.7: *Imaginary parts of the directionally averaged macroscopic dielectric functions of LiAlH$_4$, Na$_3$AlH$_6$ and Mg(AlH$_4$)$_2$.*

that the smaller differences between the LDOS of $LiAlH_4$ and the other two compounds do not influence the dielectric functions much.

Discussion

The electronic structure and the dielectric function of the binary compounds discussed in Sections 5 and 5 are foremost determined by the lattice of $(AlH_6)^-$ octahedra and $(AlH_4)^-$ tetrahedra, respectively, whereas the cations have a minor influence. In this section we will discuss this proposition in more detail. The exact value of the band gap is not important in this discussion, only its relative variation with structure and composition. Since the latter is described qualitatively by DFT/GGA calculations, see Table 5.4, we will only use GGA results in this section.

We have calculated the dielectric functions of lattices of $(AlH_4)^-$ tetrahedra in the $LiAlH_4$, $NaAlH_4$ and $Mg(AlH_4)_2$ structures, but with the Li^+, Na^+ and Mg^{2+} cations replaced by a uniform positive background charge. The results are compared to the dielectric functions of the real compounds in Figure 5.8. It can be observed that removing the cations in $LiAlH_4$ hardly changes the dielectric function. Removing the cations in $NaAlH_4$ results in a slight shift of the dielectric response to higher energies. This is related to the disappearance of the peak at the bottom of the conduction band, which has a sodium s character, see the middle panel of Figure 5.6. Also in $Mg(AlH_4)_2$ removing the cations results in small changes in the dielectric function only. These are mainly caused by the disappearance of the magnesium related peaks at the bottom of the conduction band and a resulting flattening of the conduction bands, see the right panel of Figure 5.6.

In conclusion, although removing the cations results in small changes in the conduction band, overall the dielectric function changes very little, which means that it is foremost determined by the lattice of $(AlH_4)^-$ anions. Such a behavior is not uncommon for ionic compounds. For instance, in alkali halides such as NaCl both the top of the valence band and the bottom of the conduction band are determined by the anion lattice.[49, 50]

Going one step further one can correlate the relative size of the band gap with the distance between the anions. We will illustrate this using the DOS of $Mg(AlH_4)_2$, which is shown in Figure 5.9(a). Replacing the Mg^{2+} ions by a uniform positive background does not change the DOS significantly, as can be observed in Figure 5.9(b). In Figure 5.9(c)-(e) the cell parameters are increased while the geometry of the $(AlH_4)^-$ tetrahedra is fixed. As the distance between the anions increases, the band widths of all bands decreases, but those of the valence bands decrease much more rapidly. At a large distance the DOS is essentially that of an isolated $(AlH_4)^-$ tetrahedron, where the valence states are split into states of s and p symmetry due to the tetrahedral ligand field. The upper states of p

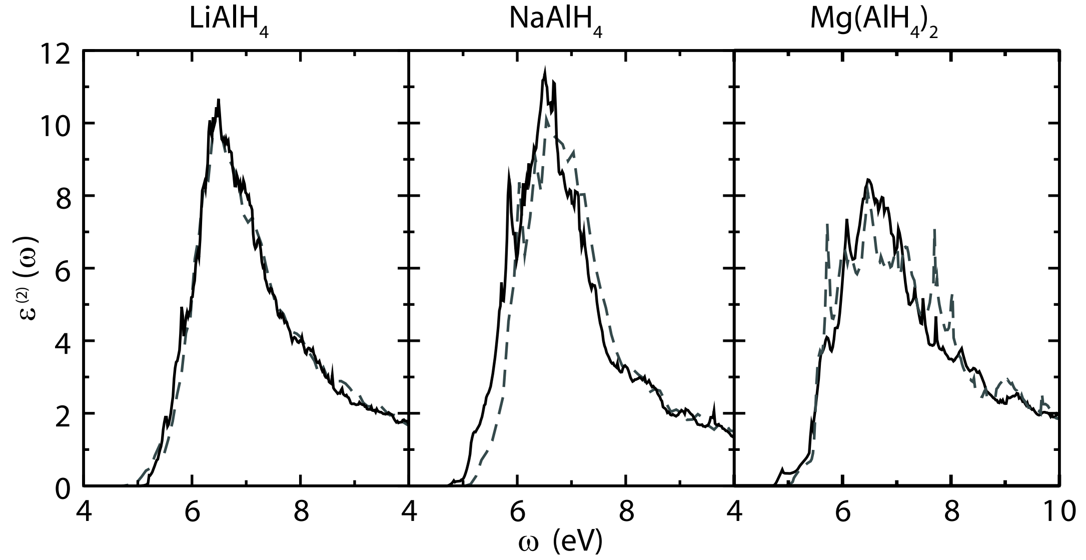

Figure 5.8: *Dielectric functions of $MAlH_4$ compounds (black, solid) and of the corresponding systems with Li^+, Na^+, and Mg^2+ ions substituted by a uniform background charge (red, dashed). These results are based upon GGA calculations without scissors operator cerrection.*

symmetry show a small splitting, since the tetrahedron has a small trigonal distortion. The gap between the highest valence state and the lowest conduction state in the isolated tetrahedron is only ~ 0.5 times the band gap in the solid, compare Figures 5.9(b) and 5.9(e).

In general, the larger the distance between the anions, the smaller the gap. This result seems to be somewhat counterintuitive, as at the same time the valence and conduction band widths are decreasing and in general this would increase the gap. The result can be understood in terms of the electrostatic (Madelung) potential.[113] Increasing the lattice constant, the electrostatic potential on the anions becomes less attractive to electrons, due to the less denser packing of the cations. The same argument also holds for a uniform positive background, i.e., an increasing lattice constant leads to a less attractive Madelung potential on the anions. All states on the anions experience this potential and increase their energy. The size of this shift, however, depends upon the degree of localization of the state. If a state is completely localized, the Madelung potential has a maximum effect. On the other hand, if a state is completely delocalized, its energy shift is zero, since the system as a whole is charge neutral.

The key point is that in our systems the valence states are much more localized than the conduction states. This is immediately evident from Figure 5.9(b)-(e), where the valence band widths decrease much faster with an increasing lattice constant than the conduction band widths. As a result, the more localized valence states increase their

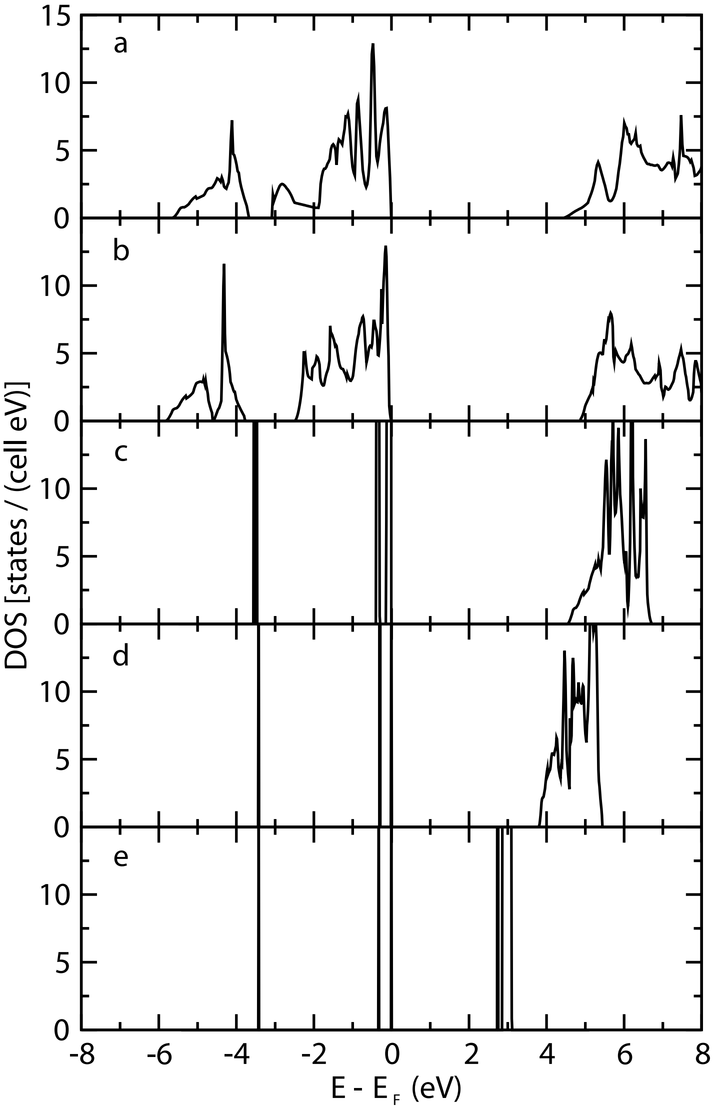

Figure 5.9: *GGA densities of state of (a)* $Mg(AlH_4)_2$ *and (b) with the* Mg^{2+} *ions replaced by a uniform background charge. While fixing the geometry of the* $(AlH_4)^-$ *ions, the lattice is expanded by a factor of 1,5 (c), 2 (d), and 5 (e).*

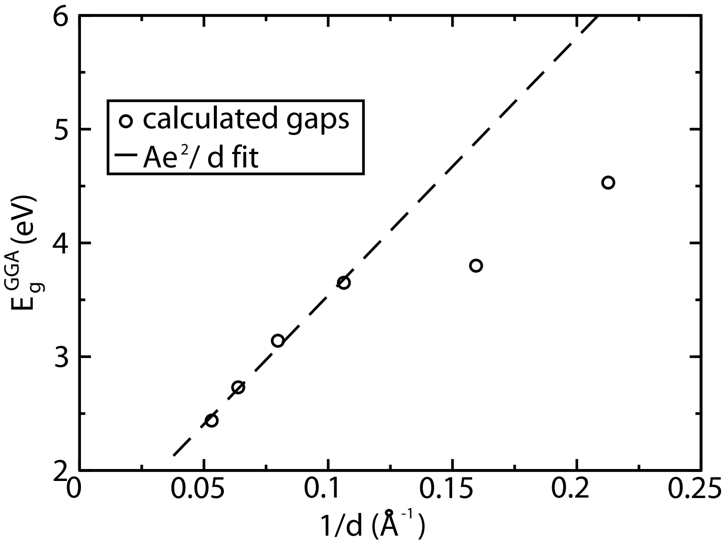

Figure 5.10: *Calculated GGA band gaps of the expanded* $(AlH_4)^-$*-lattice (circles) fitted to* Ae^2/d *(dashed line), whith* d *the distance between the anions;* $A = 1.57$*.*

energy significantly faster with an increasing lattice constant than the conduction band states. Since this effect is much larger than the effect of the decreasing band widths, increasing the lattice constant results in a smaller band gap.

This is quantified in Figure 5.10, where the band gaps of the 2, 3, 4, 5 and 6 times expanded lattice are fitted to an expression Ae^2/d, with d the distance between the anions. The constant $A = 1.57$ represents the difference in localization of the valence and conduction states. This simple model breaks down if the localization of the states strongly depends upon d, i.e. in the 1.5 and 2 times expanded lattice. It occurs if d becomes sufficiently small, see Figure 5.9(b).

This concept can be used to interpret the trend in the band gaps of the binary compounds, see Table 5.4. In $LiAlH_4$, $NaAlH_4$ and $Mg(AlH_4)_2$ the Al-Al distance, which is a measure for the distance between the anions, is almost the same, so their band gaps are very close. The Al-Al distance in Li_3AlH_6 is much smaller than in Na_3AlH_6, which explains the larger band gap in the former compound.

Summary

In this paper the electronic structures and dielectric functions of the simple hydrides LiH, NaH, MgH_2 and AlH_3, and the complex hydrides Li_3AlH_6, Na_3AlH_6, $LiAlH_4$, $NaAlH_4$ and $Mg(AlH_4)_2$, have been studied by first principles calculations. The equilibrium structures of these compounds are obtained from DFT/GGA total energy minimizations. *GW* calculations within the QP approximation provide the single particle excitation energies, i.e., the electronic band structures. We use the G_0W_0 approximation based upon LDA wave functions and eigenvalues. The difference between the dispersions of the GW and the GGA bands is less than 10%. Therefore, the band structures are well represented by GGA band structures that are corrected by applying a scissors operator between occupied and unoccupied states in order to obtain the GW band gap. From the single particle wave functions we then calculate the directionally averaged dielectric functions within RPA, neglecting exciton effects. We also neglect local field effects, but from calculations on static dielectric constants we conclude that this is a reasonable approximation.

All compounds are large gap insulators with band gaps that vary from 3.5 eV in AlH_3 to 6.5 eV in the $MAlH_4$ compounds. In all cases the valence bands are dominated by the hydrogen atoms, whereas the conduction bands have mixed contributions from hydrogen and metal cation states. The band gap in LiH, AlH_3 and Na_3AlH_6 is direct, whereas in all the other compounds it is indirect. The optical response of most compounds is qualitatively similar, notwithstanding sizeable differences in their band structure and band gap. The dielectric function $\varepsilon^{(2)}(\omega)$ rises sharply at photon energies corresponding to $\sim$ 6 eV, and around $\sim$ 8 eV it has a strong peak reaching values in the range 10-15. In the direct gap materials $\varepsilon^{(2)}(\omega)$ has a weak tail going to lower energies. Between $\sim$ 8 and $\sim$ 12 eV, $\varepsilon^{(2)}(\omega)$ gradually decreases to a value ≤ 2 at 12 eV. Most of the materials specific optical information can be found in this energy range, albeit in the form of relatively weak shoulders in $\varepsilon^{(2)}(\omega)$.

The electronic structure and the optical properties of the aluminium compounds can be interpreted in terms of aluminium hydride complexes, i.e., AlH_6 octahedra in AlH_3, Li_3AlH_6 and Na_3AlH_6, and AlH_4 tetrahedra in $LiAlH_4$, $NaAlH_4$. Explicit calculations on lattices of these complexes, without the Li, Na, and Mg cations, show that the latter have a relatively small effect on the DOS and on the optical response. The distance between the $(AlH_4)^-$ tetrahedra in $LiAlH_4$, $NaAlH_4$ and $Mg(AlH_4)_2$ is almost the same. Since the interaction between the tetrahedra is then similar, this explains why the optical spectra of these compounds are very similar.

The same reasoning can be applied to Li_3AlH_6 and Na_3AlH_6 in terms of a lattice of $(AlH_6)^{3-}$ octahedra. However, the distance between the octahedra is smaller in the Li compound because of the smaller size of the cation. The band gap then becomes larger, which can be understood from the influence of the increased Madelung potential on the more localized valence states.

Acknowledgements

The authors wish to thank R. A. de Groot and P. J. Kelly for helpful discussions, for the use of his optics package and G. Kresse for making the linear response routines in VASP available. This work is part of the research programs of ‘Advanced Chemical Technologies for Sustainability (ACTS)’ and the ‘Stichting voor Fundamenteel Onderzoek der Materie (FOM)’. The use of supercomputer facilities was sponsored by the ‘Stichting Nationale Computerfaciliteiten These institutions are financially supported by ‘Nederlandse Organisatie voor Wetenschappelijk Onderzoek (NWO)’.

Table 5.3: *Optimized atomic positions in the binary hydrides. The labels "1a" etc. refer to the Wyckoff positions. The cell parameters are taken from the references. The structures are in good agreement with previous experimental and theoretical, DFT/GGA, work.*[35, 38, 55, 74, 75, 103–110]

Compound	Space group unit cell			x	y	z
Li_3AlH_6	$R\bar{3}$ (148)[1]	$6f$	Li	0.9329	0.4396	0.7512
	$a = 5.64$ Å	$1a$	Al	0	0	0
	$\alpha = 91.4°$	$1b$	Al	1/2	1/2	1/2
		$6f$	H	0.7054	0.9287	0.0675
		$6f$	H	0.7941	0.5885	0.4518
Na_3AlH_6	$P2_1/n$ (14)[2]	$2b$	Na	0	0	1/2
	$a = 5.51$ Å	$4e$	Na	0.9908	0.4566	0.2553
	$b = 5.67$ Å	$2a$	Al	0	0	0
	$c = 7.91$ Å	$4e$	H	0.0983	0.0515	0.2125
	$\beta = 89.9°$	$4e$	H	0.2331	0.3327	0.5413
		4e	H	0.1583	0.2622	0.9347
$LiAlH_4$	$P2_1/c$ (14)[3]	$4e$	Li	0.5727	0.4650	0.8254
	$a = 4.84$ Å	$4e$	Al	0.1395	0.2016	0.9314
	$b = 7.81$ Å	$4e$	H	0.1784	0.0988	0.7614
	$c = 7.83$ Å	$4e$	H	0.3561	0.3720	0.9775
	$\beta = 112.1°$	$4e$	H	0.2394	0.0816	0.1142
		$4e$	H	0.7953	0.2631	0.8714
$NaAlH_4$	$I4_1/a$ (88)[4]	$4b$	Na	0	1/4	5/8
	$a = 5.01$ Å	$4a$	Al	0	1/4	1/8
	$c = 11.31$ Å	$16f$	H	0.2354	0.3900	0.5454
$Mg(AlH_4)_2$	$P\bar{3}m1$ (164)[5]	$1a$	Mg	0	0	0
	$a = 5.23$ Å	$2d$	Al	1/3	2/3	0.7064
	$c = 6.04$ Å	$2d$	H	1/3	2/3	0.4415
		$6i$	H	0.1680	-0.1680	0.8118

Table 5.4: *Single particle band gaps E_g (eV) of the binary hydrides calculated with DFT (GGA and LDA) and GW. $E_g^{GW,\mathrm{core}}$ refers to applying the correction of Equation (5.3); opt^{GW} refers to the direct optical gap*

	E_g^{GGA}	E_g^{LDA}	$E_g^{GW,\mathrm{core}}$	opt^{GW}
Li_3AlH_6	3.65	3.13	5.10	5.31
Na_3AlH_6	2.54	2.00	3.94	3.94
$LiAlH_4$	4.67	4.19	6.55	6.89
$NaAlH_4$	4.63	4.12	6.41	6.50
$Mg(AlH_4)_2$	4.40	3.99	6.48	6.87

Chapter 6

Rotations in Na_3AlH_6

Abstract

In this chapter *ab initio* DFT calculations are used to study the liberation modes in Na_3AlH_6. The rotation of AlH_6 clusters is investigated by mapping the barriers for a full rotation of a cluster as a function of the rotation axis. For the axis with the lowest barrier we determine the transition state and attempt frequency. We find that during the rotation the axis slightly changes orientation to facilitate the hydrogen atoms passing the sodium atoms. The final barrier is found to be 0.398 eV. Combined with an attempt frequency of 4×10^{12} Hz this implies that in a range of 200–260 K a narrowing of NMR line widths is predicted.

Introduction

In 1997 Bogdanović et al discovered that the hydrogen desorption and absorption reaction of sodium alanate, $NaAlH_4$, could be catalyzed by doping with titanium based catalysts. Since that time much research has been dedicated to sodium alanate and it has become the model system for hydrogen storage in complex hydrides.

A relative unexplored technique for studying complex hydrides is solid state NMR. In the case of sodium alanate only three of solid state NMR studies are reported.[114–116] Solid state NMR has seen a wide application in studying dynamical properties. It is therefor particularly useful to unravel the hydrogen dynamics in complex hydrides. Additionally NMR results can be compared to a number of quantities that can be calculated from first principles. Using standard density functional methods energy barriers and attempt frequencies for transition states can be calculated. Furthermore an implementation in the Vienna *Ab initio* Simulation Package (VASP) to calculate field gradients is in the final state of testing, and an implementation for calculating chemical shifts in the framework of a plane wave basis set with periodic boundary conditions is planned.

In this paper we report a computational study on a NMR related property of Na_3AlH_6. We map the barrier for rotating a AlH_6 cluster and search for the rotation with the minimal energy barrier. For this rotation we locate the transition state and calculate both the energy barrier and attempt frequency.

Computational methods

First principles density functional theory (DFT) calculations are carried out using a plane wave basis set and the projector augmented wave (PAW) method,[14,19] as incorporated in the Vienna *Ab initio* Simulation Package (VASP).[15–17] We use the PW91 generalized gradient approximation (GGA) for the exchange correlation functional.[25] The cell parameters and the atomic positions are relaxed using a conjugate gradient algorithm. Non-linear core corrections are applied.[117]

The determination of the transition state is performed using the nudged elastic band method.[118,119] In the nudged elastic band method a number of intermediate steps of a transition path, images, are relaxed instantaneously. Moreover all images are connected by springs and relaxation is only allowed orthogonal to the transition. This ensures that the images stay evenly distributed. The total energy of the entire system, the sum of the energies of all the images and the spring energies, is minimized.

In both the ground state and the transition state the phonon frequencies are calculated using a direct method,[24] i.e. the dynamical matrix is constructed from the force constants that are obtained from finite differences. Two displacements in two opposite directions of

Table 6.1: *Optimized atomic positions in the binary hydrides. The labels "2b" etc. refer to the Wyckoff positions.*

Space group unit cell			x	y	z
$P2_1/n$ (14)	$2b$	Na	0	0	1/2
$a = 5.35$ Å	$4e$	Na	0.9902	0.4548	0.2540
$b = 5.54$ Å	$2a$	Al	0	0	0
$c = 7.71$ Å	$4e$	H	0.0996	0.0496	0.2157
$\beta = 89.9°$	$4e$	H	0.2286	0.3308	0.5428
	$4e$	H	0.1605	0.2665	0.9357

0.05 Å are used for each atomic degree of freedom.

The calculations are performed in a 1 × 1 × 2 super cell, cell duplication in the **c** direction, on 4 × 4 × 2 Monkhorst-Pack **k**-point grids.[21]

Results

We relaxed all structural parameters including the cell volume. The obtained values are given in Table 6.1. The obtained figures are in good agreement with the experimental data and previous calculations.[35, 74, 103, 104, 120, 121]

In order to find the transition state lowest in energy for a rotation of an AlH_6 cluster we started by mapping the barriers for rotations around fixed axes. We mapped the full SO rotation space by set of 78 reasonably evenly spaced axes. On each axis a rotation of 360° was performed in steps of ten degrees. In each configuration, axis and rotation angle, we relaxed the atomic positions of all atoms not belonging to the rotating octahedron. The barriers (eV) of the rotations around the axes are plotted on a polar (ϕ, θ) coordinate grid using a cubic spline interpolation in Figure 6.1.

The deepest wells on the map, near the equator, lie close to two of the fourfold symmetry axes of the octahedron. Rotation around the third fourfold symmetry axis, near the north and south pole, has a larger barrier. Also the three fold symmetry axes of the octahedron show a low barrier. In general axes that have no particular symmetry show the highest energy barriers.

Next we use the nudged elastic band method on a rotation around the axis with the lowest barrier. Since this axis lies close to one of the fourfold axes we use this rotation

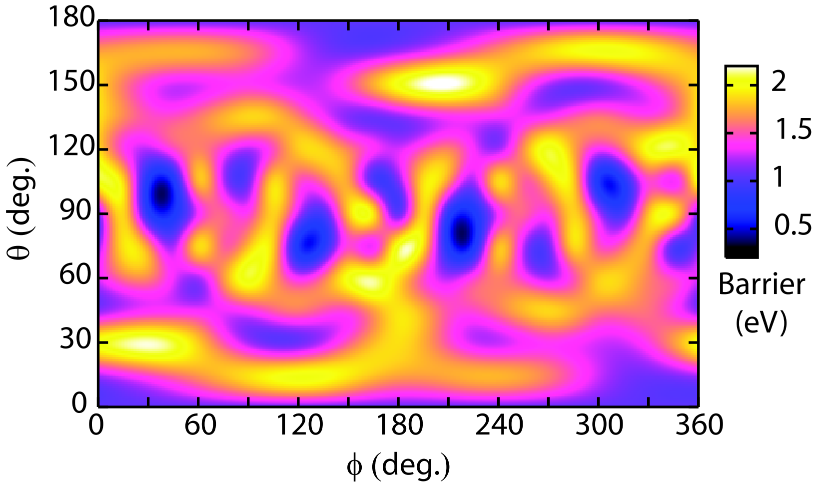

Figure 6.1: *Barrier (eV) for a full rotation of a AlH_6 cluster. The angles determine the rotation axis in polar coordinates. ϕ is the azimutal angle (with the* **a** *lattice vector) and θ is the polar angle (with the cross product of the* **a** *and* **b** *lattice vectors).*

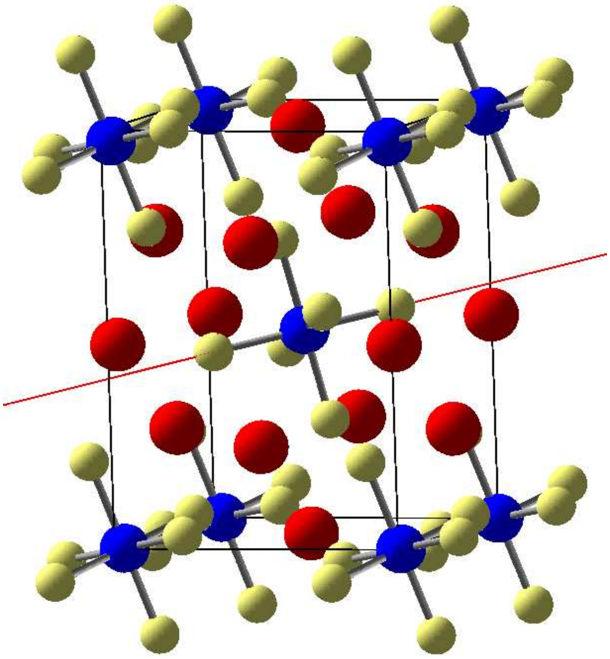

Figure 6.2: *Unit cell of Na_3AlH_6. The red line indicates the rotation axis used for the initial configurations of the steps in the elastic band method. Note that the calculations are performed in a cell duplicated in the* **c***-axes with only one cluster rotating.*

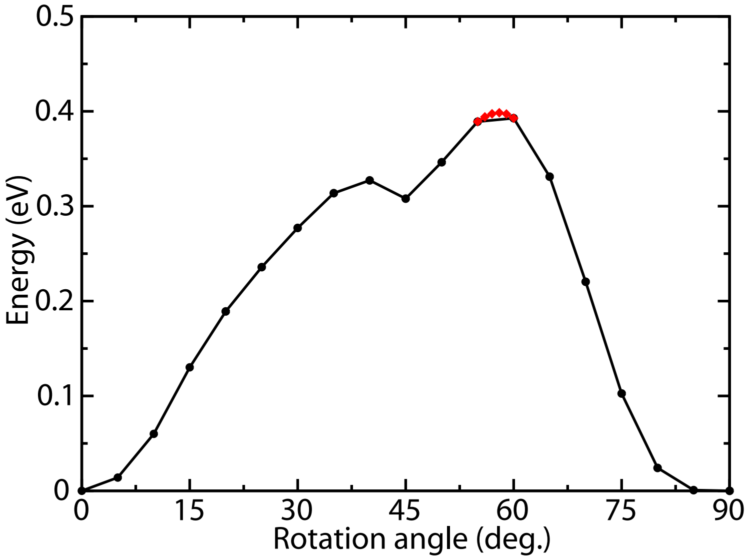

Figure 6.3: *Total energy of the ion electron system of a relaxed rotation of the* AlH_6 *cluster with respect to the ground state total energy. The calculation is performed in a 1x1x2 supercell.*

axis. The rotation then has a 90° periodicity which reduces the computational efforts significantly. The total energy of the images (the rotation is divided in steps of 5°) after the nudged elastic band relaxation is shown in Figure 6.3. Near the top of the barrier the step size was decreased to 1° in a second run to obtain the accurate position of the transition state. During the nudged elastic band relaxation all atoms are allowed to move.

The thus obtained transformation is mainly a rotation around one of the fourfold, H–Al–H, axes. During this rotation there is a small planar reorientation of the axis when the barrier is passed. This reorientation is also visible in the octahedron in the second cell, however lower extend. This "wiggling" of the axis explains the displacement of the minimums in the map away from the actual fourfold axes.

Finally in both the ground state and in the transition state the phonon frequencies were calculated. In the ground state a total of 3N−3, with N the number of atoms in the cell, real non-zero frequencies were found and in the transition state 3N−4. By dividing the products of these two sets we obtain an attempt frequency of 4×10^{12} Hz for the transition. With the energy barrier, 0.398 eV, and the attempt frequency we plot in Figure 6.4 the temperature dependent transition rate $k(T)$ of the rotation according to:

$$k(T) = \frac{\prod_i \omega_i}{\prod_j \omega_j} e^{-\frac{\Delta E}{k_{\mathrm{B}} T}},$$

where the ω_i are the 3N−3 phonon frequencies in the ground state and the ω_j are the 3N−4 phonon frequencies in the transition state.

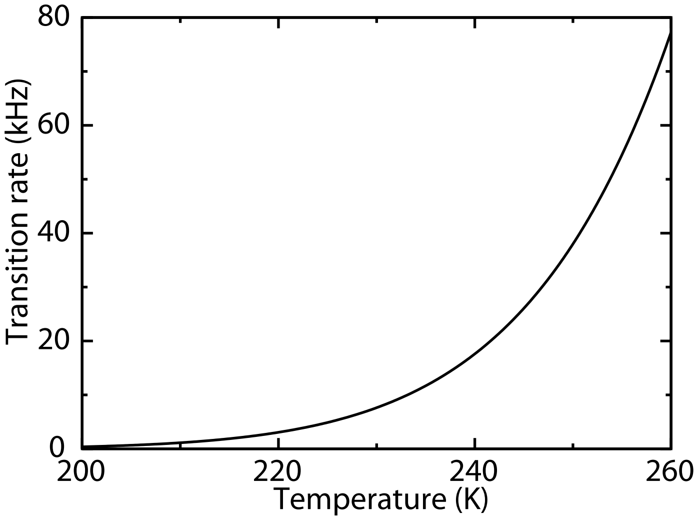

Figure 6.4: *Temperature dependent rate constant of the rotation with the lowest barrier.*

From Figure 6.4 we can see that in the range of 200–260 K the transition rated passes through the range of frequencies in which the resolution of solid state NMR lies. This indicates that, in an NMR experiment in this temperature regime, a transition to hindered rotation can be observed. This range is in perfect agreement with the observation of Majer et. al.[116]

Acknowledgements

The authors wish to thank prof. dr. R.A. de Groot, prof. dr. A. Kentgens and drs. M. Verkuijlen for helpful discussions. This work is part of the research programs of ‘Advanced Chemical Technologies for Sustainability (ACTS)’ and the ‘Stichting voor Fundamenteel Onderzoek der Materie (FOM)’, both financially supported by the ‘Nederlandse Organisatie voor Wetenschappelijk Onderzoek (NWO)’.

Chapter 7

The ground state of boron

Reproduced with permission from:
Thermodynamic stability of boron: the role of defects and zero point motion
M.J. van Setten, M.A. Uijttewaal, G.A. de Wijs, and R.A. de Groot
J. Am. Chem. Soc. **129**, 0631246 (2007)
Copywrite 2007 Americal Chemical Society

Abstract

Its low weight, high melting point and large degree of hardness make elemental boron a technologically interesting material. The large number of allotropes, mostly containing over a hundred atoms in the unit cell, and their difficult characterization put both experimentalists and theoreticians for a challenge. Even the ground state of this element is still under discussion. For over 30 years scientists have attempted to determine the relative stability of α and β rhombohedral boron. We use density functional calculations in the generalized gradient approximation to study a broad range of possible β rhombohedral structures containing interstitial atoms and partially occupied sites. The two structures lowest in energy are practically degenerate in energy and semiconducting. One contains the experimental 320 atoms in the hexagonal unit cell and the other contains 106 atoms in the triclinic unit cell. When populated with the experimental 320 electrons the 106 atom structure exhibits a band gap of 1.4 eV and an in-gap hole trap at 0.35 eV the valence band, consistent with known experiments. Their total energy is decreased by 25 meV/B with respect to the original 105 atom framework, but is still 1 meV/B above the α phase. Zero point energies finally make the β phase the ground state of elemental boron by 3 meV/B. At finite temperatures the difference becomes even larger.

Introduction

The element boron has exceptional properties such as a low volatility and a high melting point (2450 °C), it is stronger than steel, harder than corundum and lighter than aluminum.[122] Moreover, boron has a small reactivity at room temperature. It is under investigation as a constituent in hydrogen storage materials (e.g. $\mathrm{LiBH_4}$),[4] it is used in high power electronics ($\mathrm{LaB_6}$),[123] in superconductors ($\mathrm{MgB_2}$, $\mathrm{T}_C = 39$ K),[124] in heat resistant alloys, as wall coatings in nuclear reactors and as dopant in or alternatives to carbon systems (nanotubes, polymers, diamond, graphite).

Even though there is a wide interest in boron, the element is far from completely understood. As many as 16 boron allotropes are known. The cubic form is only known to encompass 1708 atoms in the unit cell and the 192 atom tetragonal and the 12 atom α rhombohedral (AR) crystal structures are the only ones that are well characterized.

However, the most stable polymorph, at least at high temperatures, is the β rhombohedral (BR) structure.[125] In 1970 a framework consisting of 105 atoms was proposed.[126] Later, in 1988, it was shown experimentally that the unit cell contains 320 valence electrons, where the electron count was corrected by interstitial atoms and partial occupations.[127,128] At the same time, BR boron was found to be a semiconductor with a band gap of 1.6 eV.

Various theoretical papers were dedicated to finding the BR structure. The first calculations on the BR 105 atom framework were performed by Bullett, Ref. 129, in 1982. He discusses the electronic structure of AR and BR boron in terms of icosahedra, the building blocks of both structures. Both structures are an attempt of nature to reconsile the five-fold symmetry of the perfect icosahedra with a space filling crystal structure. In 2001 Jemmis et al.[130,131] analyzed the bonding in the 105 atom framework by a cluster fragment approach. They gave rules for vacancies and interstitials to correct the electron deficiency. Next in 2002 Imai et al., Ref. 132, considered, using density functional theory (DFT) in the local density approximation (LDA), a single atom substitution which increased the stability. In 2005 Prasad et al., Ref. 133, concluded from DFT/LDA calculations that AR boron is more stable than the BR 105 atom framework. Finally in a very recent paper by Masago et al., Ref. 134, a DFT/LDA study is reported in which more systematic single atom replacements were made in the 105 atom framework. Furthermore, they calculated Γ-phonon modes to investigate the temperature dependence of the relative stability of AR boron and the 105 atom framework of BR boron. They concluded that above 1400 K the latter is thermodynamically more stable. However, no BR structure with the right number of electrons has yet been calculated. Moreover, no calculation produced a gap in the electronic density of states (DOS). Neither is it clear that BR boron then provides the ground state structure.

In this paper, we investigate the ground state structure of boron, by means of *ab initio* calculations. We study various atomic substitutions in, and extensions to the 105 atom BR framework and develop general rules to guide us to the ground state structure. Total energies and electronic DOS are also calculated for AR boron. Finally we investigate how phonons, both in the zero point energy (ZPE) and at finite temperatures, determine the relative stability of the BR and the AR structure.

The paper is organized as follows. First we give the details of the computational methods used. Then we discuss the AR boron structure. The next section is dedicated to the various BR structures. Then the AR and BR structures are compared and finally we state the main conclusions.

Computational methods

First-principles calculations were performed within DTF,[135] using the Perdew Wang '91 generalized gradient approximation (GGA) functional.[25] The projector augmented wave (PAW) method,[14,19] was used, as implemented in the total energy and molecular dynamics Vienna *Ab initio* Simulation Package (VASP).[15–18] Nonlinear core corrections were applied.[117]

The Kohn-Sham orbitals were expanded in plane waves with kinetic energy cutoffs of 319 eV (105 and 111 atoms per BR unit cell) and 400 eV (all other structures). The total energies finally compared were recalculated using a 700 eV kinetic energy cutoff. The Brillouin zones were sampled with $10 \times 10 \times 10$ (12 AR), $4 \times 4 \times 4$ (105 and 111 BR), $3 \times 3 \times 3$ (106 BR) and $3 \times 3 \times 1$ (320 BR) Monkhorst-Pack $\mathbf{k}$-point grids,[21] resulting in 110, 13, 14 and 5 $\mathbf{k}$-points, respectively, in the irreducible parts. The Brillouin zone integration was performed with a modified tetrahedron method.[20]

Phonon frequencies were calculated using a finite difference method.[24] Displacements of 5 mÅ and supercells of $2 \times 2 \times 2$ primitive cells for AR boron and the primitive cell for BR boron were found to give frequencies numerically converged to within 1 cm^{-1}. From the phonon modes we calculated the ZPEs and temperature dependent crystal free energies in the full Brillouin zone. Both the ZPEs and the total energies are estimated to be converged to within 0.1 meV/B.

α rhobohedral Boron

The crystal structure, bonding and lattice dynamics of AR boron are well understood and described extensively in the literature, (*e.g.*, Bullett, Ref. 129, or Vast et al., Ref. 136, 137, and references therein). However, we need a very accurate total energy for AR boron to determine whether AR or BR boron is most stable. We, therefore, perform a complete relaxation of all atomic and cell parameters and calculate the total energy and electronic DOS. Table 7.1 shows that both the lattice parameters and atomic positions of the fully relaxed cell agree with the experimental values to a degree that is usual for DFT calculations.

Table 7.1: *Optimized crystal structure of α-Boron, space group $R\bar{3}m$ (166), compared to the experimental structure*[138] *(a).*

Cell parameters		a	c	volume
this work		4.9027	12.5367	260.97
exp. (a)		4.9179	12.5805	263.50
	Wyckoff positions	x	z	
exp. (a)	B1 18h	0.1189	0.8913	
this work		0.1185	0.8914	
exp. (a)	B2 18h	0.1969	0.0243	
this work		0.1963	0.0241	

The total energy of the experimental cell with relaxed atomic positions is −6.6879 eV per boron atom (eV/B). Relaxing the cell parameters as well lowers the total energy by only 0.2 meV/B to −6.6881 eV/B. The energies are relative to those of non-spin-polarized atoms. The calculated packing fraction in this cell is 41%. [1] The calculated bulk modulus is 208 GPa, where the experimental values range from 213 to 224 GPa.[139] Previously calculated bulk moduli range from 222 to 260 GPa.[140–142]

In Figure 7.1 the calculated electronic DOS of AR boron is shown. AR boron has an indirect band gap of 1.54 eV and a direct band gap of 1.94. Previous calculations produced indirect band gaps of 1.4 to 1.7 eV.[129, 141, 143, 144] Horn, Ref. 145, reports an experimental (direct) gap of 1.9 eV. This indicates that the usual underestimation of the band gap by DFT is rather small in this case. Dipole allowed optical transitions have an onset at 2.59 eV which is in agreement with experimental results by Ternauchi et al., Ref. 146 They report an optical gap of 2.4 eV. This, seemingly, overestimation of by DFT is caused by exciton effects.

---

[1] The packing fractions are calculated using a radius of 0.89 Å for the boron atoms.

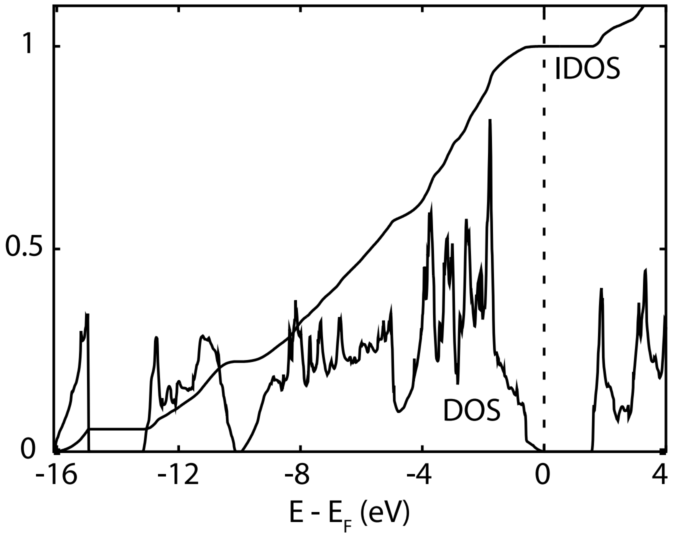

Figure 7.1: *Electronic DOS (states/eV/B), energy relative to* E_{F}*, of AR boron. Integrated DOS (IDOS) (number of electrons / 36) is also plotted*

β rhobohedral Boron

105 atom framework and B16 interstitial position

The 105 atom framework for BR boron that was proposed by Hoard, Ref. 126, is very open and consists of 15 nonequivalent boron positions (B1 up to B15). It is well described in the literature (*e.g.*, Jemmis et al., Ref. 130) and shown in Figure 7.2. We only mention here that the single B15 atom, at the center, connects two B_{28} fragments by bonding to the six atoms at B13 sites. This framework is the starting point for further study. The BR structure has space group is R$\bar{3}$m (166) with lattice constants a = 10.139 Å and $\alpha = 65.2°$.[126] These values were used for all BR structure calculations up to the point where the AR and BR structures are finally compared.

The calculated electronic DOS of this structure is plotted in Figure 7.5. There is an energy gap of 1.13 eV at an electron count of 320 whereas the structure itself holds 315 electrons. The DOS compares well with the calculated band structure by Prasad et al., Ref. 133, which has a gap of 1.03 eV. In their calculation, however, the 105 atom BR structure is 280 meV/B less stable than the AR structure while we only find a difference of 26 meV/B. We do not understand this large discrepancy. Häussermann et al., Ref. 143, found an energy difference of 20 meV/B, which agrees well with our value. Nevertheless, BR boron is known to be a semiconductor. This indicates that additional atoms are required.

The BR structure was experimentally refined by Callmer et al., Ref. 147, They found one additional boron position (B16) that was fully occupied and so get a unit cell of

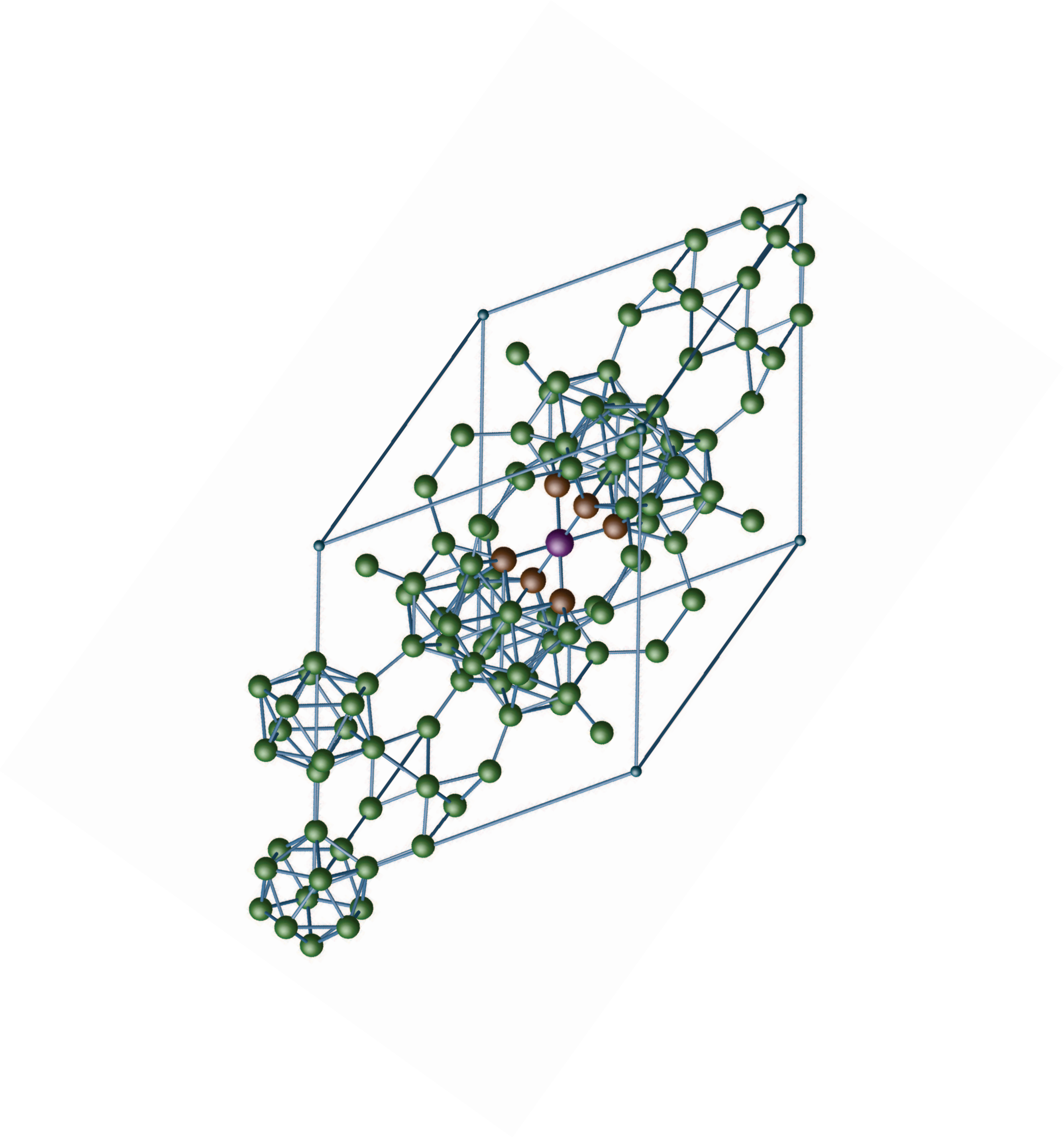

Figure 7.2: *Side view of the unit cell of 105 atom BR boron. Most atoms are part of icosahedra. The central atom (purple) is in the B15 position and connects the two groups of three interpenetrating icosahedra via atoms at B13 sites (red).*

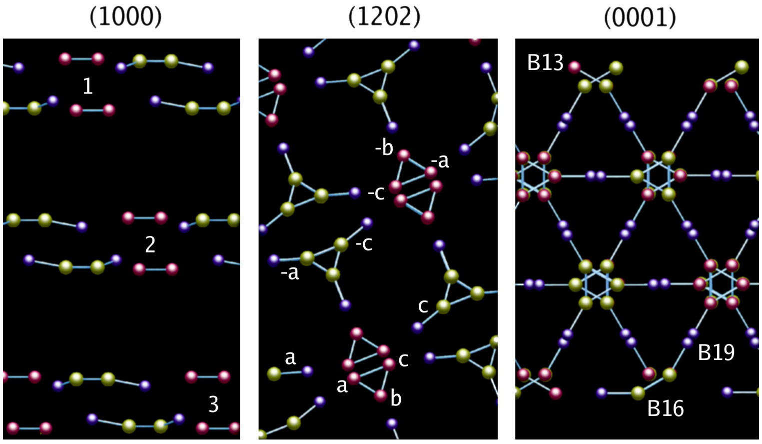

Figure 7.3: *The most important partial occupied sites of BR boron in the hexagonal cell, seen along the (1000) vector (left), along the (1202) vector (middle) and along the (0001) vector (right). B13 atoms are indicated in red, B16s in yellow and B19 positions in dark blue. The numbering scheme introduced in the text is indicated. It makes the atoms individually addressable.*

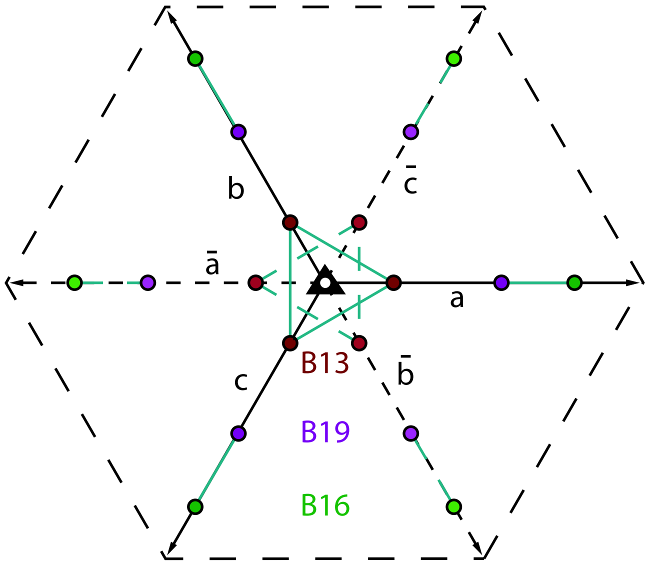

Figure 7.4: *Naming scheme for the B13, B16 and B19 sites in one slab in the hexagonal cell.*

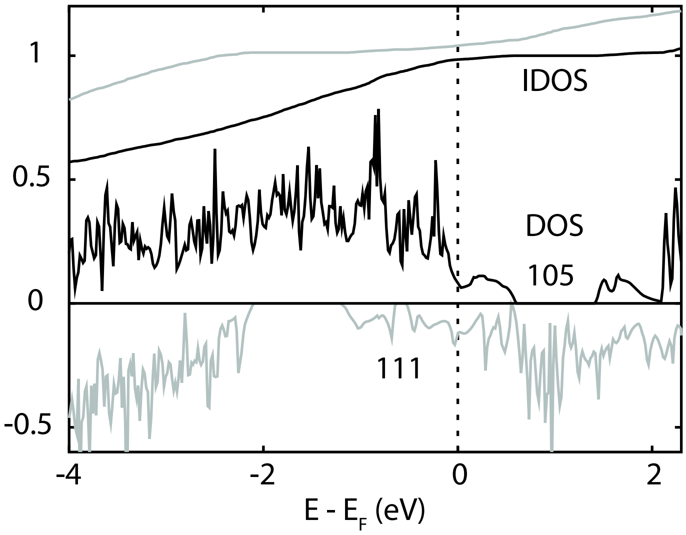

Figure 7.5: *Electronic DOS (states/eV/B), energy relative to E_F, of 105 and 111 atom BR boron. Integrated DOS (number of electrons/320) are also plotted. The energy gaps are at an electron count of 320.*

111 atoms. After structural relaxation we find that this structure is 100 meV/B less stable than the 105 atom framework. The DOS of the refined structure is also shown in Figure 7.5. The energy gap is now 0.84 eV and is positioned *below* E_F.

Table 7.2: *Partial occupation (number of atoms) of sites of BR boron according to Slack et al., Ref. 127, for the three samples reported (A, B and C).*

Site	Wyckoff position	A	B	C
B13	18h	14.0	13.4	13.1
B16	18h	4.6	4.9	5.1
B17	18h	1.2	1.5	1.7
B18	18h	1.0	1.2	1.3
B19	18h	1.3	1.2	1.3
B20	36h	0.0	1.3	0.9
Total		22.1	23.5	23.4

Partial occupations

Further experimental refinement of the BR boron structure by Slack, Ref. 127, showed that the (hexagonal) unit cell contains 320 atoms with lattice constants $a = 10.93$ Å and $c = 2.178a$. This results in a density of 2.333 g/cm^3 and a packing fraction of only 38% which is lower than the value for AR boron. The atoms are distributed over four additional sites (B17 up to B20) and the previously mentioned B13 and B16 positions are also partially occupied. The atomic occupation numbers of the B13 and B16 to B20 sites for the three samples reported are given in Table 7.2.

Jemmis et al., Ref. 130, analyzed the bonding in the 105 atom framework by means of electronic structure calculations in the molecular fragments approach. They find that three B13 sites must be vacant and eight boron atoms should be distributed over B16, B19 and B20 sites to saturate all bonds in the hexagonal unit cell. The B16, B19 and B20 sites are placed around the so called “A” hole in the framework and form tetrahedra. These tetrahedra are connected in triples by means of the atoms at the B16 sites.

The B13, B16 and B19 positions are depicted in Figure 7.3. The left panel shows that the partially occupied sites are located in three equivalent slabs in the hexagonal unit cell. Each B17 site (not shown for clarity) is located very close to two B13 sites and is somewhat displaced towards the middle of the slab. The atoms at the B18 sites bond to atoms at B17 sites and are located very close to the B19 sites on the other side of the slab. We introduce a numbering scheme to be able to address all atoms individually. The three slabs are numbered 1 to 3. Within each slab there is a $\bar{3}$ axis as schematically illustrated in Figure 7.4. Starting from a triple of B13 sites we call the 3 directions in the slab a, b and c. The other three (point symmetric) B13 sites are then positioned in the $\bar{a}$, $\bar{b}$ and $\bar{c}$ direction. The same nomenclature applies to all the B16 up to B20 sites as they are all placed within the slabs and according to the same three-fold axis. For example, the B16 site that lies along the same vector as the $3\bar{a}$ B13 site (3 is the slab number) is the $3\bar{a}$ B16 site and the B17 site connecting both $2a$ and $2b$ B13 sites is the $2\bar{c}$ B17 site. Except for a pair of B20 sites, every site has a unique designation.

The first step to the ground state structure is to consider single atom substitutions in the 105 atom framework. Theory, Ref. 130, and experiments, see Table 7.2, agree that at least one B13 site is vacant and one atom should be added at a B16 site. This is precisely what was done by Imai et al., Ref. 132, but it was not mentioned at which B16 site the boron was added. Furthermore no structural relaxation was included. The energy decreased by no less than 20 meV/B, but they indicate that their kinetic energy cutoff was not large enough to have reached convergency. The DOS from these calculations has a large band gap of 1.3 eV *above* E_F. This gap is reproduced (1.4 eV) in our DOS as shown in Figure 7.6. In our structure (labelled 105B16, see Table 7.3) the atom at the aB13 site

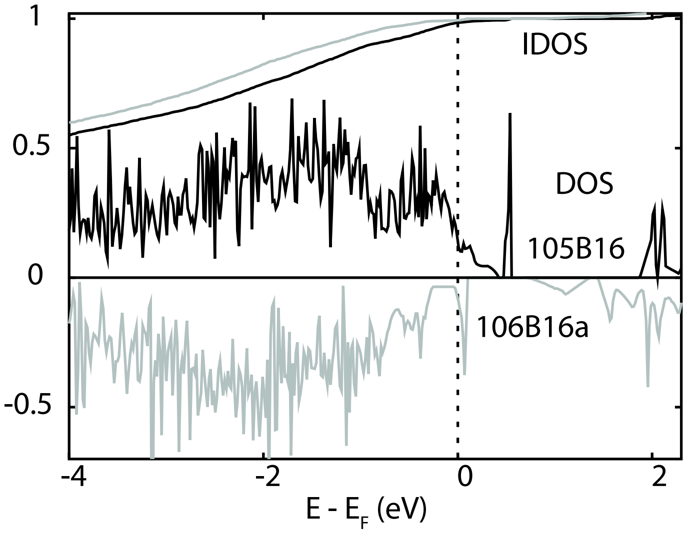

Figure 7.6: *Electronic DOS (states/eV/B), energy relative to* E_F*, of 105B16 (blue, lower graph) and 106B16a (red, upper graph) atom BR boron. The aB13 atom is removed and the aB16 and the ±aB16 atoms are added, respectively. The Fermi levels are indicated with vertical lines and the IDOS (number of electrons / 320) is also plotted.*

is moved to the (nearest) *a*B16 site. This decreases the energy by 10 meV/B. Motivated by symmetry considerations we subsequently added an atom at the $\bar{a}$B16 site (106B16a). The energy lowers by another 8 meV/B. The gap in the DOS, at an electron count of 320, has decreased quite somewhat to 0.65 eV (Figure 7.6). However, these structures are still electron deficient.

Next, calculations were done in the (three times as large) hexagonal 320 atom unit cell. We considered three vacant B13 sites and various distributions of the eight interstitial atoms. We conclude the following from these calculations:

1. A B17 site can only be occupied when two neighboring B13 sites are vacant.
2. Simultaneously, the neighboring B18 sites must be filled.
3. A B16 and B19 boron should not neighbor an occupied B17 site.
4. It is in fact favorable to leave the B17 and B18 positions vacant altogether.
5. At each side of a slab at least one B16, B19 or B20 site should be occupied.
6. No neighboring B16-B19-B20 sites should be filled simultaneously.
7. The opposite interstitial sites, *e.g.*, a and $\bar{a}$, in one slab should not be occupied simultaneously.

8. A filled B19 site is slightly more stable than a B20 site.
9. The filled B16 sites are more stable than the B19 interstitial sites.
10. When a B19 site is occupied it should neighbor a vacant B13 site.

The picture that emerges from these considerations is that in addition to the three vacant B13 sites the eight interstitial boron atoms should be distributed over six B16 and two B19 interstitial sites as homogeneously as possible in accordance with previous work by Jemmis et al., Ref. 130, Both occupied B19 sites should lie along the same vector as a vacant B13 site (*e.g.* a $2a$ and $3a$B19 where the $2a$ and $3a$B13s are vacant).

We now use these conclusions to further improve the 106 atom structure. When an atom is moved from the $\bar{a}$B16 to a $\bar{b}$ site (106B16b) the energy decreases by 5 meV/B, resulting 23 meV/B below the 105 structure. The gap in the DOS splits into two gaps, one of 0.35 eV at E_{F} and one of 1.0 eV, at an electron count of 320 (Figure 7.7). The peak above the Fermi level is analyzed to belong to atoms between the (vacant) aB13 and the (occupied) aB16 sites. We move the atom at the aB16 site to the aB19 site (106B19), since the B19 site is closer to the B13 site than the B16 site. (Two B19 atoms are needed anyway in the 320 atom unit cell, and this is a good check on their effect.) The energy, however, increases by 2 meV/B and the gaps in the DOS reunited to one gap of 1.3 eV (Figure 7.7).

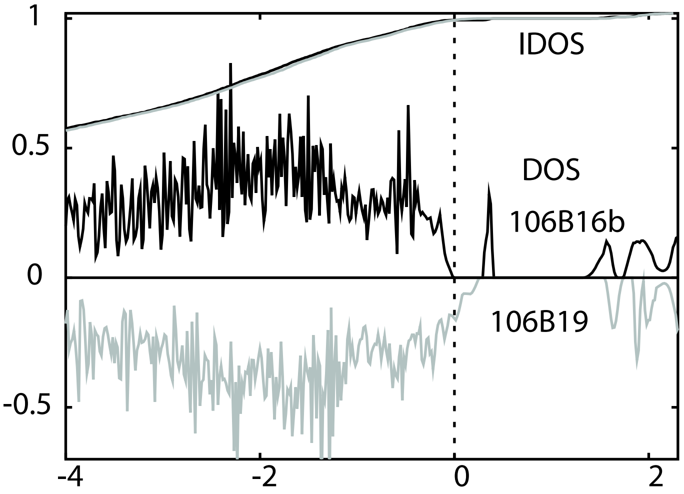

Figure 7.7: *Electronic DOS (states/eV/B), energy relative to E_{F}, of 106 atom BR boron. Integrated DOS (number of electrons / 320) is also plotted. The aB13 atom is replaced by the $\bar{b}$B16 boron and, respectively, the aB16 (106B16b) (red, upper graph), and the 106B19 (blue, lower graph) boron.*

Three final calculations are done with 320 atoms in the unit cell. The first calculation (320B16) has six B16 and two B19 interstitial sites as described above, the second one (320B19) has one B16 less and one B19 more in the same manner, and in the last one (320EXP) we modeled the experimentally observed atomic occupation numbers from Table 7.2 as well as possible. The precise positioning of interstitial atoms in the calculations are brought together in Table 7.3. No disorder in the missing B13 positions is considered since the 106 atom cell already gave very good results concerning the total energy and the gap in the DOS. The total energies of the 320 atom structures are not improved over that of the 106B16b structure. The energy of the 320EXP calculation is only 17 meV/B lower than that of the 105 structure. The 320B19d calculation is slightly lower in energy than the 320B16, but slightly higher than that of the 106B16b calculation. The DOS of 320B19 and 320EXP are displayed in Figure 7.8. That of 320EXP has a small gap (0.2 eV) just below the Fermi level and a fairly large gap (0.6 eV) just above. It is no semiconductor and therefore cannot represent the experimental structure which has an observed (optical) gap of 1.6 eV.[127] The gap of 320B19 is somewhat smaller (0.35 eV), but it leads to a semiconductor.

Summarizing the study on the interstitial atoms, we found one structure of 106 atoms and one of 320 atoms that are nearly degenerate (-23 meV/B) and show the same band gap (0.35 eV). At first sight it seems that these cannot represent the experimental structure as the observed gap is no less than 1.6 eV wide.[127] However, thermally-stimulated currents, space charge limited currents and transient photo currents measurements of the electronic structure of BR boron by Prudenziati et. al., Ref. 148,149, found that there are (localized) hole traps between 0.23 and 0.36 eV above the valence band. This agrees perfectly with the DOS of the 106B16b structure as shown in Figure 7.7. The small peak above the fermi level only has contributions from a handful of neighboring atoms and transitions from the valence band to this state are dipole forbidden. The optical gap that results is at least 1.4 eV in very good agreement with experimental findings.

Finally we relaxed the lattice parameters including the cell volume of the 106B16b structure. This led to a decrease of 0.4% in the volume and marginal changes in the lattice parameters.[2] We found a bulk modulus of 199 GPa which agrees excellently with the experimental values of 185 to 210 GPa.[139,150] With the same high kinetic energy cutoffs as used for AR structure the total energy of this structure becomes -6.687 eV/B. We conclude that on the basis of total energies the AR boron is 1 meV/B more stable than the most stable BR structure found.

---

[2] Because of the interstitials the rhombohedral symmetry is broken. As mentioned, changes are very small. The positions and cell parameters are included in the supplementary information.

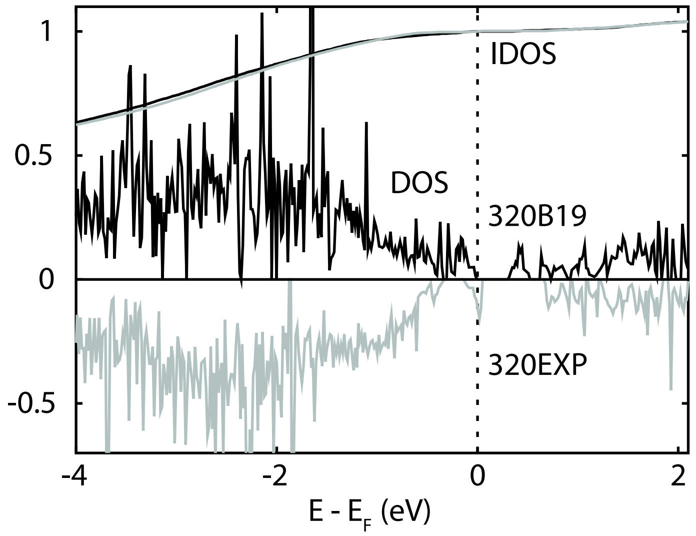

Figure 7.8: *Electronic DOS (states/eV/B), energy relative to* E_{F}*, 320 atom hexagonal boron. Both 320B19 (red, upper curve) and 320EXP (blue, lower graph) are shown as well as their IDOS (number of electrons / 960). The 320B19 structure is a semiconductor with a gap of 0.35 eV.*

Table 7.3: *Total energies (meV/B relative to the BR 105 structure) and description of all calculated structures of BR boron, indicating the vacant B13 and the filled B16 to 20B sites. The nomenclature introduced in the text is used to describe the unit cell.*

System	− B13			+ B16			B17	B18	B19	B20	E
Slab	1	2	3	1	2	3					
105	-	-	-	-	-	-	-	-	-	-	0
111	-	-	-	all	all	all	-	-	-	-	100
105B16	a	a	a	a	a	a	-	-	-	-	-10
106B16a	a	a	a	$a\bar{a}$	$a\bar{a}$	$a\bar{a}$	-	-	-	-	-18
106B16b	a	a	a	$a\bar{b}$	$a\bar{b}$	$a\bar{b}$	-	-	-	-	-23
106B19	a	a	a	$\bar{b}$	$\bar{b}$	$\bar{b}$	-	-	$123a$	-	-21
320EXP	a	a	bc	$a\bar{b}$	$\bar{b}$	$a\bar{b}$	$3\bar{a}$	$3\bar{a}$	$2a$	$2c$	-17
320B16	a	a	a	$c\bar{b}$	$c\bar{b}$	$a\bar{b}$	-	-	$12a$	-	-22
320B19	a	a	a	$c\bar{b}$	$c\bar{b}$	$\bar{b}$	-	-	$123a$	-	-23

Zero point energy and temperature dependence

Comparing total energies from static electronic structure calculations alone neglects the ZPE of a system. Whereas for heavier elements neglecting the ZPE is reasonable, for the lighter elements, including boron, it is not. Therefore, in the optimized cells, we calculated the phonon frequencies. The number of atoms in the unit cell differs greatly between AR and BR boron. This causes the band dispersion of the phonon modes, in contrast to Γ-point phonons only, to have a large (relative) effect. For AR boron the difference in ZPE with and without band dispersion is 3 meV/B whereas for BR it is only 0.2 meV/B. This is mainly caused by the acoustic modes that don't contribute when using only Γ-point phonons. In AR boron the acoustic modes account for 1/12th of total number modes whereas in BR they account for only 1/106st. All phonons contributions reported here are, therefore, integrated over the entire Brillouin zone.

In Table 7.4 the calculated Γ-point frequencies for AR boron are compared to experimental values. They agree extremely well. By integrating phonon frequencies over the Brillouin zone we obtain a ZPE of 130 meV/B. This brings the total energy, including ZPE, of AR boron to −6.558 eV/B.

The same procedure was carried out for the most stable 106 structure (106B16b). This gave a ZPE of 126 meV/B, bringing the total energy, including ZPE, of 106B16b BR boron to −6.561 eV/B. For the first time, this gives an BR energy lower than that of AR boron.

The above reported total energies are, in fact, the Helmholtz free energies at 0 K. At higher temperature the phonon modes are occupied according to Bose-Einstein statistics. In the harmonic approximation the Helmholtz free energy is determined by the harmonic lattice vibrations, i.e., the phonons, at a volume V:[152]

$$F(V,T) = U_0(V,T) + \frac{1}{\Omega_{BZ}} \\ \times \sum_i \int_{\mathrm{BZ}} \left(\frac{\hbar\omega_{\mathbf{q},i}}{2} + \ln\left[1 - e^{-\hbar\omega_{\mathbf{q},i}/k_{\mathrm{B}}T}\right] \right) d\mathbf{q}.$$

We fix the volume to the equilibrium value at 0 K and neglect thermal expansion. The bulk moduli of the AR and BR structure is rather similar, so we expect the differences in thermal expansion to be small as well. Since we are only interested in the differences between AR and BR boron we assume this to be a good approximation. The first term then becomes the potential energy of the perfect crystal. The integration is over the entire Brillouin zone of which Ω_{BZ} denotes the volume. A modified tetrahedron integration method is used.[20] The first term in the integral is the zero point energy, where the $\omega_{\mathbf{q},i}$ are the phonon angular frequencies at wave vector $\mathbf{q}$. The second term in the integral refers to the thermally induced occupation of the various phonon modes.

Table 7.4: *Gamma point phonon frequencies, symmetry and activity [Raman (R) or Infrared (IR)] of* α *rhobohedral boron (cm*$^{-1}$*), compared to the experimental values: (a) Raman, Ref. 136, 137, and (b) Infrared, Ref. 151.*

Mode	active	this work	exp.(a)	exp.(b)
A_{1g}	R	1171	1186	
E_g	R	1118	1122	
A_{2u}	IR	929		
A_{1g}	R	921	925	
E_g	R	870	870	
A_{2u}	IR	809		
E_u	IR	801		806
A_{2u}	IR	792		
A_{1g}	R	792	793	
A_{1u}		787		
E_u	IR	786		
E_g	R	773	774	
A_{2g}		714		
E_g	R	708	708	
E_u	IR	700		705
A_{1g}	R	691	692	
E_u	IR	595		
E_g	R	582	586	
E_u	IR	550		548
E_g	R	521	525	
A_{2g}		499		
A_{1u}		475		

At finite temperature there is also a contribution to the free energy from the configurational entropy (CE):

$$\Delta F^{CE} = -k_{\mathrm{B}}T \ln \left(\sum_{\mathrm{i}} g_{\mathrm{i}} e^{-E_{\mathrm{i}}/k_{\mathrm{B}}T} \right),$$

where g_{i} and E_{i} are the multiplicities and energies of the various (defect) structures. For BR boron many defect structures are possible. At a certain temperature only those structures significantly contribute whose energies are within $k_{\mathrm{B}}T$ of the ground state structure. If we consider the multiplicities of the 106B16b and 320B19 structures the ΔF^{CE} is only -0.3 meV/B at 300 K. Moreover, taking more structures into account lowers the CE of BR boron further. AR boron, on the other hand, has no defects and hence no CE contribution. The CE effects will not be considered further.

The result of the calculated temperature dependence is plotted in Figure 7.9. The difference between AR and BR boron at higher temperatures is marginally larger than at 0 K. In correspondence with experimental findings, this means that at finite temperature the BR boron structure is also the most stable.

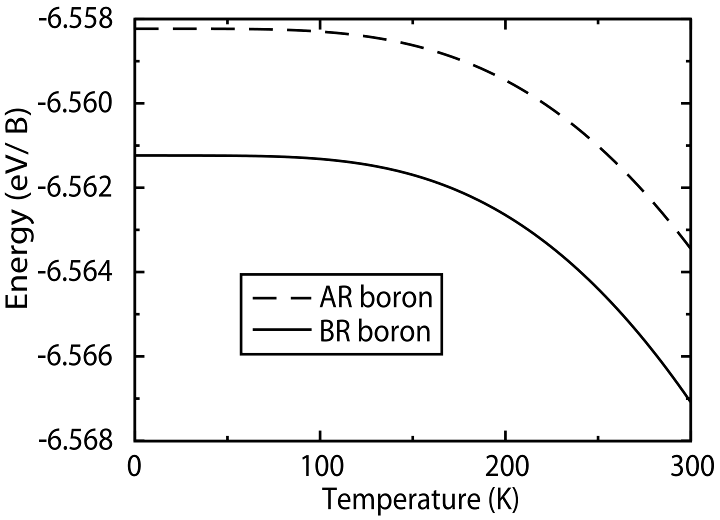

Figure 7.9: *Helmholtz free energy (eV/B) at fixed volume, 0 K equilibrium volume, of AR and BR boron as a function of temperature (K).*

Conclusions

To summarize, we used first-principles (DFT, GGA) calculations on BR and AR boron to determine the boron ground state structure. The calculated properties of AR boron, including Γ-point phonon modes, electronic band gap and bulk modulus compare very well to experimental values.

The BR 105 atom framework is 26 meV/B higher in energy than AR boron, but is stabilized by partial occupations and interstitial atoms. The most stable structure is a 106 atom structure with one B13 site vacant and two atoms added at specific B16 sites. On the basis of this structure we also constructed a 320 atom unit cell that is nearly as stable. Both are semiconductors with a band gap of 0.35 eV. The optical gap of the 106 atom structure is (at least) 1.4 eV, which compares favorably with the experimental gap of 1.6 eV.

Relative to AR boron these structures are still 1 meV/B higher in energy. However taking the ZPE into account the BR 106 atom unit cell boron wins 4 meV with respect to AR boron and becomes the most stable one. Taking temperature effects into account does not change this picture.

Finally, the experimentally determined atomic occupations of BR boron were modeled in a unit cell of 320 atoms. This structure, however, is 6 meV/B higher in energy than the most stable one and it is no semiconductor.

Acknowledgements

The authors wish to thank Dr. T. J. Frankcombe and Dr. C. M. Fang for helpful discussions. This work is part of the research programs of ‘Advanced Chemical Technologies for Sustainability (ACTS)’ and ‘Stichting voor Fundamenteel Onderzoek der Materie (FOM)’, financially supported by ‘Nederlandse Organisatie voor Wetenschappelijk Onderzoek (NWO)’.

Chapter 8

Beryllium boranate, $Be(BH_4)_2$

Reproduced with permission from:
A first-principles study of the electronic structure and stability of $Be(BH_4)_2$
M.J. van Setten, G.A. de Wijs, and G. Brocks
Phys. Rev. B , under review
Copyright 2007 by the American Physical Society

Abstract

Alanates and boranates are studied intensively because of their potential use as hydrogen storage materials. In this paper we present a first-principles study of the electronic structure and the energetics of beryllium boranate, $Be(BH_4)_2$. From total energy calculations we show that - in contrast to the other boranates and alanates - hydrogen desorption directly to the elements is likely, and is at least competitive with desorption to the elemental hydride (BeH_2). The formation enthalpy of $Be(BH_4)_2$ is only -0.12 eV/H_2 (at $T = 0$K). This low value can be rationalized by the participation of all atoms in the covalent bonding, in contrast to the ionic bonding observed in other boranates. From calculations of thermodynamic properties at finite temperature we estimate a decomposition temperature of 162 K at a pressure of 1 bar.

Introduction

In the last decade the environmental importance of reducing the CO_2 exhaust has been widely accepted. The use of hydrogen based fuel cells is an important contribution to achieve this reduction. The major obstacle for the use of hydrogen based fuel cells is the development of a method for hydrogen storage with a high gravimetric and volumetric hydrogen density.[6]

One way of storing hydrogen is in a (complex) metal hydride. The ideal hydrogen storage material should have the highest possible gravimetric hydrogen density. This obviously requires the use of lightweight materials. Moreover, the formation energy of the hydride has to be such that it is stable at atmospheric conditions, yet it has to decompose at a moderate temperature to release the hydrogen. A further important point is that the reactions involved in hydrogen de/absorption must have fast kinetics.

Over the last decade alanates and boranates have been studied extensively as potential hydrogen storage materials.[5,6] Alanates and boranates consist of a lattice of metal cations and $(AlH_4)^-$ or $(BH_4)^-$ complex anions, respectively. Generally these materials decompose by heating via intermediate complex hydrides into bulk metals, elemental hydrides and hydrogen gas. In the last few years the attention has gradually shifted from alanates towards boranates, because of the high gravimetric hydrogen density in the latter. Many boranates turn out to be too stable, however.

In principle a large variety of boranates can be synthesized by changing the metal cations, which can be used to tune the formation energy.[33] So far most effort has been devoted to the alkali boranates,[120,153–158] and more recently to mixtures of alkali boranates,[159,160] and to the alkaline earth boranates.[161–165] In order to understand the chemical trends we have recently developed a simple model for the formation energies of these compounds.[166] This model demonstrates that these boranates are ionic compounds (in the sense discussed above) and that the difference in their formation energies can be understood on the basis of the electrostatic (Madelung) lattice energy. The basic stability of the $(BH_4)^-$ cation is not affected by substituting one alkali or alkaline earth cation by another.

The stability of $(BH_4)^-$ may be lowered by adding an element that competes with boron in binding with hydrogen. To investigate this possibility we study beryllium boranate, $Be(BH_4)_2$, in this paper.[1] Establishing the electronic structure and themodynamic stability of $Be(BH_4)_2$ will assist in understanding the chemical and physical trends in alkali, alkaline earth alanates and boranates.[2]

---

[1] in the older literature also referred to as beryllium borohydride

[2] $Be(BH_4)_2$ itself, however, will probably never be used as a hydrogen storage material in large scale commercial applications because of the toxicity of beryllium gas.

We present a first principles study of the electronic structure and the thermodynamic properties of $Be(BH_4)_2$. The electronic structure in relation to the crystal structure are used to analyze the bonding in $Be(BH_4)_2$. We calculate total energies and phonon frequencies of all compounds involved in possible formation reactions of $Be(BH_4)_2$. From these data we obtain the thermodynamic properties at finite temperature.

Computational methods

First-principles calculations are carried out within the density functional theory (DFT) approach, applying a generalized gradient approximation (GGA) for the exchange correlation functional.[25] We use a plane wave basis set and the projector augmented wave (PAW) method,[14,19] as implemented in the Vienna *Ab initio* Simulation Package (VASP),[15–17] and apply non-linear core corrections.[117]

Brillouin zone integrations are performed with a tetrahedron method[20] for calculating total energies. A Gaussian smearing method is used for calculating densities of states, with a smearing parameter of 0.1 eV. The **k**-point meshes are such that total energies are converged within 0.1 meV per formula unit. The total energies used in the calculations of the reaction enthalpies are calculated with a high plane wave kinetic energy cutoff of 700 eV. By varying the computational parameters, in particular by trying different PAW potentials, we estimate that reaction enthalpies are converged on a scale of 5 meV.

The atomic positions and lattice parameters are relaxed using a conjugate gradient algorithm for a range of fixed volumes. The total energy versus volume curve obtained this way is fitted with a Murnaghan's equation of state expression, which yields the ground state volume, the bulk modulus, and its pressure derivative.[23] At the ground state volume we relaxed the atomic positions and lattice parameters to obtain the ground state structure. This procedure is followed for all compounds mentioned in this paper.

To calculate the zero point energies (ZPE) and phonon densities of state we need the vibrational phonon frequencies of all these compounds. Vibrational frequencies are obtained from the dynamical matrix, whose matrix elements (the force constants) are calculated using a finite difference method.[24] The force constants are calculated from displacements of 0.005 Å in two opposite directions for each atomic degree of freedom. For both bulk beryllium and beryllium hydride $2 \times 2 \times 2$ supercells give converged ZPEs. One does not need a supercell to calculate the phonon frequencies of $Be(BH_4)_2$, since the unit cell of $Be(BH_4)_2$ is sufficiently large. For boron we use the frequencies that have been reported earlier.[167]

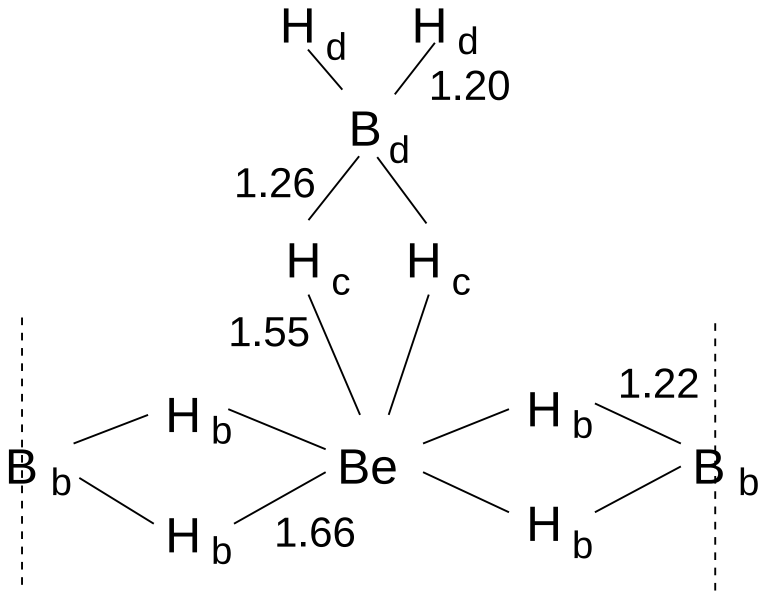

Figure 8.1: *Schematic bonding scheme and labeling of the atoms within a polymer chain in* $Be(BH_4)_2$*. The three dimensional structure is given in Figure 8.2. The numbers indicate optimized bond lengths in Å.*

Crystal structure

$Be(BH_4)_2$ can be synthesized by the reaction of lithium boranate and beryllium chloride.[26,168] Its crystal structure consists of helical polymers of alternating beryllium and boron atoms (B_b) that are connected via pairs of hydrogen atoms (H_b).[169] The polymer building block is shown schematically in Figure 8.1. A further boron atom (B_d) is attached to each beryllium atom, again via a pair of hydrogen atoms (H_c) and this B_d atom also binds two "dangling" hydrogen atoms (H_d). The polymers are packed in the crystal structure as shown in Figure 8.2. On the basis of this structure one may expect a strong bonding between the atoms in one polymer chain, and a much weaker bonding between the polymer chains. The latter is reflected in the low melting point of $Be(BH_4)_2$ of 125°C.

We relaxed the crystal structure of $Be(BH_4)_2$ as described in the previous section, including the cell volume, lattice parameters and atomic positions, while keeping the experimental space-group and Wyckoff positions. The relaxed lattice parameters and atomic positions are given in Table 8.1. Except for the cell volume, the parameters compare well to the experimental values.[169] The calculated cell volume is 15% larger than the experimental cell. This indicates that the binding between the polymer chains is indeed weak and of van der Waals type. It is well-known that, using the common functionals, DFT fails to capture van der Waals bonding. However, the total energy difference between the experimental and calculated cell volumes is less than 5 meV/H_2,

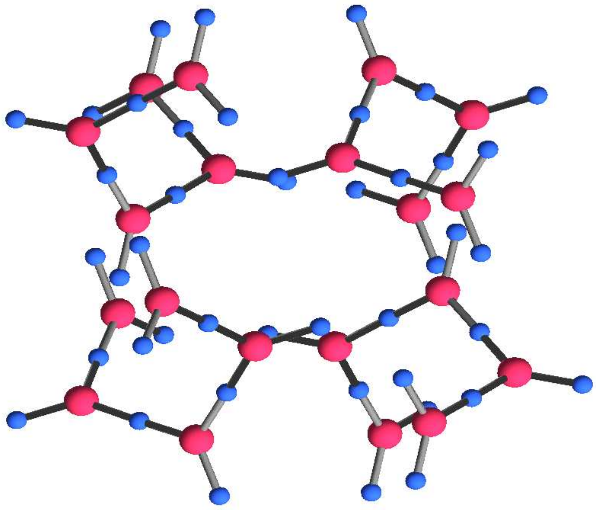

Figure 8.2: *Crystal structure of $Be(BH_4)_2$. For clarity reasons the hydrogen atoms are not shown and bonds are drawn between the beryllium (big red) and boron (small blue) atoms.*

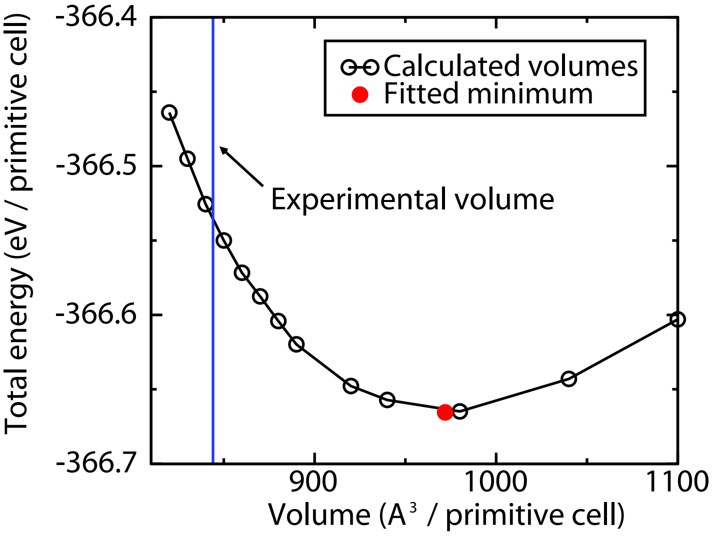

Figure 8.3: *Total energy per unit cell of $Be(BH_4)_2$ as a function of the cell volume.*

see Figure 8.3. This error only has a minor effect on the relative total energies.

The optimized B–H and Be–H bond lengths are given in Figure 8.1. As references, the B–H bond length in a $(BH_4)^-$ anion is 1.21 Å, whereas a B–H bond length in a typical three center B–H–B bond is 1.34 Å.[26] Comparison with these numbers indicates that the B–H bonding in $Be(BH_4)_2$ is closer to that in the $(BH_4)^-$, although there is some distortion

Table 8.1: *Optimized atomic positions of* $Be(BH_4)_2$. *The space group is* $I4_1cd$ *(110) and all atoms are on Wyckoff position* 16b. *The optimized lattice parameters are* $a, b, c = 14.28, 14.28, 9.54$ *Å.*

atom	x	y	z
Be	0.2050	0.0992	0.0016
B_d	0.1695	0.9702	0.0068
B_b	0.1503	0.1978	0.1237
H_d	0.0997	0.9439	0.0653
H_d	0.2183	0.9130	0.9499
H_c	0.2189	0.0123	0.0963
H_c	0.1453	0.0294	0.9157
H_b	0.1083	0.1649	0.0231
H_b	0.2281	0.1647	0.1450
H_b	0.1611	0.2813	0.1003
H_b	0.1027	0.1793	0.2269

due to the presence of the Be atom, in particular on the B_d–H_c bond. This could indicate some competition between B and Be for bonding to hydrogen. For comparison, the B–H bond lengths in alkali alanates are all very close to 1.21 Å. The Be–H bond lengths are still quite large, however, which indicates a significant ionic contribution to the bonding.

We have also optimized the structure of BeH_2, see Table 8.2. It agrees well with the experimental structure[170] and with that obtained in a previous calculation,[171] the largest difference being that our calculated bulk modulus (21.4 GPa) is $\sim$ 10 % smaller than that calculated in Ref. 171 (23.8 GPa). For elemental boron we use the β-rhombohedral structure as given in Ref. 167. For elemental beryllium (space group P-3m1 (164)) we find lattice parameters $a = 2.260$ Å and $c = 3.567$ Å, which compare well to the experimental values of 2.29 Å and 3.60 Å, respectively.[172]

Electronic structure

As discussed above the crystal structure of $Be(BH_4)_2$ indicates a weak bonding between polymer chains, and a stronger bonding within a polymer chain. The charge displacement upon bond formation can be visualized by plotting the charge density difference, i.e. the charge density of $Be(BH_4)_2$ minus that of the individual isolated atoms. Cuts through

Table 8.2: *Optimized crystal structure of* BeH_2*. The space group is Ibam (72) and the optimized lattice parameters are* $a, b, c = 8.967, 4.141, 7.643$ *Å. The experimental lattice parameters are* $a, b, c = 9.082, 4.160, 7.707$ *Å.*[170]

atom	Wycoff position	x	y	z
Be	$4a$	0	0	0.25
Be	$8j$	0.1677	0.1200	0
H	$16k$	0.0882	0.2241	0.1520
H	$8j$	0.3102	0.2771	0

the charge density difference in various planes along a polymer backbone are shown in Figure 8.4. They clearly indicate the formation of B–H covalent bonds, which are polarized somewhat towards the H atoms. The character of the Be–H bonds is much less clear from these plots. In any case these bonds are strongly polarized in the direction of the H atoms.

The electronic projected density of states (PDOS) of $Be(BH_4)_2$, projected on s, p components of the individual atoms, is shown in Figure 8.5. Tetrahedrally bonded BH_4^- generates a characteristic pattern in the valence band part of the PDOS, which is qualitatively similar to that observed for AlH_4^- tetrahedra in the alanates.[35, 54, 75, 105, 173, 174] The tetrahedral geometry of BH_4^- results in a characteristic splitting into two valence peaks, the lower one of s (A_1) symmetry and the upper one of p (T_2) symmetry, with a relative weight ratio of 1:3. Projected on atomic states, the s-peak then has contributions from H s and B s orbitals, and the p-peak has contributions from H s and B p orbitals. The p-peak can be split due to symmetry breaking caused by the crystal field. This is clearly observed in the lowest two panels of Figure 8.5, showing the PDOS on the B_d and H_d atoms with the s peak at ~ -7 eV, and a p doublet around ~ -1 eV. The splitting between s- and p-peaks is large (~ 6 eV), and the crystal field splitting is much smaller (~ 1 eV).

The interaction between the BH_4 units in the crystal lattice leads to a broadening of the peaks due to band formation. The interaction is strongest along the $B_b(H_b)_4$-Be-$B_b(H_b)_4$ polymer backbone, see Figures 8.1 and 8.2. This leads to an s-type band in the range ~ -9 to ~ -7.5 eV, involving contributions from H_b, B_b, and Be s orbitals, whose DOS has the characteristic shape of a one-dimensional structure, see the upper three panels of Figure 8.5. In the range ~ -5 to ~ -2 eV we find and a set of p-type bands. The band widths are smaller than the sp splitting, but they are not negligible, reflecting the covalent bonding along the polymer backbone.

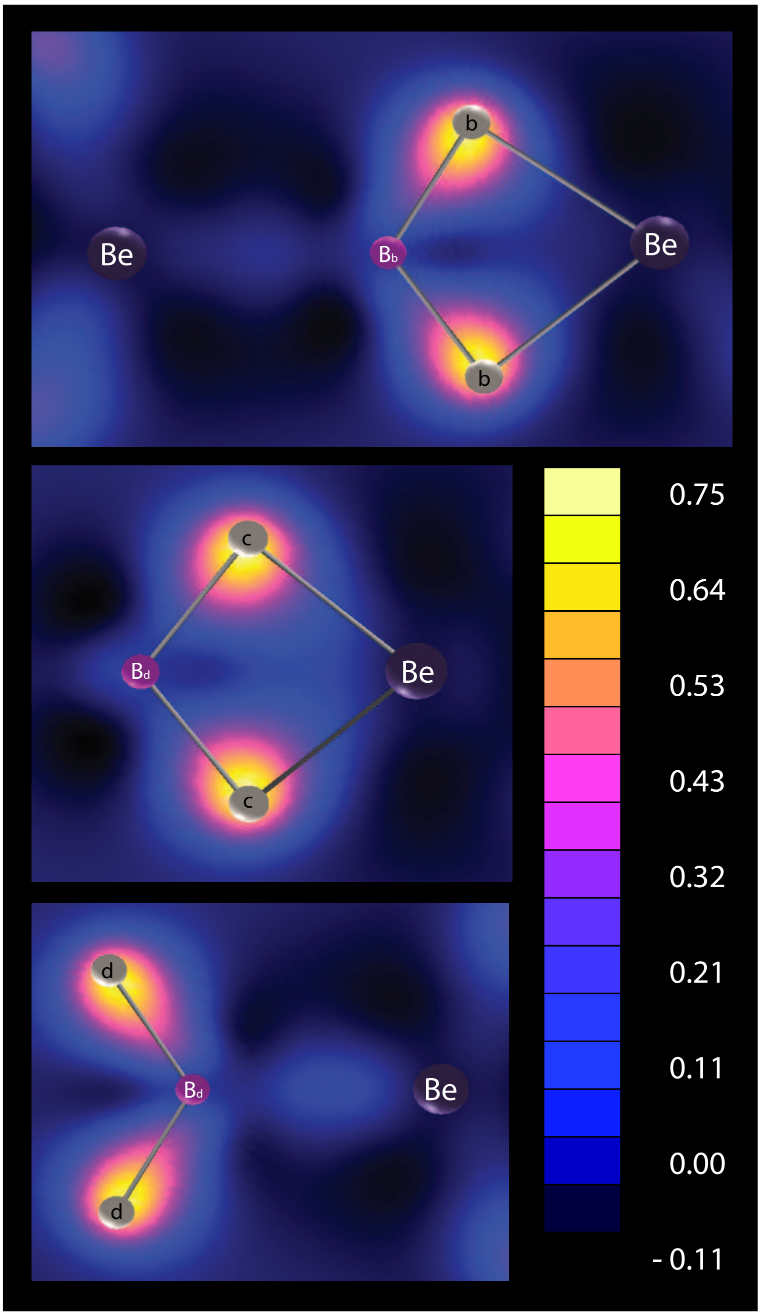

Figure 8.4: *Charge density difference plots (e/Å^3) of $Be(BH_4)_2$ with respect to the isolated atoms. The top picture gives a cut through a plane containing B_b, H_b and Be atoms of the polymer backbone, the middle picture a cut through the B_d, H_c side chain plane, and the bottom right picture a cut through the B_d, H_d side chain plane. Electrons are transferred from regions close to the Be atoms to regions close the H atoms and the B-H bonds.*

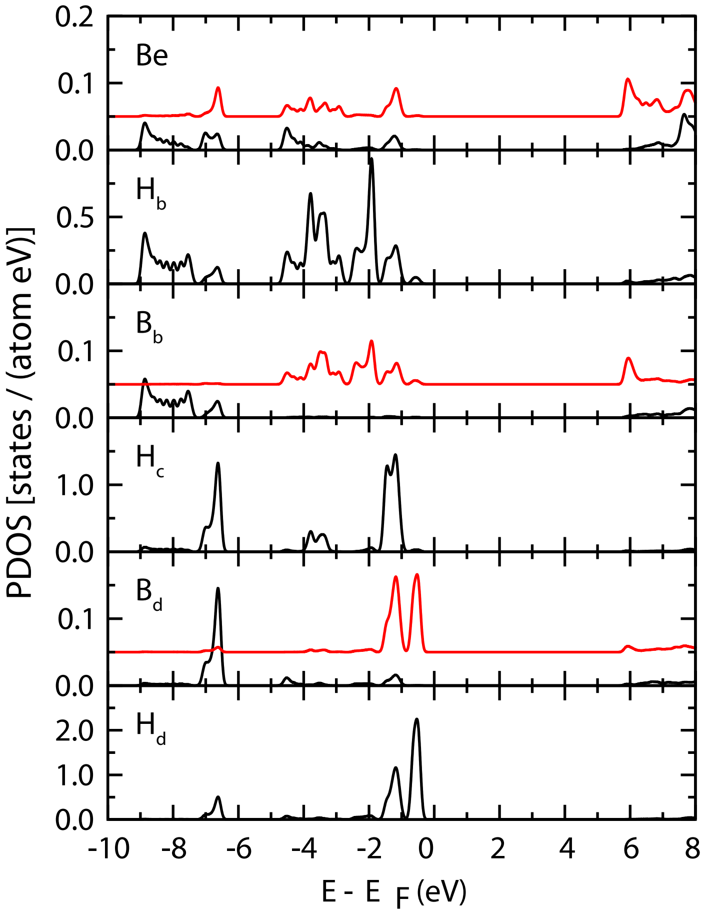

Figure 8.5: *The electronic projected densities of states (PDOS) of $Be(BH_4)_2$. The Fermi level, E_F, at the top of the valence band is the zero of energy. The upper (red) and lower curves (black) give projections on p and s atomic states, respectively. Atomic radii of 0.7, 0.5 and 1.1 Å are used for Be, B and H.*

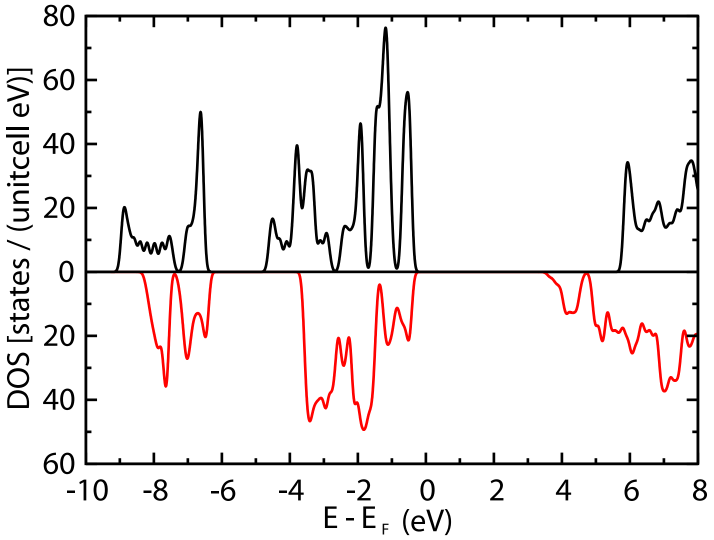

Figure 8.6: *The total electronic densities of states (DOS) of Be(BH$_4$)$_2$. The Fermi level, E_F, at the top of the valence band is the zero of energy. In the lower curve the beryllium atoms are replaced by an homogeneous background with charge* 2+*.*

The involvement of the Be atoms can be clarified by calculating the DOS for a Be(BH$_4$)$_2$ structure in which the Be atoms are replaced by a homogeneous background with charge 2+. The result is shown in Figure 8.6. The s and p valence bands discussed above are replaced by much narrower peaks that reflect electron localization on BH$_4^-$ ions in this artificial structure. In other words, the Be atoms in Be(BH$_4$)$_2$ are involved in the covalent bonding. This is in contrast to alkali or alkaline earth boranates and alanates, where the DOS changes little if the cations are replaced by a background charge. The bonding in the latter compounds can be described as an ionic bonding between BH$_4^-$ or AlH$_4^-$ anions and M$^+$ (akali) or M$'^{2+}$ (alkaline earth) cations.[174]

Reaction enthalpies

For light elements such as hydrogen, beryllium and boron the quantum character of their atomic vibrations is important. This leads to vibrational energies at zero temperature that are not negligible. For each compound involved in the reaction we calculate its zero point vibrational energy (ZPVE) from the frequencies of the vibrational modes in the optimized structure. For hydrogen molecules also the zero point rotational energy (ZPRE) is not entirely negligible. Reaction enthalpies ΔH at $T = 0$K are then calculated from

$$\Delta H = \sum_p \left(E_p^{\mathrm{TOT}} + E_p^{\mathrm{ZPVE}}\right) + E_{H_2}^{\mathrm{ZPRE}} - \sum_r \left(E_r^{\mathrm{TOT}} + E_r^{\mathrm{ZPVE}}\right) \qquad (8.1)$$

Table 8.3: *Total energies, E^{TOT}, (with respect to non spin polarized model atoms), zero point vibrational energies, E^{ZPVE}, and zero point rotational energy, E^{ZPRE}, in eV/formula unit in the relaxed structures.*

	E^{TOT}	E^{ZPVE}	E^{ZPRE}
$\mathrm{Be(BH_4)_2}$	−45.868	2.450	
$\mathrm{BeH_2}$	−10.797	0.542	
$\mathrm{H_2}$	−6.803	0.266	0.011
B	−6.687	0.126	
Be	−3.729	0.091	

where $E^{\mathrm{tot}}_{p/r}$ denotes the total energy of the reaction products p or reactants r, $E^{\mathrm{ZPVE}}_{p/r}$ are the corresponding ZPVEs, and $E^{\mathrm{ZPRE}}_{H_2}$ is the ZPRE of the hydrogen molecules involved in the reaction.

For the hydrogen molecules we calculate a vibrational frequency of 4356 cm^{-1}, in good agreement with the experimental value of 4401 cm^{-1}.[27] The ZPVE, 0.266 eV, is then calculated from the energy levels of a Morse potential:

$$E(n) = \hbar\omega\left(n+\frac{1}{2}\right) - \frac{1}{4D_e}\left[\hbar\omega\left(n+\frac{1}{2}\right)\right]^2, \tag{8.2}$$

Assuming that ortho- and para-hydrogen are produced in a proportion of three to one, the average ZPRE of a hydrogen molecule is 0.011 eV, using the energy levels given in Ref. 27.

The calculated total energies and ZPEs of all compounds involved in the reactions are listed in Table 8.3. We consider two possible reaction paths for the formation of $\mathrm{Be(BH_4)_2}$. In the first path $\mathrm{Be(BH_4)_2}$ is directly formed from the elements.

$$\mathrm{Be} + 2\mathrm{B} + 4\mathrm{H_2}(g) \rightarrow \mathrm{Be(BH_4)_2}. \tag{8.3}$$

The second path involves the formation of an intermediate compound $\mathrm{BeH_2}$.

$$\mathrm{Be} + \mathrm{H_2}(g) \rightarrow \mathrm{BeH_2}. \tag{8.4}$$

$$\mathrm{BeH_2} + 2\mathrm{B} + 3\mathrm{H_2}(g) \rightarrow \mathrm{Be(BH_4)_2}. \tag{8.5}$$

The enthalpies of these reaction are calculated using Equations (8.1) and the values given in Table 8.3.

Equation (8.3) gives a reaction enthalpy of -0.39 eV/$\mathrm{H_2}$ if ZPEs are neglected. If ZPEs are included the reaction enthalpy becomes -0.14 eV/$\mathrm{H_2}$, which indicated the importance of ZPE corrections for these lightweight compounds. In principle these values are in a range that is useful for hydrogen storage. Using the ionic model of Ref. 166 gives a reaction enthalpy of -0.02 eV/H_2 (neglecting ZPEs). In the previous section we have already concluded that the bonding in $Be(BH_4)_2$ is not purely ionic, i.e. $Be^{2+}(BH_4)_2^-$. The Be atoms are bonded (partially) covalently to BH_4, which increases the bonding as compared to the pure ionic picture, resulting in a higher dehydrogenation enthalpy.

Most alanates and other boranates form a simple alkali / alkaline earth hydride when hydrogen is released in a first step. The dehydrogenation of this simple hydride then occurs as a separate second step. Usually the enthalpies are such that only the first step is considered useful for hydrogen storage. For $Be(BH_4)_2$ these two steps correspond to the reverse reactions of Reactions 8.5 and 8.4. The calculated reaction enthalpies of Reactions 8.4 and 8.5 are -0.27 and -0.43 eV/H_2 without ZPEs, and -0.09 and -0.15 eV/H_2 with ZPE corrections, respectively.

Note that per H_2 $Be(BH_4)_2$ is slightly more stable than BeH_2. This would indicate that a one-step reaction directly from the elements, Reaction 8.4, is more favorable than the two-step reaction via the simple hydride, Reaction 8.4 and 8.5. The enthalpy difference however is very small. In addition kinetic barriers may influence the relative importance of the two reaction paths.

We will now focus on finite temperature properties. For the solids we calculate the Gibbs free energy $G(T)$ in the harmonic approximation

$$G(T) = E^{\mathrm{tot}} + H^{\mathrm{vib}}(T) - TS^{\mathrm{vib}}(T) \tag{8.6}$$

with

$$H^{\mathrm{vib}}(T) = \int d\omega g(\omega) \left\{ \frac{1}{2}\hbar\omega + \hbar\omega n(\omega) \right\} \tag{8.7}$$

and

$$S^{\mathrm{vib}}(T) = k_B \int d\omega g(\omega) \left\{ \beta\hbar\omega n(\omega) - \ln\left[1 - e^{-\beta\hbar\omega}\right] \right\} \tag{8.8}$$

where $g(\omega)$ is the phonon density of states, $n(\omega) = [exp(\beta\hbar\omega) - 1]^{-1}$ is the Bose-Einstein occupation number and $\beta = 1/k_B T$. The first term in the integral of Equation 8.7 gives the ZPVE and the second term gives the finite temperature contribution. Note that we neglect the PV term (i.e. the distinction between energy and enthalpy), which is a good approximation for solids.

For the Gibbs free energy, the enthalpy and the entropy of the hydrogen gas, we use the values given in Ref. 28. Figure 8.7 gives the free energies of $Be(BH_4)_2$ and the products of the dehydrogenation reaction, i.e. the left and right-hand-sides of Equation (8.3), at the standard pressure of 1 bar. At 162 K the free energy of the products drops below

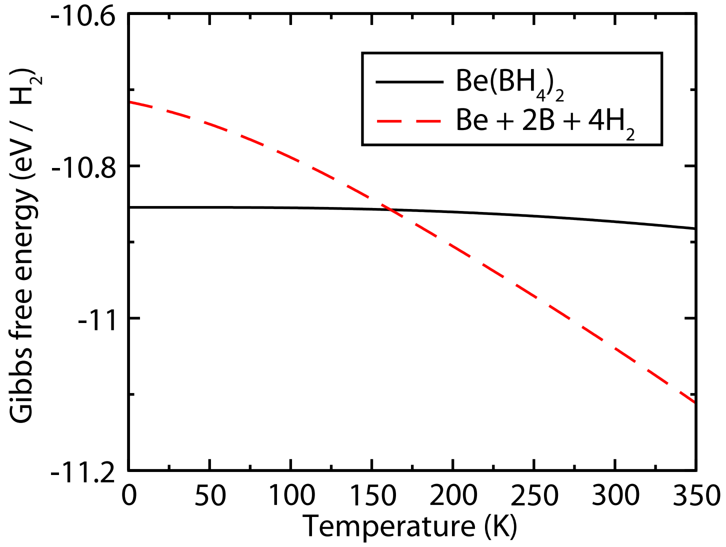

Figure 8.7: *Gibbs free energy of $Be(BH_4)_2$ and the constituting elements.*

that of the hydride phase. This intersection of the two free energy curves defines the decomposition temperature.

The predicted desorption temperature and equilibrium pressures rely only on the thermodynamics of the reaction. From the fact that experimentally $Be(BH_4)_2$ seems to be stable at room temperature one may conclude that kinetic barriers play an important role in stabilizing $Be(BH_4)_2$. In this respect $Be(BH_4)_2$ is similar to other boranates and alanates, where decomposition temperatures are much higher than what is expected on the basis of thermodynamics and catalysts have to be applied in order to overcome kinetic barriers.

Conclusions

We use DFT electronic structure calculations at the GGA level to study the crystal structure, electronic structure and thermodynamics of $Be(BH_4)_2$. We optimize the atomic positions and lattice parameters of all compounds involved in possible formation and dehydrogenation reactions. Both the crystal structure and the electronic structure indicate that the bonding between B and H atoms is covalent, and that the bonding between Be and H has covalent as well as ionic contributions. The crystal structure and the electronic density of states give evidence for $[\text{-BH}_4\text{-Be-}]_n$ (helical) polymers.

The enthalpies of possible formation reactions are calculated including zero point energy corrections. The latter are obtained by the calculating the phonon frequencies of all compounds involved in the reactions. Since not only hydrogen, but also boron and beryllium are relatively light elements, the zero points energies are relatively large for these compounds. The enthalpy of formation of $Be(BH_4)_2$ from the elements is -0.39 eV/H_2 without and -0.14 eV/H_2 with zero point energy contributions.

$Be(BH_4)_2$ differs from other boranates and alanates in that its dehydrogenation to the elements is thermodynamically slightly more favorable than dehydrogenation via the simple hydride BeH_2. In alkali or alkaline earth boranates and alanates dehydrogenation always occurs via the alkali or alkaline earth simple hydride. The different behavior of $Be(BH_4)_2$ is mainly caused by the high stability of bulk beryllium metal.

$Be(BH_4)_2$ follows the general trends in the formation energies that have been observed in alkali and alkaline earth alanates and boranates. Boranates are more stable than the corresponding alanates, lighter cations give compounds that are more unstable, and alkaline earth compounds are more unstable than alkali compounds.[174] Indeed $Be(BH_4)_2$ is less stable than $LiBH_4$ or $Mg(BH_4)_2$. We have not found mentioning of beryllium alanate in the literature, which might indicate that this compound would be too unstable.

Using the calculated phonon spectrum we have calculated free energies within the harmonic approximation to assess thermodynamic properties at finite temperature. We obtain a decomposition temperature of 162 K at a 1 bar pressure.

Acknowledgements

The authors wish to thank Prof. Dr. R.A. de Groot for helpful discussions and J.J. Attema for the use of his imaging software. This work is part of the research programs of ‘Advanced Chemical Technologies for Sustainability (ACTS)’ and the ‘Stichting voor Fundamenteel Onderzoek der Materie (FOM)’, both financially supported by the ‘Nederlandse Organisatie voor Wetenschappelijk Onderzoek (NWO)’.

Chapter 9

Magnesium boranate, $Mg(BH_4)_2$

Reproduced with permission from:
A density functional study of α-$Mg(BH_4)_2$
M.J. van Setten, G.A. de Wijs, M. Fichtner and G. Brocks
Matter. Chem. under review

Abstract

Starting from the recently reported crystal structures we have studied hydrogen desorption reactions of $Mg(BH_4)_2$ using first-principles calculations. Our results indicate that the optimized complex structure of $Mg(BH_4)_2$ is 4.4 kJ/mol H_2 more stable than present estimates based upon model structures. Nevertheless, we calculate a hydrogen desorption enthalpy for the reaction $Mg(BH_4)_2$ "arrow" MgB_2 + 4 H_2 of 40 kJ/mol H_2 at room temperature. This value is close to that of an ideal hydrogen storage material. This indicates that the presently measured high temperature for hydrogen desorption $Mg(BH_4)_2$ (563 K) results from kinetic barriers, which may be lowered by means of catalysts or nanostructuring.

Introduction

Any future economy based on hydrogen as a fuel will require a safe, reliable, and cheap method for storing hydrogen. Solid-state hydrogen storage represents one of the most likely solutions.[4,6] Recently, a very promising material, magnesium tetrahydroborate or boranate, $Mg(BH_4)_2$, was studied experimentally in this context.[165,175] Although the material has been known for more than 50 years, the crystal structure was resolved only lately.[176,177] $Mg(BH_4)_2$ has a gravimetric hydrogen content of 14.9 wt.% and, hence, is one of the few materials that might enable us to satisfy the long-term DOE requirement of 10 wt.% of hydrogen with respect to the complete storage system.

Besides the gravimetric hydrogen storage capacity, the hydrogen desorption temperature is the most crucial parameter determining the usefulness of a material for hydrogen storage. The ideal material should have an equilibrium hydrogen pressure of 1 bar at room temperature. This would enable a combined storage-fuel cell system, where the residual heat of the fuel cell is used to drive the desorption reaction. To achieve this equilibrium pressure, the desorption enthalpy of a storage material should be around 39.2 kJ/mol H_2.[4] Without the use of a catalyst, $Mg(BH_4)_2$ desorbs hydrogen at temperatures around 290°C.[165] At present, it is unclear to what an extent this temperature can be lowered by decreasing the kinetic barriers. A fundamental lower limit of the desorption temperature is defined by thermodynamics. It is the temperature at which the change in Gibbs free energy $\Delta G = \Delta H - T\Delta S$ of the reaction is zero. Kinetic barriers, which increase the practical desorption temperature, can be modified by adding catalysts or changing the particle sizes, for instance. Calculating the reaction enthalpy from first principles may help assess the limits set by thermodynamics.

In the case of $Mg(BH_4)_2$, the following desorption reactions are most important:

$$\mathrm{Mg(BH_4)_2} \rightarrow \mathrm{Mg} + 2\mathrm{B} + 4\mathrm{H_2} \tag{9.1}$$

$$\mathrm{Mg(BH_4)_2} \rightarrow \mathrm{MgB_2} + 4\mathrm{H_2} \tag{9.2}$$

Reaction 9.1 describes the decomposition of $Mg(BH_4)_2$ to the elemental solids, and H_2 gas. Reaction 9.2 is assumed to be the overall desorption reaction. These reactions have been studied before by first principles calculations using model crystal structures of $Mg(BH_4)_2$.[33,163] This paper will focus on the effects of the complete experimental crystal structure. Moreover, the full temperature dependence of the reaction enthalpies will be determined.

Computational methods

The first step in obtaining the enthalpies is to calculate the total energies of all the compounds involved in the reactions. The energies are obtained from first-principles calculations based on density functional theory (DFT). The projector augmented wave (PAW) method is applied in combination with a plane wave basis set, as incorporated in the Vienna Ab initio Simulation Package (VASP).[14–17,19] The plane wave kinetic energy cutoff is 700 eV. The PW91 generalized gradient approximation to the exchange correlation functional is adopted and nonlinear core corrections are applied.[25,117] The Brillouin zone integrations are performed with the improved tetrahedron scheme using a sampling density of one k-point per 0.05 $Å^{-1}$ in each direction.16

Crystal structure

To calculate the total energy of $Mg(BH_4)_2$, its crystal structure is needed. Two experimental crystal structures were published recently.[176,177] The structure of Cerný et al.[176] is based on XRD and neutron diffraction of $Mg(BD_4)_2$, whereas that of Her et al.[177] is based on XRD of $Mg(BH_4)_2$. The unit cell of both structures contains 330 atoms, i.e. 30 $Mg(BH_4)_2$ formula units. In both cases, the space group is P61 (no. 169) with all atoms at Wyckoff 6a positions, which leads to a total of 165 symmetry-independent coordinates. Her et al.[177] report lattice parameters of $a = 10.3414$ Å and $c = 37.086$ Å, whereas Cerný et al.[176] give $a = 10.3182$ Å and $c = 36.9983$ Å.

Starting from the structure given by Cerný et al.,[176] we optimize the atomic positions while fixing the cell parameters at their experimental values. Full details of the optimized structure are given in the supporting information. The largest changes with respect to the experimental geometry were in the BH4 tetrahedra surrounding the B9 and to a lesser extent, the B6 and B10 atoms. The inter-atomic distances relaxed to 1.23, 2.1, and 2.4 Å for the B-H, Mg-H, and Mg-B distances, respectively. During the optimization, a decrease of about 65 kJ/mol in total energy is observed. Most of the energy decrease results from optimizing bond lengths that involve hydrogen atoms, which are difficult to obtain experimentally. Our optimized B-H bond length is close to what is typically found in neutron diffraction experiments.17 We find that the optimized structure is 4.4 kJ/mol H_2 lower in energy than the most stable (Pmc21) structure reported by Vajeeston *et. al.*[163] The external pressure calculated for our optimized structure is very small, which indicates that explicitly optimizing the cell shape and volume is not necessary.

When optimizing the atomic positions starting from the structure proposed by Her et al.,[177] the final structure has the same total energy as the optimized Cerný structure. The interatomic distances are also the same. In this case, a decrease of about 150 kJ/mol in total energy is observed during optimization. This rather large energy change results from optimizing bond lengths. It can be noted that a rather short B-H distance of 1.1 Å was applied in Ref.[177] This may be due to the fact that XRD measures the electronic charge distribution instead of the nuclear positions, as in neutron diffraction. For the positions of covalently bonded light atoms, such as hydrogen, XRD and neutron diffraction experiments may therefore yield different results. In neutron diffraction, B-H bond lengths typically are close to 1.2 Å [178] which is in agreement with the calculated values. It may be concluded that both relaxed structures are essentially the same.

Electronic structure

The bonding in $Mg(BH_4)_2$ can be illustrated by the electronic density of states (DOS) shown in Figure 9.1. The DOS shows two peaks in the valence region and a large band gap, 6.64 eV, between the valence and conduction bands. Both features are also observed in other boranates.[33] The peaks in the valence region result from the covalent bonds between H and B atoms. Since the contribution of the Mg states is very small, the bonding in $Mg(BH_4)_2$ is mainly ionic between Mg^{2+} and $(BH4)^-$ ions. The tetrahedral geometry of the $(BH4)^-$ ions results in a characteristic splitting into two valence peaks, the lower one of s (A1) symmetry and the upper one of p (T2) symmetry, the relative weight ratio being 1:3. The interaction between the ions in the crystal lattice leads to a broadening of the peaks.[174] The broadening of the P61 structure is very similar to that of the simpler Pmc21 structure, as can be observed in Figure 9.1.

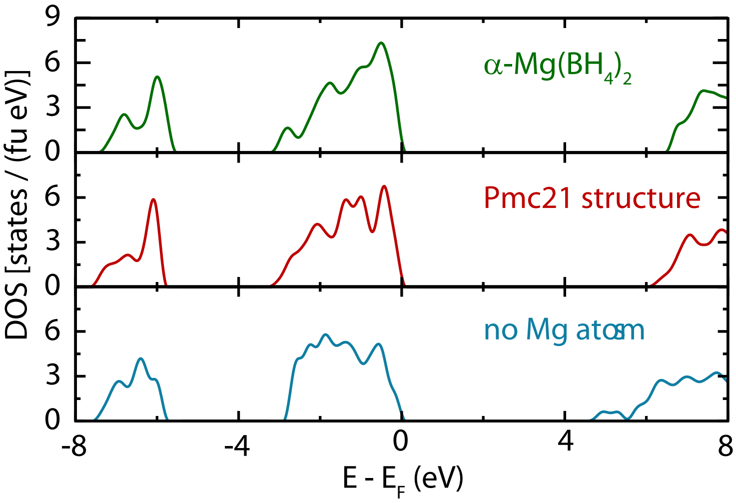

Figure 9.1: *Electronic density of states of $Mg(BH_4)_2$ in the α-structure, in the Pmc21 structure (see text), and in the α-structure with the Mg atoms replaced by a homogeneous compensating background charge. In calculation the DOS a Gaussian smearing is used.*

The influence of the crystal field of the Mg^{2+} ions is not negligible, however. This may be concluded from a comparison to the DOS calculated by replacing the Mg^{2+} ions by a homogeneous positive background charge, see Figure 9.1. The latter changes the shape of the valence peaks in the DOS and reduces the gap between the valence and conduction bands by 2 eV.

Reaction enthalpies

The total energies of bulk magnesium, bulk boron, and the H_2 molecule are calculated using the previously reported structural parameters.[54,174] For boron, the lowest energy (β rhombohedral) structure is chosen.[167] The crystal structure of MgB_2 is given by space group P6/mmm (no. 191), with Mg and B atoms at 1a and 2d Wyckoff positions, respectively. The calculated optimized lattice parameters are $a = 3.072$ Å and $c = 3.520$ Å.

Using the total energies calculated for all compounds involved in the Reactions 9.1 and 9.2, we obtain $\Delta E = 65$ kJ/mol H_2 for Reaction 9.1 and $\Delta E = 53$ kJ/mol H_2 for Reaction 9.2. Using the simpler Pmc21 structure for $Mg(BH_4)_2$,[163] $\Delta E = 60$ kJ/mol H_2 is calculated for Reaction 9.1. This value is lower than the 71 kJ/mol H_2 reported in Ref. 163 for Reaction 9.1. The origin of this difference lies in the reference point chosen for elemental boron. Whereas we use the most stable (β-rhombohedral) structure for boron as a reference, the less stable α-tetragonal structure is used in Ref. 163.

To obtain reaction enthalpies at a finite temperature, we calculate the phonon densities of states of all solids involved in the reactions using the harmonic approximation and occupy the phonon modes according to Bose-Einstein statistics. The unit cell of the P61 structure of $Mg(BH_4)_2$ is too large for first-principles phonon calculations. The phonon density of states is approximated by that of $Mg(BH_4)_2$ in the Pmc21 structure. Since the integrated density of states only is relevant to the thermal properties, the detailed structure of the density of state is less important and the approximation is expected to be reasonable. The Pmc21 structure only has two formula units per unit cell with 33 independent coordinates instead of the 30 formula units and 165 independent coordinates per unit cell of the P61 structure. Hence, the approximation decreases the computational effort of the phonon calculations by about three orders of magnitude.

The H_2 gas is modeled using the thermodynamic data given by Hemmes et al.[28] At T = 0K, the procedure described above gives the so-called zero point energy corrections. Then, a reaction enthalpy of $\Delta H(0K) = 47$ and 35 kJ/mol H_2 is obtained for Reactions 9.1 and 9.2, respectively. The value for Reaction 9.1 is in good agreement with the value of 46 kJ/mol H_2 predicted by the correlation relation between electronegativities and formation enthalpies proposed by Nakamori et al.[33]

The calculated temperature dependence of the reaction enthalpies is shown in Figure 9.2. The temperature dependence is small, but not negligible. At room temperature, $\Delta H(298K) = 53$ and 40 kJ/mol H_2 are obtained for Reactions 9.1 and 9.2, respectively. The hydrogen desorption enthalpy at the experimental temperature associated with Reaction 9.2 is $\Delta H(563K) = 43$ kJ/mol H_2. This value differs significantly from the experimental value of 16.8 kJ/mol H_2 reported by Chlopek et al.,[165] which was obtained by high-pressure differential scanning calorimetry. Combined with the experimental decomposition enthalpy for MgB_2, 40 kJ/mol, this would give 26.8 kJ/mol H_2 for Reaction 9.1. On the other hand, Matsunaga et al. report a value of 39.3 kJ/mol H_2 for the hydrogen desorption reaction of $Mg(BH_4)_2$ to MgH_2.[175] Combining this value with the decomposition enthalpy of MgH_2, 75.3 kJ/mol H_2, this would give a reaction enthalpy of 48.3 kJ/mol H_2 for Reaction 9.1. This value is in reasonable agreement with the calculated $\Delta H(563K) = 55$ kJ/mol H_2 for Reaction 9.1. The difference between the two figures for Reaction 9.1 extracted from the experimental data indicates the difficulty in measuring the dehydrogenation enthalpy of $Mg(BH_4)_2$.

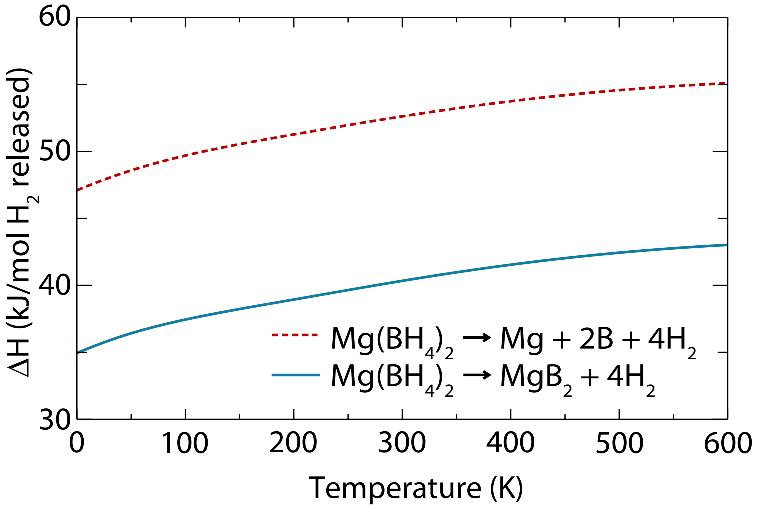

Figure 9.2: *Temperature dependence of the reaction enthalpies of reactions 1 and 2.*

Conclusion

From our calculations we conclude that the thermodynamics of the hydrogen desorption reaction of $Mg(BH_4)_2$ is close to that of an ideal hydrogen storage material. This gives hope for a possible decrease of the desorption temperature by means of catalysts or nanostructuring. Together with the high gravimetric hydrogen content, this makes $Mg(BH_4)_2$

a material having a high potential for solid-state hydrogen storage.

Acknowledgements

The authors thank R.A. de Groot for helpful discussions. This work is part of the Sustainable Hydrogen Program of Advanced Catalytic Technologies for Sustainability (ACTS) and of the research program of the "Stichting voor Fundamenteel Onderzoek der Materie (FOM)", both financially supported by the "Nederlandse Organisatie voor Wetenschappelijk Onderzoek (NWO)" Financial support under the EU project "NessHy" is gratefully acknowledged. Supporting Information Available: The crystallographic details of the crystal structures of $Mg(BH_4)_2$ as used in the calculations. This material is available free of charge at the internet via http://pubs.acs.org.

Chapter 10

A model for the formation enthalpies

Reproduced with permission from:
Model for the Formation Energies of Alanates and Boranates
M.J. van Setten, G.A. de Wijs, and G. Brocks
J. Phys. Chem. C **111**, 9592 - 95974 (2007)
Copywrite 2007 Americal Chemical Society

Abstract

We develop a simple model for the formation energies (FEs) of alkali and alkaline earth alanates and boranates, based upon ionic bonding between metal cations and AlH_4^- or BH_4^- anions. The FEs agree well with values obtained from first principles calculations and with experimental FEs. The model shows that details of the crystal structure are relatively unimportant. The small size of the BH_4^- anion causes a strong bonding in the crystal, which makes boranates more stable than alanates. Smaller alkali or alkaline earth cations do not give an increased FE. They involve a larger ionization potential that compensates for the increased crystal bonding.

Introduction

The large scale utilization of hydrogen as a fuel crucially depends on the development of compact storage materials with a high mass content of hydrogen.[6] Over the last decade alanates and boranates have been studied extensively because of their potential use as hydrogen storage materials.[5,6] These materials consist of a lattice of metal cations and AlH_4^- or BH_4^- anions, respectively. The ideal hydrogen storage material should have a high gravimetric hydrogen density, which requires the use of light metals. Moreover, the formation energy (FE) of such a material has to be such that it is stable at room temperature, yet it has to decompose at low temperature to release its hydrogen. In principle a large variety of alanates and boranates can be synthesized by changing the metal cations, which can be used to tune the formation energy.[33]

Since synthesis is a very time consuming effort, there is a need for a materials specific theory with a predictive power for the FE. At present the state of the art is formed by first principles calculations based upon density functional theory (DFT). Several papers have been dedicated to trends in the DFT FEs of alanates and boranates.[33,76,104,110,120] There exists a surprising variety of crystal structures among these compounds. In DFT calculations the crystal structure with the lowest energy has to be searched for each compound, and the cell parameters and the atomic positions have to be optimized. This procedure also makes DFT calculations a very time consuming effort. A simple theory would help to understand the trend in the FEs of alanates and boranates.

Theory and computational methods

Our aim is to construct a simple model for the FEs at 0 K of alkali alanates and boranates (MAH_4, M = Li, Na, K; A = Al, B) and of their alkaline earth counterparts ($M'(AH_4)_2$, M = Mg, Ca), avoiding the use of the actual crystal structure. We assume that these compounds can be described by ionic bonding between M^+ or M'^{2+} cations and AH_4^- anions. Our model for the FE, ΔE_f, is based upon a Born-Haber cycle,[179]

$$\Delta E_f = E_{\mathrm{elem}} + E_{\mathrm{ions}} + E_{\mathrm{crys}}. \tag{10.1}$$

Starting from bulk elemental solids and H_2 molecules, E_{elem} is the energy required to atomize the solids and the molecules. The E_{elem} of the bulk solids are listed in Table 10.1. We use a value of 4.48 eV for the dissociation energy of H_2.[26]

The second step is to create M^+, M'^{2+} and AH_4^- ions from the atoms, represented by the energy E_{ions}. The contribution to E_{ions} from the M^+ ions is simply the first ionization potential (IP) and from the M'^{2+} ions it is the sum of the first and second IPs. The numbers ΣIP are given in Table 10.1. We calculate the contribution to E_{ions} from the

Table 10.1: *Ionic radii, R_{ion} (Å), summed ionization potentials, ΣIP (eV), dissociation energies for the elemental bulks, E_{dis} (eV), and the Born exponents, n. Values are taken from Refs.[26] and .[181]*

	Li	Na	K	Mg	Ca	B	Al
R_{ion}	0.90	1.16	1.52	0.86	1.14		
ΣIP	5.39	5.14	4.34	22.67	17.98		
E_{dis}	1.64	1.08	0.93	1.48	1.81	5.81	3.38
n	5	7	9	7	9	7	9

AH_4^- anions as follows. First an electron is added to an Al or B atom, which lowers the energy by the atomic electron affinity (EA). These atoms then have four valence electrons that are used to form covalent bonds with four hydrogen atoms, Using EAs of 0.44 eV and 0.28 eV for Al and B, and 2.91 eV and 3.45 eV for the Al-H and B-H bond strengths,[26] we calculate energies of -12.08 eV and -14.08 eV to form the AlH_4^- and BH_4^- anions from the neutral atoms. The tetrahedral bonding in these anions justifies the use of standard bond strengths from Ref. 26. Note that the octrahedral Al-H bonding found in alumino hexahydrides, such as Na_3AlH_6, would require a different bond strength.

The final step consists of constructing the crystal from the M^+ (or M'^{2+}) and AH_4^- ions, which is represented by the energy E_{crys}. We use a simple Born model for the potential between cations and anions. It consists of an attractive Coulomb potential between point charges at the centers of the ions plus a repulsive short-range potential $\propto r^{-\bar{n}}$, where $\bar{n}$ is the average Born exponent. E_{crys} is then given by[180]

$$E_{\text{crys}} = \frac{M_c Z_A Z_C e^2}{4\pi\varepsilon_0 r_0}\left(1 - \frac{1}{\bar{n}}\right), \tag{10.2}$$

where $Z_A = -1$ and $Z_C = +1, +2$ are the valencies of the anions and the cations, respectively, and r_0 is the shortest cation-anion distance in the lattice. M_c represents the Madelung constant, which depends upon the type of lattice.[180]

Note that in all compounds considered here the AlH_4^- and BH_4^- anions have a tetrahedral geometry. However, in the Born model of Equation 10.2, we have approximated these tetrahedra by spheres. Our motivation for this is that we are interested in a simple model of E_{crys} without having to take into account the full details of the crystal structure, in particular the detailed shape, packing, polarization and multi-pole interactions of the complex anions. In the simple model the cation-anion distance is the sum of the ionic radii of the cation and the anion, $r_0 = r_C + r_A$. Since the cations we consider are mostly octahedrally coordinated, we use standard ionic radii r_C of 6-fold coordinated alkaline and alkaline earth ions, see Table 10.1.[181]

Neglecting the details of the crystal packing, we choose to approximate the AlH_4^- and BH_4^- tetrahedra by “averaged” spheres. A priori one would expect the radius r_A of such a sphere to be somewhere between the maximum contact distance to an AH_4^- ion (A = Al, B), i.e. the ionic radius of the complex ion, and the minimum contact distance, i.e. the radius of the central atom A. One can consider r_A as a fit parameter of the model. However, below we show that one obtains remarkably good results using the Al-H and B-H bond lengths as the average radii r_A of the complex ions. The Al-H and B-H bond lengths are 1.62 Å and 1.20 Å, respectively. The averaged sphere approximation obviously breaks down if the packing density of the anions becomes too large, such that their detailed shape becomes important. We suggest that this is the case in the Zr and Hf compounds discussed below.

Avoiding the full details of the crystal structure also leads to using average values for the Madelung constants M_c in Equation 10.2. The alkali alanates and boranates have an AB type lattice, where A is the alkali cation, and B is the boranate or alanate anion. The variation of the Madelung constant over different AB lattices is relatively small, so we use an average value $M_c = 1.76$. The root mean square deviation (rms) averaged over all AB lattice types is 4%. A similar reasoning holds for the alkaline earth alanates and boranates. They have an AB_2 lattice, whose average Madelung constant is $M_c = 2.40$ with a rms deviation of 4%.

For some of the materials the experimental FE is not known. Therefore we have also performed first principles DFT calculations. We use the projector augmented wave (PAW) method,[14,19] and the PW91 generalized gradient approximation (GGA),[25] as implemented in the Vienna *ab initio* simulation package (VASP).[15–18] To integrate the Brillouin zone we apply the tetrahedron scheme. The **k**-point mesh and the plane wave kinetic energy cutoff (700 eV) are chosen such, that total energies are converged to a numerical accuracy of 1 meV per formula unit.[1] The structures of $LiAlH_4$,[174] $NaAlH_4$,[174] $Mg(AlH_4)_2$,[174] $Ca(AlH_4)_2$,[173] $Ca(BH_4)_2$,[161] $KAlH_4$,[75] and of the alkali boranates[120] are taken from the literature. We additionally relaxed the atomic positions, but the relaxations were small and had only a minor effect on the total energies. Our calculated values compare well to those obtained in previous calculations.[33,35,76,104,120] Details on $Mg(BH_4)_2$ will be published elsewhere.[182]

---

[1] In both the DFT calculations and the model no zero point energies are taken into account.

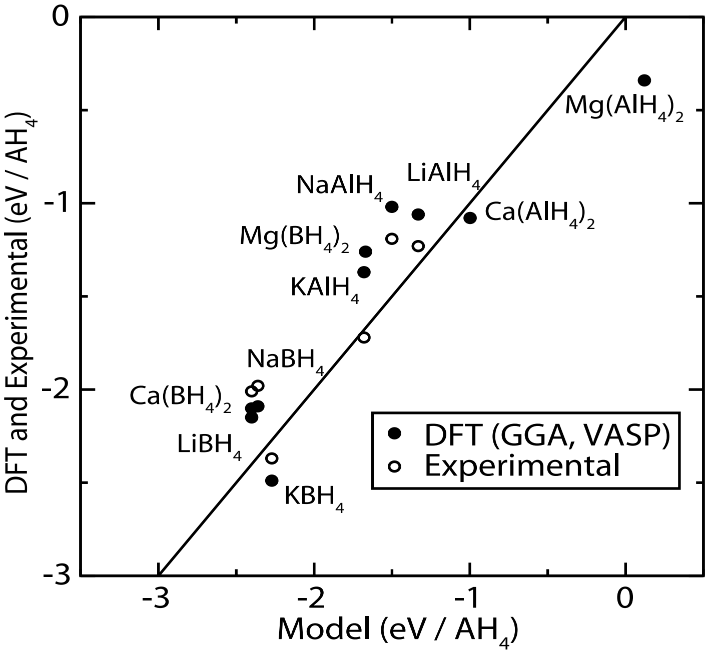

Figure 10.1: *Model formation energies (eV/AH_4) compared to DFT and experimental values.*[183]

Results

Figure 10.1 shows the most important results, i.e. the FE calculated with the model represented by Equations 10.1 and 10.2, compared to experimental[183] and DFT values. We have set r_A equal to the Al-H (1.62 Å) and B-H (1.20 Å) bond lengths. Figure 10.1 shows that, despite its simplicity, the model gives FEs that are in quantitative agreement with both the experimental, and the calculated DFT values. The rms deviation of the model with the experimental and the DFT values is 0.27 and 0.33 eV/AH_4, respectively. Note that these numbers are comparable to the rms deviation between the experimental and the first principles values, 0.19 eV/AH_4, which represents the state-of-the-art. As a check, we have also used r_A as a parameter to fit the model to the DFT results. The best fit is obtained using $r_A = 1.63$ and 1.25 Å for the alanates and the boranates, respectively. For the boranates the rms deviation between the model and the DFT values then becomes slightly smaller, i.e. 0.19 eV/BH_4.

An obvious source of error is our neglect of the details of the crystal structure, e.g., by using an average Madelung constant in Equation 10.2. Changing the Madelung constant by 5% changes the FE of the alkali compounds by 0.4 eV/AH_4 and that of the alkaline earth compounds by 0.7 eV/AH_4. As these numbers are larger than the rms deviation of the model, one can conclude that the details of the crystal structure are relatively unimportant.

The model also seems to work reasonably well for some other boranates. The model FE for $Sc(BH_4)_3$ is 0.37 eV/BH_4 higher than the DFT value calculated by Nakamori *et. al*,[33] which is within the rms error bar given above. The model FE for $Zn(BH_4)_2$ and $CuBH_4$ are 0.6 and 0.8 eV/BH_4 higher than the DFT values, respectively. This overestimation by the purely ionic model suggests a lower effective charge on the Zn and Cu atoms and the importance of covalent contributions, which makes sense in view of the larger electronegativity of Zn and Cu as compared to the alkali and alkaline earth atoms.[33] For cations with a nominal charge $Z_C = 4$, such as Zr or Hf, the model breaks down. The model FE then deviates by 2.5 eV/BH_4 from the DFT values.[33] As can be seen from Equation 10.2, for large Z_C E_{crys} becomes sensitive to small changes in the Madelung constant and the ionic radius of the cation, or in other words, to the details of the crystal structure, as well as to possible covalent contributions.

Discussion

Figure 10.1 shows that boranates are generally more stable than alanates. The origin of this stability can be analyzed by decomposing the FE into the contributions according to Equation 10.1, which is shown Figure 10.2. The differences in formation energy of the elements E_{elem} are to a large degree compensated by the differences in the formation energies E_{ions} of the ions from the atoms. The ionic crystal energy E_{crys} of the boranates is however significantly larger than that of the alanates, which results in a larger stability of the latter. This is a size effect since the BH_4^- anions are significantly smaller than the AlH_4^- anions.

It has been observed that the dissociation energies of complex alkali hydrides into simple alkali hydrides increase with the atomic number of the alkali atom.[74] For the FEs from the elements the overall trend is not that clear. E_{elem} and E_{ions} both decrease with increasing atomic number, see Figure 10.2, which increases the stability. However, this is almost compensated by E_{crys}, which increases with the cation radius r_C.

In the alkaline earth series the FE decreases with the atomic number. The dominant effect is a decreasing E_{ions}, which is due to a decrease in the ionization potentials of the cations, see Table 10.1.

Conclusions

To summarize we constructed a model for the formation energies (FEs) of alkali and alkaline earth alanates and boranates from the elemental solids and H_2 molecules. The model is based upon ionic bonding between metal cations and AlH_4^- or BH_4^- anions. It can

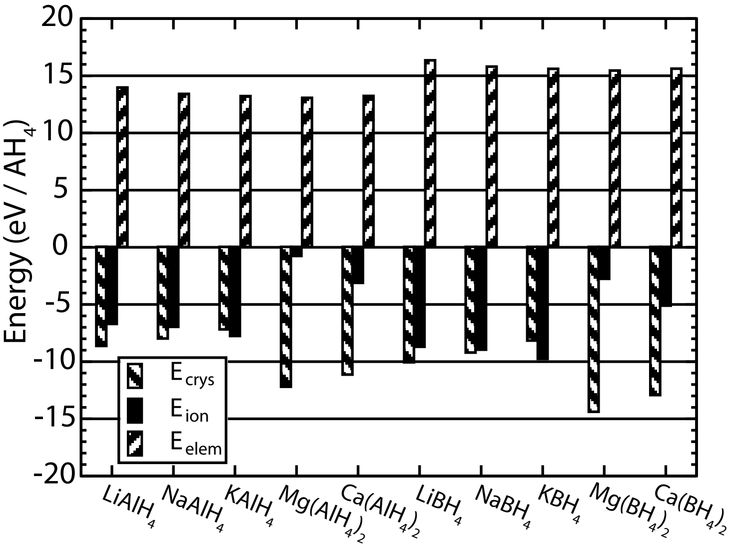

Figure 10.2: *The contributions to the formation energy (eV/AH_4) according to Equation 10.1.*

be constructed using simple energy values that are available in the literature and it does not make use of explicit crystal structure information. Compared to experimental values, the model FEs have a similar accuracy as calculated DFT values. The trends in the FEs over the series of compounds can be analyzed in terms of the individual contributions to the model.

Acknowledgments

The authors wish to thank R. A. de Groot for useful and stimulating discussions. This work is part of the research programs of ‘Advanced Chemical Technologies for Sustainability (ACTS)’ and the ‘Stichting voor Fundamenteel Onderzoek der Materie FOM)’, both financially supported by the ‘Nederlandse Organisatie voor Wetenschappelijk Onderzoek (NWO)’.

Magnesium based hydrides

Chapter 11

Introduction

The metal hydride system that is studied most intensively in the framework of hydrogen storage is that of magnesium hydride. The main reason, next to the cheap and ready availability of magnesium, is the high gravimetric amount of hydrogen (7.7 wt.%) in magnesium hydride. At least as important is the proven reversibility of the system.

In the pure magnesium / magnesium hydride system there are two obstacles for a fast hydrogen desorption and absorption reaction at practical temperatures. The most fundamental one is the thermodynamics of the desorption reaction. Magnesium hydride has a formation enthalpy of -76 kJ/mol which gives rise to an a equilibrium pressure of 1 bar slightly above 300°C.[184] Pure magnesium hydride is hence too stable to be practically used. The second one is kinetic in nature. During the absorption of hydrogen in magnesium the top layer is transformed into the hydride first. The hydride has much lower hydrogen diffusion than the metallic magnesium, causing the hydrogen absorption to slow significantly as soon as a layer of about 30 μ thickness below the surface has reacted. By using ball-milling the surface area can be increased making more magnesium available for fast hydrogen absorption.

To attack these two problems many alloys containing magnesium have been considered.[185–190] One of the most investigated is Mg_2NiH_4.[191–202] It has a hydrogen capacity of 3.6 wt.% and desorbs hydrogen at 250-300°C under pressures of 2.1-3.0 bar. The reverse reaction, the absorption of hydrogen by Mg_2Ni, takes place at temperatures of 250-350°C and pressures of 15-50 bar for poly-crystalline Mg_2Ni. Many of the properties of magnesium hydride and hydrides of magnesium based alloys are collected in a recent review on metal hydride systems.[8]

Nano-structuring of Mg_2NiH_4 has been shown, as in the case of MgH_2, to increase the kinetics of the hydrogen absorption and desorption. Ball-milled Mg_2Ni reacts with hydrogen even at room temperature. However, the thermodynamical properties of the reactions, which are better than for pure magnesium but still not favorable, cannot be changed in this way. Using ball-mill processes powders down to tens of micrometers can be produced. This scale is still too large for quantum mechanical size effects to become of influence. To obtain the scale needed for quantum size effects, nanometer sized porus media have to be used as a support. Using a support has the disadvantage to decrease the weight percentage of hydrogen.

A possible way to engineer the thermodynamics of the hydrogen absorption and desorption reactions is by alloying or doping with a second transition metal.[61,203–212] The doping of Mg_2NiH_4 with the transition metals iron cobalt and copper is studied in Chapter 12.

Alloys of magnesium with transition metals from the other end of the periodic table have als been investigated.[213,214] Alloying magnesium with scandium has shown to drastically improve the hydrogen desorption and absorption kinetics. For concentrations of scandium above about 20% the hydride has a fluorite like structure, like scandium hydride, and for lower concentrations a rutile structure, like the ground state of magnesium hydride. In the fluorite structure the hydrogen diffusion is many orders of magnitude higher than in the rutile phase.

Since scandium is rather expensive further research has shifted to the next transition metals.[214–216] Titanium, in contrast to scandium, does not form alloys with magnesium. To obtain mixed titanium magnesium hydrides non-equilibrium production methods have been used. Remarkably, these systems have been shown to be reversible over many desorption and absorption cycles. An explanation for this has been sought in the fact that titanium hydride and magnesium have the same molar volume. Since titanium hydride is more stable than magnesium hydride it is expected that the titanium atoms bind hydrogen before the magnesium atoms do. Hence a stable intermediate phase, consisting of a coherent mixture of titanium hydride and magnesium hydride "particles", is expected to form, which stabilizes the entire absorption and desorption process. With titanium the crystal structure shows the same dependence on the concentration as with magnesium. The difference in hydrogen diffusion in the two structures is also similar as in the case of scandium. Many of the details of the hydrogen desorption an absorption reaction are still subject to intensive study.

An other interesting feature of the hydrogenated magnesium titanium system is its change in the optical properties during hydrogen absorption and desorption.[215] When hydrogen is absorbed in a metal it introduces states below the Fermi level that take one of the valence electrons of the metal per absorbed hydrogen atoms. When the same amount of hydrogen atoms can be absorbed as valence electrons are available, this causes the hydride to become a semiconductor. This feature has been observed in many other metal hydride systems and is called a switchable mirror.[62,63,65,66,215,217,218] In the view of a hydrogen economy this can be used to make a hydrogen sensor.[215,219]

In the case of magnesium titanium systems experiments show that less than two hydrogen atoms per metal atom are absorbed. The hydrogenated magnesium titanium systems are therefore expected to stay metallic. It has been shown however that they form a so-called black state, i.e. low reflection and high absorption in a broad energy range including the visible range, which makes them even more interesting for sensor applications. An explanation for this phenomenon is given in Chapter 13.

Chapter 12

Doped Mg_2NiH_4

Reproduced with permission from:
Ab initio study of the effects of transition metal doping of Mg_2NiH_4
M.J. van Setten, G.A. de Wijs, and G. Brocks
Phys. Rev. B **76**, (2007)
Copyright 2007 by the American Physical Society

Abstract

Mg_2NiH_4 is a promising hydrogen storage material with fast (de)hydrogenation kinetics. Its hydrogen desorption enthalpy, however, is too large for practical applications. In this paper we study the effects of transition metal doping by first-principles density functional theory calculations. We show that the hydrogen desorption enthalpy can be reduced by ~ 0.1 eV/H_2 if one in eight Ni atoms is replaced by Cu or Fe. Replacing Ni by Co atoms, however, increases the hydrogen desorption enthalpy. We study the thermodynamic stability of the dopants in the hydrogenated and dehydrogenated phases. Doping with Co or Cu leads to marginally stable compounds, whereas doping with Fe leads to an unstable compound. The optical response of Mg_2NiH_4 is also substantially affected by doping. The direct gap in Mg_2NiH_4 is ~ 1.7 eV. Doping with Co, Fe, or Cu leads to impurity bands that reduce the direct gap by up to 0.5 eV.

Introduction

The large scale application of hydrogen as a fuel depends on the development of materials that can store hydrogen in a dense form.[5] Magnesium based hydrides are interesting candidate materials for hydrogen storage, because magnesium has a low weight. The simplest hydride, MgH_2, has a hydrogen storage capacity of 7.67 wt.%. It has, however, a high hydrogen desorption enthalpy, 0.77 eV per H_2, and hence an equilibrium plateau pressure (10^{-7} bar) at room temperature that is too low for practical applications.[184] Moreover, the hydrogen desorption and absorption reactions of MgH_2/Mg suffer from kinetic barriers, which requires operating temperatures in excess of 570 K. Various magnesium alloys have been studied to improve the thermodynamics and kinetics of the hydrogen desorption and absorption reaction.[185–190] Mg_2NiH_4, which can store 3.6 wt.% of hydrogen, has been suggested as a candidate material, primarily because of its reasonably fast hydrogen desorpion and absorption kinetics.[191–197] Several theoretical studies have been dedicated to Mg_2NiH_4.[198–202] However, its measured hydrogen desorption enthalpy of 0.70 eV per H_2 (Ref. 196) is barely lower than that of MgH_2. It leads to an equilibrium hydrogen pressure of 1 bar at 510 K.[197] This temperature is far too high for applications using polymer electrolyte membrane (PEM) PEM fuel cells, for instance. Apart from its possible role in hydrogen storage, Mg_2Ni is also interesting because it can act as switchable mirror.[65–67,218] Mg_2Ni is a metal, whereas Mg_2NiH_4 is a semiconductor with a band gap of 1.7–2.0 eV.[220–222] This leads to a remarkable change in the optical properties of the material upon hydrogenation and dehydrogenation. Especially if Mg_2Ni is applied in thin films, the optical switching can be fast, reversible, and robust.[61] The high optical contrast opens up possibilities for Mg_2Ni as a hydrogen sensing material.[219,223,224]

For both applications the reaction enthalpy of the hydrogen desorption and absorption at typical operating conditions is too high. Preferable would be an equilibrium hydrogen pressure of 1 bar at room temperature. To reach this condition a hydrogen desorption enthalpy of 0.40 eV per H_2 is required. A substantial amount of experimental work has been dedicated to study the effects of doping of Mg_2NiH_4 in order to reduce its hydrogen desorption enthalpy.[61,203–212] In this context "doping" means substituting a fairly large amount of Ni (or Mg) by other metals.

In this paper we report a study on the effects of doping Mg_2NiH_4 with transition metals by first principles density functional theory (DFT) calculations. We restrict ourselves to the low temperature (LT) phase of Mg_2NiH_4, since the high temperature (HT) phase is stable only at elevated temperatures (i.e. $T > 500$ K) and therefore less relevant for applications.[196] We consider substitution of nickel by cobalt, iron, or copper in a concentration of 12.5%, which means substituting one in eight nickel atoms. This concentration is close to that used in recent experiments.[225] Our first aim is to monitor the change in hydrogen desorption enthalpy and, in particular, to establish which dopants (if any) lead to a reduction of the enthalpy. We show that zero point energies (ZPEs) associated with the hydrogen phonon modes considerably influence the enthalpies. Our second objective is to study the change in optical properties that results from doping. In particular we show that dopants in this concentration markedly alter the dielectric function.

Computational methods

First principles DFT calculations are carried out using a plane wave basis set and the projector augmented wave (PAW) method,[14,19] as incorporated in the Vienna *Ab initio* Simulation Package (VASP).[15–17] We use the PW91 generalized gradient approximation (GGA) for the exchange correlation functional.[25] The cell parameters are kept at the experimental values and the atomic positions are relaxed using a conjugate gradient algorithm. Non-linear core corrections are applied.[117]

It has been shown for different classes of hydrides that to obtain accurate reaction enthalpies, ZPE contributions are important.[54,226,227] To calculate ZPEs we need the phonon frequencies of the materials involved. Phonon frequencies are calculated using a direct method,[24] i.e., the dynamical matrix is constructed from the force constants that are obtained from finite differences. Two opposite displacements of 0.05 Å are used for each atomic degree of freedom. In general one needs to carry out such calculations on a supercell containing several primitive unit cells, as the force constants do not go to zero within a distance corresponding to a single unit cell. However, the unit cells of the materials studied in this paper turn out to be sufficiently large, except for bulk magnesium, for which a $2 \times 2 \times 2$ supercell is used. An advantage of large unit cells is that the phonon dispersion is small. It is therefore sufficient to calculate ZPEs from the phonon frequencies obtained at Γ.

The dielectric functions are calculated in the independent particle, random phase approximation taking into account direct transitions from occupied to unoccupied Kohn-Sham orbitals only. We neglect excitonic, local field and quasi-particle effects. The imaginary part of the macroscopic dielectric function then has the form

$$\begin{aligned}\varepsilon^{(2)}(\hat{\mathbf{q}},\omega) &= \frac{8\pi^2 e^2}{V} \lim_{|\mathbf{q}|\to 0} \frac{1}{|\mathbf{q}|^2} \sum_{\mathbf{k},v,c} \\ &\quad \times \left|\langle u_{c,\mathbf{k}+\mathbf{q}} | u_{v,\mathbf{k}} \rangle\right|^2 \delta(\epsilon_{c,\mathbf{k}+\mathbf{q}} - \epsilon_{v,\mathbf{k}} - \hbar\omega),\end{aligned} \tag{12.1}$$

where $\hat{\mathbf{q}}$ gives the direction of $\mathbf{q}$; $v, \mathbf{k}$ and $c, \mathbf{k}$ label single particle states that are occupied, unoccupied in the ground state, respectively; ϵ, u are the single particle energies and the translationally invariant parts of the wave functions, respectively; V is the volume of the unit cell. Further details can be found in Ref. 29.

Almost all experimental optical data on hydrides are obtained from micro- or nanocrystalline samples whose crystallites have a significant spread in orientation. The most relevant quantity then is the directionally averaged dielectric function, i.e., $\varepsilon^{(2)}(\omega)$ averaged over $\hat{\mathbf{q}}$. In this paper we only report directionally averaged dielectric functions.

The Brillouin zone integrations are performed using a modified tetrahedron method.[20] All calculations on the hydrides use a $7\times7\times7$ Monkhorst-Pack **k**-point mesh for sampling the Brillouin zone, and the calculations on the metals use a $7 \times 7 \times 3$ Monkhorst-Pack **k**-point mesh.[21] We use 480 bands to calculate the dielectric function. This number of bands includes all transitions up to 30 eV. For the materials containing copper a plane wave kinetic energy cutoff of 341 eV is used, and for the other materials a cutoff of 337 eV. To obtain accurate formation and reaction enthalpies, the total energies of all final structures are calculated using a plane wave kinetic energy cutoff of 700 eV.

Structure and stability of undoped materials: Mg_2NiH_4, Mg_2CoH_5, Mg_2FeH_6, Mg_2Ni and elemental metals

In order to assess the stability of doped Mg_2NiH_4 we first need the total energies of the undoped hydrides and of all elemental metals involved. The optimized structures of Mg_2NiH_4, Mg_2CoH_5, Mg_2FeH_6 are given in Table 12.1. They are in good agreement with the experimental structures.[228–230] The metal atoms in LT Mg_2NiH_4 form a distorted CaF_2-type structure. Four hydrogen atoms are arranged around each nickel atom in a tetrahedron. In Mg_2FeH_6 and Mg_2CoH_5 the Mg and Fe/Co atoms form an undistorted CaF_2-type structure. In Mg_2FeH_6 the hydrogen atoms form regular octahedra around the iron atoms. In Mg_2CoH_5 the hydrogen atoms occupy five corners of a slightly distorted octahedron around each cobalt atom.

The experimental structure of Mg_2Ni can be found in Ref. 194. The unit cell contains 12 Mg and 6 Ni atoms, which are basically hexagonally closed-packed. The optimized structure given in Table 12.1 is in good agreement with experiment. For MgH_2 we use a previously calculated structure.[54] For the elemental metals and $MgCu_2$ we use the experimental lattice parameters, i.e., $a(c) = 3.21(5.21)$ Å, $a = 2.87$ Å, $a(c) = 2.51(4.07)$ Å, $a = 3.52$ Å $a = 3.61$ Å and $a = 7.03$ Å for Mg, Fe, Co, Ni, Cu, and $MgCu_2$, respectively.[26] The magnetic elements iron, cobalt and nickel are treated by spin-polarized calculations. The calculated pressures are small, indicating that it is unnecessary to explicitly optimize the lattice parameters. We explicitly tested the latter for iron, since there the external pressure was largest, and obtained an energy gain of less than 0.01 eV.

In order to obtain accurate enthalpies for reactions involving materials that contain hydrogen, one has to take ZPEs into account. All calculated total energies and ZPEs

Table 12.1: *Calculated atomic positions of* Mg_2NiH_4 *(experiment, Ref. 228),* Mg_2CoH_5 *(experiment, Ref. 229),* Mg_2FeH_6 *(experiment, Ref. 230) and* Mg_2Ni *(experiment, Ref. 194). In the calculations the lattice parameters were kept at the experimental values.*

Compound	Space group unit cell			x	y	z
Mg_2NiH_4	C2/c (15)	Mg	$8f$	0.2646	0.4863	0.0833
	$\beta = 113.52°$	Mg	$4e$	0	0.0252	0.2500
	a = 14.343 Å	Mg	$4e$	0	0.5264	0.2500
	b = 6.4038 Å	Ni	$8f$	0.1199	0.2294	0.0801
	c = 6.4830 Å	H	$8f$	0.2088	0.3048	0.3041
		H	$8f$	0.1390	0.3192	0.8760
		H	$8f$	0.0096	0.2908	0.0527
		H	$8f$	0.1243	0.9866	0.0727
Mg_2CoH_5	P4/nmm (129)	Mg	$2a$	3/4	1/4	0
	a = 4.463 Å	Mg	$2b$	3/4	1/4	1/2
	c = 6.593 Å	Co	$2c$	1/4	1/4	0.2567
		H	$2c$	1/4	1/4	0.4947
		H	$8j$	0.4914	0.4914	0.2268
Mg_2FeH_6	Fm3m (225)	Mg	$8c$	1/4	1/4	1/4
	a = 6.437 Å	Fe	$4a$	0	0	0
		H	$24e$	0.2425	0	0
Mg_2Ni	$P6_222$ (180)	Mg	$6i$	0.1639	0.3278	0
	$\gamma = 120°$	Mg	$6f$	1/2	0	0.1165
	a = 5.205 Å	Ni	$3b$	0	0	1/2
	c = 13.236 Å	Ni	$3d$	1/2	0	1/2

Table 12.2: *Calculated total energies, E^{TOT}, and ZPEs, E^{TOT}, of the undoped hydrides and metals per formula unit.*

	E^{TOT} (eV)	E^{ZPE} (eV)		E^{TOT} (eV)	E^{ZPE} (eV)
H_2	−6.803	0.266	MgH_2	−8.983	
Mg	−1.524	0.030	Mg_2Ni	−9.133	0.102
Fe	−8.150		Mg_2FeH_6	−34.511	
Co	−6.841		Mg_2CoH_5	−29.355	
Ni	−5.459		Mg_2NiH_4	−24.053	0.852
Cu	−3.725		$MgCu_2$	−9.45	

are given in Table 12.2. We neglect the ZPEs of the elemental metals. The ZPE for magnesium is only 0.03 eV/atom. The ZPEs of iron, cobalt, nickel, and copper will be even smaller, since the atomic weight of those elements is more than twice that of Mg.

ZPE corrections are significant in reactions where hydrogen molecules are adsorbed or desorbed. They arise mainly from the difference between the number and frequencies of the vibrational modes of the hydrogen atoms in a solid host and those of the hydrogen molecules. If the bonding of hydrogen atoms does not change much in a reaction, the ZPE correction is small. One can expect this to be the case for the possible phase segregation reaction of doped Mg_2NiH_4, see Equation 12.5, where we neglect the ZPE correction. We checked this assumption explicitly for Fe-doped Mg_2NiH_4 and found the ZPE correction to be 1 meV/H_2.

To calculate hydrogen desorption enthalpies we also need the total energy of the hydrogen molecule. It is calculated using a cubic cell with sides of 13 Å. We find an equilibrium distance of 0.7486 Å, a vibrational frequency of 4350 cm^{-1}, and a dissociation energy of 4.57 eV, which compare reasonably well with the experimental values of 0.7461 Å, 4401 cm^{-1} and 4.48 eV, respectively.[26,27] The 0.1 eV deviation in the dissociation energy of H_2 is relatively large in view of the accuracy required for calculating hydrogen desorption enthalpies. This 0.1 eV may be considered as a correction to the reaction enthalpies discussed below.

We calculate the ZPE for the hydrogen molecule from the energy levels of a Morse potential,

$$E(n) = \hbar\omega\left(n + \frac{1}{2}\right) - \frac{1}{4D_e}\left[\hbar\omega\left(n + \frac{1}{2}\right)\right]^2, \tag{12.2}$$

where ω is the vibration frequency and D_e is the dissociation energy. The result is given in Table 12.2.

Doped Mg_2NiH_4 and Mg_2Ni

Structure

The unit cell of the LT phase of Mg_2NiH_4 contains eight formula units. To simulate doping we replace one of the Ni atoms by a Fe, Co, or Cu atom, thus achieving a 7:1 ratio between Ni and dopant atoms. In simple terms one can think of undoped Mg_2NiH_4 as being constructed from Mg^{2+} and $(NiH_4)^{4-}$ ions. The latter involve 18 valence electrons and are closed shell ions. Upon doping it is likely that in the fully hydrogenated phase the closed shell character is maintained. This means that $(NiH_4)^{4-}$ is replaced by $(FeH_6)^{4-}$, $(CoH_5)^{4-}$, or $(CuH_3)^{4-}$. Thus for a Fe atom we add two extra hydrogen atoms, one for a Co atom and for a Cu atom we remove one hydrogen atom. For all doped systems we fix the unit cell to that of undoped Mg_2NiH_4 and we optimize the atomic positions. The external pressures on the doped systems are small, which indicates that the gain in energy when relaxing the cell volumes will not be significant. From Vegard's law one can estimate the volume relaxation caused by the Fe and Co dopants, using the volumes of Mg_2NiH_4, Mg_2CoH_5 and Mg_2FeH_6. The expected volume relaxation is less than 0.5%. Its effect on the hydrogen desorption enthalpy is less than 1 meV/H_2.

The geometry of the hydrogens around the Fe and Co dopant atoms resembles the geometry in Mg_2FeH_6 and Mg_2CoH_5 respectively. In Mg_2FeH_6 each Fe atom is in the center of a perfect octahedron of hydrogen atoms with a Fe–H distance of 1.56 Å. In Fe doped Mg_2NiH_4 the octahedron is distorted. The H–Fe–H angles range from 80 to 100° and the Fe–H distances range from 1.55 to 1.58 Å in the case where a H atom is only bonded to a Fe atom. However, four of the hydrogen atoms surrounding a Fe atom also bond to Ni atoms, in which case the Fe–H distance is enlarged to 1.64–1.76 Å. The hydrogen tetrahedra around such Ni atoms are distorted with Ni–H distances ranging from 1.51 to 1.80 Å, whereas in undoped Mg_2NiH_4 they are between 1.56 and 1.58 Å.

In the case of Co doping the distortions are much smaller. In Mg_2CoH_5 the hydrogen atoms surrounding each Co atom form a four-sided pyramid with the Co atom just above the basal plane of the pyramid. To describe the geometry we denote the basal plane hydrogens by H_b and the top hydrogen by H_t. The H_b–Co–H_b angle is 89°, the Co–H_b distance is 1.52 Å, the H_b–Co–H_t angle is 97.6° and the Co–H_t distance is 1.59 Å. The Co-Mg distances range from 2.75 to 2.80 Å. The hydrogens surrounding the Co atom in doped Mg_2NiH_4 form a slightly distorted pyramid, with H_b–Co–H_b angles ranging from 83.1° to 94.1° and Co–H_b distances ranging from 1.53 to 1.56Å. The H_b–Co–H_t angle is 93.4° to 105.1° and the Co–H_t distance is 1.57Å. The Co–Mg distances vary from 2.69–2.80 Å. The Ni–H bond lengths are not affected by Co doping.

We cannot compare the geometry of the hydrogens in Cu doped Mg_2NiH_4 to Mg_2CuH_3, since the latter compound is not stable with respect to decomposition into MgH_2 and $MgCu_2$.[203] The Ni–H distances in Cu doped Mg_2NiH_4 are similar to those in undoped Mg_2NiH_4. The hydrogen atoms surrounding the Cu atom are located at three corners of a tetrahedron with the Cu atom in the center. The Cu–H distances, 1.62 to 1.64 Å, are slightly larger than the Ni–H distances, 1.56 to 1.59 Å.

Reaction enthalpies

In order to calculate the hydrogen desorption enthalpy of doped Mg_2NiH_4 we also need the total energy of doped Mg_2Ni. The unit cell of Mg_2Ni contains six formula units per cell. If we replace one of the Ni atoms in this cell by a dopant atom, this gives a 5:1 Ni:dopant ratio, instead of the required 7:1 ratio. We approximate the total energy of the 7:1 ratio by the average energy of three 5:1 doped unit cells and one undoped cell. All calculated total energies and ZPEs of the doped hydrides and metals are given in Table 12.3.

From the data in Table 12.3 we calculate the desorption enthalpy per H_2 molecule,

$$\begin{aligned} E_{\text{des}} &= E(\mathrm{H_2}) + \frac{2}{x}\Big[E(\mathrm{Mg_2Ni_{\frac{7}{8}}TM_{\frac{1}{8}}}) \\ &\quad -E(\mathrm{Mg_2Ni_{\frac{7}{8}}TM_{\frac{1}{8}}H_{\mathit{x}}})\Big], \end{aligned} \tag{12.3}$$

where $E(\mathrm{M})$ is the total energy of compound M and x is the number of hydrogen atoms in the hydride. The latter depends upon the dopant atom, as discussed in the previous section. The values of x are given in Table 12.3.

The calculated desorption enthalpy of undoped Mg_2NiH_4 is 0.66 eV/H_2 without ZPE and 0.55 eV/H_2 with ZPE. The corresponding experimental value is 0.70 eV/H_2.[196] We find that the ZPE corrected desorption enthalpies are consistently lower than the experimental values by 0.1-0.2 eV/H_2.[54,166] However, the relative error in similar compounds, such as the MgTM hydrides studied here, is less than $\sim$ 0.05 eV/H_2. One source of error could be the overestimation of the H_2 dissociation energy by 0.1 eV, mentioned in Section 12. If we assume that the desorption enthalpies can be corrected (i.e. increased) by this amount, it brings them within $\sim$ 0.1 eV/H_2 of the experimental values. In the following we give the uncorrected results only. Note however that this correction opposes the ZPE correction. It has been observed before that calculated desorption enthalpies without ZPE corrections can be closer to experimental values.[33,166]

The results for E_{des} of doped Mg_2NiH_4 are given in Figure 12.1. These results clearly demonstrate that the desorption enthalpy can be tuned by an appropriate doping. The desorption enthalpy decreases considerably both for Fe and for Cu doping, i.e. by 84 and 71 meV per H_2, respectively. However, Co doping increases the desorption enthalpy

Table 12.3: *Calculated total energies, E^{TOT}, ZPEs, E^{ZPE}, and hydrogen content, x, of the doped hydrides, $Mg_2Ni_{7/8}TM_{1/8}H_x$, and the metals, $Mg_2Ni_{7/8}TM_{1/8}$. The values are per formula unit.*

TM	E^{TOT} (eV)	E^{ZPE} (eV)	x (no. H)
Fe	−24.952	0.914	4.250
Co	−24.677	0.876	4.125
Ni	−24.053	0.852	4.000
Cu	−23.207	0.826	3.875
Fe	−9.278	0.100	
Co	−9.233	0.100	
Ni	−9.133	0.102	
Cu	−8.890	0.102	

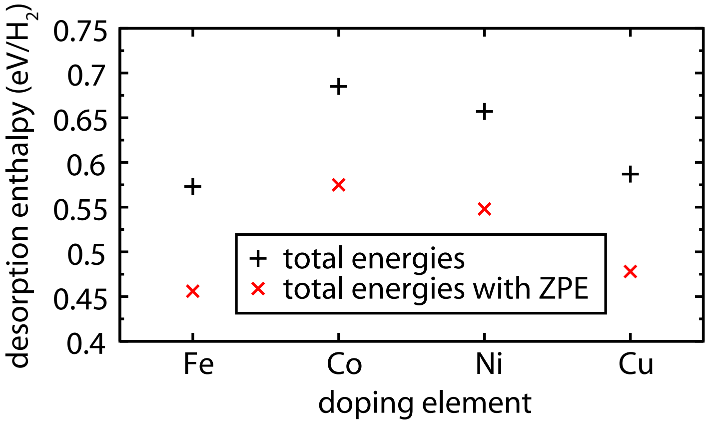

Figure 12.1: *Desorption enthalpies E_{des} (eV/H_2) of the doped hydrides.*

by 28 meV per H_2. The trends for Cu and Fe doping are in qualitative agreement with experimental data.[203, 209, 212]

Figure 12.1 also shows the calculated desorption enthalpies corrected with ZPEs. The ZPEs of all the metals are almost identical, see Table 12.3, and the ZPEs of the hydrides scale linearly with the amount of hydrogen atoms. This means that the ZPE per hydrogen atom is almost constant and independent of the dopant atom. Therefore, the ZPE correction to the desorption enthalpy per H_2 is 0.1 eV for all compounds studied.

Stability

Doped Mg_2NiH_4 is stable in thin films.[225] In order to assess whether kinetics plays an important role in stabilizing these compounds, we study the thermodynamic stability of the doped materials with respect to phase segregation. For the dehydrogenated doped Mg_2Ni metal we consider decomposition into Mg_2Ni, bulk magnesium and bulk doping metal,

$$\mathrm{Mg_2Ni_{\frac{7}{8}}TM_{\frac{1}{8}}} \rightarrow \frac{7}{8}\mathrm{Mg_2Ni} + \frac{1}{8}\mathrm{TM} + \frac{2}{8}\mathrm{Mg}, \tag{12.4}$$

where TM = Fe, Co, or Cu. Fully hydrogenated undoped $Mg_2NiH_4$is compared to bulk nickel and MgH_2. For the hydrogenated doped Mg_2NiH_4 we consider decomposition into phase segregated Mg_2NiH_4 and Mg_2FeH_6 or Mg_2CoH_5,

$$\mathrm{Mg_2Ni_{\frac{7}{8}}TM_{\frac{1}{8}}H}_x \rightarrow \frac{7}{8}\mathrm{Mg_2NiH_4} + \frac{1}{8}\mathrm{Mg_2TMH}_y, \tag{12.5}$$

with x as in Table 12.3, and $y = 5, 6$ for Co, Fe, respectively. Since Mg_2CuH_3 is unstable with respect to decomposition into MgH_2 and $MgCu_2$, we consider for the hydrogenated Cu doped Mg_2NiH_4 the possible decomposition reaction

$$\mathrm{Mg_2Ni_{\frac{7}{8}}Cu_{\frac{1}{8}}H}_x \rightarrow \frac{7}{8}\mathrm{Mg_2NiH_4} + \frac{1}{16}\mathrm{MgCu_2} + \frac{3}{16}\mathrm{MgH_2}. \tag{12.6}$$

The results are shown in Figure 12.2.

Fe doped Mg_2Ni is thermodynamically unstable with respect to phase segregation into Mg_2Ni bulk Mg and bulk Fe. Co doped Mg_2Ni is a marginally unstable material in which segregation is favored by only ~ 0.01 eV per formula unit. Fe, Co doped Mg_2NiH_4 are thermodynamically unstable with respect to segregation into Mg_2NiH_4 and Mg_2FeH_6, Mg_2CoH_5, respectively. Doping of Mg_2Ni with Cu leads to a stable material. Experimental work proved the stability of $Mg_2Ni_{1-x}Cu_x$ solid solutions;[203,211] for $0 < x < 0.85$ these compounds are iso-structural with Mg_2Ni. Experiment indicates that the hydrogenated phase decomposes into MgH_2, $MgCu_2$ and Mg_2NiH_4.[203] This is confirmed by our calculations, see Figure 12.2.

In conclusion, many of the doped phases are thermodynamically unstable. This does not need to hamper their usefulness, however, since kinetics plays an important role in stabilizing the doped compounds. The hydrogen desorption temperature lies far below the temperatures that is used to anneal these materials.[225] The Cu doped Mg_2Ni metal is thermodynamically stable, and hydrogenating this material can lead to a useful metastable compound.

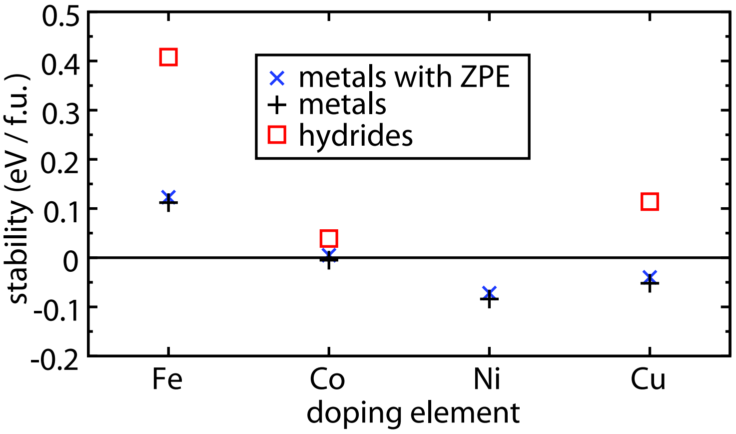

Figure 12.2: *Stability with respect to phase segregation (eV/f.u.). Values are negative if the compound is stable, see Equations 12.4-12.6*

.

Optical properties

The imaginary part of the dielectric function and the electronic density of states (DOS) of undoped Mg_2NiH_4 are shown in Figures 12.3 and 12.4, respectively. They are in good agreement with the results of previous calculations.[201,202] We find an indirect band gap of 1.6 eV and an direct gap of 1.7 eV. This is in good agreement with the experimental direct gap of 1.7–2.0 eV.[220–222] The agreement is in fact remarkable since DFT usually underestimates the band gap by 30-50%. For Mg_2FeH_6 and Mg_2CoH_5 we obtain direct gaps of 1.8 and 1.3 eV, respectively. The latter is in good agreement with the experimental gap of 1.5 eV.[231] Shifts in band gaps upon doping can therefore be calculated reliably. The agreement between the calculated DFT gaps and the experimental optical gaps for these MgTM hydrides might be somewhat fortuitous. However, it means that we can refrain from calculating the quasi-particle spectrum, which is often needed to obtain the correct band gaps in hydrides.[43,44,174]

The dielectric function of Mg_2NiH_4 has two peaks, which can be directly related to the two peaks in the DOS of the valence bands. The dielectric functions of doped Mg_2NiH_4 are also shown in Figure 12.3. Doping alters the dielectric function and, remarkably, the size of the change correlates with the change in hydrogen desorption enthalpy caused by the dopants, see Figure 12.1. This can be explained by noticing that both changes have a common cause. The changes in desorption enthalpy are due to changes in metal–hydrogen bond lengths and bond energies. Changes in bond energies shift the energy levels and hence can be detected in the optical spectrum. Such changes are largest in Fe doped Mg_2NiH_4. An Fe dopant atom includes two extra hydrogen atoms. It gives the largest perturbation in the Mg_2NiH_4 lattice, with almost half of the metal–hydrogen bond lengths

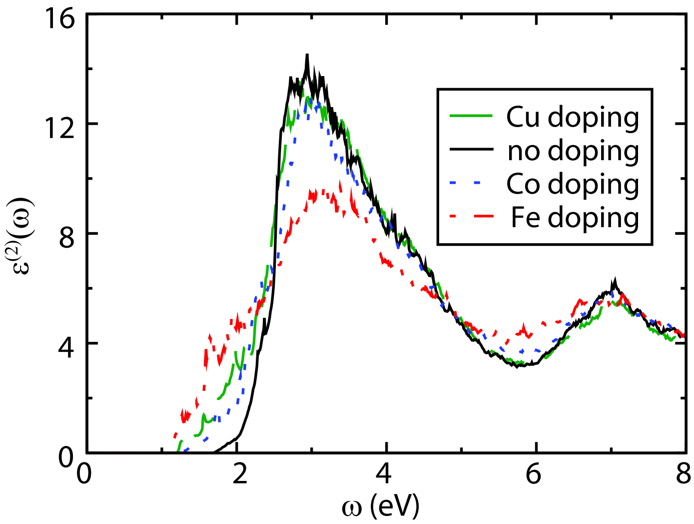

Figure 12.3: *Imaginary part of the frequency dependent dielectric functions of doped* Mg_2NiH_4.

being changed with respect to the undoped case.

The DOS of doped Mg_2NiH_4 is given in Figure 12.4. To facilitate an internal comparison the DOS of all compounds is aligned at the bottom of the valence band. Besides the fundamental gap between the valence and conduction bands, we can identify a clear gap in the valence bands, between 2.4 and 3.6 eV below the Fermi level in undoped Mg_2NiH_4. The states above this valence gap have a strong metal *d* character, whereas the lower valence states have a dominant hydrogen character. Cu and Fe doping introduces states in the valence gap, whereas all dopants introduce states in the fundamental gap. In the case of Cu doping these appear near the top of the valence band, whereas for Co and Fe doping gap states appear near the bottom of the conduction band. Since we have adjusted the amount of hydrogen upon doping, all doped materials are semiconducting.

The DOS can be used to interpret the dielectric functions. The decrease in the fundamental gap in the DOS upon doping gives a decrease in the direct gaps. The largest changes in the dielectric function are observed upon Fe doping. The highest peak decreases as compared to the undoped case and the valley between the two peaks is less deep. In addition, a distinct shoulder appears at low energy. Fe doping gives a clear peak in the DOS at the bottom of the conduction band, which yields the distinct shoulder in the dielectric function. The two main peaks in the dielectric functions are not shifted upon doping. This indicates that the dopants mainly give rise to additional features via the introduction of gap states, as can be observed in the DOS. Similar conclusions hold for the Cu and Co doped cases, but the perturbation of the Mg_2NiH_4 DOS caused by doping is smaller than for the Fe doped case.

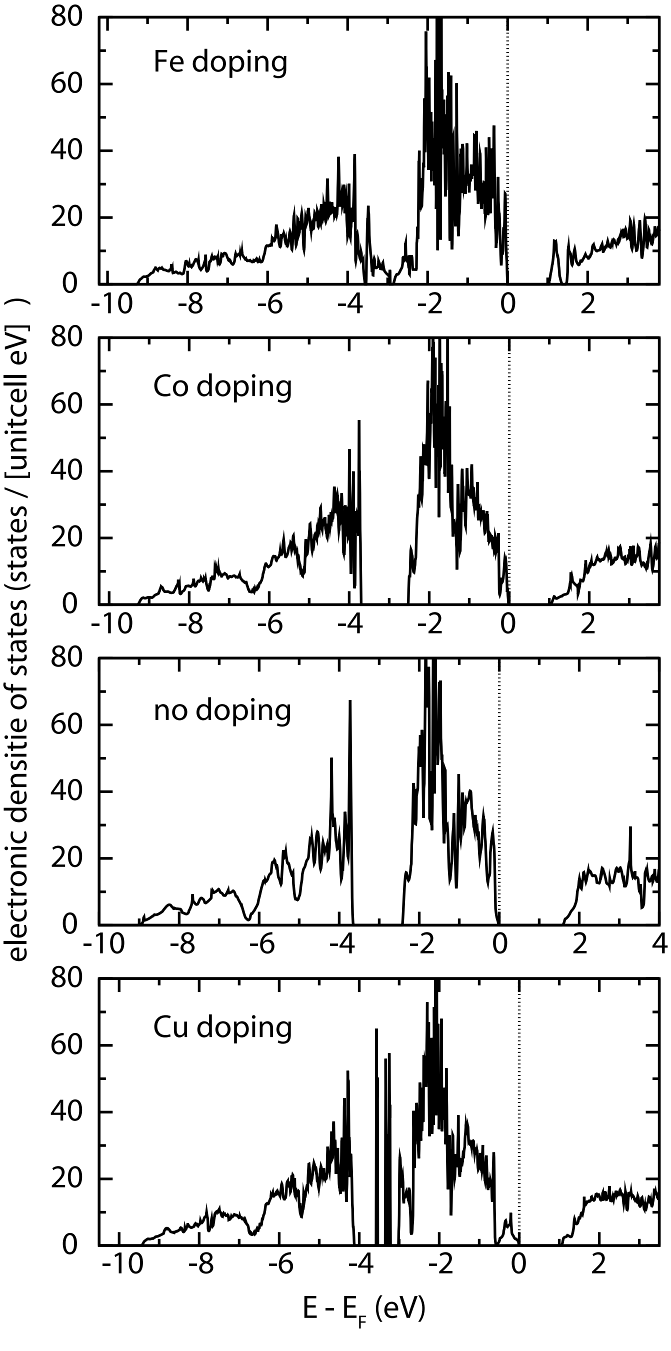

Figure 12.4: *Electronic densities of state of doped Mg_2NiH_4. The Fermi level is at the top of the valence bands. The four DOSs are aligned at the bottom of the valence band.*

Conclusions

Mg_2NiH_4 is a promising hydrogen storage material with fast (de)hydrogenation kinetics. Its hydrogen desorption enthalpy, however, is too large for practical applications. In this paper we study the effects of transition metal doping by first-principles density functional theory calculations. We show that the hydrogen desorption enthalpy can be reduced by 0.1 eV/H_2 if one in eight Ni atoms is replaced by Cu or Fe. Replacing Ni by Co atoms, however, increases the hydrogen desorption enthalpy. We study the thermodynamic stability of the dopants in the hydrogenated and dehydrogenated phases. All hydrides turn out to be unstable with respect to phase segregation. Doping with Co or Cu leads to marginally stable metals, whereas doping with Fe leads to an unstable metal. The optical response of Mg_2NiH_4 is also substantially affected by doping. The direct gap in Mg_2NiH_4 is $\sim$ 1.7 eV. Doping with Co, Fe, or Cu leads to impurity bands that reduce the direct gap by up to 0.5 eV.

We study the effects of transition metal doping on the hydrogen desorption enthalpy and the optical properties of Mg_2NiH_4 by first-principles DFT calculations. The desorption enthalpy is reduced by 84 meV per H_2, if one in eight Ni atoms is replaced by an Fe atom. Replacing one in eight Ni atoms by a Cu atom reduces the desorption enthalpy by 71 meV/H_2, but replacement by a Co atom increases it by 28 meV/H_2. Including energy corrections due to the zero point motions of the atoms changes the absolute values of the desorption energies by 0.1 eV/H_2. Since, however, the zero point energies per hydrogen atom are almost independent of the compound studied, the relative values of the desorption energies are not affected.

The thermodynamic stabilities of the doped dehydrogenated Mg_2Ni and the fully hydrogenated Mg_2NiH_4 compounds are studied by considering possible decomposition reactions. The results show that Cu doped Mg_2Ni is stable, Co doped Mg_2Ni is marginally stable, and Fe doped Mg_2Ni is unstable with respect to phase separation into Mg_2Ni, bulk Mg and the bulk transition metal dopant. The doped hydrogenated Mg_2NiH_4 compounds are either marginally unstable in the case of Co or Cu doping, or, in the case of Fe doping, clearly unstable. Kinetic barriers could be be sufficiently high to stabilize metastable doped compounds since the hydrogen desorption temperatures are smaller than the temperatures used to anneal these materials. Nevertheless, thermodynamics indicates that Cu is the most promising candidate to lower the hydrogen desorption enthalpy of Mg_2NiH_4.

By calculating the dielectric function within the random phase approximation we study the effects of doping on the optical properties of Mg_2NiH_4. The changes in the dielectric function can be interpreted in terms of the electronic densities of states of the corresponding compounds. The dopant atoms introduce states in the fundamental gap, as well as below the valence Ni *d*-band. These states cause a shift in the onset of absorption to lower energy by up to 0.5 eV and they decrease the relative heights of the peaks in the Mg_2NiH_4 absorption spectrum. The sizes of these changes correlate with the change in the hydrogen desorption enthalpy caused by the dopants. Fe doping causes the largest disruption in the Mg_2NiH_4 lattice, and the largest change in the optical properties.

Acknowledgements

The authors wish to thank R. A. de Groot (FOM) and R. Griessen (Vrije Universiteit Amsterdam) for helpful discussions and G. Kresse (University of Vienna) for use of the optical package. This work is part of the research programs of ‘Advanced Chemical Technologies for Sustainability (ACTS)’ and the ‘Stichting voor Fundamenteel Onderzoek der Materie (FOM)’, both financially supported by ‘Nederlandse Organisatie voor Wetenschappelijk Onderzoek (NWO)’.

Chapter 13

Optical properties of $Mg_xTi_{(1-x)}H_2$

Abstract

The optical and electronic properties of Mg-Ti hydrides are studied using first-principles density functional theory. Dielectric functions are calculated for $Mg_xTi_{(1-x)}H_2$ with compositions $x = 0.5$, 0.75, and 0.875. The structure is that of fluorite TiH_2 where both Mg and Ti atoms reside at the Ti positions of the lattice. In order to assess the effect of randomness in the Mg and Ti occupations we consider both highly ordered structures, modeled with simple unit cells of minimal size, and models of random alloys. These are simulated by super cells containing up to 64 formula units ($Z = 64$). All compositions and structural models turn out metallic, hence the dielectric functions contain interband and intraband free electron contributions. The former are calculated in the independent particle random phase approximation. The latter are modeled based upon the intraband plasma frequencies, which are also calculated from first-principles. Only for the models of the random alloys we obtain a black state, i.e. low reflection and transmission in the energy range from 1 to 6 eV.

Introduction

Since the discovery of the switchable mirror YH_x by Huiberts *et al.*[62] in 1996 several other metal hydride systems that behave as switchable mirrors have been discovered.[62,65,66,215,217,218] The metals are reflective, but after hydrogenation become semiconductors and hence in most cases become transparent. Especially when an alloy with high hydrogen mobility is used and when applied as thin films the optical switching can be fast, reversible and robust.[61]

Recently, meta-stable thin films composed of various ratios of magnesium and titanium have been shown to exhibit remarkable optical properties which could be especially useful for smart solar cell coatings and hydrogen sensor applications.[215,232] In the dehydrogenated state the films are highly reflective. Upon hydrogenation they become black, i.e. have a low reflection and high absorption in the energy range of the solar spectrum. The structural and electronic characteristics of this black state are a topic of intensive research.[216,233]

Obtaining structural data for these systems is difficult. Single crystals cannot be grown easily and the films can not be annealed to increase the crystallinity because the mixed films are meta stable. For a 7:1 ratio of magnesium to titanium Kyoi *et al.*, using a sample prepared at high pressure, could determine the crystal structure.[234] It is similar to the fluorite TiH_2 structure. Notten and co-workers (Refs. 213,214) and Borsa *et al.*[215,216] have shown that for higher titanium content ($x < 0.8$) the structure is fluorite-like as well. At lower lower titanium concentrations a rutile (α-MgH_2 like) structure is found. Interestingly, the kinetics of the hydrogen ab/desorption reactions are much faster in the fluorite structures than in the rutile structures.[235] The equality of the molar volume of TiH_2 and Mg has been used to explain the structural stability of the meta-stable "phases".[216] Calculations using density functional theory (DFT) find the same composition dependence of the relative stability of the rutile and fluorite structures.[233]

The origin of the "black state" is not understood. Its explanation is, of course, intimately related to the electronic structure of the hydride. In experiments, usually less than two hydrogen atoms per metal atom can be reversibly absorbed and desorbed.[216] Electrochemically 1.7 hydrogen atoms per metal atom can be stored reversibly.[235] Moreover, the crystal structure of Mg_7TiH_x as determined by Kyoi *et al.*[234] is estimated to contain 1.6 hydrogen atoms per metal atom. All this suggests that maximally two metal electrons per metal atom can be transferred to hydrogen.[216] Hence the Ti atoms remain in an open-shell configuration with at least two d-electrons left. The above reasoning has been confirmed by DFT calculations on crystalline $Mg_xTi_{(1-x)}H_2$ structures.[233] The calculated densities of states show predominant hydrogen-s character below the Fermi level, which is typical for metal hydrides, and titanium-d states at the Fermi level. These are likely to form metallic bands, so one expects $Mg_xTi_{1-x}H_2$ to be reflective instead of black. Moreover, experimental investigation of the electrical transport properties reveal high resistivity 1.32–1.9 mΩcm, with a logarithmic, hence non-metallic, temperature dependence.[216] In order to explain these results the formation of a so-called coherent crystal structure was proposed,[216] wherein regions of insulating MgH_2 and metallic TiH_2 coexist.

In an effort to advance the understanding of the black state, in this paper we report a computational study of the optical and electronic properties of $Mg_xTi_{(1-x)}H_2$ for $x = 0.5$, 0.75 and 0.875. We employ both simple (i.e. minimal) unit cells and large super cells of the same compositions. The latter model random alloys wherein the Mg and Ti are distributed over the lattice sites of a TiH_2-like structure. Details of these models are presented in Ref. 233.

The dielectric functions consist of intra and interband contributions:

$$\varepsilon(\omega) = \varepsilon_{\text{inter}}(\omega) + \varepsilon_{\text{intra}}(\omega) \quad . \tag{13.1}$$

These are calculated separately. For the interband contribution $\varepsilon_{\text{inter}}$ we use first-principles DFT in the independent particle random phase approximation. Since the materials in question are metals, the intraband dielectric part $\varepsilon_{\text{intra}}$ does not vanish. It is modeled from the plasma frequencies ω_{p}, which are calculated from first-principles as well.

In Section 13 the technical details of the calculations are summarized. Section 13 contains a concise description of the structural models used. Results on the dielectric functions are presented in Section 13. Finally, in the discussion section (Section 13) results are compared with experiment.[216]

Computational methods

First-principles DFT calculations were carried out with the Vienna *Ab initio* Simulation Package (VASP),[15–17] using the projector augmented wave (PAW) method.[14,19] A plane wave basis set was used and periodic boundary conditions applied. The kinetic energy cutoff on the Kohn-Sham states was 312.5 eV. For the exchange-correlation functional we used the generalized gradient approximation (GGA).[25] Non-linear core corrections were applied.[117]

The Brillouin zone integrations were performed using a Gaussian smearing method with a width of 0.1 eV..[20] The **k**-point meshes were even grids containing Γ so that the band extrema are typically included in the calculation of the dielectric functions. In order to obtain converged dielectric functions and intraband plasma frequencies a typical mesh spacing of about 0.01 Å^{-1} was needed in the Brillouin zone integrations.

The calculations of the complex interband dielectric functions, $\varepsilon_{\text{inter}}(\omega) = \varepsilon^{(1)}_{\text{inter}}(\omega) + i\varepsilon^{(2)}_{\text{inter}}(\omega)$, were performed in the random phase independent particle approximation, i.e.

taking into account only direct transitions from occupied to unoccupied Kohn-Sham orbitals. Local field effects were neglected. The imaginary part of the macroscopic dielectric function, $\varepsilon^{(2)}_{\text{intra}}(\omega)$, than has the form:

$$\begin{aligned}\varepsilon^{(2)}_{\text{inter}}(\hat{\mathbf{q}},\omega) &= \frac{8\pi^2 e^2}{V}\lim_{|\mathbf{q}|\to 0}\frac{1}{|\mathbf{q}|^2}\times \\ &\sum_{\mathbf{k},v,c}|\langle u_{c,\mathbf{k}+\mathbf{q}}|u_{v,\mathbf{k}}\rangle|^2\,\delta(\epsilon_{c,\mathbf{k}+\mathbf{q}}-\epsilon_{v,\mathbf{k}}-\hbar\omega)\end{aligned} \tag{13.2}$$

where $\hat{\mathbf{q}}$ denotes the direction of $\mathbf{q}$ and $v, \mathbf{k}+\mathbf{q}$ and $c, \mathbf{k}$ label single particle states that are occupied and unoccupied in the ground state, respectively. ϵ, u are the single particle energies and the translationally invariant parts of the wave functions. V is the volume of the unit cell. The real part, $\varepsilon^{(1)}_{\text{inter}}(\omega)$, is obtained via a Kramers-Kronig transform. Further details can be found in Ref. 29.

Most optical data on hydrides are obtained from micro- and nano-crystalline samples whose crystallites have a significant spread in orientation. Therefore the most relevant quantity is the directionally averaged dielectric function, i.e. $\varepsilon^{(2)}_{\text{inter}}(\omega)$ averaged over $\hat{\mathbf{q}}$.

The intraband dielectric function, $\varepsilon_{\text{intra}}(\omega) = \varepsilon^{(1)}_{\text{intra}}(\omega) + i\varepsilon^{(2)}_{\text{intra}}(\omega)$, is calculated from the free electron plasma frequency ω_{p}:

$$\varepsilon^{(1)}_{\text{intra}}(\omega) = 1 - \frac{\omega_{\text{p}}^2}{\omega^2+\gamma^2} \tag{13.3}$$

$$\varepsilon^{(2)}_{\text{intra}}(\omega) = \frac{\gamma\omega_{\text{p}}^2}{\omega^3+\omega\gamma^2} \tag{13.4}$$

where an inverse lifetime, $\gamma = 0.01$ eV, is used. For $\gamma = 0$ the reflection would be perfect up to the plasma frequency and zero beyond. Finite values of γ decrease the reflection below ω_{p} and smoothen the reflection edge at ω_{p}. For metals γ values are in the order of 0.1 eV. By using a small value the influence of the interband part is emphasized. Calculating γ from first principles obviously goes beyond DFT. For three values of γ the free electron $\varepsilon_{\text{intra}}$ is plotted in Figure 13.1.

The plasma frequency ω_{p} is calculated as an integral over the Fermi surface according to:

$$\omega^2_{\text{p}(\alpha\beta)} = \frac{4\pi e^2}{V\hbar^2}\sum_{n,\mathbf{k}} 2g_{\mathbf{k}}\frac{\partial f(\epsilon_{n\mathbf{k}})}{\partial\epsilon}\left(\mathbf{e}_\alpha\frac{\partial\epsilon_{n\mathbf{k}}}{\partial\mathbf{k}}\right)\left(\mathbf{e}_\beta\frac{\partial\epsilon_{n\mathbf{k}}}{\partial\mathbf{k}}\right) \tag{13.5}$$

with $g_{\mathbf{k}}$ the weight factors, and $f(\epsilon_{n\mathbf{k}})$ the occupation function. Again we use directionally averaged values. Further details on the calculation of the plasma frequency can be found in Ref. 30.

Finally the optical constants, the refraction index, n, and the extinction coefficient, κ, and the absorption, A, reflection, R, and transmission, T, are calculated using the

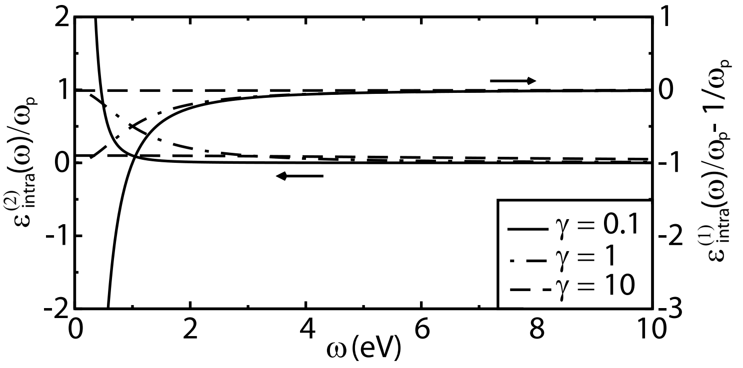

Figure 13.1: *Dielectric functions of a free electron gas according to Equation 13.3.*

standard expressions:

$$n = \frac{1}{\sqrt{2}}\sqrt{\varepsilon^{(1)} + \sqrt{\left(\varepsilon^{(1)}\right)^2 + \left(\varepsilon^{(2)}\right)^2}} \tag{13.6}$$

$$\kappa = \frac{1}{\sqrt{2}}\sqrt{-\varepsilon^{(1)} + \sqrt{\left(\varepsilon^{(1)}\right)^2 + \left(\varepsilon^{(2)}\right)^2}} \tag{13.7}$$

$$A = 1 - \exp(-\kappa\omega d/c) \tag{13.8}$$

$$R = \frac{(n-1)^2 + \kappa^2}{(n+1)^2 + \kappa^2} \tag{13.9}$$

$$T = (1-R)(1-A), \tag{13.10}$$

with $\varepsilon^{(1)}$ and $\varepsilon^{(2)}$ the real and imaginary part of ε, d the slab thickness and c the speed of light in vacuum. The reflection and transmission spectra are constructed to simulate the substrate/$Mg_xTi_{(1-x)}H_2$/palladium setup as was used in the experiments by Borsa *et al.*[215,216] All internal reflections and absorptions in the three layer system are taken into account.

Structures

The calculation of the dielectric functions is performed using the crystal structures developed in Ref. 233. A brief summary of compositions and cell parameters is given in Table 13.1. In short they were constructed in the following way.

In the case of $x = 0.875$ the simple cell is just the optimized experimental cell with composition $Mg_{28}Ti_4H_{64}$. For $x = 0.5$ and 0.75, two and three atoms, respectively, out of the four titanium atoms in the conventional fcc TiH_2 cell were replaced by magnesium. Thus the unit cells have compositions $Mg_2Ti_2H_8$ and Mg_3TiH_8 respectively.

To simulate the random alloys super cells are used. These are also based on the fluorite Ti_4H_8 ($Z = 1$) building block. For $x = 0.5$ and 0.75 $2 \times 2 \times 2$ super cells were constructed

Table 13.1: *Number of formula units, Z, lattice parameters (Å) and shortest Ti–Ti interatomic distances (Å). The first row for each composition contains the data of the simple cell and the second of the super cell.*

x	Z	a	b	c	Ti–Ti
0.5	4	4.72	4.72	4.65	3.16
	32	9.08	9.03	9.09	3.15
0.75	4	4.62	4.62	4.62	4.62
	32	9.29	9.30	9.27	3.13
0.875	32	9.36	9.36	9.36	6.62
	64	18.75	9.42	9.73	3.08

and for $x = 0.875$ a $2 \times 1 \times 1$ super cell. Again Ti were replaced by Mg, but now such as to approximate random alloys most efficiently (see Ref. 233 for details).

For all the models constructed the positional and cell parameters were relaxed. The cells remain close to cubic, see Table 13.1. The angles between the crystal axes are close to 90°, except for the $x = 0.75$ and 0.875 super cells where there is a small deviation.

Dielectric functions

Interband dielectric functions

Figures 13.2 and 13.3 show the calculated imaginary parts of the interband dielectric functions in the simple and super cells respectively. In general the dielectric functions exhibit a peak at low energy, below 2 eV, followed by a relatively flat tail. In the super cells the dielectric functions have higher peaks and flatter tails. An exception is the dielectric function of the $x = 0.875$ super cell. It does not have a peak at low energy.

To understand the main features of the dielectric functions we study the densities of states (DOS', Figure 13.4). Below the Fermi level the DOS' have an approximately triangular shape with a predominant hydrogen-s and magnesium-s and p character. At the Fermi level the DOS' are dominated by titanium-d states. Above the Fermi level the DOS' have a mixed character of hydrogen-s and p, magnesium-s and p and titanium-d. As an illustration the angular momentum projected partial DOS' of the simple cell with $x = 0.75$ is shown in Figure 13.5.

The electron density is localized at both the hydrogen and titanium atoms. This is illustrated in Figure 13.6, where the electron localization function (Ref. 236) is plotted,

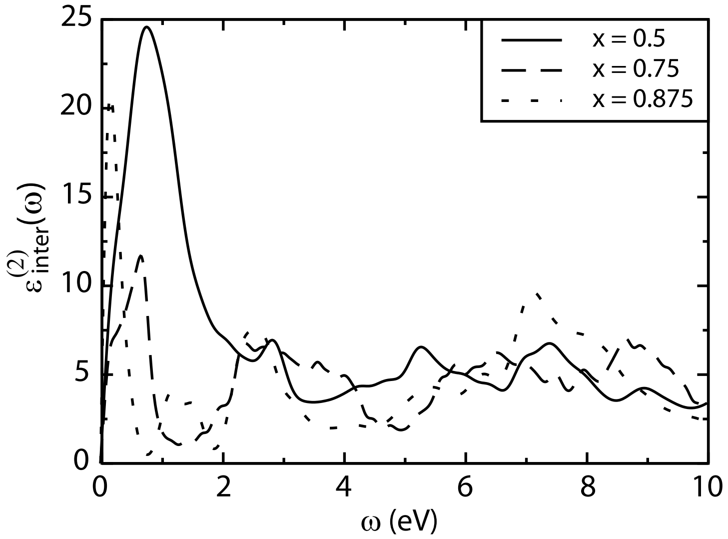

Figure 13.2: *Imaginary parts of the interband dielectric functions of* $Mg_xTi_{(1-x)}H_2$ *in the primitive cells.*

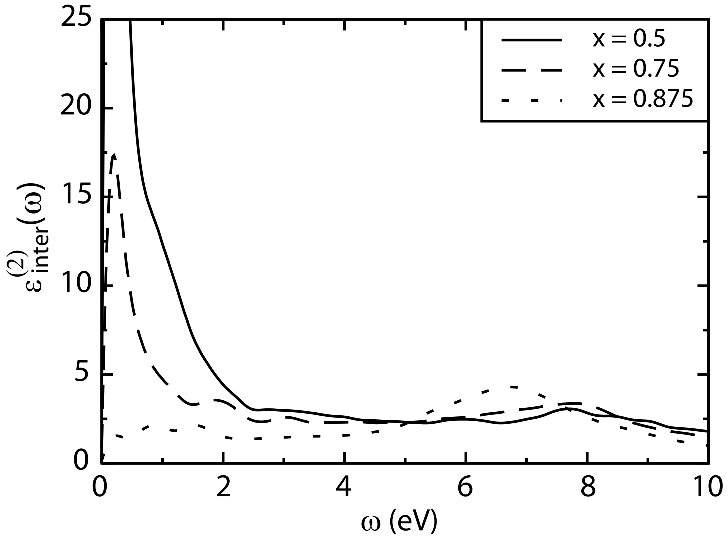

Figure 13.3: *Imaginary parts of the interband dielectric functions of* $Mg_xTi_{(1-x)}H_2$ *in the super cells. For* $x = 0.5$ *the dielectric function peaks to a value of 130.*

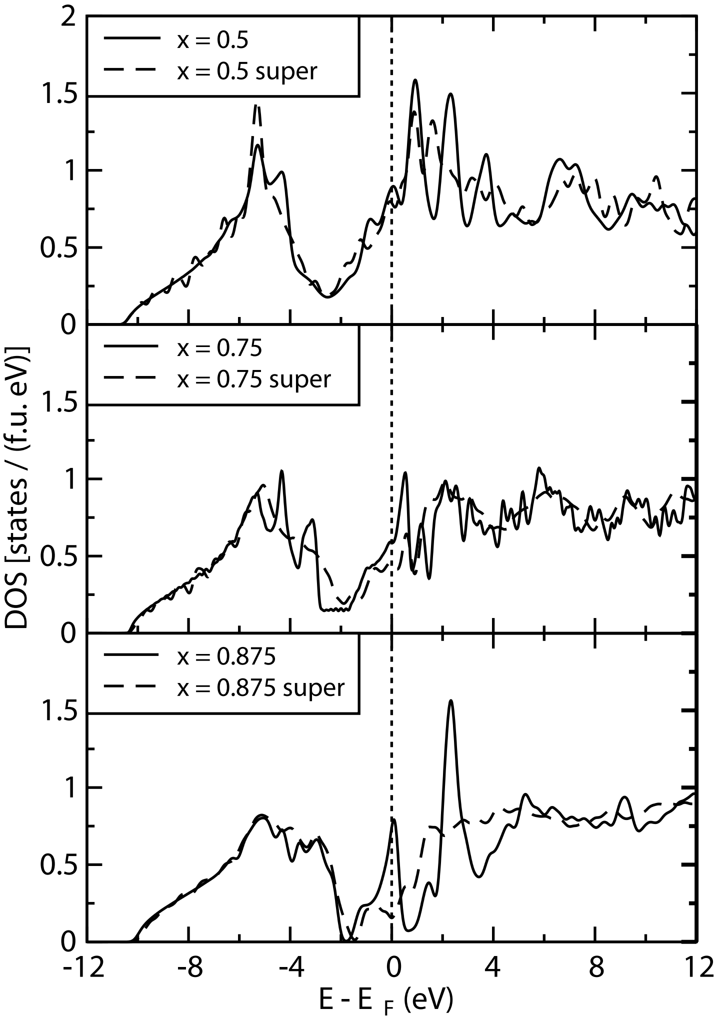

Figure 13.4: *Electronic densities of state of the simple and super cells for the three compositions of* $Mg_x Ti_{(1-x)} H_2$*. The zero of energy is taken at the Fermi level.*

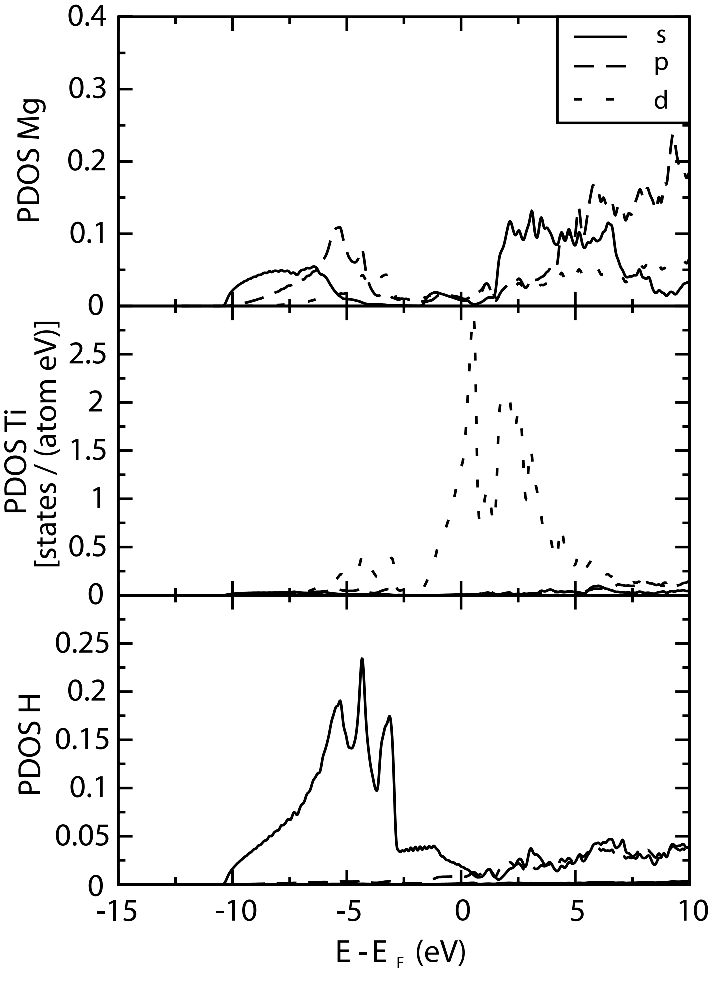

Figure 13.5: *Angular momentum projected partial densities of states (PDOS) [states/(atom eV)] of $Mg_{0.75}Ti_{0.25}H_2$ in the simple unit cell. The zero of energy is at the Fermi level. The PDOS' are calculated in spheres with radii of 1.3, 1.3 and 0.8 Å for Mg, Ti an H respectively.*

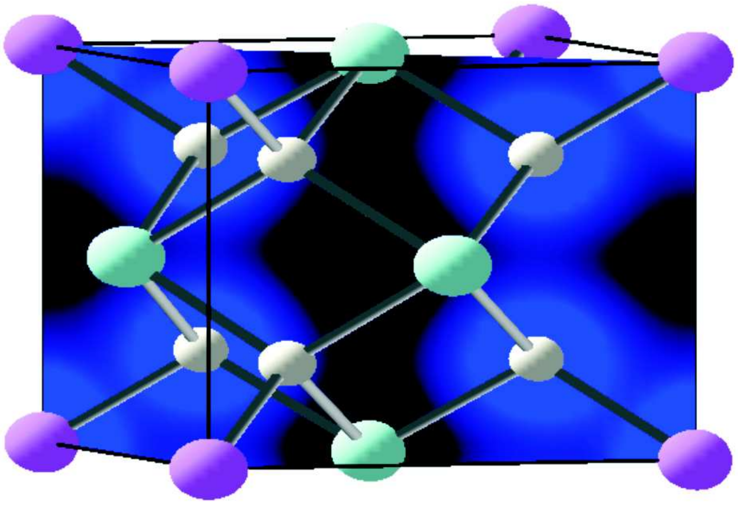

Figure 13.6: *Electron localization function of* $Mg_{0.75}Ti_{0.25}H_2$ *in the simple unit cell. The Ti atoms are at the corners, the Mg atoms at the face centers and the H atom (small) are inside the cell. The electron localization function is plotted on a (110) cut-plane. Localization at the H and Ti atoms is evident.*

also for the simple cell $\mathrm{Mg}_{0.75}\mathrm{Ti}_{0.25}\mathrm{H}_2$. At the titanium atoms the only available states are of d-character. Since $d-d$ transitions are very weak the main contribution to the dielectric function is from $s-p$ transitions on the hydrogen atoms.

In first order the imaginary part of the dielectric function can be described as the joint density of states (JDOS) divided by ω^2. The hydrogen DOS has a dip near the Fermi energy. It increases when moving away from the Fermi energy, both to lower and higher energies. This causes the JDOS at the hydrogen atoms to increase more than linearly (in the region from 0 to about 8 eV). When divided by ω^2 this increase is rather effectively compensated. Hence the dielectric function does not vary much in the interval from 2 to 8 eV. This reasoning applies for all titanium concentrations that we considered. In the super cells the averaging over the various hydrogen DOS' gives rise to a further leveling out of the dielectric functions. Of course vibrational effects, that are lacking in our 0 K calculation, will even further smoothen the dielectric functions.

The peaks at the lower end of the energy range do arise from d-d transitions on the Ti atoms. Although their oscillator strength is small, division by ω^2 causes them to stand out nevertheless. For $x = 0.875$ the Ti DOS at E_{Fermi} is strongly suppressed in the super cell (see Figure 13.4). This correlates with the absence of the peak in $\epsilon^{(2)}_{\mathrm{inter}}$ for the super cell at this composition (Figures 13.2, 13.3). At the other two compositions, we see no clear correlation between difference in DOS and peak shape (comparing simple and super cells). The higher peaks in the DOS in the super cells can be understood when we realize

Table 13.2: *Squared plasma frequencies, ω_p^2 (eV^2), from intraband transitions.*

	simple cell	super cell
$x = 0.5$	10.7	1.3
$x = 0.75$	12.8	0.4
$x = 0.875$	8.6	0.1

that the effective "back folding" of the d bands *and* their mutual interactions (caused by the randomization) results in a flattening of the bands. Some of these bands will be very close to E_{Fermi} and their transitions will thus be "boosted", both by the flatness of the bands and the small transition energy. This discussion anticipates the discussion in the next section.

Intraband plasma frequencies

The intraband plasma frequencies, which have been calculated according to Equation 13.5, are listed in Table 13.2. The squared plasma frequencies from the super cell calculations are between one and two orders of magnitude smaller than those of the simple cells. Therefore the edge on the free carrier reflectively occurs at considerably lower energies in the random alloys. In our models the maximum ω_p is 1.1 eV. This is, however, for only one realization of a random model at $x = 0.5$ and it is well conceivable that calculations on large models could yield even lower ω_p. For the simple cells, the plasma frequencies are approximately 3 eV, hence these systems are highly reflecting for $\omega < 3$ eV.

Equation 13.5 is a good starting point for a discussion of the trends across Table 13.2. It basically states that the squared plasma frequency is proportional to the product of the electron density and the square of the slope of the energy bands, both calculated at the Fermi level. In the super cells ω_p^2 clearly follows the density of states (see, Figure 13.4) as a lower concentration of titanium means a lower amount of free electrons. In the simple cells this trend is not obvious. Subtle changes in the shape of the DOS, i.e. bandstructure effects, make for less changes in the electron density at the Fermi level. Consistently the plasma frequency shows little variation. This, however, does not imply that small changes in the slope of the energy bands do not play an equally important role here.

The difference between the simple and super cells of the same composition is explained by a decrease in energy band slope. The DOS' at the Fermi level are of comparable size, at least for compositions with $x = 0.5$ and $x = 0.75$. This clearly points to the change in $\partial\epsilon_{n\mathbf{k}}/\partial\epsilon_{\mathbf{k}}$ as the cause of the significant decrease of ω_p. This is corroborated by inspection

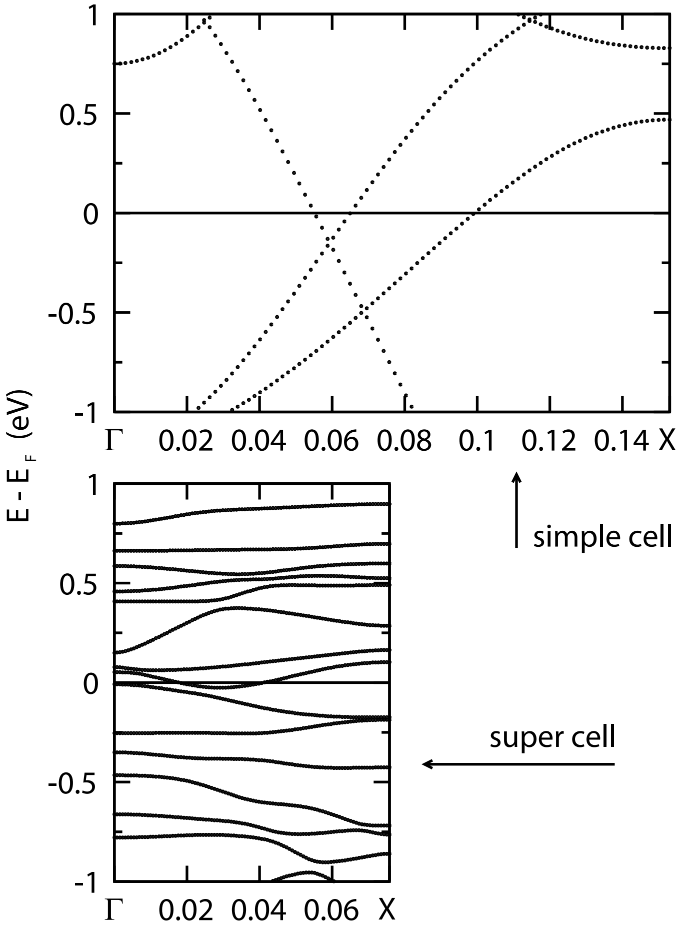

Figure 13.7: *Electronic energy band structure of* $Mg_{0.75}Ti_{0.25}H_2$ *in the simple and super cell along the* Γ*–*X *direction.*

of the band structure, that is plotted in Figure 13.7 for $Mg_{0.75}Ti_{0.25}H_2$ for both the simple and super cell. We see that the bandstructure of the supercell cannot be understood as a simple back-folding of the bands. The randomness in the structure has induced many interactions between the *d*-bands, leading to a dramatic reduction of their slopes. Going to even larger super cells, the effect may become even stronger, and the free carrier reflection concomitantly reduced. Such a calculation goes beyond the present study. It may require a different formalism as the reciprocal space description of Equation 13.5 is bound to break down for truly random systems.

Interestingly, the flatness of the energy bands also makes that the effective mass of the "free" electrons is rather high. This goes some way to explain the rather high resistivity measured for these systems. The "flat bands" also point to a possible localization of carriers.

For $x = 0.875$ the reduction of ω_p^2 cannot be understood as a reduction of only $\partial\epsilon_{n\mathbf{k}}/\partial\mathbf{k}$. From Figure 13.4 a substantial reduction of the DOS at E_Fermi is evident. Hence reduction of ω_p^2 is much stronger than for $x = 0.5$ and $x = 0.75$.

To obtain the dielectric functions of the materials we just add the interband part of Section 13 and intraband parts obtained from ω_p according to Equation 13.1. It was already noted above that the impact on the reflection in the visible range will be substantial for the simple cells. The values of ω_p^2 in the super cells are low enough to only induce minor corrections to the interband dielectric function. The implications of the corrections will be discussed in the next Section.

Discussion

The calculations on the random alloy super cells clearly demonstrate that breaking of the short range order results in two important effects: (a) The interband dielectric function is smoothened and (b) the plasma frequency is lowered. The first translates in smoother reflection and transmission spectra for the super cells. The second results in a lower reflection edge. The simple cells have almost full reflection up to 1–2 eV whereas in the super cells full reflection only occurs below $\sim$0.3 eV.

Figure 13.8 shows the calculated reflection and transmission of a film simulating closely the experimental setup as used by Borsa *et al.*[216] The simulated film consists of 10 nm Paladium / 200 nm $Mg_xTi_{(1-x)}H_2$ / ($k = 0$) quartz substrate layers, were we use the $\varepsilon(\omega)$ calculated in the super cells for the $Mg_xTi_{(1-x)}H_2$ layer. The plotted range is that of a Perkin Elmer Lambda 900 diffraction spectrometer. For comparison; visible light lies in the range of 1.65–3.26 eV. The general features and trends as a function of Ti content in both reflection and transmission are in agreement with the trends observed in the

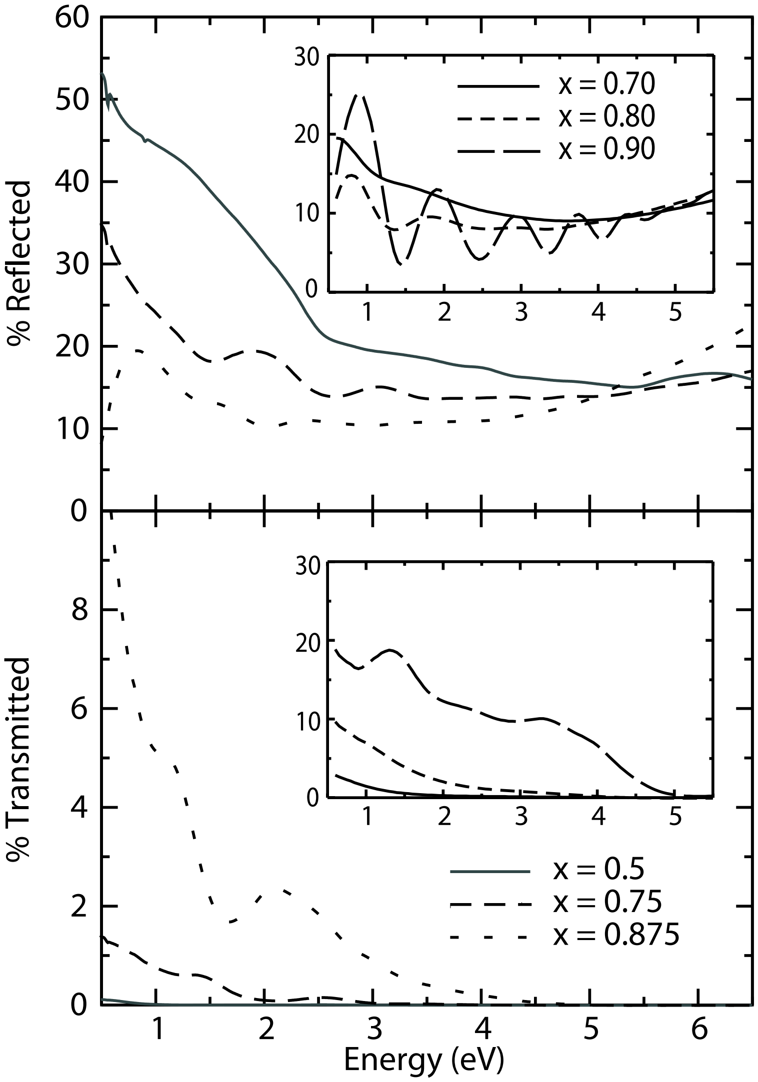

Figure 13.8: *Reflection and transmission of a 10 nm Paladium / 200 nm* $Mg_xTi_{(1-x)}H_2$ */ (*$k = 0$*) quartz substrate film. For the dielectric function of* $Mg_xTi_{(1-x)}H_2$ *the results for the supercell, including inter and intraband contributions, are used. The inset shows experimental results from Ref. 216, reproduced with permission, copyright American Physical Society (2007).*

experiments.[216] Indeed the reflection is low and our calculations describe a “black state”. With decreasing Ti content the reflection decreases and the transmission increases.

Since experiments were performed on magnesium/titanium ratios $x = 0.7$, 0.8, and 0.9, that would have required very large super cells, a detailed comparison can only be made partially. Interpolating between the experimental values for 0.7 and 0.8 we can make a reasonable comparison with the calculated results for $x = 0.75$. The experimental reflection lies about 5 %Pt. lower than the calculated one but the shape of the curve is very similar. The experimental transmission drops from 6.5%–0% in the range from

0.5–3 eV, it hence lies about a factor 3 higher than the calculated one. The shapes of the transmission curves, however shows good agreement.

Comparing the calculated values for $x = 0.875$ to the experimental results for $x = 0.9$ we again see somewhat lower values for the experimental reflection. Furthermore, the slight oscillation seen in the calculated spectrum, caused by interference, is much stronger in the experimental spectrum. The main difference in the transmission lies in the energy range below 1 eV where the calculated transmission is much larger than the experimental values. This difference could point to an underestimation of the ω_p^2 in the super cell $x = 0.875$ calculation.

From the correspondence between the experimental and calculated optical spectra we conclude that the "black state" can already be explained from moderate-size randomized super cells. Put into other words: randomized models containing only 32 to 64 formula units allow for a breaking of the order on a length-scale such as to lower the reflection edge and smoothen the spectra. This does not necessarily imply that a randomization at larger length scales, with a concomitant increase of the short range order, e.g. in the coherent crystal picture proposed by Borsa *et al.*,[216] would be inconsistent with experiment. Indeed, the coherent crystal model is supported by various observations, e.g. the large positive enthalpy of mixing of Ti and Mg. Moreover, for $x = 0.875$ our modeling seems to underestimate ω_p, suggesting that the short range disorder may have disrupted the band dispersion to much. A full first-principles study of necessarily larger models with more short range order is beyond present computational capabilities. Such a study is desirable. However, with the present randomized models we can capture most of the essential physics of $\mathrm{Mg}_x\mathrm{Ti}_{1-x}\mathrm{H}_2$.

Acknowledgements

The authors thank Prof. G. Kresse and J. Harl (Universität Wien) for the use of the optical packages and R. Gremaud (Vrije Universiteit) for running the reflection/transmission simulations. This work is part of the Sustainable Hydrogen Programme of the Advanced Catalytic Technologies for Sustainability (ACTS) and the Stichting voor Fundamenteel Onderzoek der Materie (FOM), both financially supported by the Nederlandse Organisatie voor Wetenschappelijk Onderzoek (NWO).

Chapter 14

Conclusions

In this thesis several materials have been discussed that can be used for hydrogen storage. This final chapter begins with a discussion on the current status of computational solid state methods in their relation to calculations of the properties of hydrogen storage materials. The classes of materials studied in the theses are discussed subsequently, summarizing the results of previous chapters. The chapter ends with an outlook on solid state hydrogen storage.

Solid state DFT calculations

State-of-the-art methods for performing solid state calculations are reaching a point where a useful comparison with experimentally determined quantities can be made. Using DFT, structural properties of systems with up to several hundreds of atoms in the unit cell can be calculated with reasonable accuracy. Especially vibrational spectra and hence the thereof derived thermodynamic properties can be calculated accurately.

One of the main impediments of DFT is the large discrepancy between calculated and experimentally obtained reaction enthalpies. When the type of bonding stays the same DFT usually provides very reasonable energy differences due to cancelation of errors. In the case of hydrogen desorption reactions one needs to compare a molecule to solids. To make things worse the hydrides are often insulators whereas the desorbed state usually contains metals. In this case the bonding changes significantly and a cancelation of errors is not likely.

A typical example is the reaction enthalpy of the seemingly simple decomposition of magnesium hydride:

$$\mathrm{MgH_2} \rightarrow \mathrm{Mg} + \mathrm{H_2} \tag{14.1}$$

The experimental reaction enthalpy at standard conditions is 76 kJ/mol, the calculated value is 62 kJ/mol with GGA and 90 kJ/mol with B3LYP functionals. One may find these numbers in reasonable agreement but in a field like hydrogen storage a better accuracy is needed to judge feasibility and suitability of the material. To increase this accuracy a better exchange correlation functional is needed. However, when we keep this discrepancy in mind and do not try to pretend it does not exist it must be possible to come to a mutual understanding between experimental and computational scientists.

On the other hand many recent developments are making computational methods more and more useful. Implementations of (partially) self consistent GW techniques in existing DFT codes makes it possible to calculate accurate bandgaps. This can be combined with an implementation of the the Bethe Salpeter equation to include excitons. Currently it is possible to calculate dielectric functions of realistic systems going beyond the usual test systems like crystalline silicon. For several hydrides these have been shown to have excellent agreement with experimental dielectric functions. Calculated dielectric functions can be useful in interpreting the results of a recently developed combinatorial optical method called hydrogenography.[237,238] In this method thin films containing gradients in composition are exposed to a hydrogen atmosphere. By monitoring the change in reflection and transmission as a function of hydrogen pressure it is possible to study a large amount of compositions in one experiment.

Implementations for calculating nuclear magnetic resonance (NMR) related properties like field gradients, see e.g. Ref. 239, and chemical shifts, see e.g. Ref. 240, for crystals are currently being developed. Especially in the field of solid state NMR we can expect much from the collaboration between experimental and computational scientists. Since both probe the structure of a material at an atomic level (the combination of) both may be essential in studying the desorption process and effects of catalysts.

The research of the solid state reactions involved in the desorption of hydrogen from complex hydrides will benefit especially from a close collaboration of computational and experimental research. Performing calculations inside the isolation of a theoretical group without regular contact to experimental work may be less efficient. The main problem is the limited length and time scale of *ab initio* calculations. It is not yet, and may never will be, possible to perform calculations at the quantum mechanical level on realistic scales that are needed to truly simulate the entire dynamical process involved in reactions as complex as hydrogen desorption from complex hydrides. It is hence necessary to isolate events that can be studied at quantum mechanical level. When such events are selected on the basis of an educated guess alone there is a reasonable possibility that one is studying a process that has little to do with the actual reaction.

In close contact with experimental work it is possible to isolate relevant events that can be studied on DFT level. Studying these on an atomic scale at a quantum mechanical level can lead to insights that may lay beyond the capabilities of experimental techniques. A close cooperation can therefore lead to a fundamental understanding which may not be reached by either pure experimental or pure computational research.

Magnesium based hydrides

Hydrides of alloys of magnesium and one or more transition metals have been, and still are, the topic of much research. The large amount of possible compounds makes it an extensive field where active research continues. For the use of actual hydrogen storage, in particular for mobile applications, these materials may not be very useful. This is mainly caused by the gravimetric hydrogen capacity being too low. It must be said, however, that, when used for electrochemical storage in batteries various combinations have been found that can at least double the capacity of currently used batteries.[241] We have shown that for one of the more promising compounds, Mg_2NiH_4, it is possible to affect the thermodynamics of the hydrogen desorption reaction by doping with other transition metals. The calculated results indicated that it is possible to change the thermodynamics in both directions, making the hydride either more or less stable with respect to the dehydrogenated phase.

An other important application of these materials lies in the producing of hydrogen sensors.[215,232] In an economy based on hydrogen as a fuel there will always be a demand for cheep an robust sensors to detect leaking hydrogen. This is mainly important because hydrogen is has neither color nor smell and is therefore not easily detected by our own senses. Thin films of magnesium based hydrides have been shown to be very useful in this perspective. One of the most recent and promising is a mixture of magnesium and titanium. Although magnesium and titanium do not form bulk alloys it is possible to obtain thin films that can reversibly be loaded and unloaded with hydrogen. The unloaded film is metallic and highly reflective, the hydrogenated film is black; It has low reflectivity and high absorption in the optical spectrum. This black state was, however, somewhat puzzling because the hydride still has valence electrons at the Fermi level and is therefore expected to be reflective as well. We have studied the electronic structure and optical properties of magnesium titanium hydrides and given an explanation for this black state. In these calculations it turned out that it was necessary to perform the calculations in super cells to simulate the effect of a random alloy.

Alanates and boranates

Chapters 3 to 10 in this thesis were dedicated to the alanates and the boranates. For the alanates many of the basic properties seem to be clear by now. The crystal structures of the ground states and, in many cases of high temperature or high pressure states, are known. The electronic structure of and binding in these materials is understood and the reaction enthalpies of the reactions that could be useful for hydrogen storage are known.

For the alanates we have shown that the electronic structure is strongly dominated by the sublattice of the $(AlH_4)^-$ anions. Both the valence bands and the bottom of the conduction band are dominated by the anions. The interaction between them therefore determines the bandgap in these materials. This can be explained in terms of electrostatic interactions and is mainly caused by the difference in localization between the valance and conduction wavefunctions.

The state of knowledge of the boranates lags a bit behind of that of the alanates. One reason is that the crystal structures of the alkaline earth boranates are rather complex.

Especially magnesium and calcium boranate turn out to form complex structures.[161,176,177] The crystal structure of calcium boranate even seems to be extremely sensitive to the preparation method. This indicates that many different crystal structures exist that are close in energy but with large energy barriers in transforming one into an other. For some of the higher boranates, like titanium boranate, the determination of the crystal structure is not yet completed.

An other issue is that of the reaction mechanisms of hydrogen desorption. Although the reaction steps and intermediate products are known in many cases (a summary of the reactions is given by Züttel *et al.*[9]) the microscopic mechanisms and especially the role of the titanium catalyst in the case of the alanates are still unclear. Several mechanisms have been proposed to explain the catalytic effect of titanium. In one, titanium atoms act in the subsurface to help tearing open the material.[242] In others, the titanium helps to lower the formation energy of vacancies in the materials.[243] The vacancies then facilitate further mass transport. An other important recent result is that the mobile species during the desorption reaction are heavier than hydrogen and most likely AlH_x or MH_x. This was shown by measuring the isotope effect of replacing hydrogen by deuterium on the reaction kinetics.[244]

For the hydrogen desorption and absorption reactions of the boranate systems up until now no working catalysts have been found. The problem with the catalyst of the alanates, titanium, is that it is very likely to form the stable TiB_2. After the first desorption step the titanium will therefore be passivated and is not available in subsequent absorption and desorption steps. A solution could be found by studying transition metals that form less stable compounds with boron.

The stability of both the alanates and boranates can be understood from a fairly simple Born-Haber model. Taking into account the energy to form the covalently bond anions and the crystal energy of the lattice of anions and cations, the binding energy of the complex hydride can be calculated rather accurately.

Solid state hydrogen storage

With fossil fuels reaching their peak production and CO_2 concentrations in the atmosphere reaching a level that can have an unpredictable effect on the climate, we will have to change to alternative energy sources. To use alternative energy sources like wind and solar power for mobile applications we also need alternative energy carriers. The targets that governments and industry have set for hydrogen storage systems have stimulated a large scientific effort in the field of hydrides. One can say that in this field science has the chance to save the way of life as we know it.

In the last decade various classes of complex hydrides have been studied for their potential use as hydrogen storage material. Of all materials studied up until now, none has shown to be able to fulfill all requirements. However the ever more complex materials, mechanisms and reactions that are being thought of give hope that the problem eventually will be solved.

Each class of materials has its own problems. Alloys of transition metal hydrides can be reversible under practical conditions but have a far too low gravimetric density. The amide-imide systems, which also show reversibility have a higher but still too low gravimetric density. Alkali and alkaline earth hydrides, of which the lightest have high gravimetric density, are too stable both thermodynamically and kinetically. Some alkali alanates have been shown to be reversible but suffer from a too low gravimetric hydrogen density. The alkaline earth alanates that have a high gravimetric density are too unstable and hence suffer from reversibility problems originating from the thermodynamics. The boranates, having the highest gravimetric hydrogen density, are in general too stable from the thermodynamical point of view and suffer furthermore from high kinetic barriers.

The gravimetric demands on a storage system include the complete storage system. This involves for instance protective outer tanks, a heat exchange system, and pressure regulators. The gravimetric demand on the actual storage material is therefore much higher than that of the total system. A reasonable guess is that the material will take up half of the weight of the entire system and hence needs a twice as large storage capacity. When we take the more reasonable 5 wt.% mentioned by the European and Japanese car industries we still need a material able to reversibly store about 10 wt.% of hydrogen.

At the moment there seem to be only two (pure) complex hydrides that may be able to form the basis of a hydrogen storage system that can reach the gravimetric targets. One is $\mathrm{LiBH_4}$ and the other $\mathrm{Mg(BH_4)_2}$. Both these boranates suffer from high kinetic barriers. These barriers originate in part from the strong B–H and B–B bond that have to be broken during absorption an desorption. In the case of $\mathrm{LiBH_4}$ the thermodynamics are also unfavorable.

In the case of $\mathrm{Mg(BH_4)_2}$ the prospects are a bit better. The reaction that seems to be the overall desorption reaction:

$$\mathrm{Mg(BH_4)_2} \rightarrow \mathrm{MgB_2} + 4\mathrm{H_2} \tag{14.2}$$

has about the right thermodynamics, 40 kJ/mol $\mathrm{H_2}$ at room temperature and 43 kJ/mol $\mathrm{H_2}$ at the experimental desorption temperature. The calculated thermodynamics of $\mathrm{Mg(BH_4)_2}$ predict an equilibrium pressure of 1 bar at room temperature. The experimental desorption temperature, however, lies at 290°C, which may indicate that a more complicated reaction occurs.

The ratio of magnesium and boron in both $Mg(BH_4)_2$ and MgB_2 are the same. One might imagine that the decomposition could occur without much mass transport. The decomposition of $Mg(BH_4)_2$ occurs, however, in a number of steps and in one of the first steps even bulk magnesium is formed. Only after the very last step MgB_2 can be found. This leads to the conclusion that complicated reaction steps occur that separate the magnesium and boron. One possible explanation for these many reaction steps is a stepwise formation for higher boranes. Starting from BH_4 in a first step B_2H_7 could form. In each subsequent step hydrogen is released and higher boranes are formed. Eventually, the stable $B_{12}H_{12}$ cluster can be formed. This would be the final stage before elemental boron. Such a mechanism would explain the gradual hydrogen desorption and the formation of MgB_2 only at the very end of the desorption process. Although very interesting and intriguing, these steps are unpractical from the hydrogen storage point of view because they increase the desorption temperature and cause a temperature range at which the desorption takes place.

When we turn out not to be able to solve the problems involved with the absorption and desorption reactions of either $LiBH_4$ or $Mg(BH_4)_2$, the problem concerning gravimetric density might only be solved by relaxing the targets on the storage system, which will demand a change in our view on personal transportation.

References

[1] W. Zittel and J. Schindler, *Crude oil the supply outlook, EWG-Series No 3/2007*, Energy Watch Group, 2007.

[2] W. Zittel and J. Schindler, *Coal: Resources and future production, EWG-Series No 1/2007*, Energy Watch Group, 2007.

[3] W. Zittel and J. Schindler, *Uranium resorces and nuclear energy, EWG-Series No 1/2006*, Energy Watch Group, 2006.

[4] L. Schlapbach and A. Züttel, Nature **414**, 353 (2001).

[5] A. Züttel, Naturwissenschaften **91**, 157 (2004).

[6] F. Schüth, B. Bogdanovíc, and M. Felderhoff, Chem. Commun. **20**, 2249 (2004).

[7] S. Satyapal, J. Petrovic, C. Read, G. Thomas, and G. Ordaz, Catal. Today **120**, 246 (2007).

[8] B. Sakintuna, F. Lamari-Darkrim, and M. Hirscher, Int. J. Hydrog. Energy **32**, 1121 (2007).

[9] A. Züttel, A. Borgschulte, and S. Orimo, Scripta Mat. **56**, 823 (2007).

[10] M. Hirscher and B. Panella, Scripta Materialia **56**, 809 (2007).

[11] J. J. Vajo and G. L. Olson, Scr. Mater. **56**, 829 (2007).

[12] W. Kohn and L. J. Sham, Phys. Rev. **140**, A1133 (1965).

[13] R. O. Jones and O. Gunnarsson, Rev. Mod. Phys. **61**, 689 (1989).

[14] P. E. Blöchl, Phys. Rev. B **50**, 17953 (1994).

[15] G. Kresse and J. Furthmüller, Phys. Rev. B **54**, 11169 (1996).

[16] G. Kresse and J. Furthmüller, Comput. Mater. Sci. **6**, 15 (1996).

[17] G. Kresse and J. Hafner, Phys. Rev. B **47**, 558 (1993).

[18] G. Kresse and J. Hafner, Phys. Rev. B **49**, 14251 (1994).

[19] G. Kresse and D. Joubert, Phys. Rev. B **59**, 1758 (1999).

[20] P. E. Blöchl, O. Jepsen, and O. K. Andersen, Phys. Rev. B **49**, 16223 (1994).

[21] H. J. Monkhorst and J. D. Pack, Phys. Rev. B **13**, 5188 (1976).

[22] S. Goedecker and K. Maschke, Phys. Rev. B **45**, 1597 (1992).

[23] F. D. Murnaghan, PNAS **30**, 244 (1944).

[24] G. Kresse, J. Furthmüller, and J. Hafner, Europhys. Lett. **32**, 729 (1995).

[25] J. P. Perdew et al., Phys. Rev. B **46**, 6671 (1992).

[26] R. C. Weast and M. J. Astle, *CRC Handbook of Chemistry and Physics*, CRC press, New York, 62 edition, 1982.

[27] K. P. Huber and G. Herzberg, *Molecular Spectra and Molecular Structure*, Van Nostrand Reinhold Company, 1979.

[28] H. Hemmes, A. Driessen, and R. Griessen, J. Phys. C **19**, 3571 (1986).

[29] M. Gajdoš, K. Hummer, G. Kresse, J. Furthmüller, and F. Bechstedt, Phys. Rev. B **73**, 045112 (2006).

[30] J. Harl, G. Kresse, L. D. Sun, M. Hohage, and P. Zeppenfeld, Phys. Rev. B **76**, 035436 (2007).

[31] B. Bogdanovíc and M. Schwickardi, J. Alloys Compd. **253**, 1 (1997).

[32] X. T. X et al., J. Alloy. Compd. **446**, 228 (2007).

[33] Y. Nakamori et al., Phys. Rev. B **74**, 045126 (2006).

[34] B. Bogdanovíc et al., Adv. Math. **15**, 1012 (2003).

[35] A. Peles, J. A. Alford, Zhu Ma, Li Yang, and M. Y. Chou, Phys. Rev. B **70**, 165105 (2004).

[36] M. Fichtner and O. Fuhr, J. Alloys Compd. **286**, 345 (2002).

[37] M. Fichtner, O. Fuhr, and O. Kircher, J. Alloys Compd. **356-357**, 418 (2003).

[38] M. Fichtner et al., Inorg. Chem. **42**, 7060 (2003).

[39] A. Fossdal, H. W. Brinks, M. Fichtner, and B. C. Hauback, J. Alloys Compd. **387**, 47 (2004).

[40] K. Bohmhammel, U. Wolf, G. Wolf, and E. Königsberger, Thermo. Acta. **337**, 195 (1999).

[41] P. Claudy, B. Bonnetot, and J. M. Letoffe, J. Thermal Analysis. **119**, 15 (1979).

[42] F. Aryasetiawan and O. Gunnarsson, Rep. Prog. Phys. **61**, 237 (1998).

[43] P. van Gelderen, P. A. Bobbert, P. J. Kelly, and G. Brocks, Phys. Rev. Lett. **85**, 2989 (2000).

[44] P. van Gelderen, P. A. Bobbert, P. J. Kelly, G. Brocks, and R. Tolboom, Phys. Rev. B **66**, 075104 (2002).

[45] N. Troullier and J. L. Martins, Phys. Rev. B **43**, 1993 (1991).

[46] M. M. Rieger, L. Steinbeck, I. D. White, H. N. Rojas, and R. W. Godby, Comput. Phys. Commun. **117**, 211 (1999).

[47] P. Pullumbi, Y. Bouteille, and L. Manceron, J. Chem. Phys. **101**, 3610 (1994).

[48] B. K. Rao, P. Jena, S. Burkhart, G. Ganteför, and G. Seifert, Phys. Rev. Lett. **86**, 692 (2001).

[49] P. K. de Boer and R. A. de Groot, Am. J. Phys. **67**, 443 (1999).

[50] P. K. de Boer and R. A. de Groot, Eur. Phys. J. B **4**, 25 (1998).

[51] R. Griessen and A. Driessen, Phys. Rev. B **30**, 4372 (1984).

[52] O. M. Løvvik and P. N. Molin, Phys. Rev. B **72**, 073201 (2005).

[53] C. Wolverton, V. Ozolins, and M. Asta, Phys. Rev. B **69**, 144109 (2004).

[54] M. J. van Setten, G. A. de Wijs, V. A. Popa, and G. Brocks, Phys. Rev. B **72**, 073107 (2005).

[55] O. M. Løvvik, S. M. Opalka, H. W. Brinks, and B. C. Hauback, Phys. Rev. B **69**, 134117 (2004).

[56] A. Andreasen, T. Vegge, and A. S. Pedersen, J. Solid State Chem. **178**, 3672 (2005).

[57] M. Mamatha, C. Weidenthaler, A. Pommerin, M. Felderhoff, and F. Schuth, J. Alloy. Compd. **416**, 303 (2006).

[58] T. N. Dymova, D. P. Aleksandrov, V. N. Konoplev, T. A. Silina, and A. S. Sizareva, Russ. J. Coord. Chem **20**, 263 (1994).

[59] C. H. Olk, G. G. Tibbetts, D. Simon, and J. J. Moleski, J. Appl. Phys. **94**, 720 (2003).

[60] R. Gremaud et al., Appl. Phys. A-Mater. Sci. Process. **84**, 77 (2006).

[61] W. Lohstroh et al., J. Alloy. Compd. **430**, 13 (2007).

[62] J. N. Huiberts et al., Nature **380**, 231 (1996).

[63] M. Kremers et al., Phys. Rev. B **57**, 4943 (1998).

[64] J. W. J. Kerssemakers, S. J. van der Molen, N. J. Koeman, R. Gunther, and R. Griessen, Nature **406**, 489 (2000).

[65] T. J. Richardson et al., Appl. Phys. Lett. **78**, 3047 (2001).

[66] W. Lohstroh et al., Phys. Rev. Lett. **93**, 197404 (2004).

[67] W. Lohstroh et al., Phys. Rev. B **70**, 165411 (2004).

[68] P. Kumar and L. K. Malhotra, Thin Solid Films **491**, 270 (2005).

[69] A. C. Lokhorst et al., J. Alloy. Compd. **404**, 465 (2005).

[70] J. A. Dilts and E. C. Ashby, Inorg. Chem. **11**, 1230 (1972).

[71] T. N. Dymova, V. N. Konoplev, D. P. Aleksandrov, A. S. Sizareva, and T. A. Silina, Koord. Khim. **21**, 175 (1995).

[72] K. J. Gross, E. H. Majzoub, and S. W. Spangler, J. Alloys Compd. **356**, 423 (2003).

[73] A. Züttel et al., J. Alloys Compd. **356**, 515 (2003).

[74] M. E. Arroyo y de Dompablo and G. Ceder, J. Alloys Compd. **364**, 6 (2003).

[75] P. Vajeeston, P. Ravindran, R. Vidya, H. Fjellvåg, and A. Kjekshus, Cryst. Growth Des. **4**, 471 (2004).

[76] O. M. Løvvik, O. Swang, and S. M. Opalka, J. Mater. Res. **20**, 3199 (2005).

[77] W. G. Aulbur, L. Jonsson, and J. W. Wilkins, Solid. State. Phys-adv. Res. Appl. **54**, 1 (2000).

[78] G. Onida, L. Reining, and A. Rubio, Rev. Mod. Phys. **74**, 601 (2002).

[79] J. P. Perdew and A. Zunger, Phys. Rev. B **23**, 5048 (1981).

[80] M. S. Hybertsen and S. G. Louie, Phys. Rev. B **34**, 5390 (1986).

[81] R. W. Godby, M. Schlüter, and L. J. Sham, Phys. Rev. B **37**, 10159 (1988).

[82] M. van Schilfgaarde, T. Kotani, and S. Faleev, Phys. Rev. Lett. **96**, 226402 (2006).

[83] V. A. Popa, G. Brocks, and P. J. Kelly, cond-mat/0507013 (2005).

[84] H. N. Rojas, R. W. Godby, and R. J. Needs, Phys. Rev. Lett. **74**, 1827 (1995).

[85] J. W. van der Horst et al., Phys. Rev. B **61**, 15817 (2000).

[86] V. G. Plekhanov, V. A. Pustovarov, A. A. O‘Konnel-Bronin, T. A. Betenekova, and S. O. Cholakh, Fiz. Tverd. Tela **18**, 2438 (1976).

[87] S. Baroni, G. Pastori Parravicini, and G. Pezzica, Phys. Rev. B **32**, 4077 (1985).

[88] S. L. Adler, Phys. Rev. **126**, 413 (1962).

[89] N. Wiser, Phys. Rev. **129**, 62 (1963).

[90] R. Del Sole and R. Girlanda, Phys. Rev. B **48**, 11789 (1993).

[91] B. Arnaud and M. Alouani, Phys. Rev. B **63**, 085208 (2001).

[92] B. Adolph, J. Furthmüller, and F. Bechstedt, Phys. Rev. B **63**, 125108 (2001).

[93] S. Lebègue, M. Alouani, B. Arnaud, and W. E. Pickett, Europhys. Lett. **63**, 562 (2003).

[94] S. Lebègue, B. Arnaud, M. Alouani, and P. E. Bloechl, Phys. Rev. B **67**, 155208 (2003).

[95] E. L. Shirley, Phys. Rev. B **58**, 9579 (1998).

[96] J. Isidorsson, I. A. M. E. Giebels, H. Arwin, and R. Griessen, Phys. Rev. B **68**, 115112 (2003).

[97] C. Moysés et al., J. Appl. Phys. **98**, 096106 (2005).

[98] P. Vajeeston, P. Ravindran, A. Kjekshus, and H. Fjellvåg, Phys. Rev. Lett. **89**, 175506 (2002).

[99] J. L. Martins, Phys. Rev. B **41**, 7883 (1990).

[100] M. Bortz, B. Bertheville, G. Böttger, and K. Yvon, J. Alloys Compd. **287**, L4 (1999).

[101] R. Yu and P. K. Lam, Phys. Rev. B **37**, 8730 (1988).

[102] J. W. Turley and H. W. Rinn, Inorg. Chem. **8**, 18 (1969).

[103] E. Rönnebro, D. Noréus, K. Kadir, A. Reiser, and B. Bogdanovíc, J. Alloys Compd. **299**, 101 (2000).

[104] S. C. Chung and H. Morioka, J. Alloys Compd. **372**, 92 (2004).

[105] A. Aguayo and D. J. Singh, Phys. Rev. B **69**, 155103 (2004).

[106] P. Vajeeston, P. Ravindran, R. Vidya, H. Fjellvåg, and A. Kjekshus, Apl. Phys. Lett. **82**, 6951 (2003).

[107] B. C. Hauback, H. W. Brinks, and H. Fjellvåg, J. Alloys Compd. **346**, 184 (2002).

[108] Y. Song, R. Singh, and Z. X. Guo, J. Phys. Chem. B **110**, 6906 (2006).

[109] P. Vajeeston, P. Ravindran, R. Vidya, H. Fjellvåg, and A. Kjekshus, Phys. Rev. B **68**, 212101 (2003).

[110] P. Vajeeston, P. Ravindran, A. Kjekshus, and H. Fjellvåg, Phys. Rev. B **69**, 020104 (2004).

[111] H. W. Brinks and B. C. Hauback, J. Alloys Compd. **354**, 143 (2003).

[112] B. C. Hauback, H. W. Brinks, C. M. Jensen, K. Murphy, and A. J. Maeland, J. Alloys Compd. **358**, 142 (2003).

[113] J. C. Slater and W. Shockley, Phys. Rev. **50**, 705 (1936).

[114] J. Senegas, M. Villepastour, and B. Bennetot, J. Phys. Chem. Solids **42**, 1061 (1981).

[115] B. Bogdanovic et al., J. Alloy. Compd. **350**, 246 (2003).

[116] G. Majer et al., J. Alloy. Compd. **404**, 738 (2005).

[117] S. G. Louie, S. Froyen, and M. L. Cohen, Phys. Rev. B **26**, 1738 (1982).

[118] G. Mills, H. Jonsson, and G. K. Schenter, Surface Science **324**, 305 (1995).

[119] H. Jonsson, G. Mills, and K. W. Jacobsen, *Classical and Quantum Dynamics in Condensed Phase Simulations*, World Scientific, 1998.

[120] P. Vajeeston, P. Ravindran, A. Kjekshus, and H. Fjellvåg, J. Alloy. Compd. **387**, 97 (2005).

[121] X. Ke and I. Tanaka, Phys. Rev. B **71**, 024117 (2005).

[122] D. B. Sullenger and C. H. L. Kennard, Sci. Am. **215**, 96 (1966).

[123] H. Zhang, Q. Zhang, I. Tang, and L. C. Qin, J. Am. Chem. Soc. **127**, 2862 (2005).

[124] J. Nagamatsu, N. Nakagawa, T. Muranaka, Y. Zenitani, and J. Akimitsu, Nature **410**, 63 (2001).

[125] J. L. Hoard and A. E. Newkirk, J. Am. Chem. Soc. **82**, 70 (1960).

[126] J. L. Hoard, D. B. Sullenger, C. H. L. Kennard, and R. E. Hughes, J. Solid State Chem. **1**, 268 (1970).

[127] G. A. Slack, C. I. Hejna, M. F. Garbauskas, and J. S. Kasper, J. Solid State Chem. **76**, 52 (1988).

[128] G. A. Slack, C. I. Hejna, M. Garbauskas, and J. S. Kasper, J. Solid State Chem. **76**, 64 (1988).

[129] D. W. Bullett, J. Phys-c-solid. State. Phys. **15**, 415 (1982).

[130] E. D. Jemmis and M. M. Balakrishnarajan, J. Am. Chem. Soc. **123**, 4324 (2001).

[131] E. D. Jemmis, M. M. Balakrishnarajan, and P. D. Pancharatna, J. Am. Chem. Soc. **123**, 4313 (2001).

[132] Y. Imai, M. Mukaida, M. Ueda, and A. Watanabe, J. Alloy. Compd. **347**, 244 (2002).

[133] D. L. V. K. Prasad, M. M. Balakrishnarajan, and E. D. Jemmis, Phys. Rev. B **72**, 195102 (2005).

[134] A. Masago, K. Shirai, and H. Katayama-Yoshida, Phys. Rev. B **73**, 104102 (2006).

[135] W. Kohn, Rev. Mod. Phys. **71**, 1253 (1999).

[136] N. Vast et al., Phys. Status Solidi B-Basic Res. **198**, 115 (1996).

[137] N. Vast et al., Phys. Rev. Lett. **78**, 693 (1997).

[138] G. Will and B. Kiefer, Z. Anorg. Allg. Chem. **627**, 2100 (2001).

[139] R. J. Nelmes et al., Phys. Rev. B **47**, 7668 (1993).

[140] N. Vast, J. M. Besson, S. Baroni, and A. D. Corso, Comput. Mater. Sci. **17**, 127 (2000).

[141] D. Li, Y. Xu, and W. Y. Ching, Phys. Ref. B **45**, 5895 (1992).

[142] C. Mailhiot, J. B. Grant, and A. K. McMahan, Phys. Ref. B **42**, 9033 (1990).

[143] U. Häussermann, S. I. Simak, R. Ahuja, and B. Johansson, Phys. Rev. Lett. **90**, 065701 (2003).

[144] D. M. Bylander, L. Kleinmann, and S. Lee, Phys. Rev. B **42**, 1394 (1990).

[145] F. H. Horn, J. Appl. Phys. **30**, 1611 (1959).

[146] M. Terauchi, Y. Kawamata, M. Tanaka, M. Takeda, and K. Kimura, J. Solid State Chem. **133**, 156 (1997).

[147] B. Callmer, Acta Crystallogr. Sect. B-Struct. Commun. **33**, 1951 (1977).

[148] M. Prudenziati, G. Majni, and A. Alberigi Quaranta, J. Phys. Chem. Solids **33**, 245 (1972).

[149] M. Prudenziati, J. Less-Common Met. **47**, 113 (1976).

[150] D. N. Sanz, P. Loubeyre, and M. Mezouar, Phys. Rev. Lett. **89**, 245501 (2002).

[151] C. L. Beckel, M. Yousaf, M. Z. Fuka, S. Y. Raja, and N. Lu, Phys. Rev. B **44**, 2535 (1991).

[152] D. C. Wallace, *Thermodynamics of Crystals*, Wiley, New York, 1972.

[153] T. J. Frankcombe, G. J. Kroes, and A. Züttel, Chem. Phys. Lett. **405**, 73 (2005).

[154] K. Miwa, N. Ohba, S. I. Towata, Y. Nakamori, and S. I. Orimo, Phys. Rev. B **69**, 245120 (2004).

[155] Y. Wu and R. M. Mohring, Abstr. Pap. Am. Chem. Soc. **226**, U576 (2003).

[156] M. Au, A. Jurgensen, and K. Zeigler, J. Phys. Chem. B **110**, 26482 (2006).

[157] J. H. Wee, K. Y. Lee, and S. H. Kim, Fuel Process. Technol. **87**, 811 (2006).

[158] M. An and A. Jurgensen, J. Phys. Chem. B **110**, 7062 (2006).

[159] K. Miwa, N. Ohba, S. Towata, Y. Nakamori, and S. Orimo, J. Alloy. Compd. **404**, 140 (2005).

[160] Y. Nakamori et al., J. Power Sources **155**, 447 (2006).

[161] K. Miwa et al., Phys. Rev. B **74**, 155122 (2006).

[162] Y. Nakamori, H. W. Li, K. Miwa, S. Towata, and S. Orimo, Mater. Trans. **47**, 1898 (2006).

[163] P. Vajeeston, P. Ravindran, A. Kjekshus, and H. Fjellvåg, Appl. Phys. lett. **89**, 071906 (2006).

[164] X. B. Yu, D. M. Grant, and G. S. Walker, Chem. Commun. **37**, 3906 (2006).

[165] K. Chłopek, C. Frommen, A. Léon, O. Zabara, and M. Fichtner, J. Mater. Chem. **17**, 3496 (2007).

[166] M. J. van Setten, G. A. de Wijs, and G. Brocks, J. Phys. Chem. C **111**, 9592 (2007).

[167] M. J. van Setten, M. A. Uittewaal, G. A. de Wijs, and R. A. de Groot, J. Am. Chem. Soc. **129**, 0631246 (2007).

[168] H. I. Schlesinger, H. C. Brown, and E. K. Hyde, J. Am. Chem. Soc. **75**, 209 (1953).

[169] D. S. Marynick and W. N. Lipscomb, Inorg. Chem. **11**, 820 (1972).

[170] G. Smith et al., Solid State Comm. **67**, 491 (1988).

[171] P. Vajeeston, P. Ravindran, A. Kjekshus, and H. Fjellvåg, Appl. Phys. Lett. **84**, 34 (2004).

[172] E. S. Makarov and K. I. Tobelko, Doklady Akademii Nauk SSSR **275**, 91 (1984).

[173] O. M. Løvvik, Phys. Rev. B **71**, 144111 (2005).

[174] M. J. van Setten, V. A.Popa, G. A. de Wijs, and G. Brocks, Phys. Rev. B **75**, 035204 (2007).

[175] T. Matsunaga et al., J. Alloys Compd. , doi:10.1016/j.jallcom.2007.05.054. (2007).

[176] R. Cerný, Y. Filinckuk, H. Hagemann, and K. Yvon, Angew. Chem. Int. Ed. **46**, 5765 (2007).

[177] J. Her et al., Acta Cryst. **B63**, 561 (2007).

[178] M. R. Hartman, J. J. Rush, T. J. Udovic, R. C. Bowman, and S. J. H. Jr., J. Solid State Chem. **180**, 1298 (2007).

[179] M. Born, Verhandl. Deut. Physik. Ges. **21**, 679 (1919).

[180] F. Seitz and D. Turnbull, *Solid State Physics 16*, Academic press, New York and London, 1965.

[181] R. D. Shannon, Acta. Cryst. A **32**, 751 (1976).

[182] M. J. van Setten, G. A. de Wijs, M. Fichtner, and G. Brocks, Mater. Chem. , submitted (2008).

[183] M. B. Smith and G. E. Bass Jr., J. Chem. Eng. Data **8**, 342 (1963).

[184] J. F. Stampfer, C. E. Holley, and J. F. Suttle, J. Am. Chem. Soc. **82**, 3504 (1960).

[185] B. Bogdanovíc and B. Spliethoff, Int. J. Hydrog. Energy **12**, 863 (1987).

[186] M. Bortz et al., J. Alloy. Compd. **279**, L8 (1998).

[187] G. Liang, J. Huot, S. Boily, A. V. Neste, and R. Schulz, J. Alloy. Compd. **291**, 295 (1999).

[188] S. Bouaricha et al., J. Alloy. Compd. **297**, 282 (2000).

[189] G. Liang, J. Huot, S. Boily, A. V. Neste, and R. Schulz, J. Alloy. Compd. **297**, 261 (2000).

[190] H. Y. Leng et al., J. Phys. Chem. B **108**, 8763 (2004).

[191] J. J. Reilly and R. H. Wiswall, Inorg. Chem. **7**, 2254 (1968).

[192] K. Yvon, J. Schefer, and F. Stucki, Inorg. Chem. **20**, 2776 (1981).

[193] D. Noreus and P. E. Werner, Mater. Res. Bull. **16**, 199 (1981).

[194] J. L. Soubeyroux, D. Fruchart, A. Mikou, M. Pezat, and B. Darriet, Mater. Res. Bull. **19**, 1119 (1984).

[195] P. Zolliker, K. Yvon, J. D. Jorgensen, and F. J. Rotella, Inorg. Chem. **25**, 3590 (1986).

[196] M. L. Post and J. J. Murray, J. Less-common. Metals. **134**, 15 (1987).

[197] K. J. Zeng, T. Klassen, W. Oelerich, and R. Bormann, J. Alloy. Compd. **283**, 151 (1999).

[198] M. S. Liao and Q. E. Zhang, Inorg. Chem. **36**, 396 (1997).

[199] G. N. Garcia, J. P. Abriata, and J. O. Sofo, Phys. Rev. B **59**, 11746 (1999).

[200] G. N. Garcia, J. P. Abriata, and J. O. Sofo, Phys. Rev. B **65**, 064306 (2002).

[201] U. Häussermann, H. Blomqvist, and D. Noreus, Inorg. Chem. **41**, 3684 (2002).

[202] W. R. Myers, L. W. Wang, T. J. Richardson, and M. D. Rubin, J. Appl. Phys. **91**, 4879 (2002).

[203] J. P. Darnaudery, M. Pezat, and B. Darriet, J. Less-Common Met **92**, 199 (1983).

[204] Y. Q. Lei, Y. M. Wu, Q. M. Yang, J. Wu, and Q. D. Wang, Z. Phys. Chemie-Int. J. Res. Phys. Chem. Chem. Phys. **183**, 379 (1994).

[205] D. L. Sun et al., J. Alloy. Compd. **231**, 621 (1995).

[206] K. Ikeda, S. Orimo, A. Züttel, L. Schlapbach, and H. Fujii, J. Alloy. Compd. **280**, 279 (1998).

[207] G. Liang, S. Boily, J. Huot, A. van Neste, and R. Schulz, Mater. Sci. Forum. **269-2**, 1049 (1998).

[208] J. L. Bobet, E. Akiba, Y. Nakamura, and B. Darriet, Int. J. Hydrog. Energy **25**, 987 (2000).

[209] J. L. Bobet et al., J. Alloy. Compd. **345**, 280 (2002).

[210] T. Sato, H. Blomqvist, and D. Noreus, J. Alloy. Compd. **356**, 494 (2003).

[211] L. Q. Li, I. Saita, K. Saito, and T. Akiyama, J. Alloy. Compd. **372**, 218 (2004).

[212] M. V. Simicic, M. Zdujic, R. Dimitrijevic, L. Nikolic-Bujanovic, and N. H. Popovic, J. Power Sources **158**, 730 (2006).

[213] R. A. H. Niessen and P. H. L. Notten, Electrochem. Solid State Lett. **8**, A534 (2005).

[214] P. Vermeulen et al., Electrochem. Solid State Lett. **9**, A520 (2006).

[215] D. M. Borsa et al., Appl. Phys. Lett. **88**, 241910 (2006).

[216] D. M. Borsa et al., Phys. Rev. B **75**, 205408 (2007).

[217] P. van der Sluis, M. Ouwerkerk, and P. A. Duine, Appl. Phys. Lett. **70**, 3356 (1997).

[218] J. Isidorsson, I. A. M. E. Giebels, R. Griessen, and M. Di Vece, Appl. Phys. Lett. **80**, 2305 (2002).

[219] M. Pasturel et al., Appl. Phys. Lett. **89**, 021913 (2006).

[220] D. Lupu, R. Grecu, and S. I. Farcas, Z. Phys. Chemie-Int. J. Res. Phys. Chem. Chem. Phys. **181**, 143 (1993).

[221] P. Selvam, B. Viswanathan, and V. Srinivasan, J. Electron Spectrosc. Relat. Phenom. **46**, 357 (1988).

[222] D. Lupu, R. Sarbu, and A. Biris, Int. J. Hydrog. Energy **12**, 425 (1987).

[223] M. D. Vece et al., Mater. Chem. Phys. **91**, 1 (2005).

[224] R. J. Westerwaal et al., J. Appl. Phys. **100**, 063518 (2006).

[225] W. Lohstroh personal communication.

[226] T. J. Frankcombe, G. J. Kroes, and A. Züttel, Chem. Phys. Lett. **405**, 73 (2005).

[227] J. F. Herbst and L. G. Hector, Phys. Rev. B **72**, 125120 (2005).

[228] P. Zolliker, K. Yvon, J. D. Jorgensen, and F. J. Rotella, Inorg. Chem. **25**, 3590 (1986).

[229] P. Zolliker, K. Yvon, P. Fischer, and J. Scheffer, Inorg. Chem. **24**, 4177 (1985).

[230] J. J. Didisheim et al., Inorg. Chem. **23**, 1953 (1984).

[231] A. C. Lokhorst, *Relections on Switchable Mirror Devices*, PhD thesis, Vrije Universiteit Amsterdam, 2006.

[232] M. Slaman et al., Sens. Actuator B-Chem. **123**, 538 (2007).

[233] S. Er, M. J. van Setten, G. A. de Wijs, and G. brocks, in preparation (2007).

[234] D. Kyoi et al., J. Alloy. Compd. **372**, 213 (2004).

[235] P. Vermeulen, R. A. H. Niessen, and P. H. L. Notten, Electrochem. Commun. **8**, 27 (2006).

[236] B. Silvi and A. Savin, Nature **371**, 683 (1994).

[237] R. Gremaud et al., Adv. Mater. **19**, 2813 (2007).

[238] R. Gremaud, M. Slaman, H. Schreuders, B. Dam, and R. Griessen, Appl. Phys. Lett. **91**, 231916 (2007).

[239] P. H. P. Blaha, K. Schwarz, Phys. Rev. Lett. **54**, 1192 (1985).

[240] C. Pickard and F. Mauri, Phys. Rev. B **63**, 245101 (2001).

[241] P. H. L. Notten et al., J. Power Sources **129**, 45 (2004).

[242] A. Marashdeh, R. A. Olsen, O. M. Løvvik, and G. J. Kroes, J. Phys. Chem. C **111**, 8206 (2007).

[243] R. Cantelli et al., J. Alloy. Compd. **446**, 260 (2007).

[244] W. Lohstroh and M. Fichtner, Phys. Rev. B **75**, 184106 (2007).

Samenvatting

In 1873 beschreef Jules Verne in “L’Île mystérieuse” al een verre toekomst waarin, door elektriciteit gesplitst water de brandstof zou zijn. De kolenruimen van schepen en de tenders van locomotieven zouden vervangen worden door tanks waarin waterstof en zuurstof opgeslagen kunnen worden.

Waterstof als brandstof gebruiken is gebaseerd op de volgende reactie:

$$\text{waterstof} + \text{zuurstof} \rightarrow \text{water} + \text{energie} \tag{14.3}$$

of, in chemische formules

$$2H_2 + O_2 \rightarrow 2H_2O \tag{14.4}$$

Zoals aan de reactie te zien is, is het enige uitlaatgas van deze reactie is waterdamp. Waterstof kan gebruikt worden in een verbrandingsmotor. Als er echter lucht wordt gebuikt voor de zuurstof toevoer onstaan er ook zuurstof-stikstof verbindingen (NOx). Een schonere en efficiëntere manier is het gebruik van een brandstof cel. In een brandstof cel is het centrale element een membraan dat alleen protonen, waterstof kernen, doorlaat. Aan de ene kant van het membraan worden de waterstofmoleculen aangevoerd en aan de andere kant de zuurstofmoleculen. De waterstofmoleculen splitsen in twee protonen en twee elektronen. De protonen gaan door het membraan en de elektronen gaan door een elektrische circuit, bijvoorbeeld een elektromotor of een lamp, naar de andere kant van het membraan. Aan de andere kant worden zuurstofmoluculen gesplitst en vormen samen met de protonen en de elektronen water.

Dit klinkt allemaal heel mooi. Vooral omdat je het proces andersom, met een spanningsbron in plaats van een motor, kan gebruiken om van water waterstof en zuurstof te maken. Het probleem zit hem er echter in dat het waterstof opgeslagen moet worden. Als je een auto 500 km wil laten rijden heb je ongeveer 5 kg waterstof nodig. Onder normale druk neemt 5 kg waterstof echter een volume in van 55.000 liter. Zelfs onder een druk van 800 bar, 800 keer de luchtdruk op zee niveau of de druk op ongeveer 9 km diepte in zee, zou een waterstoftank nog 4 keer zoveel ruimte innemen als een benzinetank om dezelfde afstand te kunnen rijden.

Dit opslagprobleem zou kunnen worden opgelost door waterstof op te slaan in (complexe) metaalhydriden. Hierin is waterstof opgenomen in een metaal, als losse atomen tussen de metaal atomen, of als onderdeel van clusters in een complexe structuur. Op deze manier kan, in principe, een dichtheid van waterstof worden bereikt die drie keer zo groot is als die van vloeibaar waterstof. In het onderzoek beschreven in dit proefschrift zijn met behulp van computerberekeningen dit soort opslagmaterialen onderzocht.

De berekeningen zijn gedaan met de zogenaamde “dichtheids functionaal theorie”. Deze theorie maakt het mogelijk om eigenschappen van materialen te berekenen op het niveau van de quantum mechanica, door te rekenen met de elektronendichtheid in plaats van de zogenaamde elektronen-golffuncties. Ter vergelijking, in termen van golffuncties is het alleen mogelijk om de eigenschappen van simpele moleculen zoals H_2O (het watermolecuul) exact te berekenen.

Een materiaal dat veel is bestudeerd in het kader van waterstof opslag is Mg_2NiH_4, de zogenaamde hydride van een legering van magnesium en nickel. Als het wordt verwarmd komt het waterstof eruit en blijft er Mg_2Ni over. De temperatuur waarbij dit gebeurd is echter te hoog voor praktisch gebruik. Uit onze berekeningen blijkt dat het mogelijk is om deze temperatuur aan te passen door andere transitiemetalen zoals ijzer en koper toe te voegen.

Een ander materiaal gebaseerd op magnesium, magnesium-titanium in dunne films, kan gebruikt worden om waterstof te detecteren. Als er geen waterstof aanwezig is zijn deze films weerspiegelend, als de film met waterstof in contact komt ontstaat er een hydride en wordt de film zwart. We hebben in dit proefschrift een verklaring gegeven voor deze zogenaamde zwarte fase.

Een klasse van potentiele opslag materialen zijn de alanaten. Alanaten bestaan uit aluminium, waterstof en een metaal uit de eerste of tweede kolom van het periodiek systeem, bijvoorbeeld natrium of magnesium. Een van de resultaten in dit proefschrift is dat in de alanaten de elektronische en optische eigenschappen in grote mate hetzelfde zijn en niet veel afhangen van het specifieke metaal dat ze bevatten.

Een andere belangrijke klasse materialen zijn de boranaten. Deze lijken op de alanaten maar bevatten boor in plaats van aluminium. Omdat boor veel lichter is dan aluminium bevatten de boranaten per kilogram meer waterstof dan de alanaten. We hebben laten zien dat de stabiliteit van de alanaten en boranaten op een redelijk eenvoudige manier te modeleren valt.

Een bepalende factor om te bepalen of een materiaal geschikt is voor waterstofopslag is de energie die nodig is om het waterstof vrij te laten komen, de zogenaamde enthalpie van de desorptie reactie. Als deze de juiste waarde heeft kan de restwarmte die een brandstofcel produceert worden gebuikt om het waterstof uit het opslagmateriaal te halen. Om deze energie te berekenen moet de structuur van het materiaal zelf en die van de materialen die overblijven als het waterstof eruit is bekend zijn. Van boor, het vijfde element in het periodiek systeem, was de structuur bij lage temperaturen niet duidelijk. We hebben aangetoond dat de kristalstructuur van elementair boor bij lage temperaturen hetzelfde is als bij hoge temperaturen.

Pas recentelijk is de structuur van magnesiumboranaat bepaald. Deze structuur is zeer veel complexer dan die van de andere boranaten en alanaten. Berekeningen aan magnesiumboranaat kosten daardoor relatief veel computertijd. We hebben laten zien dat de energie die nodig is om het waterstof uit magnesiumboranaat te halen precies goed is voor waterstof opslag. In de toekomst zal moeten blijken of magnesium boranaat ook reversibel kan worden gemaakt, dat wil zeggen, of het mogelijk is om ook weer magnesiumboranaat te vormen door de reactie producten onder waterstofdruk te zetten. Hiervoor zal vermoedelijk nanostructurering van het materiaal en het gebruik van een geschikte catalizator nodig zijn. Tevens zal moeten worden onderzocht of het mogelijk is om de desorptiereactie, het eruit laten komen van het waterstof, te versnellen.

Publications

- *Ab initio* study of $Mg(AlH_4)_2$
  M.J. van Setten, V.A. Popa, G.A. de Wijs, and G. Brocks
  Phys. Rev. B **72**, 073107 (2005)
- Electronic structure and optical properties of lightweight metal hydrides
  M.J. van Setten, V.A. Popa, G.A. de Wijs, and G. Brocks
  Phys. Rev. B **75**, 035204 (2007)
- Thermodynamic Stability of Boron: The Role of Defects and Zero Point Motion
  M.J. van Setten, M.A. Uijttewaal, G.A. de Wijs, and R.A. de Groot
  J. Am. Chem. Soc. **129**, 0631246 (2007)
- Model for the Formation Energies of Alanates and Boranates
  M.J. van Setten, G.A. de Wijs, and G. Brocks
  J. Phys. Chem. C **111**, 9592 (2007)
- *Ab initio* study of the effects of transition metal doping of Mg_2NiH_4
  M.J. van Setten, G.A. de Wijs, and G. Brocks
  Phys. Rev. B **76**, 075125 (2007)
- Electronic structure & formation enthalpies of hydroaluminates & hydroborates
  M.J. van Setten
  MS 2192 Encyclopedia of Materials: Science and Technology-Updates (invited)
- HF Species and Dissolved Oxygen on the Epitaxial Lift-Off Process of GaAs Using AlAsP Release Layers
  A.T.J. van Niftrik, J.J. Schermer, G.J. Bauhuis, P. Mulder, P.K. Larsen, **M.J. van Setten**, J.J. Attema, N.C.G. Tan, and J.J. Kelly
  J. Electrochem. Soc. **155**, D35 (2008)
- A first-principles study of the electronic structure and stability of $Be(BH_4)_2$
  M.J. van Setten, G.A. de Wijs, and G. Brocks
  Phys. Rev. B **77**, 165115 (2008)
- A density functional study of α-$Mg(BH_4)_2$
  M.J. van Setten, G.A. de Wijs, M. Fichtner, and G. Brocks
  under review, Matter. Chem.
- First principles modeling of magnesium titanium hydrides
  S. Er, **M.J. van Setten**, G.A. de Wijs, and G. Brocks
  to be submitted

- First principles study of the optical properties of $Mg_xTi_{(1-x)}H_2$
  M.J. van Setten, S. Er, G. Brocks, R.A. de Groot, and G.A. de Wijs
  to be submitted

Curriculum Vitae

Michiel Jan van Setten was born in the Netherlands in Vlissingen on 14th of April 1978. Here he attended primary school. He went to secondary school in Goes at the St. Willibrord college. In 1997 he moved to Utrecht to study theoretical physics and mathematics at the University of Utrecht. It was here that, in 1998, he met his future wife, Vera van Noort, with whom he married on the 23th of December 2002. Together they moved to Arnhem in 2003.

On the 13th of February 2004 Michiel received his Master of Science in theoretical physics. His graduation work was conducted at the group of professor H.T.C Stoof and consisted of a theoretical study of molecular Bose Einstein condensates. Adjacently he started his PhD. research at the Electronic Structure of Materials group of professor R.A. de Groot at the Radboud University Nijmegen under the supervision of dr. G.A. de Wijs on the 1st of March of that year. Starting 1st of July 2007 he spent half a year as a guest scientist at the hydrogen storage group of dr. M. Fichtner at the Institut für Nanotechnologie in the Forschungszentrum Karlsruhe.

His current research focuses on atomistic modeling of light metal hydrides in view of their possible applicability as hydrogen storage devices. As hydrogen is seen as the fuel of the future this research has, besides its fundamental challenges, a strong social and economical motivation. The research described in this thesis was conducted within the ACTS sustainable hydrogen program. Working in this program implied working on the crossing point of physics, chemistry, and materials science and having a strong interaction with several experimental groups. These two aspects have been both inspiring and fruitful.

Besides his academic interests Michiel likes to play he bassoon in symphonic orchestras as well as military bands and chamber music ensembles. During his stay in Utrecht he undertook several large musical projects, among others the organization of the fully staged production of the opera Falstaff by Giuseppe Verdi with 9 performances in Utrecht and 5 in Italy. On the 2nd of March 2005 his son Raphael and on de 14th March 2008 his daughter Gabrielle are born.

Radboud University Nijmegen

Complex Hydrides

This thesis contains a collection of Density Functional studies of complex hydrides that were performed within the ACTS Sustainable hydrogen program. The first part deals with alanates and boranates. The electronic structure, optical properties, and thermodynamics of the hydrogen desorption reactions are studied. Additionally, a model to describe the formation enthalpy of these materials is presented. An intermezzo in this part is formed by a discussion of the ground state of elemental boron. The second part contains studies of magnesium based complex hydrides. One chapter deals with the effects on the optical properties and thermodynamics of doping of Mg_2NiH_4 with transition metals, the other with the mysterious black state of magnesium titanium hydrides.

ISBN/EAN 978-90-6464-254-8